Kent Academic Repository

Makin, Sally Victoria (2019) *Molecular jets and outflows from young stellar objects in Cygnus-X, Auriga, and Cassiopeia.* **Doctor of Philosophy (PhD) thesis, University of Kent,.**

Downloaded from

The version of record is available from

This document version

DOI for this version

Licence for this version

Additional information

Versions of research works

UNIVERSITY OF KENT

DOCTORAL THESIS

Molecular jets and outflows from young stellar objects in Cygnus-X, Auriga, and Cassiopeia

Author:
Sally Victoria MAKIN

Supervisor:
Dr. Dirk FROEBRICH

A thesis submitted in fulfilment of the requirements
for the degree of Doctor of Philosophy

in the

Centre for Astrophysics and Planetary Science
School of Physical Sciences

January 30, 2019

Declaration of Authorship

I, Sally Victoria MAKIN, declare that this thesis titled, "Molecular jets and outflows from young stellar objects in Cygnus-X, Auriga, and Cassiopeia" and the work presented in it are my own. I confirm that:

- This work was done wholly or mainly while in candidature for a research degree at this University.

- Where any part of this thesis has previously been submitted for a degree or any other qualification at this University or any other institution, this has been clearly stated.

- Where I have consulted the published work of others, this is always clearly attributed.

- Where I have quoted from the work of others, the source is always given. With the exception of such quotations, this thesis is entirely my own work.

- I have acknowledged all main sources of help.

- Where the thesis is based on work done by myself jointly with others, I have made clear exactly what was done by others and what I have contributed myself.

Signed:

_____

Date:

_____

Abstract

Molecular jets and outflows from young stellar objects in Cygnus-X, Auriga, and Cassiopeia

by Sally Victoria MAKIN

An unbiased, systematic survey for jets and outflows from young stars has been performed in two distinct and different regions in the Galactic plane. It utilised the $1-0\,S(1)$ near-infrared line of molecular hydrogen (H_2) to trace shock-excited emission, using data from the UKIRT Widefield Infrared Survey for H_2 (UWISH2) survey. A total of 572 outflows were found in the high-mass star forming complex of Cygnus-X, and 98 in the low-mass regions of Auriga and Cassiopeia. Of these outflows found, 84 % are entirely new discoveries, and now 40 % of all the currently known H_2 outflows are a result of the UWISH2 survey. The properties of the outflows were consistently measured and a large statistical sample has been built. Similarities and differences between the outflow populations in the two regions were explored in order to discover which properties are universal and which depend on local factors. In both regions, most outflows are located in isolated (60 %) and not clustered environments, but those from clusters are longer and more luminous. Almost fifty new infrared cluster candidates have also been discovered as a result of this work, and the typical cluster is around 0.5 pc in diameter. About 10 % of outflows form crossing pairs of outflows, and 40 % of these show signs of precession compared to 20 % in the general population.

The outflow position angles are in agreement with a homogeneous distribution. Most of the outflows are driven by protostars (Class 0/I) rather than the more evolved young stellar objects (Class II), as determined using their mid-infrared magnitudes. The typical outflow has a length of < 0.4 pc, and is slightly asymmetric with one lobe around 30 % longer than the other. The length distribution follows an exponential behaviour and there appears to be a maximum length. The typical outflow luminosity is faint ($1 \times 10^{-3}\,L_\odot$) and most of the outflows are driven by low or intermediate-luminosity protostars. The lobe luminosity ratios (the faint lobe over the bright lobe) are highly asymmetric in H_2. There is a correlation between the length and luminosity of an outflow, and these do not depend on the evolutionary stage of the driving source. There is also a correlation between the luminosity of the driving source and the outflow luminosity, but the length distribution does not follow their behaviour. Therefore, the outflow lengths must also, to some extent, be governed by the density distribution of the local environment.

Acknowledgements

Contents

List of Figures

List of Tables

Chapter 1

Introduction

The formation of stars via the fragmentation and gravitational collapse of molecular clouds has become a burgeoning field of research over the past several decades. However, the interplay of physical processes involved in star formation are both complex and subtle. Every rule is swiftly followed by a dozen exceptions, and every question solved only raises new ones to be answered. A full theoretical understanding therefore remains elusive. The gravitational collapse of material towards a central object leads to the formation of rotating accretion disks. The accretion mechanism is also tied to the ejection of a fraction of that material along the axis of the disk's rotation in the form of a collimated stream, or jet. Jets can be observed when they collide with material in the local environment, creating shockwaves that excite the ambient material. This link between jets and accretion is well-observed and well-documented over multiple scales and from a range of astrophysical objects, but the processes governing this phenomenon are still poorly understood.

Jets from young stars were first detected in the 1950s independently by Herbig (1951) and Haro (1952) as nebulous objects near sites of star formation. Dubbed as Herbig-Haro (HH) objects, these emission-line nebulae are optical tracers of the interactions between supersonic jets and the local, ambient medium. However, it was not until 30 years later that they would be correctly recognised as such by Snell, Loren, and Plambeck (1980). Since then, numerous studies have been conducted and it is now understood that jets and outflows can be observed even at the earliest stages of star formation. This makes them excellent tracers of the very youngest stars, which are notoriously difficult to observe directly. Jets and outflows are therefore considered to be important signposts of early star formation activity that may otherwise go undetected.

Jets and outflows have since been observed using a wide range of atomic and molecular tracers, and each one reveals different aspects of the outflow evolution. The youngest stars are shrouded in dense envelopes of obscuring dust and gas which means, although jets were originally discovered using optical emission lines, HH objects are not visible close to their driving sources due to interstellar extinction. Infrared (IR) and radio tracers are best used to observe the shocked molecular gas close to the driving sources for a range of shock temperatures and densities, and to pinpoint the existence of deeply embedded, very young stars. Multi-wavelength views of outflows are ideal, but not feasible for large populations. Small, highly targeted samples or studies of individual, well-behaved objects which are assumed to be representative are a perennial problem. In terms of determining the "typical" properties of objects, observational feedback into theoretical models requires unbiased statistics with large populations.

The work presented in this Thesis attempts to address this issue and involves the systematic search for outflows from young stellar objects (YSOs) with the aim of building an unbiased sample of them. The rotational-vibrational molecular hydrogen $1-0\,S(1)$ line, observable at $\lambda = 2.122\,\mu m$ in the near-infrared (NIR), was used in the UWISH2 (UKIRT Widefield Infrared Survey for H_2) survey. This line is a proven, successful tracer of the hot ($T \sim 2\,000\,K$), shocked molecular gas produced during collisions between jets and the local environment. Two regions in the Galactic plane, distinctly different in terms of their environmental compositions and distributions, will be studied. Their outflows will be catalogued and characterised, then statistically analysed, in order to investigate their typical properties and whether those properties are likely a result of environmental factors, or develop as a result of protostellar evolution.

1.1 Structure of this Thesis

Theoretical background (Chapter 2)
In this Chapter, the current state of the literature will be reviewed. Important concepts from the Introductory Overview will be revisited in more detail, including a discussion of previous works in the field in order to support the methodology used in this Thesis. The motivations for this work, and the key questions being investigated, will be summarised at the end of this Chapter.

Methodology (Chapter 3)
The work was conducted during three distinct time periods, each of which builds upon the previous and lays the groundwork for the next. This Chapter has been separated into three chronological parts in order to reflect this as follows:

> **Part I: The search for extended H_2 emission** (Chapter 3.1)
> For the initial phase of this work, extended H_2 emission-line sources from the UWISH2 survey were systematically searched for, classified, and catalogued. Part I of this Chapter describes the methodology used in the automatic detection, and subsequent manual classification, of the H_2 emission features. Pertinent results from this work will then be presented.

> **Part II: Identifying outflows and their driving sources** (Chapter 3.2)
> Using the catalogue of extended H_2 emission-line sources as a basis, Part II details the systematic search for outflows and the measurement of their properties such as lengths, fluxes, position angles, etc. The methods detailed here were used to obtain the results presented in Chapter 4 for the Auriga and Cassiopeia region, and in Chapter 5 for Cygnus-X.

> **Part III: Determining distances toward the outflows** (Chapter 3.3)
> Part III describes the difficulties that are faced in determining accurate distances toward objects inside our own Galaxy, common methods for achieving this, and the method chosen for this work. The process of statistically correcting the smaller samples will be discussed. The results are presented in Chapter 6.

Results, part I: Outflows in Auriga and Cassiopeia (Chapter 4)
The results of the search for outflows in Auriga and Cassiopeia are presented in this Chapter. The

population of outflows in this region is comparable in size to those of previous surveys for outflows in H_2. The data and image sets associated with the results in this Chapter have been published and are available online.

Results, part II: Outflows in Cygnus-X (Chapter 5)

This Chapter presents a more detailed look at the population of outflows uncovered in Cygnus-X. This population is considerably larger than the population for Auriga and Cassiopeia, and a wider range of parameters were recorded for each outflow. Thus, this Chapter provides a more detailed census of outflows and their properties, with a larger statistical sample. The data and image sets associated with the results in this Chapter have been published and are available online.

Results, part III: Corrected distributions and multi-region comparison (Chapter 6)

Using more accurate distances obtained towards each outflow, the distributions of the outflow properties that depend upon the distance will be revised in this Chapter. Statistical corrections will be applied in order to account for uncertainties and to derive fits for the distributions of the lengths and luminosities of the outflows. A multi-regional comparison will be performed using data from previous surveys in other regions of the Galactic plane.

Discussion, conclusions, and future work (Chapter 7)

A detailed discussion of the findings presented in the previous three Chapters will lead into a summary of the main conclusions drawn from this work. Finally, there will be a brief highlight of follow-up works that could build upon the results presented in this Thesis in the future.

1.2   Publications

Peer-reviewed publications arising from the work undertaken in this thesis;

1. "Extended H_2 emission line sources from UWISH2"
   D. Froebrich, **S. V. Makin**, C. J. Davis, T. M. Gledhill, Y. Kim, B.-C. Koo, J. Rowles, J. Eislöffel,
   J. Nicholas, J. J. Lee, J. Williamson, A. S. M. Buckner, (2015), *MNRAS*, Volume 454, Issue 3,
   p. 2586

2. "YSO jets in the Galactic plane from UWISH2 - III. Jets and outflows in Cassiopeia and
   Auriga"
   D. Froebrich and **S. V. Makin**, (2016), *MNRAS*, Volume 462, Issue 2, p. 1444

3. "YSO jets in the Galactic plane from UWISH2 - IV. Jets and outflows in Cygnus-X"
   S. V. Makin and D. Froebrich, (2018), *ApJS*, Volume 234, Issue 1, Article 8
   (Associated press release)

4. "YSO jets in the Galactic plane from UWISH2 - VI. Outflow length and luminosity distri-
   butions across the Galactic Plane"
   S. V. Makin and D. Froebrich, (2019), (*in preparation*)

**Publications made with contributions from the Thesis author, not directly related to the
Thesis topic;**

1. "Optical brightness and colours of V 2492 Cyg before, during and after the recent record
   peak in brightness"
   D. Froebrich, J. Campbell-White, T. Zegmott, S. J. Billington, **S. V. Makin**, J. Donohoe, (2017),
   The Astronomer's Telegram, No. 10259

2. "A survey for variable young stars with small telescopes: First results from HOYS-CAPS"
   D. Froebrich, J. Campbell-White, A. Scholz, J. Eislöffel, T. Zegmott, S. J. Billington, J. Donohoe,
   S. V. Makin, R. Hibbert, R. J. Newport, R. Pickard, N. Quinn, T. Rodda, G. Piehler, M. Shelley,
   S. Parkinson, K. Wiersema, I. Walton, (2018), *MNRAS*, Volume 478, Issue 4, p. 5091

3. "Variability in IC 5070: two young stars with deep recurring eclipses"
   D. Froebrich, A. Scholz, J. Campbell-White, J. Crumpton, E. D'Arcy, **S. V. Makin**, T. Zegmott,
   S. J. Billington, R. Hibbert, R. J. Newport, C. R. Fisher, (2018), *RNAAS*, Volume 2, Issue 2,
   article 61

Chapter 2

Theoretical background

2.1 The interstellar medium

The interstellar medium, or ISM, is hugely varied in terms of composition and temperature, depending on the stellar population it contains and where in the Galaxy is it. The review of Ferrière (2001) details the recycling of the material in the ISM and the properties of each "phase". The ISM is also hugely important, in that it provides the raw materials from which stars can form, given the right conditions. Inside Giant Molecular Clouds (GMCs) the ISM is primarily composed of very cold ($T \sim 10 - 20$ K) dust and molecular gas (Goldsmith, 1987; Lagache et al., 1998). The density of material can vary due to supersonic turbulent motions inside the cloud, but typically ranges from 10^2 to 10^6 cm^{-3} (Larson, 2003). If the densities are high enough, gravitationally bound cores can form which collapse to form stars. This phase is usually referred to as the "molecular medium".

Clouds can also exist in more diffuse states with slightly higher temperatures ($T \sim 50 - 100$ K) and lower densities ($n \sim 20 - 50$ cm^{-3}) which are referred to as the "cold neutral" or "cold atomic" medium where the gas component is primarily neutral atomic hydrogen (HI). These clouds are often arrayed into sheets and filaments due to the presence of large-scale magnetic fields, but their lower density means that they are not fully opaque to light from stars behind them. As the light passes through, it can become linearly polarized by the dust grains in the magnetic fields (Davis and Greenstein, 1951) into the direction of the magnetic field.

At the surfaces of these clouds, radiation from the stellar population is sufficiently energetic ($\lambda < 0.112\,\mu$m) to dissociate H$_2$ molecules (Federman, Glassgold, and Kwan, 1979) creating photodissociation regions ($n \sim 0.2 - 0.5$ cm^{-3}). This phase is known as the "warm atomic" medium, given the typical temperature range of $6\,000 < \mathrm{T} < 10\,000$, and can be traced by the 21 cm forbidden HI emission line. Around O and B type stars, the ultraviolet (UV) radiation is capable of ionizing HI atoms completely ($\lambda < 0.0912\,\mu$m), forming a HII region around the star ($T \sim 10\,000$ K, Anderson et al. 2009), which will grow until the photoionisation of HI atoms is balanced by the recombination of ions and free electrons (the "warm ionised" medium). Since this process heats the surrounding gas, HII regions are surrounded by a photodissociation region.

Gas temperatures of up to around 10^6 K can be generated through powerful shocks from supernova remnants and stellar winds from groups of massive stars (e.g. Spitzer 1990), creating cavities with a hydrogen density as low as 6.5×10^{-3} cm^{-3} (Snowden et al., 1994) and producing diffuse soft
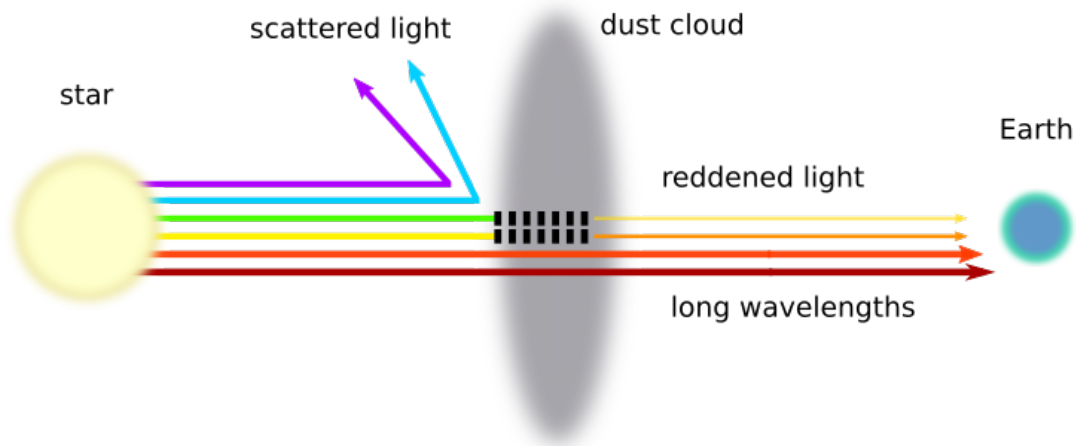
FIGURE 2.1: A cartoon representing interstellar extinction and reddening, with a cloud be-
tween the observer at Earth and the star being observed. Photons with wavelengths of the same
scale as typical dust grains in the ISM are either scattered, or absorbed by gases (black lines)
and re-radiated at longer wavelengths. Photons with wavelengths of scales much larger than
the dust grains can pass through the cloud with little interaction. Consequently, the star appears
dimmer and redder than it truly is.

X-ray emission. These expanding cavities can trigger star formation via compression of the clouds
that surround them.

Dust grains in the ISM can be heated by the absorption of photons to around $20\,\mathrm{K}$ (Dwek et
al., 1997), which cool again via the re-emission of a cascade of photons at longer wavelengths
than those originally absorbed. This is termed thermal dust emission, and is hugely important
in infrared (IR) and radio astronomy. Maps of this thermal emission show a strong correlation
between the column densities of dust and H_2 in molecular clouds (e.g. Boulanger et al. 1988;
Jenkins and Savage 1974; Schlegel, Finkbeiner, and Davis 1998) with a fairly constant $\sim 1\,\%$ dust
fraction by mass. The range of grain temperatures depends upon the sizes of the dust grains in a
particular cloud (Bernard et al., 1999; Lagache et al., 1999). Dust grains can also scatter photons
if the wavelength is about the same as the physical size of the grain, so that they do not reach the
observer. The degree of extinction A_λ from absorption and scattering therefore depends upon the
column density of material along the line of sight, the wavelength being observed, and upon the
distance toward the star (Gordon et al., 2003; Mathis, 1990).

The preferential absorption of light at shorter wavelengths by clouds has the effect of making
objects behind (or embedded inside) the cloud appear to be "redder" than they are (as demonstrated
in Fig. 2.1). This reddening effect can be measured via the "colour excess", i.e., the difference
between the colour index of a star as it is observed, and the colour index of an idealised object of
the same spectral type:

$$E(B - V) = A(B) - A(V) = (B - V) - (B - V)_0 \tag{2.1}$$

Where $A(B)$ and $A(V)$ are the extinction in the B and V bands respectively, $(B - V)$ is the

measured colour index and $(B - V)_0$ is the intrinsic colour of the object. This reddening is particularly noted around young stars, and can be caused by the dust surrounding them in their thick natal clouds, or in their accretion disk, or both. In the near-infrared (NIR), the extinction law (the variation in extinction as a function of wavelength) takes the form of:

$$\frac{A(\lambda)}{A(J)} = \left(\frac{\lambda}{1.25\,\mu\text{m}} \right)^{\alpha} \tag{2.2}$$

Where α is measured to be $\sim 1.70 \pm 0.08$ such that the colour excess $\text{E}(J - H)/\text{E}(H - K)$ is $\sim 1.61 \pm 0.04$ (Froebrich et al., 2007; Whittet et al., 1988). It is relatively constant across lines of sight, and an order of magnitude smaller than in the optical (Mathis, 1990).

2.2 Molecular hydrogen transitions

Molecular hydrogen (H_2) is a homonuclear diatomic molecule composed of two hydrogen atoms in a covalent bond (i.e., where a bonding pair of electrons are shared between the two atoms). It is one of the most abundant species in the Universe, after atomic hydrogen and helium. H_2 is most commonly found in cold ($T < 100\,\text{K}$), dense clouds in the interstellar medium where it usually forms. High column densities ($> 20\,\text{M}_\odot\,\text{pc}^{-2}$, Elmegreen 1993) are required in order to provide sufficient opacity to shield the gas from UV radiation, and in many molecular clouds, column densities can reach $\sim 100\,\text{M}_\odot\,\text{pc}^{-2}$ (Larson, 2003).

Inside such clouds, neutral hydrogen atoms (HI) can bind weakly to the surface of cold dust grains. They readily pair with other HI atoms that land upon the same grain due to the sharing of valence electrons. Once paired, the H_2 molecule evaporates from the surface of the dust grain, existing as H_2 gas in the molecular cloud (e.g. Duley and Williams 1993; Hollenbach and Salpeter 1971; Katz et al. 1999). Although H_2 can form during the gas phase, the formation rate is much lower than found in the presence of dust grains (see e.g. Shull and Beckwith 1982 and references therein for detailed information on molecular formation conditions and rates).

Neutral hydrogen (HI) is composed of a proton and a single electron. In atomic spectra, photons are absorbed and emitted electronically, i.e. by electrons transitioning between energy levels. For atomic hydrogen the longest wavelengths for which the electron can be excited out of the ground state is in the UV (Lyman α transition at $\lambda = 0.1216\,\mu\text{m}$). In the radio regime it can be detected via the 21 cm emission line (Ewen and Purcell, 1951). This line results from the fact that the ground state has two energy levels due to the spin state of the electron. When the electron spin is parallel to that of the proton, the energy is slightly higher ($\sim 5.874\,\mu\text{eV}$) than when the electron spin is anti-parallel. If the electron spin "flips" from parallel to anti-parallel, a photon is emitted with $\lambda = 21\,\text{cm}$. The Doppler shifts in this line are used to probe distant galaxies, while absorption (Hagen, Lilley, and McClain, 1955) can be used to resolve ambiguities in the distances towards objects in our own Galaxy (e.g. Clark, Radhakrishnan, and Wilson 1962; Williams and Davies 1954).
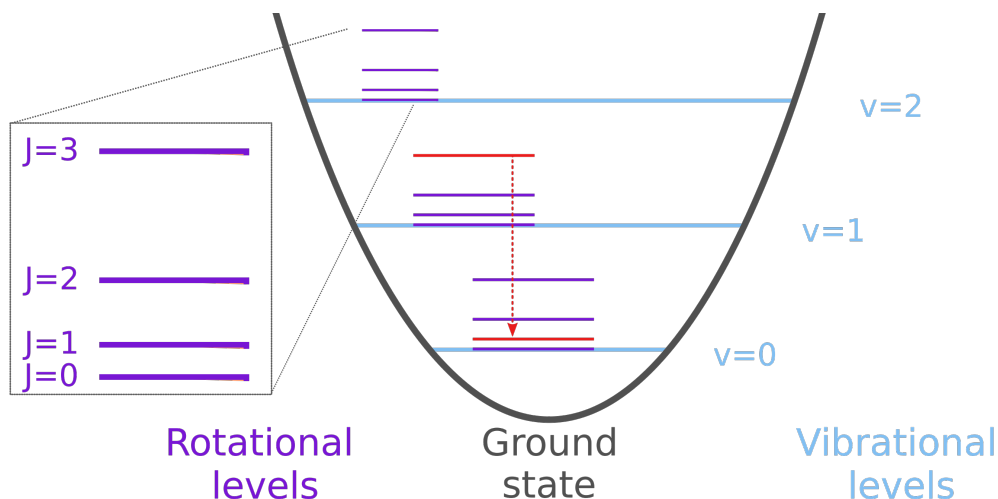
FIGURE 2.2: A schematic of the lowest rotational (purple) and vibrational (pale blue) energy levels in the electron ground state. The $1-0\,S(1)$ transition that is the subject of this Thesis is indicated with the red dotted arrow. This is the transition from $v = 1 \rightarrow 0$ and $J = 3 \rightarrow 1$.

The internal energy of a molecule can be described by the sum of its rotational, vibrational and electronic energies. Each electronic state has multiple vibrational energy levels (designated by vibrational quantum number v). Each vibrational state has, in turn, multiple rotational energy levels (designated by rotational quantum number J). A diagram of the lowest rotational-vibrational states associated with the electron ground state is shown in Fig. 2.2.

The rotation of a molecule causes a rotation in the electric dipole moment of that molecule. Transitions from higher to lower rotational energy levels generate microwave emission. However, H_2 is symmetrical, so unlike other molecular species such as CO, it has an electric dipole moment of zero. This means that electric dipole transitions ($\Delta J = 0,\ \pm 1$) are forbidden in H_2 and thus it cannot be detected at radio frequencies (Field, Somerville, and Dressler, 1966). These rules also prevent the pure vibrational emission that comes from changes in the electric dipole due to vibrations in the internal bonds of the molecule.

Nevertheless, electric quadrupole transitions are permitted, so it is much more common to observe H_2 in NIR emission via rotational-vibrational transitions. There are no selection rules for v-states in quadrupole transitions, and ΔJ can be -2 (O), 0 (Q), or +2 (S). However, it should be noted that $J = 0 \rightarrow 0$ and $J = 1 \rightarrow 0$ are excluded as forbidden dipole transitions. Transitions between two $J = {}^1/_2$ states are also not allowed. With regards to terminology, it is usual to refer to the vibrational transition first, followed by the letter corresponding to the ΔJ transition and the final J-state in brackets. Therefore, the line of H_2 with which this Thesis is concerned is the $1-0\,S(1)$ line, or the transition from $v = 1 \rightarrow 0$ and from $J = 3 \rightarrow 1$.

At the typical temperature conditions found in molecular clouds, H_2 cannot be excited and is almost exclusively in the ground state. The lowest allowed transition of H_2 that can be observed is the $0-0\,S(0)$ transition, with an excitation energy of 0.0439 eV and which can hence be seen in the mid-infrared (MIR; $T \sim 500$ K, $\lambda \sim 28.221\ \mu$m). Higher electronic and vibrational energy levels can be populated by the absorption of UV and optical photons with energies lower than the

dissociation energy of H_2 ($E < 4.48$ ev, $\lambda > 0.2767\,\mu$m). The molecule gradually returns to the ground state via a cascade of transitions from higher to progressively lower ro-vibrational states. Each transition sees the release of a photon whose energy corresponds to the change in quantum numbers. This can also occur through recombination after the molecule has been dissociated when the molecule is typically in a higher state of excitation. These photons have a range of energies across the NIR and are observed as diffuse, fluorescent emission, particularly in the H- and K-bands (e.g. Black and Dalgarno 1976).

An additional cause of excitation for H_2 molecules, and more relevant in the context of this work, is that caused by collisions in hot, dense gas from shocks (although collisional excitation can still lead to fluorescent emission). Shocks that are fast enough to compress and heat gas to sufficient temperatures to excite quadrupole emission in H_2 are typically generated by outflows, supernova remnants and planetary nebulae. Temperatures of a few thousand Kelvin are sufficient to populate the lowest vibrational levels, and shocked, excited H_2 is particularly well traced by the $1-0\,S(1)$ and $2-1\,S(1)$ transitions at $\lambda = 2.12\,\mu$m and $2.24\,\mu$m respectively (Smith, 1995; Wolfire and Konigl, 1991). This will be discussed further in Chapter 2.6.

2.3   Star formation

Since most star formation in the Galaxy occurs in the spiral arms (Herbst, 1975; Lynds, 1970) the perturbations caused by spiral shocks were predicted to be responsible for the formation of molecular clouds (Blitz and Shu, 1980; Dobbs, 2008; Dobbs, Bonnell, and Pringle, 2006). Inside the molecular clouds, supersonic turbulence can cause instabilities, which then leads to the fragmentation of the cloud into filaments and over-dense regions known as cores, the collapse of which forms stars (André et al., 2014; Elmegreen and Falgarone, 1996). The precise mechanisms by which this occurs are complex and not well understood, although it is being unravelled through observations of low-mass cores in nearby star-forming regions, and with simulations. The general evolutionary progression of a low-mass star can be characterised as shown in Fig. 2.3.

Historically, collapsing clouds have been modelled as spherical in order to simplify the mathematics (e.g. Hayashi 1966; Shu 1977). In a stable cloud that is in hydrostatic equilibrium, the Virial Theorem, $-E_{potential} = 2\,E_{kinetic}$ is satisfied. Therefore, in order for a stable cloud core to undergo runaway collapse, the density must become high enough for the mutual attraction felt by the molecules under gravity to overcome the outward-acting thermal pressure. In other words, $-E_{potential} > 2\,E_{kinetic}$. In order to find the critical conditions for instability, the system can be assumed to be spheroidal and composed of an ideal gas. Under such conditions, the thermal kinetic and gravitational potential energies are as follows:

$$E_{kinetic} = \frac{3\,N\,k_B\,T}{2} \quad \text{and} \quad E_{potential} = \frac{-3\,G\,M^2}{5\,R}, \tag{2.3}$$

where N is the number of particles, k_B is the Boltzmann constant and T is the temperature, and where G is the gravitational constant, M is the total mass of the core, and R is the core radius. By
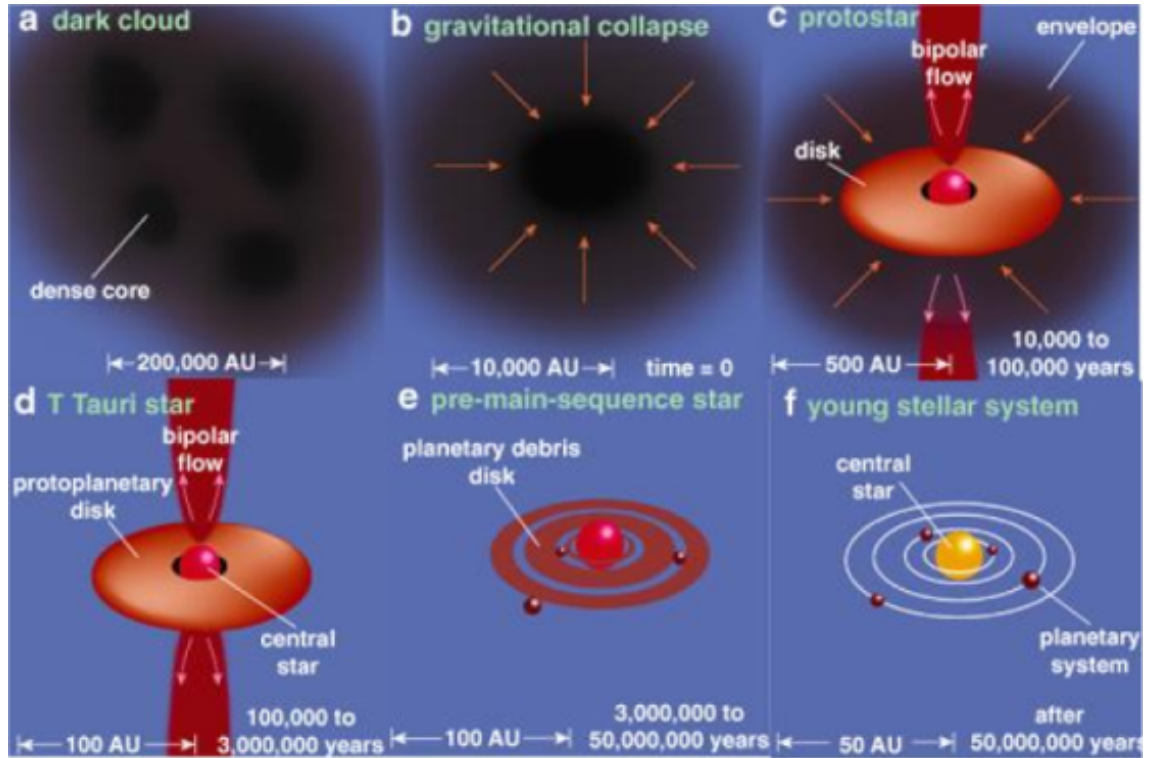
FIGURE 2.3: A cartoon by Greene (2001) showing a general overview of the star formation process for a low-mass ($M < 2\,\mathrm{M_\odot}$) star.

substituting these relations into the inequality above, we can obtain:

$$\frac{3\,G\,M^2}{5\,R} > 3\,N\,k_B\,T. \tag{2.4}$$

Given that the core can be $5-10$ times higher in density than the local cloud (André, Basu, and Inutsuka, 2009), we can treat the core as if it has a constant density in order to find the Jeans mass, M_J (Jeans, 1902), which is the critical mass required to make the core unstable, via substitution of the radius. In this case:

$$\rho = \frac{M}{V} = \frac{3\,M}{4\,\pi\,R^3} \longrightarrow R = \left(\frac{3M}{4\pi\rho}\right)^{1/3} \tag{2.5}$$

After making this substitution, we then rearrange to isolate M, as follows:

$$M^{2/3} > \frac{5\,N\,k_B\,T}{G}\left(\frac{3}{4\,\pi\,\rho}\right)^{1/3} \tag{2.6}$$

$$M_J = \left(\frac{5\,N\,k_B\,T}{G}\right)^{3/2}\left(\frac{3}{4\,\pi\,\rho}\right)^{1/2} \tag{2.7}$$

The cold, dense core (Fig. 2.3 (a)) begins as a starless core, which may be transient and disperse again without ever forming a star (André, Basu, and Inutsuka, 2009), for instance if the objects are confined by external pressure and not bound by gravity (Lada et al., 2008). If the core continues

to collapse under self-gravity and hence shows evidence of infall motions (Gregersen and Evans, 2000; Motte et al., 2001), it becomes a prestellar core (Fig. 2.3 (b)), and finally a Class 0 protostar (Andre, Ward-Thompson, and Barsony, 1993). There has been considerable debate on the subject of whether cores can form solely through runaway gravitational collapse in a marginally stable core (Hartmann, 2002; Hayashi, 1966; Larson, 1985), or if there is a significant role to be played by magnetic fields through the classical "standard model" of ambipolar diffusion (e.g. Shu 1977; Shu, Adams, and Lizano 1987a) where the star forms slowly given initial magnetic support. This debate is yet to be fully settled, and the reality is beginning to appear to be somewhere between the two.

Most prestellar cores are observed to be magnetically supercritical (i.e. are magneto-statically unstable, see e.g. Crutcher 1999). However, this model fails to explain the lifetimes of cores given that the ambipolar diffusion timescales are considerably higher ($> 10^7$ years compared to the observed $10^5 - 10^6$ years, Bergin and Langer 1997). Additionally, observed density profiles in the prestellar cores imply that they are flattened into Bonnor-Ebert spheres (Alves, Lada, and Lada, 2001), which have an initially fast collapse that slows over time. However, observations of their temperatures (which are lower than expected) and density contrasts (higher than expected) suggests that they must already be undergoing contraction, or are being supported by magnetic fields (e.g. Kirk, Ward-Thompson, and André 2005; Ward-Thompson, André, and Kirk 2002). Recent simulations suggest that ambipolar diffusion is not required in order to form low-mass cores, and that the star formation efficiency is likely to be non-linear (Chen and Ostriker, 2014; Gong and Ostriker, 2015; Murray et al., 2017), but it is nevertheless important in the regulation of angular momentum transport and the resulting core-disk system (Masson et al., 2016).

Given that molecular clouds contain sufficient mass to exceed the Jeans mass limit several times over, but do not globally collapse, it is most likely that the observed supersonic turbulence within molecular clouds is supporting them on large scales. However, turbulence decays on the scale of about a free-fall time (Mac Low et al., 1998; Stone, Ostriker, and Gammie, 1998) and hence must be reinjected into the ISM in order for the support to continue. Since star formation is observed to be inefficient (currently estimated at $\sim 1\%$; Padoan et al. 2014), most of the kinetic energy must be found in small-scale turbulence, however the inefficiency is not constant (Lada, Lombardi, and Alves, 2010; Lee, Miville-Deschênes, and Murray, 2016; Mooney and Solomon, 1988).

More recent models suggest that turbulence in the clouds may have a key role to play in creating the small-scale density fluctuations that can compress clouds and trigger gravitational collapse (André, Basu, and Inutsuka, 2009; Mac Low and Klessen, 2004; Padoan and Nordlund, 2002). Thus, there is considerable interest in investigating the interplay between interstellar turbulence and magnetic support (Bate and Bonnell, 2005; Myers and Fuller, 1992), and whether turbulence decays over time or is continuously injected (Tilley and Pudritz, 2007; Vázquez-Semadeni, Kim, and Ballesteros-Paredes, 2005). This might occur over scales of a few parsec, for example, via feedback from outflows or stellar winds etc, or on much larger scales if other factors such as gravitational instability in the cloud are more dominant (Kritsuk, Lee, and Norman, 2013).

Certainly there is some observational evidence in favour of magnetically-supported cores, in that

the velocity fields around cores are relatively quiescent (Nakamura and Li, 2005), whereas if turbulence from supersonic, large-scale shock waves were the sole cause, velocity fields around the cores would be much larger (e.g. Klessen et al. 2005). However, this is only observed in the case of isolated cores and does not apply in the more turbulent regions around protoclusters (Caselli and Myers, 1995) where infall velocities and rates of mass accretion are higher (Di Francesco et al., 2001; Motte et al., 2005; Peretto, André, and Belloche, 2006). Further, the formation of young clusters has been found to be hierarchical, both spatially and temporally (Grasha et al., 2017), in agreement with the models that predict turbulence as the main driver.

Overall, neither support from magnetic fields, nor from turbulent pressure, can satisfactorily explain the observed star formation efficiencies on their own (Myers et al., 2014; Padoan and Nordlund, 2011) and it is likely that the real cause incorporates a combination of both of these factors (Federrath, 2015). It also is possible that a one-size-fits-all solution simply does not exist, and that stars can form irrespective of whether turbulence or magnetic support are dominant (Mocz et al., 2017).

2.4   Classification of young stars

The detection of protostars at the earliest stages of their formation is certainly difficult, and pre-stellar cores can only be detected in sub-mm, mm and radio regimes. As they collapse and the energy released begins to heat the interior of their envelopes, they can produce molecular outflows, and be seen in the MIR at wavelengths longer than about 20 μm, but cannot be detected at all in the NIR (see Fig. 2.3 (b) and (c)). At this early stage, the protostar is dubbed a Class 0 protostar (Andre, Ward-Thompson, and Barsony, 1993). The lifetime of this stage is estimated to be between 1.3 and 2.6 $\times 10^5$ yrs (Dunham et al., 2015; Evans et al., 2009). The outflows produced by Class 0 protostars have been found to be able to grow to parsec-scale lengths, despite this relatively short lifetime (Federrath et al., 2014; Stanke, 2003), making the presence of outflows an invaluable tool in locating these elusive objects.

As they continue to evolve and the infalling material flattens into an accretion disk, the envelope becomes less dense and the protostar can be seen in the MIR. At this phase, the protostar is considered a Class I protostar (Fig. 2.3 (c)). Diagnosing the evolutionary stage becomes possible using the shape of the Spectral Energy Distribution (SED) as originally done by Adams, Lada, and Shu (1987), and by the bolometric temperature (Myers and Ladd, 1993). Adams et al. defined three distinct morphological classes of T Tauri stars, from Class I to Class III, using the Spectral Index, α:

$$\alpha = \frac{d \log(\lambda F_\lambda)}{d \log(\lambda)}, \tag{2.8}$$

where F_λ is the flux density at wavelength λ. Originally this was measured between 1 and 10 μm (Lada and Wilking, 1984), and then later between 2 and 20 μm (Adams, Lada, and Shu, 1987). In order to avoid the silicon absorption feature at 10 μm (Dyck and Beichman, 1974), it has become more usual to either use Spitzer's IRAC bands (between 3.6 and 8 μm) or WISE (3.4 to 22 μm).

As the least evolved of the three classes, Class I protostars are still surrounded by an envelope of dust and a thick accretion disk, so the light they produce is heavily scattered towards longer wavelengths and hence α is positive. Outflows are still produced at this stage. The lifetime of the Class I phase is estimated to be between 2.7 and 5.2×10^5 years (Dunham et al., 2015; Evans et al., 2009). However, the lifetimes vary depending on factors such as the stellar mass, and estimates of the evolutionary stage can be further complicated by e.g. the inclination of the star with respect to the line of sight. The boundary between Class I and Class II objects is not well defined, so the lifetimes are usually considered median values (Dunham et al., 2015).

Eventually, the dust and gas in the envelope is either settled into the accretion disk, or is dispersed out of the system by the outflow. At this point, the disk is visible as a proto-planetary disk and the star is recognisable as a star in the NIR and, if the extinction is not too high in the parent cloud, at optical wavelengths. This stage is the Class II phase, and the star is considered to be a Young Stellar Object (YSO) rather than a protostar (Fig. 2.3 (d)). The spectral index for these objects is negative, and the SED resembles the standard blackbody curve, but with some excess emission at longer wavelengths due to scattering by the disk (Adams, Lada, and Shu, 1987). Class II YSOs have estimated typical ages of less than 3×10^6 years (Appenzeller and Mundt, 1989).

In 1994, an intermediate classification was added between Class I protostars and Class II YSOs, being "flat spectrum" sources which have a spectral index of $-0.3 < \alpha < 0.3$ (Greene et al., 1994), but Heiderman and Evans (2015) found that flat spectrum sources have no distinguishing features and that the "flat spectrum" category has no physical significance. By the time the protoplanetary disk has been largely evaporated by radiation from the Class II star, all that is left is the transition disk from which planetesimals are forming into planets. This is the Class III phase, and can be diagnosed with a spectral index $\alpha < -1.6$. By this point the YSO is no longer actively accreting material and has cleared its surroundings of molecular gas (Fig. 2.3 (e)). Hence, Class III YSOs are not typically associated with molecular outflows and are not considered in this study.

This evolutionary progression was suggested by Adams, Lada, and Shu (1987) as a mode of star formation for low-mass ($< 2\,M_\odot$) stars. Class II and Class III YSOs are certainly more easily studied than their protostellar counterparts since they are observable at NIR and optical wavelengths and can be classified by their spectra and H_α line emission (e.g. Fernandez et al. 1995), and Class II objects also show differences in their evolution according to their mass. Low mass Class II objects ($< 2\,M_\odot$) are known as classical T Tauri stars (CTTS), which are typically characterised as being highly variable in optical regimes (Cohen and Kuhi, 1979; Herbig, 1962; Joy, 1945; Rydgren, Strom, and Strom, 1976). Their counterparts in the Class III phase are known as weak-line T Tauri stars (Appenzeller and Mundt, 1989; Walter, 1986). Intermediate-mass Class II objects (2 to $8\,M_\odot$) are known as Herbig AeBe stars (Herbig, 1960).

2.5   High-mass stars

High-mass stars ($> 8\,M_\odot$) are more complex to pin down, since they are relatively few in number and they evolve quickly. Indeed, their embedded (infrared quiet) protostellar phase has been found

to have the same timescale as their embedded HII (infrared-bright) protostellar phase (3×10^4 years protostellar lifetime, Motte et al. 2007). Their Ultra-Compact HII (UCHII) lifetime is typically only around 10^5 years (Wood and Churchwell, 1989), which is an order of magnitude lower than the low-mass protostellar lifetime (Kenyon and Hartmann, 1995). However, when compared to the typical main sequence lifetime of a massive star, it represents a significant fraction (particularly for the most massive stars).

It remains unclear whether high-mass stars form via accretion, in a scaled-up version of low-mass star formation (Krumholz, Klein, and McKee, 2007; Yorke and Sonnhalter, 2002) or hierarchically, via competitive accretion (e.g. Bonnell, Vine, and Bate 2004; Bonnell et al. 2001). Although the Jeans instability does allow for further fragmentation after runaway collapse has begun, it could also be that multiple systems form as a result of dynamical gravitational instabilities in the collapse of massive cores (Goodwin et al., 2007). The matter remains a topic of contention and a thorough review of the current models and their drawbacks is provided in Tan et al. (2014).

The main reason for this controversy is the significant radiation pressure from the star, once fusion begins at around $10\,\mathrm{M}_\odot$, which would prevent further accretion, and yet we know that stars can reach masses far in excess of this limit (Kahn, 1974) as expansion of the star can lead to a reduction in the radiation pressure. Several studies since then have showed that higher accretion rates can theoretically counter the radiation pressure, and that the outflows produced are extremely important since by removing angular momentum and radiation from the system, they limit the turbulent fragmentation of the core into clusters of small stars (Krumholz et al., 2009; Krumholz and Burkert, 2010; McKee and Tan, 2003). Self-shielding by the disk against the radiation pressure from the star would therefore impose no theoretical limit on the mass of a star that can be formed (Kuiper et al., 2010). However, it is currently accepted that there is an upper limit of around $150\,\mathrm{M}_\odot$(Figer, 2005), even though exceptions have been found with proposed higher masses than this (e.g. R136a1 in Crowther et al. 2010). The upper limit has been shown to depend on the metallicity (Z) of the star (Ziebarth, 1970), and this Z-dependence is primarily due to radiation-driven winds mediated by line opacity (Vink, 2018).

In the competitive accretion model, the gas inside a turbulent molecular cloud that is forming a cluster migrates toward the centre of the cloud where the most massive object forms. Low and intermediate-mass stars could thereby form around the most massive object(s) at the centre, segregated according to the remaining mass available to them, which has some observational evidence (Gennaro et al., 2011). It is probable that the reality is more complex, and again lies somewhere in the middle (Motte, Bontemps, and Louvet, 2017). The greatest hindrance to the settling of this issue is the small number statistics available which surveys such as the Red MSX (Midcourse Space Experiment) survey have begun to address (Lumsden et al., 2013). Future studies using ALMA (the Atacama Large Millimeter Array) will hopefully be our greatest tool in understanding high-mass star formation, and early results are promising. A recent study by Cesaroni et al. (2018) using ALMA has found the first direct evidence of a radio outburst linked with an IR accretion event in a massive YSO. They suggest that recurring accretion-ejection may be the main component in the assembly of massive stars, particularly since accretion disks are increasingly being found around O and B type stars (Cesaroni et al., 2017; Ilee et al., 2016).

2.6   Outflows

Jets and outflows are, simply put, streams of gas and dust particles extended in diametrically opposing beams away from some central driving source. Whilst a comprehensive model of the launching and collimation mechanisms of outflows is yet to be achieved, they are nonetheless ubiquitously associated with rotating, magnetised accretion disks. The outflow direction is universally observed to coincide with the axis of rotation of the driving source, perpendicular to the accretion disk. The fact that they are seen to be associated with objects as massive as Active Galactic Nuclei (AGN, e.g. Marshall et al. 2002) and with objects as low in mass as brown dwarf stars (e.g. Scholz and Jayawardhana 2006; Whelan et al. 2005) and YSOs (e.g. Bally 2007, 2016) suggests that even if their observed properties (e.g. velocities, mass loss rate, etc) are different on varying scales, there must be some common physics involved in the accretion mechanism that produces them (Livio, 1999, 2011). Additionally, recent observational evidence is growing that outflows from high-mass stars are produced in a scaled-up version of those from low-mass stars (McLeod et al., 2018; Reiter et al., 2017; Zhang et al., 2013b).

Outflows have a significant impact on their surroundings and as such, could be a critical contributor to the regulation of star formation. If the jets and outflows produced by massive, distant objects such as AGN and quasars are simply scaled-up versions of the low-mass analogues in our own Galaxy, then the more easily observed protostellar jets hold the key to unlocking our understanding of these objects elsewhere in the Universe. The reviews of e.g. Arce et al. (2007), Bachiller (1996), Bally (2016), Bally, Reipurth, and Davis (2007), Frank et al. (2014), and Ray et al. (2007) explore in detail the subject of outflows and their creation, impact, and morphology.

A serious hindrance to the understanding of star formation through accretion is the so-called "angular momentum problem" (Mestel, 1965). The essence of this problem is that as a star accretes material from its disk, the net torque applied to the star through the transfer of angular momentum should cause it to spin at an increased rate until the rotation of the star is high enough for it to break up (Shu, Adams, and Lizano, 1987b). However, observations have shown that pre-main-sequence stars rotate at only around 10 % of the critical breakup velocity (Bodenheimer, 1995). T Tauri stars, for instance, are generally observed to rotate at less than $10\,\mathrm{km\,s^{-1}}$ (e.g. Bouvier et al. 1993; Hartmann and Stauffer 1989; Vogel and Kuhi 1981) and with considerably lower angular momentum than was contained in the parent cloud. This discrepancy between the observed and predicted rotation rates of young stars means that somewhere along the way, this angular momentum must be "lost" in order to maintain a net zero torque (Matt and Pudritz, 2005).

One possible explanation for this missing angular momentum is the fragmentation of cores into wide binary or multiple systems. Such systems are thought to be extremely common, and would allow for the conservation of the angular momentum in the rotation of the two (or more) young stars about their barycentre (e.g. Jappsen and Klessen (2004), Larson (1972), and Narita, Hayashi, and Miyama (1984)). Close binaries could be formed via the orbital decay of such systems and dynamical interactions in multiple systems (Bate, Bonnell, and Bromm, 2002), since the spin angular

momentum of the original system can be converted into orbital angular momentum in the resulting components. This is especially likely if the initial angular momentum is high (Bodenheimer, 1995).

Another explanation is that winds from protostars can provide a mechanism for angular momentum to essentially "escape" the accreting system, and this has been shown to be possible even for slow rotators (Matt and Pudritz, 2005). Outflows have been shown to be extremely efficient at removing angular momentum and energy from forming stellar systems, thus allowing accretion to continue (Banerjee and Pudritz, 2006; Ouyed and Pudritz, 1997; Pudritz and Norman, 1983, 1986). Mass loss phases are associated with rotational braking, with actively-accreting stars showing indications of disk braking and in stars where the disk has become decoupled, rotation rates increase (Weise et al., 2010). The extraction of energy by outflows may be especially crucial for high-mass star formation, by creating an avenue for the escape of thermal radiative flux (Kuiper, Yorke, and Turner, 2015) which would otherwise prevent accretion due to the outward thermal flux pressure. Effectively, the presence of an outflow allows accretion to continue for longer and create higher mass stars than the non-outflow case, despite the loss of mass through the outflow mechanism, and does not theoretically limit the fragmentation into binary systems (Banerjee and Pudritz, 2006; Banerjee, Pudritz, and Anderson, 2006).

It has also been proposed that outflows aid in the dispersion of the protostellar envelope via the cavities they carve (Seale and Looney, 2008) which would limit the final stellar mass. In addition to this, the propagation of the outflow into the local ISM disturbs the ambient material, thus injecting turbulent motions into the parent cloud. These disruptions can frustrate the growth of neighbouring stars and prevent further ongoing collapse (Arce et al., 2010), but it has also been shown that this turbulent momentum can increase the overall number of stars formed in a cluster (Federrath et al., 2014). Although it has been suggested that feedback from jets and outflows could provide sufficient turbulent momentum to prevent ongoing collapse, observations and simulations have thus far provided mixed results (Arce et al., 2010; Federrath, 2015; Ioannidis and Froebrich, 2012b; Murray, Goyal, and Chang, 2018; Offner and Chaban, 2017; Wang et al., 2010; Zhang et al., 2015). Since star formation occurs quickly (around one crossing time according to Elmegreen 2000), multiple epochs of star formation and outflows would be required to continuously support a molecular cloud over its typical lifetime, given the relatively rapid decay time of turbulence.

2.6.1   Formation of outflows

Jets and outflows result from charged particles interacting with magnetic fields of the accretion disk and protostar. These fields can be incredibly complex to model and given the lack of resolution at (sub)mm regimes, we are yet to observe the launch regions directly. This seriously limits the ability of astronomers to fully constrain theoretical models. For detailed discussion of the different models, see the reviews of e.g. Arce et al. (2007), Frank et al. (2014), Li et al. (2014), McKee and Ostriker (2007), Pudritz, Hardcastle, and Gabuzda (2012), and Shang, Li, and Hirano (2007). Figure 2.4 shows a cartoon representation of the current understanding of the launch regions for the jet, outflow and winds.
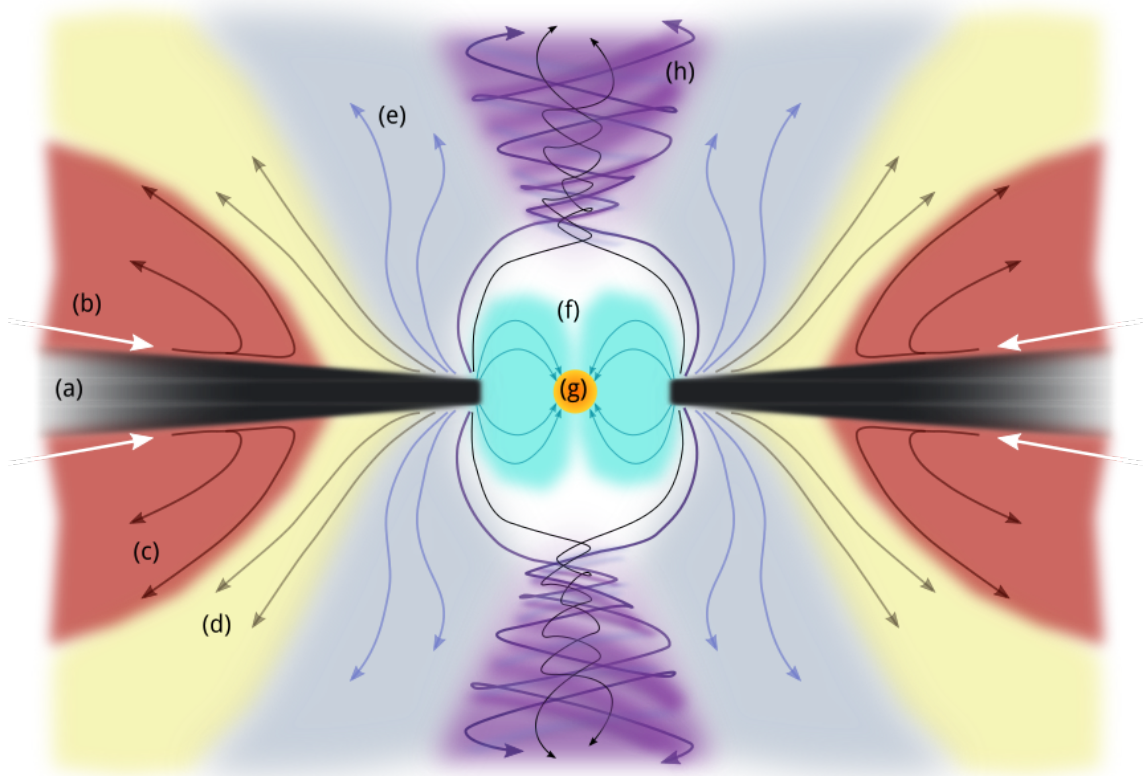
FIGURE 2.4: A cartoon (not to scale) demonstrating how the generation of jets and outflows is generally understood to occur, with arrows denoting the direction of travel for ionised particles trapped in magnetic field lines. The labels, discussed in more depth in the accompanying text, are as follows: (a) the accretion disk; (b) infalling particles from further out in the disk; (c) the "D-wind" region; (d) the "X-wind" region; (e) conical winds; (f) accretion columns; (g) the protostar; and (h) the collimated jet.

In general, it is thought that the disk (a) magnetic field consists of two components; a poloidal component caused by the infall motions of the core, and a toroidal component due to the disk. If the magnetic field reaches an angle of $< 60°$ with respect to the plane of the disk, the poloidal component skims fast-moving gas (b) from the disk surface and channels it towards the protostar (g). At the inner edge of the disk, magnetic field lines connect to the protostar, forming accretion columns (f) along which the infalling material can reach the star.

Not all of the material is accreted onto the protostar, however. The differential rotation of the disk creates a toroidal angular momentum component, along which some of the ionised material can be funnelled (h) into a collimated wind (e.g. Blandford and Payne 1982; Fendt 2011; Zapata et al. 2010). This would naturally lead to helical structures or "pinching" at the base of the outflow, which then causes acceleration along open field lines into a fast, highly collimated jet. This jet pierces and propagates into the ambient medium, sweeping out a cavity into which the outflow can expand and entrain ambient material (the "jet-driven" case Canto and Raga 1991; Raga and Cabrit 1993; Smith, Suttner, and Yorke 1997; Stone and Norman 1993). There is certainly some observational evidence for helical structures near the bases of outflows (e.g. Carrasco-González et al. 2010; Ching et al. 2016), and acceleration of the particles by magnetic fields would help to

explain why the momentum carried by outflows is orders of magnitude higher than what radiation pressure could supply (Lada, 1985).

The greatest discussion remains around the origin of the disk winds that are observed, although the general mechanism by which they originate (the acceleration of particles away from the protostar and disk along magnetic field lines) is less controversial. Several models exist which are largely similar, but each proposes a different location for the origin of winds and the jet material. Observational evidence is limited, suggesting that there is no straightforward, single mechanism that can be reliably applied to all cases. The first of these models is the "D-wind" or disk-wind model (c), in which heating of the outer layers of the disk can be sufficient to ionise particles, which then become trapped in the poloidal magnetic field of the disk and are thus accelerated magneto-centrifugally (Blandford and Payne, 1982; Nolan et al., 2017; Pudritz, Hardcastle, and Gabuzda, 2012; Pudritz and Norman, 1983). The second model is the "X-wind" model (d), in which the inner edge of the accretion disk is ionised by radiation from the protostar and the wind is hence launched centrifugally from the disk in the region nearest the star (Offner and Arce, 2014; Shang et al., 2004; Shu et al., 1997; Shu et al., 1994). There are some models which posit that the winds are generated at the stellar surface (Banerjee and Pudritz, 2006; Hartmann and MacGregor, 1982). Finally, there are wide-angle wind models (e) where conical winds are launched from the inner disk region by slowly rotating stars, with wide opening angles, and are primarily magnetically driven (Arce and Goodman, 2002; Gardiner et al., 2003; Kuiper, Turner, and Yorke, 2016; Lovelace et al., 2014; Shu et al., 1991).

Very recent ALMA results have confirmed that in the case of HH 212, the jet is launched and collimated from a region very close to the star ($< 0.05 \, \text{AU} \pm^{0.05}_{0.02}$ Lee et al. 2017). Simulations from Banerjee and Pudritz (2006) showed similar results, with $\sim 0.07 \, \text{AU}$ for the magneto-centrifugally powered jet, and a lower velocity outflow magnetically coupled to the accretion disk, where both followed from the toroidal build-up of the magnetic field. There is also observational evidence for the anchoring of the outflow to the accretion disk (e.g. Kwan and Tademaru 1988; Shang, Li, and Hirano 2007) from 10 to 100 AU, but the distance ranges are not yet well constrained. Collimation in the jets has been observed even at early Class 0 phases (e.g. Cabrit et al. 2007; Davis et al. 2010), and does not necessarily cease once the jet has escaped the parental cloud. Both jets and outflows have been observed to rotate, whether driven by Class 0 protostars or by Class II YSOs, and across all mass ranges (e.g. Bacciotti et al. 2002; Chrysostomou et al. 2008; Coffey et al. 2007; Greenhill et al. 1998, 2013; Hirota et al. 2017; Lee et al. 2017; Pech et al. 2012; Tan et al. 2016; Zapata et al. 2010). The entrained material in the cavities can show signs of (very slow) rotation, and even some earlier observations have shown that individual outflows can display a large variety of parameters which could easily populate both the wind-driven and jet-driven categories (Lee et al., 2000). For instance, objects such as VLA 0548 appear typical of outflows produced in wind-driven simulations, whilst HH 212 is a particularly good example of a jet-driven outflow (Lee et al., 2001). It is inescapable, however, that such small sample sizes are unlikely to lend much weight to one model over another, and thus uncertainties will remain in the jet/wind generation mechanism until observations are able to reveal the processes to us in greater detail.

2.6.2   Morphology

The HH 212 outflow (Fig. 2.5) is often cited as a prototypical example of a protostellar outflow, and it is certainly one of the most spectacular cases known to date. It is 0.6 pc long and driven by IRAS 05413−0104, an isolated, low-mass Class 0 protostar (Zinnecker, McCaughrean, and Rayner, 1998), viewed close to the plane of the sky (4°, Claussen et al. 1998). Located in the nearby Orion nebula (around 400 pc from the Sun), it is an unparalleled laboratory for studying shock-excitation and outflow morphology. However, can this magnificent outflow truly be considered as representative of outflows in general, or is it a unique individual? Certainly there is a sufficiently large variation in the appearance of the shock-excited H_2 emission that outflows observed in H_2 cannot be neatly categorised on the basis of their appearance. However, HH 212 does share common features with other outflows, and the most typical jet / outflow features are detailed in Fig. 2.6. Note that this represents an illustration of a molecular (partly ionised) outflow and does not represent the typical HH object, since these tend to be far longer (tens of parsec) and are primarily seen in atomic, rather than molecular species far from the source (Bally and Devine, 1997; Eislöffel, 2000; Reipurth, Bally, and Devine, 1997). The labels indicated in the figure will be summarised in the following discussion.

Inside the core, the material is primarily molecular and the ionisation fraction is low except at the region of jet launching. The magnetised accretion disk (a) rotates and has a toroidal magnetic field. Fast material in the disk falls inward along magnetic field lines in the disk (b) toward the centre, where it is accelerated and funnelled into the collimated microjet. The jet is fast-moving ($> 100 \, \mathrm{km \, s^{-1}}$, but up to $1\,000 \, \mathrm{km \, s^{-1}}$ for HH objects) and most usually observed in SiO and CO (c) near the jet launching region (Cabrit et al., 2012; Leurini et al., 2013). There is evidence that jets can quickly grow to parsec-scale lengths (Federrath et al., 2014; Stanke, 2003). Magnetic field lines twist into helical structures that may maintain the collimation of the jet further from the driving source (e). In HH 212, despite the knotty structure seen in the H_2 emission knots, recent observations in CO and SiO have revealed a more-or-less continuous collimated jet, with temporal velocity variations ("pulses") creating the internal working surfaces (g, h, i) that are traced by knots and bow shocks (Lee et al., 2015), typically in H_2.

In addition to this fast component, there is typically a lower velocity ($< 100 \, \mathrm{km \, s^{-1}}$), wide-angle outflow that surrounds the jet and carves out the cavity (d), sweeping up (entraining) molecular material. In a bipolar outflow, the cavities give the appearance of an hourglass. Near the base of the jet, the low-velocity outflow and the cavity are seen primarily in rotational lines of CO, H_2O, and other species that are readily collisionally excited by the faster-moving H_2. Complex organic molecules (those with > 6 atoms) have been discovered in the outflow cavities of both low and intermediate-mass stars (Arce et al., 2008; Codella et al., 2015; Palau et al., 2017). In HH 212, the microjet is also seen in CO, associated with the H_2 shock-excited emission. Once the jet has emerged from the core into the lower-density ambient medium of the parental cloud, the cavity boundary is not so well defined due to the viscous mixing of ambient material with the entrained molecules (f) along the border of the slow-moving ($< 10 \, \mathrm{km \, s^{-1}}$), cooling cavity.

At (l) are the interfaces between the jet and the ambient medium, also known as the "bow shock"

FIGURE 2.5: The HH 212 outflow (Zinnecker, McCaughrean, and Rayner, 1998) in Orion A, shown in a deep $1-0$ S(1) emission taken using the ISAAC instrument on Antu (McCaughrean et al., 2002). The internal knots are symmetrically matched about the embedded driving source, implying that they have arisen as a result of major accretion / ejection events.
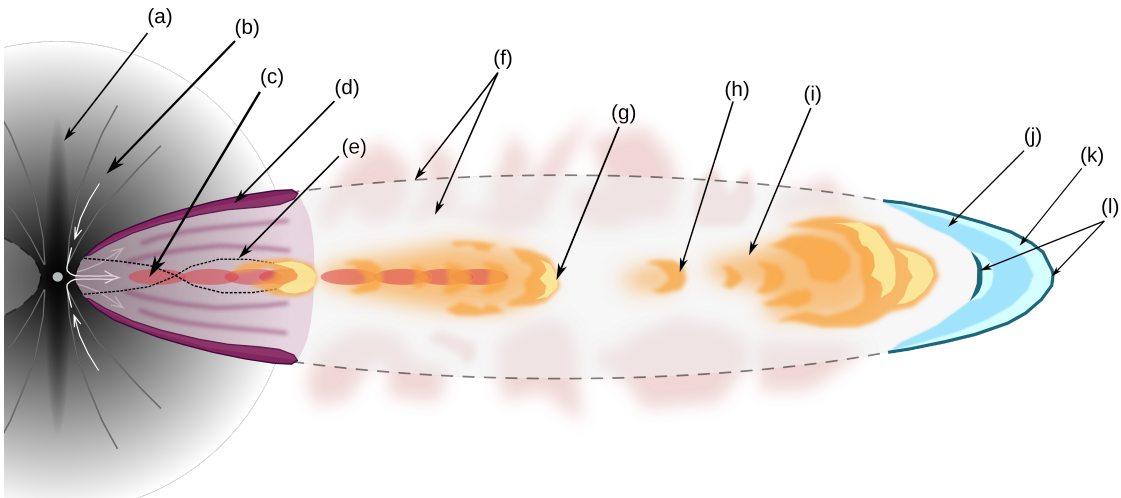
FIGURE 2.6: An illustration (not to scale) of a young protostellar outflow and the multiwavelength morphology of the lobe. From left to right, the accretion disk and infalling material (grey), the molecular CO cavity and SiO micro-jet (red / magenta), the collimated CO jet and H_2 shocks (orange / yellow) surrounded by entrained ambient material inside the cavity, and the bow shock (blue). The labels are explained in the text in more detail.

or "forward shock", and between the internal jet and the back of the bow shock, also known as the "Mach disk" or "reverse shock" (Hollenbach, 1997). The structure as a whole is referred to as a "working surface" but is often colloquially referred to as the bow shock. At both interfaces, the compression induced by fast shocks heats the gas to dissociative temperatures and can be traced using ionised / atomic species. The properties of the gas, such as the temperature, velocity, density, ionisation fraction, entropy and so on, vary greatly over a very short distance (usually on the order

of the mean free path of the gas particles) and are referred to as "jump-shocks" (J-shocks). HH objects in particular are examples of J-shocks and are typically observed in optical forbidden lines (j) such as [SII], [OI] – [OIII] and [NII], or in H_α (k), all of which trace the inner shock. Although molecular jets can seldom be observed as HH objects due to the obscuring effects of extinction, NIR lines such as [FeII] can be used to trace the strongest shocks, which cannot typically be seen in the ro-vibrational lines of H_2 as the temperatures are too high.

The H_2 emission in outflows (g, h, i) is caused by the passage of shock fronts through the gas, which collisionally excites (and heats) the H_2 molecules. The dissociation threshold of H_2 occurs at shock velocities of around $45-50\,km\,s^{-1}$ (Draine, Roberge, and Dalgarno 1983; Lepp and Shull 1983). Strong ($\geq 100\,\mu G$) magnetic fields may be responsible for protecting the H_2 molecules even up to tangential velocities of around $80\,km\,s^{-1}$ (Panoglou et al., 2012; Smith and Brand, 1990). Although this is stronger than would be expected in typical ISM densities of $10^2 - 10^3\,cm^{-3}$, the densities measured in shock-excited outflow knots are typically higher than $10^3\,cm^{-3}$. Even higher measured H_2 radial velocities ($100-200\,km\,s^{-1}$) are likely due to the relative motion of the jet in an already-moving medium (Fedriani et al., 2018). In faster, hot shocks where magnetic support does not prevent the dissociation of H_2 molecules, the presence of H_2 emission may be generated through recombination in the post-shocked gas phase (Raga, Williams, and Lim, 2005). Molecular hydrogen shocks represent continuous regions ("C-shocks") over which the kinetic energy transferred to the molecules via collisional excitation, and the other hydrodynamic properties of the gas, can be efficiently cooled radiatively via ambipolar diffusion (Smith and Brand, 1990). The vast majority of shocks seen in molecular clouds are representative of C-shocks, and molecular hydrogen may provide an important means for cooling gas in the ISM (Draine, Roberge, and Dalgarno, 1983; Field et al., 1968; Shull and Beckwith, 1982).

Outflows vary in the degree of collimation shown, and their morphologies and structures can be remarkably different (e.g. Arce et al. 2011; Reipurth and Bally 2001). The DR 21 outflow in Cygnus-X, for instance, tapers from a wide base obscured by $A_V \sim 100\,mag$ extinction, to the tip of the bow shocks. It is still debated whether this massive outflow was caused by an explosion (Zapata et al., 2013) given the bullet-like appearance of some H_2 knots along the outside of the outflow lobe (similar to those seen in Orion BN / KL), or if it is a merging of multiple semi-aligned outflows into a common outflow (Murphy et al., 2008; Peters et al., 2014) such as in L 1551 IRS 5 (Mundt, Ray, and Raga, 1991; Snell, Loren, and Plambeck, 1980). Outflows may also display reflection nebulae, such as in Cha IRN (Feldt et al., 1998; Zinnecker et al., 1999), where light is scattered by dust and ice in the cavity walls in the NIR.

They may be seen to precess about their axis (e.g. Eisloffel et al. 1996), although it is difficult to measure the opening angle from H_2 data alone (Davis et al., 2008). The exact cause of precession is unknown, but it could be a result of the jet suffering gravitational disruption from a binary partner to its driving source, or two misaligned outflows (Bate et al., 2000; Terquem et al., 1999). It is expected in the youngest and most embedded outflows, before the system is able to dynamically correct for the instability. Asymmetry in the lobes of outflows from low-mass objects is also typical (e.g. Scholz and Jayawardhana 2006), although the extent to which asymmetry occurs in outflows from more massive objects is unclear. HH objects have been detected from brown dwarf

stars (mass range $0.01 - 0.08 \, M_\odot$), with similar, albeit scaled-down properties to the more typical HH objects from YSOs (e.g. HH 1165, Riaz et al. 2017). So, outflows seem to be robust even at low masses (the minimum to date is a $24 \, M_{Jup}$ brown dwarf) and in evolved systems (Whelan et al., 2007).

2.6.3 Accretion and mass loss

The mass lost from the protostellar system, through the both the fast jet and the material entrained by it through viscous mixing along the cavity, has been found to be inextricably tied to the process of accretion, and observations have shown that accretion is an episodic, rather than continuous, process (Audard et al., 2014; Caratti o Garatti et al., 2012; Evans et al., 2009; Frank et al., 2014; Plunkett et al., 2015) particularly for binary systems (Riaz, Vanaverbeke, and Schleicher, 2018). Young stars frequently show variations in their measured magnitudes, and accretion is one of the key causes of this variability (e.g. Günther 2013). Recent observations have shown a radio outburst following an infrared accretion event from a massive protostar (Cesaroni et al., 2018). On the other end of the mass scale, short term variations in brown dwarf stars due to outflow activity lag behind the variations due to accretion on scales as short as about an hour (Scholz and Jayawardhana, 2006).

The rates of accretion and mass loss are not straightforward to measure, however, and depend on both the mass of the protostellar system and its evolutionary stage. Indeed, at the earliest stages of protostellar formation (Class 0), the luminosity of the protostar is found to be dominated by the accretion luminosity, L_{acc} (Frank et al., 2014; McKee and Ostriker, 2007) which follows:

$$L_{acc} = \frac{G \, M_* \, \mathring{M}_{acc} \, (1 \, - \, R_* \, / \, R_{in})}{R_*} \, , \qquad (2.9)$$

where G is the gravitational constant, M_* is the protostellar mass, $\mathring{M}_{acc}$ is the accretion rate, R_* is the protostellar radius and R_{in} is the inner radius of the accretion disk, which is usually assumed to be co-rotating with the star (e.g. Bouvier et al. 2007). If the accretion occurs from across the surface of the disk, $R_{in} >> R_*$ can be assumed. Order-of-magnitude estimates of the accretion luminosity can then be obtained (as was done in e.g. Ioannidis and Froebrich 2012b) using the further simplified relation:

$$L_{acc} \propto \frac{G \, M_* \, \mathring{M}_{acc}}{R_*} \, . \qquad (2.10)$$

The accretion and mass-loss rates are both found to peak strongly during the early evolution and to decrease over time, with less evolved objects (Class 0 / Class I) having higher mass-loss rates than more evolved objects of comparable mass (Caratti o Garatti et al., 2012; Curtis et al., 2010; Hartmann et al., 1998; Offner and Chaban, 2017; Stanke, 2000). For embedded protostars, the mass-loss rates can be as high as $10^{-5} \, M_\odot \, yr^{-1}$ (Bally, 2016). As the protostar evolves into a Class II YSO, this rate decreases considerably, to orders of about 10^{-7} to $10^{-9} \, M_\odot yr^{-1}$ (Dougados et al. 2010; Frank et al., 2014; Lada, 1985; Offner and Arce, 2015). The accretion rate has also been

shown to decrease over time (Riaz, Vanaverbeke, and Schleicher, 2018; Schmeja and Klessen, 2004).

The accretion rate seems to be proportional to the envelope mass for high mass protostars (Duarte-Cabral et al., 2013) in a scaled-up version of the low-mass case, and the ratio between the mass-loss rate and accretion rate is relatively constant across a range of mass scales (mass-loss / accretion rate $\sim 10\%$, Agra-Amboage et al. 2009; Antoniucci et al. 2008; Cabrit et al. 2007; Ellerbroek et al. 2013; Frank et al. 2014). The mass also seems to determine the velocity of the jets and outflows (Frank et al., 2014), with the slowest jets being associated with low-mass objects such as brown dwarf stars ($v_j \sim$ a few $\mathrm{km\,s^{-1}}$, e.g. Bally 2016) and in the case of black holes, higher gas accretion rates are observed to be associated with higher velocity jets (King et al., 2015). However, this result is also contradicted by Reiter et al. (2017) who found no dependence upon protostellar mass in the ejection velocities of their jets.

Accretion histories can be pieced together using the morphologies and kinematics of outflow knots, like a "fossil record" of previous mass ejection events (Antoniucci et al., 2008; Bally, 2016; Beck et al., 2007; Zhang et al., 2013a). This can be crucial in identifying the driving sources of outflows, particularly if the source is embedded. However, proper motion studies are extremely complicated, given the fast cooling time of H_2 and the nature of the shocks themselves. Some proper motion studies have shown systematic decreases in knot velocity with increasing distance from the driving source. It is not clear whether this is due to changes in the velocity of the outflow over time, or a result of "drag" from the local environment (Cabrit and Raga, 2000; Devine et al., 1997). However, other studies have shown that the knot velocities remain constant and thus are unaffected by the local environment (McGroarty, Ray, and Froebrich, 2007). The results from Zhang et al. (2013a) were mixed between the two. It is still not clear whether this means that the jet velocity decays over time, or if the jet velocity remains constant.

Long temporal baselines are required, with high resolutions, and until recently these have not been available on large scales. As pointed out by Noriega-Crespo et al. (2014), jet velocities of $100\,\mathrm{km\,s^{-1}}$ would produce observable shifts of less than $0''\!.2$ over a 6 year baseline (at a distance of 730 pc for their study of Cep E). Most outflows in the $1-0\,S(1)$ line of H_2 have velocities lower than this. Thus, proper motion studies have historically focused on individual objects (in the NIR lines of H_2) or on HH objects where optical data is available over much longer baselines (e.g. Hartigan et al. 2005; Noriega-Crespo et al. 2014), although larger-scale studies are now becoming feasible to study in H_2 for very nearby regions (Caratti o Garatti et al., 2009; Zhang et al., 2013a). Since historical data in the $1-0\,S(1)$ line of H_2 only exists for a small fraction of the outflows in the UWISH2 survey area, and those for outflows at greater distances than 1 kpc and with typical baselines of $5-10$ years, proper motions will not be measured as part of this Thesis. However, the data and images from the UWISH2 survey will be useful for such studies in the future.

2.7   Previous outflow surveys in H_2

The earliest studies of outflows using the $1-0\,S(1)$ line of H_2 were highly targeted. The first of them was a study of 33 known HH objects by Wilking et al. (1990) who confirmed that the H_2 emission primarily corresponds to low-velocity shocks ($v < 50\,km\,s^{-1}$). Other early studies exploring the nature of outflows include investigations of HH 46 / 47 by Eisloffel et al. (1994) and Hodapp and Ladd (1995) who discovered 6 new outflows, an investigation of the Orion Molecular Clouds OMC-2 and OMC-3 by Yu, Bally, and Devine (1997), which yielded a dozen more outflows, the discovery of bow shocks around AFGL 961 by Aspin (1998), and the addition of 28 new outflows in L1448, NGC 2071, and NGC 7129 by Eislöffel (2000).

The first truly unbiased search for outflows with the $1-0\,S(1)$ line was performed by Stanke, McCaughrean, and Zinnecker (2002). From a 1.2 square degree field in the Orion A GMC came 76 newly-identified outflows. However, most studies searching for outflows still remained targeted on specific objects or regions of interest, such as in S 269 (Jiang et al., 2003), IC 348 (Eislöffel et al., 2003), ρ Ophiuci (Khanzadyan et al., 2004), and IRAS 20231+3440 (Jiang et al., 2004). The numbers of outflows discovered remained relatively small and were not always measured consistently between the different studies, which often led to contradictory results in differing regions and conclusions drawn from very small samples. More recent works attempted to address this issue, with several large-scale studies that significantly increased the number of outflows discovered using molecular hydrogen as a tracer in various regions across the Galactic plane. The first of these studies was performed in the DR 21 and W 75 N regions of Cygnus-X, which found over 50 outflows in four distinct sites along the DR 21 ridge (Davis et al., 2007). The second was a wide but shallow survey of Perseus west, which found 26 outflows (Davis et al., 2008), and the third was a survey of the Orion A molecular ridge, which built upon the earlier survey done by Stanke et al. 2002 and increased the number of known outflows in that region to 116 (Davis et al., 2009).

Despite this, many important recent studies have still contributed towards biases in the known sample of jets by focusing primarily on high-mass star forming regions and complexes (due in large part to the enduring interest in high-mass star formation amongst astronomers). For example, some studies have targeted specific parts of high-mass star forming regions, such as the GM $2-4$ nebula (Khanzadyan et al., 2011) and the Braid nebula in Cygnus OB 7 (Khanzadyan et al., 2012), the Gulf-of-Mexico and Pelican nebulae (Bally et al., 2014), and M17 (Samal et al., 2018). Others have targeted high-mass objects in various places across the Galactic plane, e.g. Caratti o Garatti et al. (2015), Navarete et al. (2015), and Varricatt et al. (2010). So, even if the methods used to measure outflows are becoming standardised, a bias still exists in that most of the targeted studies focus on outflows from high-mass stars, or from stars in high-mass star-forming regions. The results from such studies, whilst useful for theoretical models of high-mass star formation, may not necessarily apply to the low- and intermediate-mass regimes which are not represented by the results of such surveys. The need for a large-scale, unbiased census of molecular outflows from across the Galactic plane should therefore be clear, and is one of the reasons for the existence of the UWISH2 survey.

The early results from the UWISH2 survey in the Serpens and Aquila region of the Galactic plane (Ioannidis and Froebrich, 2012a,b) investigated a continuous area of 33 square degrees ($\sim 20\%$ of the original UWISH2 survey area) and was the first such survey of this size. By analysing the molecular outflows in two additional regions of similar size but differing environmental structure, with consistent methodology and the same instrumental set-up, it is possible to build an unbiased and statistically significant sample of outflows. Using this sample, their properties can be measured and contrasted in order to also investigate the wider context; that is, the dependence of star formation upon the local environment in which the forming stars and their outflows are found.

2.8 MHOs

The term Molecular Hydrogen emission-line Objects (MHOs) was first coined by Davis et al. (2010) in order to describe outflows detected via shocked molecular hydrogen emission, primarily in the $1-0\,S(1)$ line of H_2. Studies prior to this investigated them in conjunction with their optical counterparts, which were already known of as HH objects (e.g. Eisloffel et al. 1994; Garden, Russell, and Burton 1990; Wilking et al. 1990). However, MHOs are detected in the NIR and often cannot be detected at optical wavelengths due to heavy extinction. Thus MHOs are not always associated with a HH object as they trace different parts of the outflow. As the number of studies discovering new MHOs grew, so did the need for a naming convention that would define and describe these objects in a consistent way. A naming convention of [MHO XXXX] was adopted in order to be able to identify these objects more easily in catalogues, where the Xs represent numeric characters. The MHO catalogue therefore gathered all outflows that had been measured up until that point in the $1-0\,S(1)$ line of H_2 into a single database and standardised the process by which such outflows are catalogued and defined.

MHOs are defined by the catalogue as spatially resolved, shock-excited H_2 emission features produced by jets and outflows from YSOs and protostars. Emission produced via non-thermal excitation (i.e. fluorescence) are not included, nor are emission features produced by evolved stars (such as Asymptotic Giant Branch (AGB) stars) or planetary nebulae. The emission must be visible in one of the NIR lines of H_2, so that outflows that are only visible in other lines are excluded from the catalogue. However, for the sake of completeness, if an MHO has a counterpart HH object then the HH designations are listed in the catalogue as well. The original catalogue contained almost a thousand MHOs gathered from the literature, and they are grouped into regions (based on the boundaries of the 88 IAU[1] constellations) in order to make the list manageable. Since the UWISH2 survey was conducted using the $1-0\,S(1)$ line of H_2, the identification and analysis of the emission features that form the basis of this Thesis were performed consistently with the requirements set out in Davis et al. (2010), so that all outflows discovered could be defined as MHOs (see Chapter 3 for details).

---

[1]International Astronomical Union, https://www.iau.org/

2.9   The Milky Way

The Milky Way is a barred-spiral galaxy, in which we are located approximately 8 kpc from the centre (Bland-Hawthorn and Gerhard, 2016) along the Orion-Cygnus arm. Since our solar system lies in the plane of the Galactic disk, this creates difficulties in performing observations of our own Galaxy, particularly at low Galactic latitudes due to the high densities of dust, gas and stars along any given line-of-sight. Towards the Galactic centre, the field is so crowded by stars that it is not yet possible to observe beyond the Galactic centre to the other side of the Galaxy.

Studies of the structure of our own Galaxy are aided by a statistical view of Milky Way analogues outside the Galactic neighbourhood, and it is well known from observations of other galaxies that stars most typically form along the spiral arms. This is where the concentrations of dust and gas are highest. Since our solar system is located at the edge of a spiral arm, we can study the star formation activity and the stellar populations in our own locality where surveys have the greatest sensitivity. However, this high column-density of dust and gas in the spiral arms increases the interstellar extinction, hindering our efforts to observe young stars.

There are three main regions that will be covered by the analysis performed in this Thesis. Cygnus-X, Auriga, and Cassiopeia. The Auriga region is a relatively low-mass, low-density region near the Galactic anti-centre. The IAU boundaries of the constellation cover an area of about 650 square degrees, and includes open clusters such as M36, M37, M38, and the Flaming Star nebula. Most of the objects in the region are associated with the Perseus spiral arm, projected at a distance of around 2 kpc from the Sun. Cassiopeia has a similar size on the sky, with around 600 square degrees, and at a similar distance, although it does also contain some nearby giant stars. The region hosts two supernova remnants (SNR), 3C 10 and Cassiopeia A, and several open clusters, and has a similar environmental density distribution as Auriga. Although they are not contiguous regions on the sky, they are compositionally similar and representative of low-mass star-forming environments, and hence will be treated as one region for the duration of this Thesis.

The Cygnus constellation covers about 800 square degrees on the sky. It contains a wealth of astronomical objects of interest, including several OB associations, hundreds of HII regions, planetary nebulae (PNe), SNRs, star-forming complexes, stellar clusters, and the spectacular radio galaxy Cygnus A. The Cygnus-X region that is the focus of this Thesis was originally discovered in 1952 as a diffuse radio source and given its designation in order to differentiate it from the already well-known Cygnus-A (Piddington and Minnett, 1952). Much of Cygnus-X is invisible at optical wavelengths due to its location behind the Great Cygnus Rift. However, in IR and radio regimes it is revealed as a rich, dynamic and complex site of massive star formation in the Galaxy. Since Cygnus-X lies at a relatively nearby distance of around 1.4 kpc from the Sun, it is an ideal laboratory for detailed studies of massive star formation that are difficult at larger distances.

For a number of decades, there was considerable debate regarding the distance toward the Cygnus-X complex, and whether it was a single complex being excited by the Cygnus OB 2 association (e.g., Ikhsanov 1961; Véron 1965), or an interlayering of molecular clouds at a range of distances projected along the line of sight due to its position near the Galactic tangent, with distances for

individual nebulae and H II regions ranging between 1 and over 4 kpc (e.g., Dickel, Wendker, and Bieritz 1969; Kerr and Westerhout 1965; Sharpless 1965). The matter is still not fully settled. Although the work of Schneider et al. (2006), which traced molecular clouds in ^{13}CO, showed that the clouds in Cygnus-X are likely to be connected parts of the same complex (and therefore at the same distance), the maser parallax study of Rygl et al. (2012) showed that even if the clouds around the Cygnus OB 2 association are related (located at 1.4 kpc), there are objects that can be projected much further away (e.g. AFGL 2591 at 3.3 kpc).

Cygnus OB 2 is the most massive OB association nearby to the Sun, and it has been suggested that it could be a proto-globular cluster (Knödlseder, 2000) given that it contains in the region of 2600 ± 400 stars of OB type, with around 120 ± 20 O-type stars, and an estimated cluster mass of $10^5 \, M_\odot$ (Berlanas et al., 2018; Comerón et al., 2002; Knödlseder, 2000). On the eastern and western edges of the ionised region created by Cygnus OB 2 are the Cygnus-X north and Cygnus-X south regions, respectively, as defined in Schneider et al. (2006). Cygnus-X north covers an area of 3.3 square degrees from:

RA: $20^h 35^m 15.0^s - 20^h 43^m 00.0^s$

Decl: $40:30:00 - 43:20:00$

and includes several well-studied star forming complexes (including DR 17, DR 18, DR 20 – DR 23, and W 75 N). Cygnus-X south encompasses a 7.5 square degree region from:

RA: $20^h 28^m 30.0^s - 20^h 39^m 45.0^s$

Decl: $38:00:00 - 40:30:00$

and is home to the massive star-forming cluster AFGL 2591, DR 15 and IC 1318 (b / c). The mass of the Cygnus-X north region is estimated as $2.8 \times 10^5 \, M_\odot$, whilst the Cygnus-X south region has an estimated mass of $4.5 \times 10^5 \, M_\odot$ (Schneider et al., 2006). For the total Cygnus-X region encompassed by their survey, Schneider et al. (2006) calculate a total cloud mass of $4.7 \times 10^6 \, M_\odot$ (assuming a distance of 1.7 kpc towards the OB 2 association). Despite the overall lower mass in Cygnus-X north, the mass per square degree is higher than in Cygnus-X south, and Kryukova et al. (2014) found in their YSO study of Cygnus-X that the two regions are dissimilar environments with very different morphologies, and that the luminosities of the YSOs in Cygnus-X north were higher than those in Cygnus-X south.

In addition to these related clouds in the centre of Cygnus-X, on the eastern side of the region is an area dubbed W 80 (Wendker, Benz, and Baars, 1983) which is likely to be much closer to us. This region is composed of a H II region approximately $3°$ in diameter, whose reflection nebulae, the North American nebula (NGC 7000) and the Pelican nebula (IC 5070) are visible at optical wavelengths and are bisected by the Lynds dark cloud L 935 (Lynds, 1962). This cloud obscures the star (or stars) responsible for ionising the region. Comerón and Pasquali (2005) suggest this is a single star of O5V spectral type (2MASS J205551.25+435224.6), but Straižys and Laugalys (2008) found 4 – 5 candidate O-type stars that could be contributing to it. Various distances have been suggested for the L 935 cloud, providing a minimum distance for the stars behind it. The earliest was around 550 pc (Straizys et al., 1989), which has been periodically revised from 520 pc

(Laugalys et al., 2006) up to 610 pc (Laugalys and Straižys, 2002). Distances toward the stars behind the cloud are more difficult to determine and have large uncertainties. It is also difficult to determine the extent of this nearby region due to the high extinction, which is found to be up to $A_V \sim 35$ mag (Cambrésy et al., 2002). However, mass estimates of the molecular clouds forming the shell of the HII region are of the order of a few 10^4 M$_\odot$ (Bally and Scoville, 1980; Feldt and Wendker, 1993). The North American nebula region contains about three quarters of the dust and dense gas in the W 80 complex, and the most massive Bolocam Galactic Plane Survey (BGPS) clumps (Bally et al., 2014).

In short, the Auriga and Cassiopeia region provides us with a relatively low-mass and low-density environment, W 80 with a fairly low-mass but dense environment, and the Cygnus-X north and south regions with two high-mass environments that are distributed differently. This means that by searching for the outflows in Cygnus-X and Auriga and Cassiopeia, a unique astrophysical laboratory is presented such that the environments in which outflows are found can be probed statistically to determine the extent to which those environments affect the outflow properties.

2.10   Summary of the UWISH2 survey

The UKIRT Wide-Field Imaging Survey for H$_2$ (UWISH2) was completed in 2011 (Froebrich et al., 2011) as an unbiased survey in the narrow-band $1-0$ S(1) ro-vibrational line of molecular hydrogen at $\lambda = 2.122 \pm 0.021$ µm. For convenience this line will be referred to as H$_2$ for the remainder of this Thesis, as distinct from any other ro-vibrational lines of molecular hydrogen. The original survey covered a 209 square degree region of the Galactic plane between $10° \le l \le 65°$ and $-1.5° \le b \le +1.5°$, with an extension (UWISH2-E) proposed in 2012 to increase coverage in the Galactic Plane to $l \sim 357°$, i.e. through the Galactic Center. This extension was completed in 2013, running between 6th April and 11th December of that year (Froebrich et al., 2015). UWISH2-E also observed the Cygnus-X (42 square degrees) and the Auriga and Cassiopeia regions (35.5 square degrees). The coverage was not homogeneous across the longitude and latitude ranges due to time constraints, hence some preference was given to high-extinction regions. In Fig. 2.7 the line-of-sight coverage of the UWISH2 survey is demonstrated.

The UWISH2 survey was undertaken using the Wide-Field Camera (WFCAM; Casali et al. 2007) which is an IR camera with eight filters. The camera itself consists of four Rockwell Hawaii-II (HgCdTe 2048 × 2048 pixel) arrays that are cooled to 75 K during observations, and is mounted on the United Kingdom Infrared Telescope (UKIRT) in Mauna Kea, Hawaii. The UWISH2 survey used the H$_2$ filter centered on $\lambda = 2.122$ µm with bandwidth $\Delta\lambda = 0.021$ µm. The WFCAM filters available are listed in Table 2.1.

The arrays which comprise the WFCAM camera are arranged in a two-by-two configuration as shown in Fig. 2.8 (a), spaced by 94% in the focal plane, with the auto-guider array fixed between them and oriented at 45°. A single telescope pointing produces an image as shown in Fig. 2.8 (b), covering an area of 0.19 square degrees. To produce a filled image it is necessary to perform four
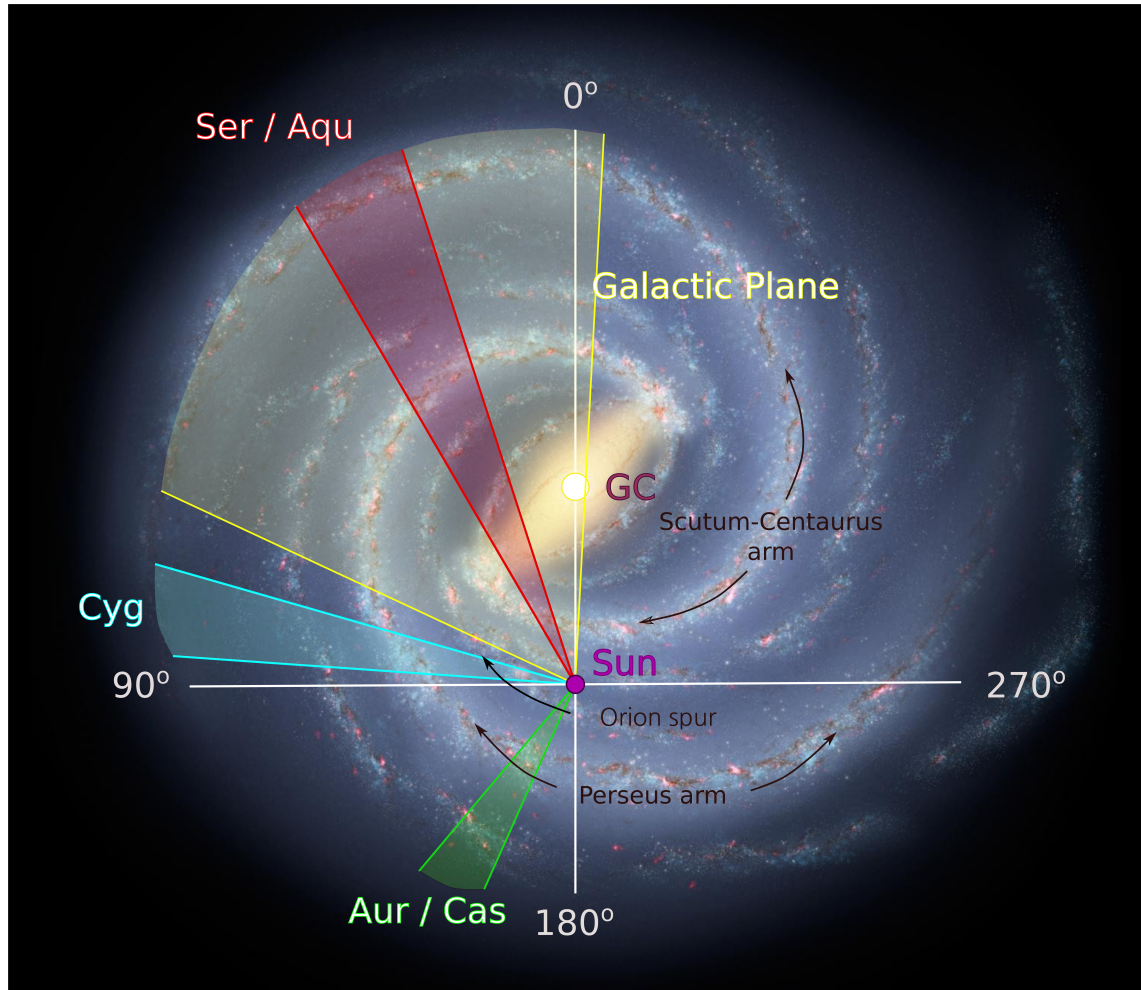
FIGURE 2.7: A schematic demonstrating the fields-of-view of the UWISH2 survey elements. The background image (not to scale) is courtesy of NASA / JPL – Caltech / R. Hurt (SSC/Caltech). The Perseus and Scutum-Centaurus spiral arms are indicated, along with the Orion (local) spur and the Galactic centre (GC). The approximate location of the sun is shown with a purple circle. The coloured cones represent the fields-of-view of Serpens and Aquila (red), and the Cygnus-X (cyan) and Auriga/Cassiopeia (green) extensions. The yellow cones represent the coverage in the Galactic plane that is yet to be analysed. The lengths of the cones are illustrative and not intended to show the actual depth of field achieved by the survey.

separately pointed observations which can be tiled together as demonstrated in Fig.2.8 (c), thereby increasing the area of coverage to 0.75 square degrees for each tile.

The pixel scale of $0''.4$ per pixel is rather large and means that given the typical seeing in good conditions at UKIRT ($< 0''.6$), the point spread function (PSF) is under-sampled. To remedy this, micro-stepping is used (a 2×2 sequence with step size $N + 0.5$ pixels) and the resulting images interlaced into a grid with $0''.2$ pixel spacing. This results in 4096×4096 images with a $0''.2$ pixel scale that fully sample the expected seeing.

The UKIDSS Galactic Plane Survey (Lucas et al. (2008), hereafter UGPS) obtained broadly the same coverage as UWISH2 in the J-, H- and K-bands, and UWISH2 used the same set-up to ensure that the data obtained were equivalent in quality and coverage. The major difference between UGPS and UWISH2 is the choice of filter, and hence exposure time, i.e. since the flux through

TABLE 2.1: Table listing the WFCAM filters available at the UK Infrared Telescope (UKIRT). Filter specifications are obtained from Hewett et al. (2006).

WFCAM filter	Central wavelength [μm]	Bandwidth [μm]	50 % cut-on [μm]	50 % cut-off [μm]
Z	0.878	0.095	0.830	0.925
Y	1.020	0.100	0.970	1.070
J	1.250	0.160	1.170	1.330
H	1.635	0.290	1.490	1.780
K	2.200	0.340	2.030	2.370
H_2	2.122	0.021	2.111	2.132
[FeII]	1.645	0.028	1.631	1.659

the narrow-band filter is lower than through the broad-band filters, the narrow-band filters require longer exposure times in order to achieve comparable signal. Table 2.2 lists the integration times used in each filter, and the typical 5σ depth. The uncertainty values vary across each of the surveys due to variations in seeing, the brightness of the sky, atmospheric transmission and thermal background (Lucas et al., 2008). The UKIRT Widefield Infrared Survey for Fe^+ (UWIFE), the sister survey to UWISH2, was also performed with the same instrument and covered the same regions of the Galactic plane in [FeII], albeit without the Cygnus-X and Auriga and Cassiopeia extensions (Lee et al., 2014).

TABLE 2.2: Table listing the integration times per filter, median 5σ depth in each filter and the uncertainty in the depth for the UGPS survey and UWISH2 survey. Data for (a) obtained from Lucas et al. (2008), and for (b) from Froebrich et al. (2011).

Survey	Filter	Integration time	Median 5σ depth [mag]
UGPS[a]	J	80 s	19.77 ± 0.20
	H	80 s	19.00 ± 0.20
	K	40 s	18.05 ± 0.20
UWISH2[b]	H_2	720 s	18.30 ± 0.20

The J, H, K, and H_2 data are reduced via the Cambridge Astronomical Survey Unit (CASU; Dye et al. 2006), with the astrometric and photometric calibration being based on 2MASS (Dye et al., 2006; Hewett et al., 2006). The pipeline processing is described in detail in Irwin et al. (2004). These reduced data are then archived and distributed by the Wide Field Astronomy Unit (WFAU) Science Archives (Hambly et al., 2008). The UWISH2 website[2] also supplies these data, in addition to continuum-subtracted, H_2-K FITS versions of each tile. The methods by which these images were generated will be described in more detail in Chapter 3.1.1.

---

[2] UWISH2 website; http://astro.kent.ac.uk/uwish2/index.html

(a) Focal plane layout of the WFCAM arrays with respect to the auto-guider array (AG).

(b) Single-pointing image.

(c) Tiling set up.

FIGURE 2.8: A schematic demonstrating the layout of the WFCAM focal plane (Dye et al., 2006) (a) and the image that results from a single pointing of the telescope (b). Four separately pointed observations are needed to fill the gaps and create a single 4×4 WFCAM tile, the order of which is shown in (c).

2.11 Aims of this Thesis

The first aim, and chief among them, is to mine the UWISH2 data and build a large, unbiased sample of young stellar outflows from the Cygnus-X and the Auriga and Cassiopeia regions of the Galactic plane. By doing this, the community is provided with a statistically significant population of outflows whose properties can be investigated, without selection effects that skew the known population in favour of high-mass objects. These samples will be comparable with the earlier works of Ioannidis and Froebrich (2012a,b) in the Serpens and Aquila region, which also used the

UWISH2 data. Comparing these samples statistically will allow several scenarios and questions to be addressed.

1. Evolutionary stage - The outflow properties will be investigated as a function of their evolutionary stage in order to test the results of Stanke (2003), who found that more evolved stars drive shorter, fainter outflows than the less evolved stars (proposed to be a result of time-variable mass accretion that decays over time).

2. Length distributions - There is a great deal of interest in parsec-scale outflows, so the fraction of these will be investigated across the different regions. The nature of the distributions will be constrained statistically. The luminosity function will also be constrained.

3. Environment - The question of feedback also applies to outflows in clustered environments. Since most stars form in clusters (Lada and Lada, 2003), it is pertinent to ask what effect nearby neighbours have on any outflows produced by stars in clusters.

4. Orientation - Previous studies have produced conflicting results with regard to the position angle of outflows. In Serpens and Aquila, Ioannidis and Froebrich (2012a) found that there is a preference for outflows to be aligned perpendicularly to the Galactic plane, however Zhang et al. (2015) found the orientation to be random in Aquila. The orientation of outflows was also found to be random in Orion A (Davis et al., 2009; Stanke, McCaughrean, and Zinnecker, 2002) and Perseus west (Davis et al., 2008). However, in DR 21 (in the Cygnus-X region) the brightest outflows were found to be oriented perpendicularly to the local filament whilst the fainter outflows were randomly oriented (Davis et al., 2007). The orientation in Cygnus-X and Auriga and Cassiopeia will therefore be investigated on multiple scales in order to probe these conflicting results.

5. Accretion history - Different classes of young stars outburst on very different timescales, but these special objects are difficult to locate and can only be distinguished by their spectral features. The best known class of eruptive variable star is the FU Orionis type (FUors, coined by Ambartsumyan 1971) of which there are still only 33 objects currently known (Connelley and Reipurth, 2018). If the accretion/ejection history can be inferred by the gaps between subsequent knots of ejected material, then it should be possible to identify potential eruptive variable stars by the lengths of these gaps.

These questions can be distilled into a straightforward question that the author shall attempt to answer: are the outflow properties most dependent upon the evolutionary stage of the driving source, or on the environment through which it propagates?

Chapter 3

Methodology

Author's note: The work presented in this chapter has been peer-reviewed and published in the Monthly Notices of the Royal Astronomical Society (Froebrich and Makin, 2016; Froebrich et al., 2015), and the Astrophysical Journal Supplement Series (Makin and Froebrich, 2018). It was undertaken from September 2014 – 2018 in collaboration with Dirk Froebrich at the Centre for Astrophysics and Planetary Science (CAPS), at the University of Kent. The program used to perform photometry on the H_2 emission features was written by Jack Nicholas and Dirk Froebrich and submitted as part of a Masters Thesis (Nicholas, 2016).

3.1 Part I: The search for extended H_2 emission

As described in Chapter 2.10, the UWISH2 survey imaged large regions of the Galactic plane in the $1-0\,S(1)$ narrow-band transition line of H_2. It was then necessary to search each tile systematically in order to isolate the shock-excited emission features, and these were catalogued and published in Froebrich et al. (2015) (hereafter F15). However, the narrow-band images also contain emission from point sources (i.e., stars) that emit radiation over a broad continuum that includes the $1-0\,S(1)$ line. Therefore, before the tiles could be searched, it was first necessary to subtract this continuum emission and ensure that all measured fluxes only contain contributions from extended sources and not point sources.

3.1.1 Continuum subtraction

The H_2 transition line at $\lambda = 2.122\,\mu m$ falls within the K-band. This means that it is possible to subtract the continuum flux by using K-band images from the UKIDSS Galactic Plane Survey (UGPS; Lucas et al. 2008). By design, the UWISH2 survey followed the same tiling procedure as UGPS and used the same instrument. Therefore the H_2 images (from UWISH2) and K-band images (from UGPS) were, for the most part, obtained at the same positions (typically within small offsets of about $1'$). This allows for straightforward subtraction of the K-band continuum images from the H_2 narrow-band images, which was done separately for each image. In the small fraction of cases where the offset was larger than one arcminute, composite K-band images were created by

combining adjacent images using the Montage software package[1]. The image subtraction routine follows the method described in detail in Lee et al. (2014), and was implemented and run by Dirk Froebrich. The routine aligns each H_2 and corresponding K-band image. A $1\,000 \times 1\,000$ pixel sub-image is used to locate isolated, unsaturated stars so that the scaling factor can be calculated, which is then applied to the whole K-band image. The K-band images are scaled to the H_2 images, rather than the other way around, in order to preserve the H_2 flux data. This sub-image is also used to determine the point-spread function (psf) shape, so that psf-fitting can be used to subtract the stars. The result is H_2-only images, which will be referred to as "difference" images. In these, H_2 flux is represented in positive-valued regions. An example of a difference image is shown in Fig. 3.1 (a).

3.1.2 Using images to identify features

In addition to the H_2-K difference images, colour-composite images were used to aid in the identification of H_2 emission features. The pairing of UWISH2 and UGPS data provides a number of possibilities for creating RGB colour-composites and each combination of filters highlights different features and objects. Figure 3.1 shows a bright-rimmed-cloud near IRAS 20294+4255 (discovered in the Cygnus-X region) using each of the potential filter / colour channel configurations, in order to examine the utility of the different combinations.

3.1.2.1 JHK

This configuration, demonstrated in Fig. 3.1 (b), places the K-band image in the red (R) channel, the H-band image in the green (G) channel, and and the J-band image in the blue (B) channel. Foreground objects, i.e. those which lie in front of most molecular clouds, are not typically subjected to a large amount of reddening. They will therefore have a roughly equal amount of flux in each of the RGB channels and appear mostly white (or blue-green). By contrast, stars located behind (or within) molecular clouds are reddened by dust and therefore have a lower relative flux in the blue channel, making them appear green, brownish, or red, depending on how deeply embedded they are. Individual objects might be intrinsically red, but clusters of stars will typically exhibit a similar degree of reddening when compared to foreground (and background) stars. This makes JHK images very useful for uncovering near-infrared clusters of stars that may be embedded in their natal clouds and not observable at optical wavelengths.

However, most of the outflows are not observable in the JHK images since the K-band is not dominated by the 2.122 μm line emission. There are some exceptions to this, if the shocks are strong enough, where they may be visible very faintly in the K-band. More usual is for the strongest shocks to appear as green extended emission in JHK images. This is due to the 1.644 μm transition line of [FeII] which falls in the H-band. This traces the strongest outflow shocks and can also be found around HII regions.

---

[1] Montage: http://montage.ipac.caltech.edu/index.html

(a) H$_2$-K difference image

(b) JHK colour-composite image

(c) JHH$_2$ colour-composite image

(d) JKH$_2$ colour-composite image
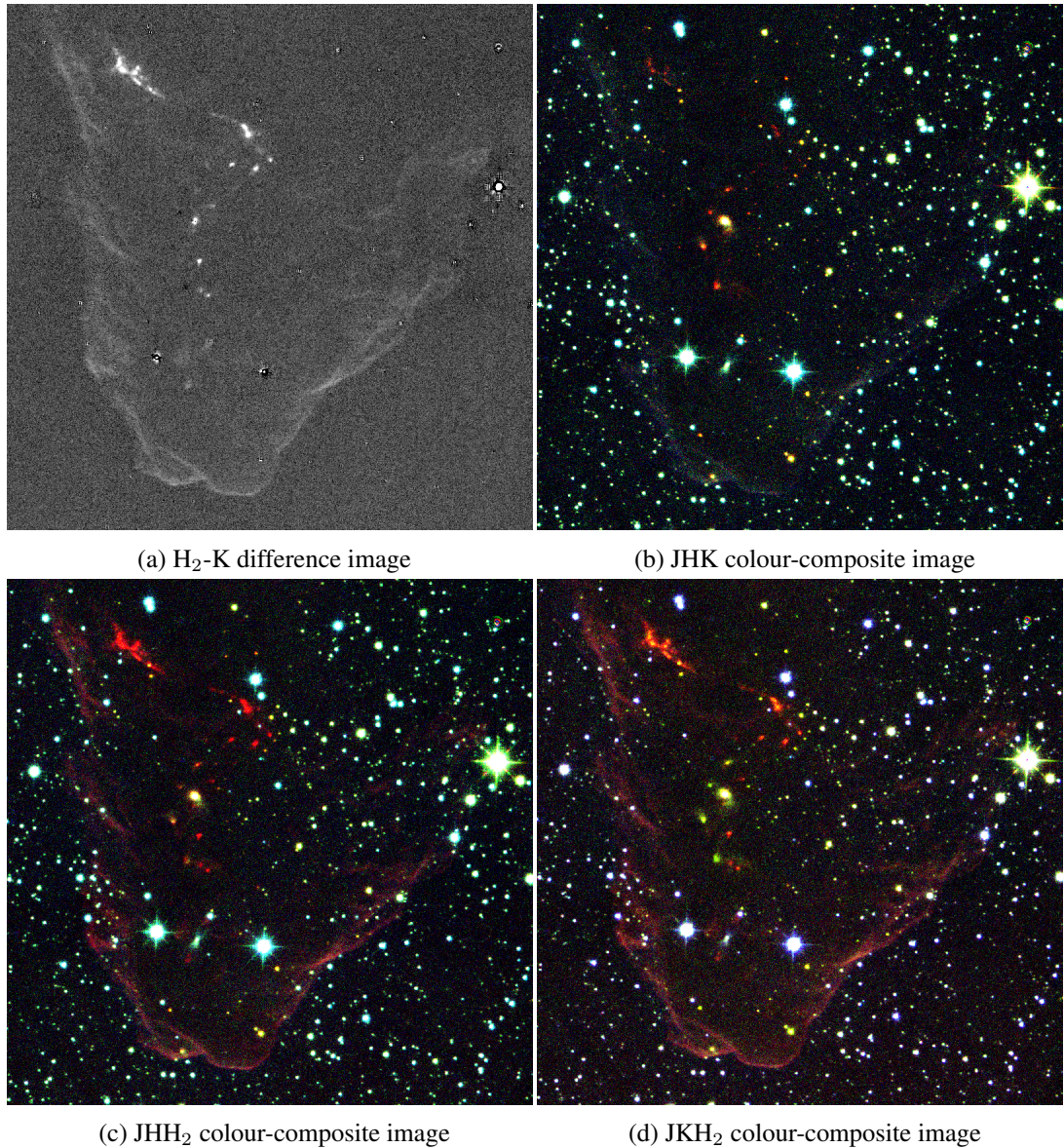
FIGURE 3.1: A low-mass bright-rimmed cloud near IRAS 20294+4255 in Cygnus-X, shown here in various configurations in order to demonstrate the ways in which images can be combined in the RGB colour channels to highlight different features in the images. The images are oriented such that north is toward the top of the image, and east to the left. The image represents an area of about 4 square arcminutes.

3.1.2.2   JHH$_2$

This configuration is shown in Fig. 3.1 (c), showing $R = H_2$, $G = $H, and $B = $J. Without the contribution from additional emission lines in the K-band, shocked H$_2$ emission appears as pure red, and outflows with very strong shocks will also contain a large amount of H-band emission, mainly from the 1.644 μm [FeII] line. These outflows will appear in the JHH$_2$ images to be more orange-brown. The inclusion of fluorescent emission in the H- and K-bands means that the edges of molecular clouds, which are being ionised by UV-radiation in the ISM, can be more clearly viewed than in the JHK images and are seen as brownish-red. In Fig. 3.1 this outlining of the molecular cloud is strongest on the edges that face the bottom of the image, implying that the source of the ionising

radiation is to the south of the cloud and outside of the image (most likely in the Cygnus OB2 association).

However, it can be noted that it is difficult to distinguish between the bright red outflow knots and the embedded stars that drive them. This is because the H_2 emission is of a longer wavelength than the H-band and these embedded stars have their light re-radiated at longer wavelengths, so they appear in the images as red, just as the outflow knots are. Therefore, although this configuration is useful for finding reddened / fluorescing objects, it does not help us to distinguish between them.

3.1.2.3   JKH$_2$

The final configuration, and the one selected for use in conjunction with the difference images, is shown in Fig. 3.1 (d) ($R = H_2$, $G = K$, and $B = J$). This provides the optimum view of the pure H_2 emission, whilst allowing the viewer to distinguish between reddened objects. As before, most continuum sources appear to be blue-white or blue-green, since they contain equal flux contributions from all three channels. As with the JHH$_2$ images, radiatively-excited and fluorescing cloud edges are easier to distinguish than in the JHK images due to the inclusion of additional ro-vibrational emission lines in the K-band. This means that the cloud edges appear as diffuse and brownish compared to the compact, bright red H_2 emission knots.

Unlike in the JHH$_2$ configuration, it is possible to differentiate between the emission knots (in red) and the bright green of the embedded YSOs that likely drive them. They appear green since the $1 - 0\,S(1)$ line of H_2 is on the shorter-wavelength end of the K-band, hence objects which are intrinsically red or which display excess emission emit most of their radiation at longer wavelengths than $2.122\,\mu m$. This is typically the case for embedded Class I protostars, which may also be flanked by reflection nebulae in the direction of the outflow axis. These are the partly-illuminated cavities through which the jets escape.

As with the JHK images, this configuration also highlights clusters, since stars in a cluster tend to be spatially grouped and appear similar in colour when compared to the background and foreground field stars. Crosstalk artefacts can also be more easily distinguished from real emission since, although they usually appear positive-valued in the difference images, they are typically dark in the JKH$_2$ image due to the fact that they have only, at most, about $1\,\%$ of the differential flux of the saturated star producing them (which progressively reduces further away from the source) and thus they do not have the appearance of stars. The JKH$_2$ combination in the RGB channels is therefore ideal for highlighting knots of emission from outflows, distinguishing them from cloud edges, and for identifying nearby young stars. For this reason, a JKH$_2$ image was created to correspond to every difference image to ensure the greatest accuracy in classifying emission features (an example is shown in Fig. 3.2).

(a) H_2-K difference image   (b) JKH_2 colour-composite image
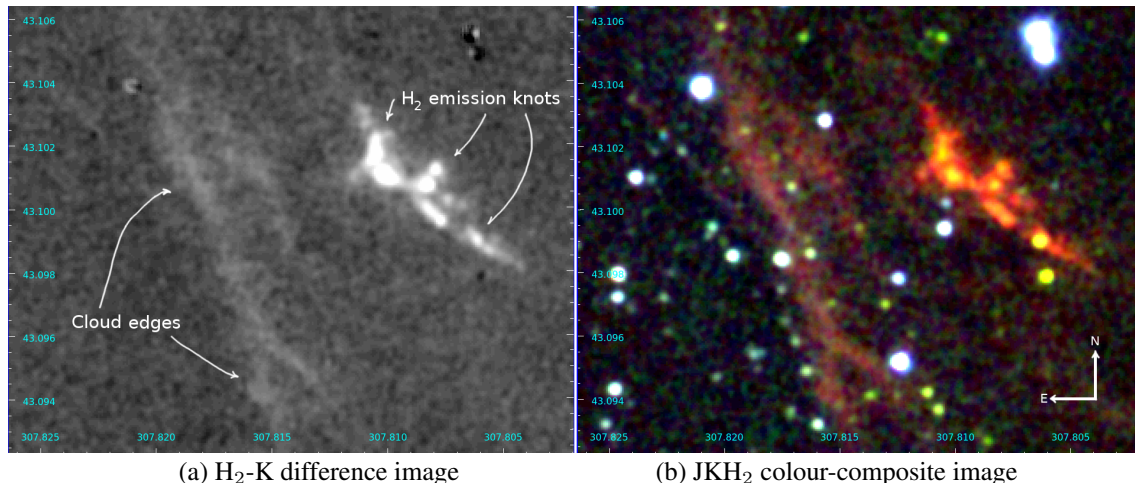
FIGURE 3.2: A closer view of the object in Fig. 3.1, demonstrating the identification and classification of H_2 emission. There is a clear difference between the bright, compact chain of H_2 emission features (labelled "H_2 emission knots") produced via shock excitation and the brownish photo-dissociation region (labelled "Cloud edges") produced via radiative emission.

3.1.3 Automated detection of H_2 features

The typical background in the difference images is spatially variable, which can generate false-positives in the automatic detection of H_2 features unless compensated for. To remove both the variability in the background (over large scales) and small point-sources not subtracted via psf-fitting, the small-scale structures were replaced with the median pixel value within $20''$, which represents the local background. Small-scale structures refers to those areas in the image smaller than $2'' \times 2''$ where the pixel value is above the $5\,\sigma$ noise level.

After this was completed for every image, contours were plotted in the DS9 software package[2] around each H_2 emission feature in the H_2-K difference images as the first step. These contours enclose every region in the background-corrected, point-source-removed difference images where the pixel values are greater than half the root mean squared (rms) noise level. The polygons described by these contours will be referred to hereafter as "regions". The coordinates describing the boundary of each region generated by DS9 were then saved as a plain text file where each region appears on a separate line. A script was then used to search this text file for, and remove, regions that are most likely to be considered false positives under the following conditions:

- In order to exclude any remaining point-sources or other noise, a minimum size limit was imposed on each of these regions. Any regions bounding an area smaller than $4'' \times 4''$ were removed from the final list of regions.

- Any region whose centre is within $3''$ of a 2MASS point source be removed in order to exclude saturated stars.

- For those stars with a magnitude of (K < 7 mag), regions within $35''$ of their centre were also removed in order to avoid erroneously detecting diffraction rings as extended emission,

---

[2] DS9 (versions 7.2.1 to 7.5): http://ds9.si.edu/site/Home.html

since they can span areas too large to be automatically removed in the background correction of the earlier steps.

- Finally, regions within $10''$ of the edge of an image were also removed, but this distance is smaller than the typical overlap between adjacent images. Therefore, emission features are not lost simply by virtue of being located near an image boundary.

3.1.4   Feature verification

Despite using the above-mentioned process to remove artefacts and false-positives in the list of regions, some inevitably remained. Figure 3.5 shows a series of examples of the different types of false-positives that can be included during the automatic selection process, and these will be explained in more detail in Chapter 3.1.5. It was therefore necessary to manually check every image (with contours) and remove regions belonging to any artefacts contaminating the sample. During this step, the morphologies and arrangement of the H_2 emission features were examined and classified according to their type.

All images were searched systematically by at least one person. For 35 % of the images, two people searched independently so that the completeness and level of contamination in the rest of the survey field could be estimated. Based on the comparison between these catalogues generated by individuals searching the same fields independently, the contamination by false-positives is estimated to be between $1-2$ %, and the completeness of the F15 catalogue is around 95 %. The 5 % of regions that are "missing" were not automatically detected, typically due to being faint and located within much larger regions of extended fluorescent emission, and they are not significant in terms of their area or flux when compared to the H_2 emission-line feature catalogue as a whole.

Ioannidis and Froebrich 2012a (hereafter IF12a) found that features tend to be spatially distributed in small clusters of ~ 5 pc in diameter at distances between $3-5$ kpc (Ioannidis and Froebrich 2012b, hereafter IF12b). Therefore, based on this work done in Serpens and Aquila using the early UWISH2 data, emission features were automatically "grouped" together in the H_2 emission-line feature catalogue if they had nearby neighbours within an angular distance of $0°.1$ (F15). Each individual region is examined and then labelled with a letter to designate the "type" (or apparent source) of emission, as follows:

- Planetary nebula (PN)
  Planetary nebulae tend not to be found directly in star-forming regions, and usually form ring-like or bipolar formations. Although they can be easily mistaken for jets and outflows, if they occur in relatively sparsely populated regions they are classified as PNe. Four catalogues of known PNe were cross-checked against the coordinates of the suspected PNe found in the survey: the SIMBAD catalogue; MASH (Parker et al., 2006); MASH2 (Miszalski et al., 2008); and IPHAS (Sabin et al., 2014). If the emission features appeared within a few arcminutes of any known PN, each of the regions bounding those features were labelled with "p". These objects are presented and discussed in Gledhill and Froebrich (2017) and Gledhill et al. (2018).

- Supernova remnant (SNR)

  Similarly to PNe, supernova remnants often form ring-like structures of shock-excited emission but can be very large in extent and have sections of low surface brightness. Therefore, the Green (2009) catalogue of known SNRs was checked against the positional data of the suspected SNR candidates. If the emission features lay within the approximate bounds of a known SNR, or if the features looked like a PN (but were not positively identified as one), the regions were classified with an "s". These objects have been discussed in Lee, Koo, and Lee (2014).

- Jets / outflows

  H_2 features (knots) that are extended (whether they are isolated, or situated in a clear chain with other nearby features), have a high surface brightness, and are not identified as being from a PN or SNR are most likely to be part of outflows from young stars. This is particularly applicable in regions of active star-formation. Regions that appear most likely to belong to a jet or outflow were labelled with "j". Contrary to the previous two categories, the list of jet knots was not cross-referenced with any catalogues for the purposes of classifying the emission objects.

- Unclassified

  This category applies generally to regions which cannot be classified as either a PN, SNR or knot from an outflow. Typically, this applies to knots with a low surface brightness, or those that are bright but located within areas containing high amounts of fluorescent emission related to photo-dissociation regions (PDRs) around HII regions (i.e., cloud edges).

Not all of the false-positives created by the subtraction process are artefacts. Indeed, some may be of scientific interest, which is why a simple threshold is not used in order to "flatten" the background variations. The K-band images were obtained several years before the H_2 images. This means that when the scaled K-band flux is subtracted from the H_2 flux, stars which vary over at least that timescale will leave either a positive or negative residual in the difference image. A positive residual indicates a decrease in brightness during H_2 imaging, whilst negative residuals indicate the star was brighter during H_2 imaging, as shown in Fig. 3.3. Contours around positive-valued stars were removed, and the positions marked using circles labelled with "v".

High proper-motion (HPM) stars usually appear in the images as extended objects with one half being positive and one negative. In the case of very fast (or potentially nearby) objects, they may appear to be two resolved variables very close together (one positive and one negative). The direction of travel of the object is implied, since, as with the variable stars, the negative "half" of the HPM is brighter during H_2 imaging and the positive "half" shows where the star was located during the earlier K-band imaging. The locations of HPM stars were recorded manually by removing any contours surrounding them and replacing those with circles labelled with "h".

Figure 3.4 shows an example of how HPM stars appear in the images. This image is unusual in that it contains several HPM stars, four of which are in apparent binary pairs ((a) and (c); this is implied by their proximity to each other and their direction of travel). The HPMs labelled (a) are travelling in the opposite direction to (b) and (c), although these two could form a triplet system

(a) H$_2$-K difference image   (b) JKH$_2$ colour-composite image
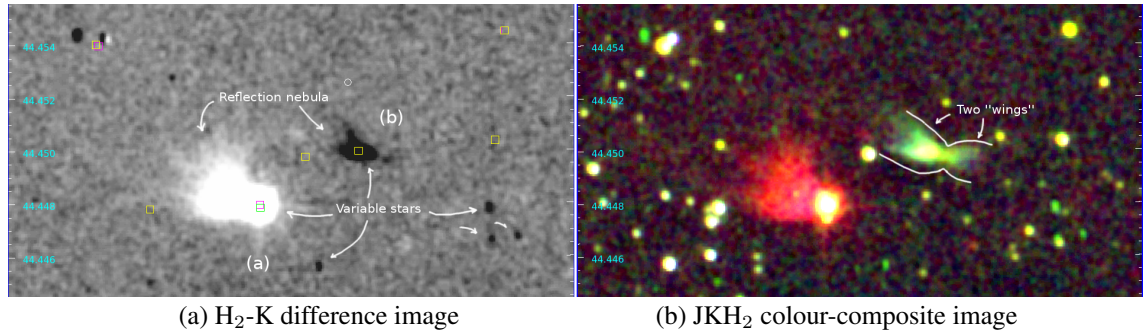
FIGURE 3.3: An example image of many potentially variable stars. The two central stars are of particular interest; the positive-valued star has a wide flare of H$_2$ emission towards the north-east and is known as a YSO. The negative-valued star to the north-west of this YSO has two "wings" which indicate a cavity that is reflecting light from the central object.

(a) H$_2$-K difference image   (b) JKH$_2$ colour-composite image
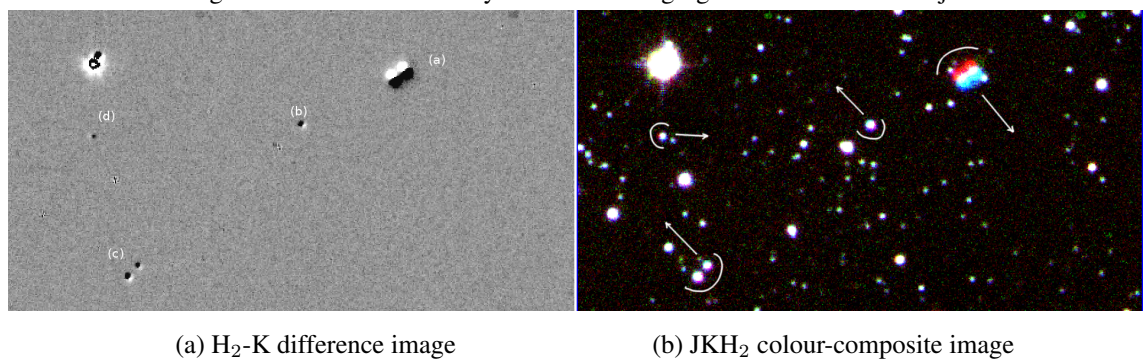
FIGURE 3.4: Examples of HPM stars. The stars labelled (a) and (c) are binary pairs, implied by their direction of travel (indicated with arrows) and close proximity to each other. It is possible that (b) could be a companion to (c), forming a wide triplet system.

since they appear to be travelling in the same direction and at similar velocities. HPMs can also be identified by their appearance in the colour images if they are moving quickly enough; they typically have a border around the central star which is blue on one side and red on the other.

3.1.5   Image artefact removal

Examples of the false positives deleted from the catalogue are demonstrated in the panels of Fig. 3.5. In addition to these examples, stars may not be completely removed and can escape the automatic point-source rejection where the seeing in the H$_2$ and K-band images was very different. None of these artefacts have any scientific interest and all automatically generated regions surrounding these objects were manually removed.

Figure. 3.5 (a) shows a star bright enough to saturate the detector which has caused diffraction spikes to appear. The saturation limit is at $K = 11$ mag so stars brighter than this are often not completely removed (as with the star just beneath the brightest star in this image). Very bright stars (where $K < 7$ mag) will also show diffraction rings, which have striations bright and extended enough to be automatically selected as real emission. In the case of the most extreme bright stars, the outer edges of the diffraction ring can lay outside the $35''$ automatic deletion radius around the star. Also highlighted are residual stars which were not completely removed from the
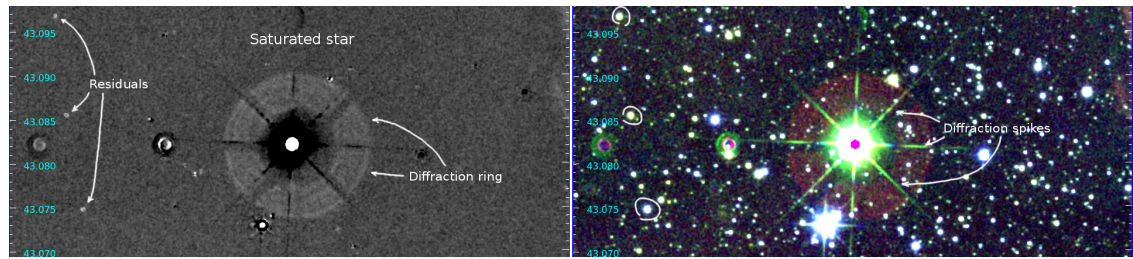
(a) Very bright, saturated star with a diffraction ring and diffraction spikes.
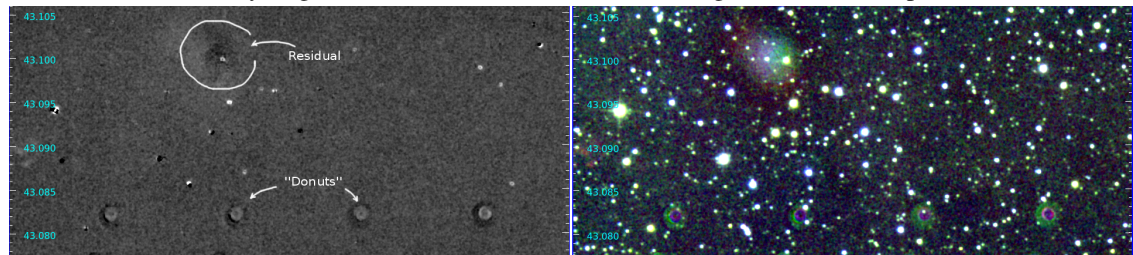
(b) Electronic cross talk ("donuts") and a residual memory effect.
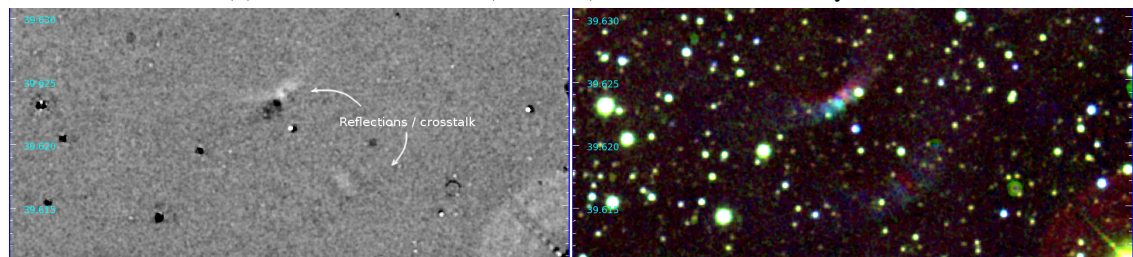
(c) Reflections from a very bright foreground star.
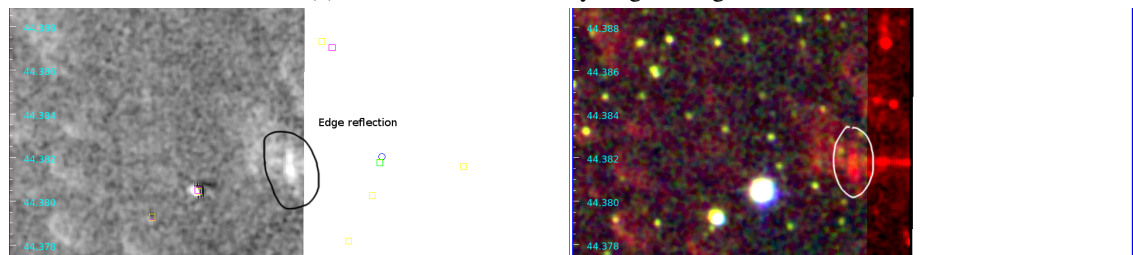
(d) Reflections from a bright star on the edge of the adjacent image.

FIGURE 3.5: A sequence of images demonstrating how different types of false-positives appear in the H_2-K difference images (left column) and the JKH_2 images (right column). These are discussed in the text.

difference image; the JKH_2 image confirms that these residuals (circled) are stars and not extended H_2 emission knots.

This same very bright star also caused the electronic cross-talk (labelled as "donuts") shown in Fig. 3.5 (b), whose morphology can lead to them being mistaken for PNe. These ring-shaped features can be diagnosed as artefacts by the fact that several of them will occur at evenly spaced intervals away from that star. There is also a memory effect shown in this image (labelled as "residual") that is caused by a very bright star that has saturated the detector in the same location during the previous exposure.

An example of reflections caused by a bright star is shown in Fig. 3.5 (c). The bright part of these artefacts can often look like bow shocks and be automatically selected as extended emission,

(a) Seeing   (b) Per-pixel noise   (c) Magnitude zero point
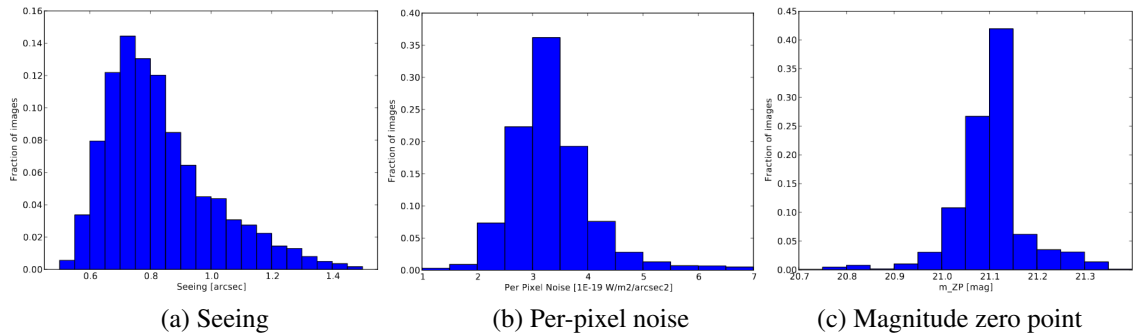
FIGURE 3.6: Histograms showing the distributions of (a) atmospheric seeing, (b) the $1\,\sigma$ per-pixel noise, and (c) the photometric zero-points mag_{zp} in the images, from F15.

but they have a tell-tale dark bow-shaped feature adjacent to them. Similarly, Fig. 3.5 (d) shows reflections caused by stars on the edges of adjacent images, which can look like bright flares of emission that may be mistaken for outflows. Most of these are automatically removed by virtue of being within $10''$ of the image edge, but can escape if they are longer than this. In these cases, the adjacent image is consulted and if there is a bright star nearby that could cause the reflection, the regions are removed.

3.1.6 Results

The labelled and verified contours from every region of the UWISH2 survey were collated into a single DS9 master region file and published in the F15 catalogue. Objects of each separate type can be extracted separately in order to form sub-catalogues of objects of interest; as the basis of this Thesis, the regions labelled as "j" (indicating jet or outflow emission) were extracted and investigated, as will be described in Chapter 3.2. Over $33\,000$ H_2 emission-line features are included in the final catalogue. Most of the flux contained in the regions comes from photo-dissociation regions (cloud edges) and SNRs, accounting for almost half of the total flux. The jets and PNe only contain between $7\,\%$ and $9\,\%$ of the total flux, and the flux per square degree (from jet-related emission features) is six times higher in Cygnus-X than in the rest of the Galactic plane, whilst in Auriga and Cassiopeia, it is six times lower.

The distribution of the seeing in the UWISH2 images is shown in Fig. 3.6 (a). The best seeing was obtained in the Galactic plane, with the two extension regions, Cygnus-X and Auriga and Cassiopeia, being responsible for much of the poor seeing. However, the inner Galactic plane suffers far more from crowding by field stars than even Cygnus-X, and so the photometry measurements in the regions covered by this Thesis should not be heavily impacted by slightly poorer seeing in some areas. Indeed, most of the survey ($82.9\,\%$) was conducted with seeing of less than $1''$, and the median seeing value of the entire survey was $0''.79$. In Fig. 3.6 (b) the distribution of the per-pixel noise level is shown, which was calculated for each image using the rms scatter in the background pixels. The median $1\,\sigma$ per-pixel noise is $3.25 \times 10^{-19}\,\mathrm{W\,m^{-2}\,arcsec^{-2}}$, which is consistent with the noise in the original UWISH2 survey area (Froebrich et al., 2011). The typical

$5\,\sigma$ noise (or surface brightness detection limit) is $4.10 \times 10^{-19}\,\mathrm{W\,m^{-2}\,arcsec^{-2}}$ when averaged over the median seeing (F15).

The distribution of the magnitude zero point values (mag_{zp}) is shown in 3.6 (c). Most of the images had $mag_{zp} \sim 21.1\,\mathrm{mag}$, which suggests that the atmospheric conditions were comparable for about two-thirds of the images. The zero-point magnitudes are used to calculate the average surface brightness. The methods used for performing photometry will be described in detail in Chapter 3.2.6 since this was redone for the jets and outflows as part of this Thesis.

3.2   Part II: Identifying outflows and their driving sources

3.2.1   Groups of emission features

As discussed in Chapter 3.1.4, if "jet" region contours were closer together than 0°.1 they were grouped together in the F15 catalogue (for "PN" region countours, the limit was 0°.05). These groups of contours were fully enclosed by circular markers whose coordinate position and radius were recorded. As the basis of this work, any groups containing "jet" emission contours were extracted from the master catalogue for investigation. There are 210 such groups of "jet" emission in Cygnus-X, and 51 in Auriga and Cassiopeia.

In order to avoid introducing systematic bias in the order that each group was investigated, it was necessary to randomise the selection of groups prior to inspection. Each group was given an arbitrary number, and that list of numbers was then sorted according to some other parameter (in the case of Cygnus-X, Galactic latitude, b) so that the group numbers were not in numerical order. After this, each group was selected at random for inspection, the emission features analysed and solved into outflows, and then the solutions were independently viewed by a second person; in Cygnus-X the author of this Thesis performed the initial analysis, whilst Dirk Froebrich performed the secondary check, and these roles were reversed in Auriga and Cassiopeia.

3.2.2   Setting up the images

The DS9 software was used in order to visualise the images, analyse the region contours and identify likely driving sources for the outflows. DS9 was chosen due to the large feature set in the software. It has, for example, the ability to create RGB frames and display multiple FITS files side-by-side; to match the coordinate systems and scaling of those various images; to query published catalogues and display the results as overlays on top of the images; to manually draw and edit contours and vectors, so that outflow properties could be measured; and the ability to load and save multiple region files. See Chapter 3.2.3 for discussion of the catalogues that were queried in order to infer likely locations of outflow driving sources. DS9 can be fully controlled from the command line, allowing the ability to script the opening of images associated with each group number in a consistent way.

In Auriga and Cassiopeia all of the outflows were new discoveries, with no already-known outflows listed as MHOs (see Chapter 2.8) found inside the UWISH2 survey area. In Cygnus-X the situation was complicated by the fact that there were 147 known MHOs inside the survey area. The positions of these already-known outflows were loaded into DS9 as a single region file, using circles as positional markers for all known MHOs labelled with their respective MHO numbers. When assigning contours to outflows, nearby MHO numbers were noted down but not checked at this point, in order to avoid confirmation bias in the solutions. These outflows were then revisited after all the groups were analysed in order to compare solutions.

Some groups fell across the edges or the corners of an image. They frequently contained outflows that spanned two or more images and thus could not be fully seen on the original image they

(a) Pre-analysis F15 catalogue contours   (b) Post-analysis contours
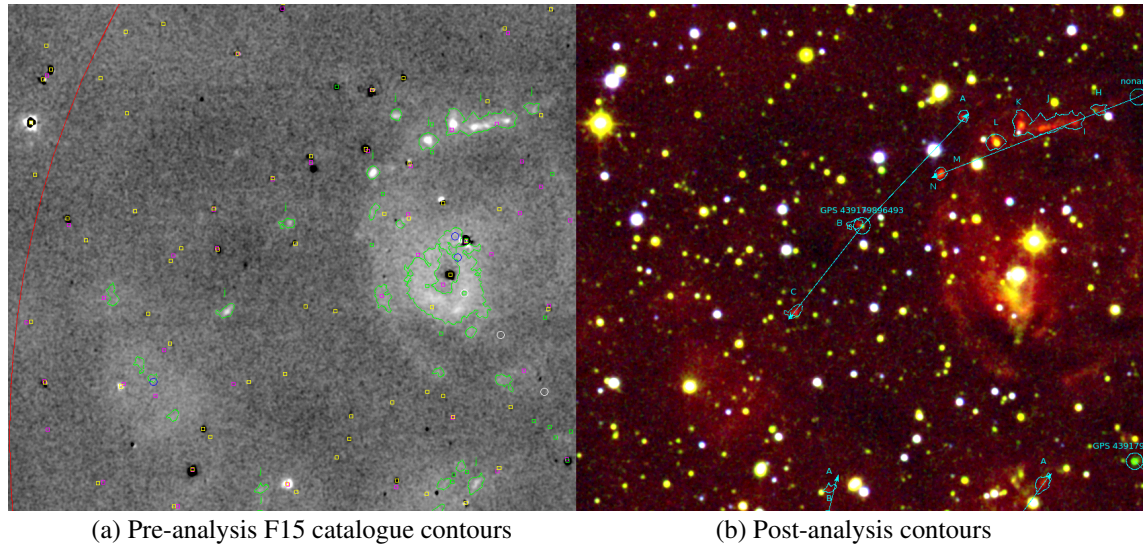
FIGURE 3.7: A demonstration of (a) pre-analysis and (b) post-analysis contours using H_2-K
and JKH_2 images of the L 906 E region in Cygnus-X. The red circle in the difference image
corresponds to the "jet" group that fully encloses all the related contours, and the small coloured
symbols are explained in Section 3.2.3.

were assigned to. Where these groups were encountered, composite H_2-K and JKH_2 images were
created (stitching adjacent images together) using the Montage software.

For each group of H_2 features, DS9 was opened with the H_2-K difference image and the JKH_2
images side-by-side. Logarithmic pixel scaling was used in order to show features more clearly
than can be seen in linear scaling. The catalogue of "jet" emission regions was overlaid onto both
images as a single region file, and for Cygnus-X the catalogue of already-known MHOs was also
overlaid for reference. The DS9 query facility was used to display point-source catalogue entries.
Using these catalogues allowed the pinpointing of potential driving sources in the vicinity of the
emission objects, which aided with the assignment of individual emission contours into the most
likely outflow configurations. Figure 3.7 shows an example of the H_2-K image overlaid with both
the F15 catalogue contours prior to analysis and the JKH_2 image with the fully analysed outflow
contours after analysis.

3.2.3   Point-source catalogues

All-sky point-source catalogues were used so that the comparison of driving source properties
between the Cygnus-X and the Auriga and Cassiopeia regions would be performed with consis-
tent data sets. The selected catalogues represent a broad range of wavelengths from across the
infrared and towards the sub-mm regime. Each catalogue was overplotted onto the difference im-
ages using different markers (as can be seen in e.g. Fig. 3.7). The SIMBAD catalogue was also
included so that any nearby objects of interest would not be missed (i.e., outflows detected at other
wavelengths, known clusters, etc).

Near-infrared: 2-Micron All Sky Survey

The 2-Micron All-Sky Survey (2MASS, Skrutskie et al. 2006) utilised three near-infrared filters; J ($\lambda = 1.24\,\mu$m), H ($\lambda = 1.66\,\mu$m), and K$_s$ ($\lambda = 2.16\,\mu$m), indicated using yellow squares. For each candidate driving source with a detection in the 2MASS catalogue, the 2MASS ID and the magnitudes in each filter were recorded. The resolution of the 2MASS images is around $4''$.

Near-infrared: UKIDSS Galactic Plane Survey

Data from the UKIDSS Galactic Plane Survey (UGPS, Lucas et al. 2008) was also used as a complement to 2MASS in the near-infrared. Both surveys used the same filters but ran at different epochs, providing a long baseline for measuring variability in the driving sources. For most of the detections in Cygnus-X, UGPS has two K-band detections (K$_1$ and K$_2$), so many of these driving sources have up to three K-band magnitudes. DS9 was not used to overlay the UGPS catalogue onto the images since the vast number of detections would obscure the images. Instead, the UGPS catalogue was queried manually via the WFCAM Science Archive[3] and the UGPS identifier was recorded, along with the magnitudes in each filter.

Mid-infrared: Wide-field Infrared Survey Explorer

The evolutionary stage can often be inferred by building the Spectral Energy Distribution (SED) of a given star as discussed in Chapter 2.4. However, building a full SED is not a trivial process. It requires reliable flux measurements across a large wavelength range to accomplish, and is far beyond the scope of this Thesis due to the number of outflows identified. However, protostars typically have an SED profile which slopes positively between 3.6 μm and 24 μm, whilst YSOs display negative slopes in this range. The mid-infrared slope of the SED can therefore be used as a diagnostic tool in order to infer the approximate evolutionary stage of each of the driving source candidates (see Chapter 2.4). Historically, the slope has been calculated using Spitzer data (IRAC + MIPS), but Spitzer coverage is not complete across the UWISH2 survey fields. It was shown in Majaess (2013) that the slope can also be calculated using data from the Wide-field Infrared Survey Explorer (WISE, Cutri and et al. 2013) catalogue. The WISE survey has four wave-bands, $W1$ ($\lambda = 3.4\,\mu$m), $W2$ ($\lambda = 4.6\,\mu$m), $W3$ ($\lambda = 12\,\mu$m), and $W4$ ($\lambda = 22\,\mu$m). The spatial resolution of bands $W1$ to $W3$ are in the region of $6''.3$, whilst $W4$ has a resolution of $12''$.

$$\alpha = 0.36\,(W1 - W2) + 0.58\,(W2 - W3) + 0.41\,(W3 - W4) - 2.9 \qquad (3.1)$$

The original WISE catalogue was later superseded by the AllWISE data release, so identifiers and magnitudes from the AllWISE data release were recorded and the positions were indicated using magenta square markers. Equation 3.1 from Majaess (2013) shows the calculation of the slope of the SED (α) using the magnitudes from the four WISE bands ($W1$ to $W4$). Any source that did not have magnitudes in all four bands was excluded. The

---

[3] WFCAM Science Archive; http://wsa.roe.ac.uk/

traditional cut-off of $\alpha > 0$ for Class I protostars and $\alpha < 0$ for Class II YSOs was used to estimate the evolutionary stage for each candidate driving source.

In this Thesis, the terms Class II and CTTS will be used interchangeably, as will Class I and protostar, hence use of the terms CTTS and protostars will be intended to refer to stars of an approximate evolutionary stage that may not strictly limited to Class II and Class I objects respectively. The classification of driving sources will be based upon Equation 2.8 using the traditional cut-off of $\alpha = 0$ to distinguish between Class I and Class II stars, since this is widely used. Spectroscopic confirmation of driving sources is beyond the scope of this work, so any individual objects referred to as CTTS or protostars should be considered to be candidates and not confirmed objects of each class.

The far-infrared and millimetre regimes

Both of the AKARI surveys were used: The mid-infrared all-sky survey taken with the Infra-Red Camera (IRC, Ishihara et al. 2010), and the Far-Infrared Survey point-source catalogue (FIS, Yamamura et al. 2010). Both were over-plotted onto the images using dark blue circles. The IRC samples at $9\,\mu m$ and $18\,\mu m$ (with a pixel scale of $\sim 10''$), whilst the FIS operates between $45\,\mu m$ and $180\,\mu m$ (with typical resolutions of $1'.5$). In the mm regime, the Bolocam Galactic Plane Survey (BGPS, Rosolowsky et al. 2010) was used, and white circles denoted the catalogue positions. It operated at 1.1 mm as a continuum survey with an effective resolution of $33''$, mapping thermal dust emission and high density gas (particularly associated with dense cloud cores). Where there are multiple possible driving sources for outflows, those with long wavelength (AKARI, BGPS or both) detections were given precedence since they most likely point to highly embedded sources, especially where there are no detections at shorter wavelengths. In addition, nearby detections from the Infrared Astronomical Satellite (IRAS, Neugebauer et al. 1984), marked using red circles, were noted but the flux measurements were not. The resolution of the IRAS images is about $4'$, so the point sources cannot be resolved reliably enough for our purposes, particularly in the crowded Cygnus-X field.

3.2.4   Sorting emission-line objects into outflows

The analysis was done in two "passes" so that each outflow was essentially analysed twice (and checked by the secondary checker), with the second pass occurring several months after the first. This should mitigate any bias in the analysis that might have arisen through an evolution in the method. The outline of the method for creating the outflows is as follows, with each step described more fully in the subsequent sections:

1. "First pass":

    (a) Identify "chains" of knots

    (b) Select the most likely driving sources

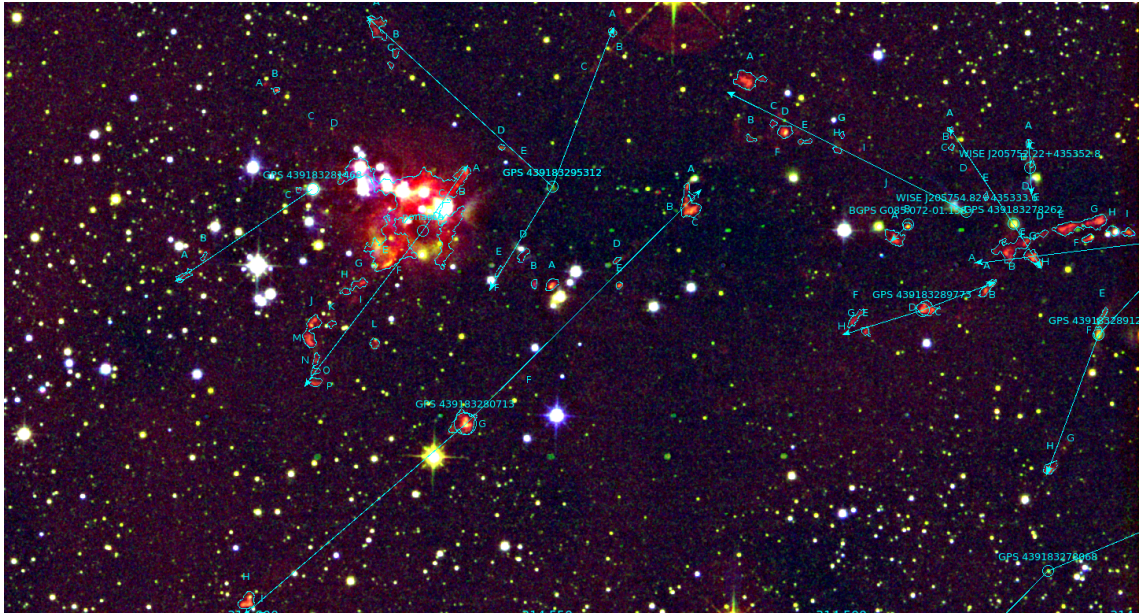   (c) Record outflow and source properties

FIGURE 3.8: An example of the assignment of knots to outflows in an extremely complex field in the W 80 region. Many of these outflows were already known of in the MHO catalogue (mainly from Bally et al. 2014).

    (d) $\longrightarrow$ Review performed by secondary checker to agree or dispute the solutions

    (e) Investigate further and adjust solutions

    (f) $\longrightarrow$ Second review performed by secondary checker

2. "Second pass":

    (a) Review each outflow again, checking measurements and completeness of data

    (b) Create region files and images

    (c) Perform photometry

    (d) Assign MHO numbers

For every jet group, the morphology and alignment of the H_2 emission knots contained within that group were examined. Likely outflow solutions were sketched and then refined until the most reasonable configuration to explain the group as a whole were reached. At all times, efforts were made to minimise the number of outflows created. In some cases this could be carried out straightforwardly, but in more complicated regions with many outflows crossing each others' paths, other factors more related to the driving source were taken into consideration. An example of a complex region is shown in Fig. 3.8. Knots that had too low a surface brightness to be included in the original F15 catalogue were labelled and grouped together with the rest of the outflow to which they most likely belong. At this stage, the small number of false-positives that remained in the F15 catalogue were also removed.

Once the assignment of knots to a particular outflow was completed, the outflow was given an "outflow ID" number to identify it within the UWISH2 outflow catalogue, in the format [OF XXX]

where XXX are numeric characters starting from 001 in each region. For single outflows, only one ID number was assigned irrespective of whether both lobes, or only one lobe, can be seen in the images. In complex fields where there is no alignment in nearby knots and the morphology suggests multiple possible outflows that cannot be resolved without follow-up observations, the knots were simply collected together under one ID number, rather than treating them each as individual objects (as was often done historically).

For any chain of knots that can be identified as a probable outflow, the star that drives it must exist somewhere along the outflow axis. Therefore, potential driving sources were highlighted if they aligned with the implied outflow axis. The point-source catalogue detections were then checked to prioritise the most likely driving source. Where several possible candidates existed, a number of factors were taken into account, with preference given in the following order:

1. Long-wavelength detections, such as in BGPS or AKARI FIS, may imply potential embedded Class 0 sources (which are not detectable at wavelengths shorter than about $20\,\mu\mathrm{m}$), and SIMBAD allows us access to additional, localised catalogues that can highlight other nearby objects indicative of very early star formation (such as masers).

2. Mid-infrared dections from WISE and AKARI IRC can reveal partially embedded Class I sources. SIMBAD also gives access to known YSOs from the catalogues of Kryukova et al. (2014) and Rebull et al. (2011) in the Cygnus-X region.

3. An excess of continuum emission in the JKH_2 images forming "wings" on opposite sides of a young star. Where these wings align with the implied outflow axis they can provide a strong indicator that the young star is the correct driving source (e.g. Fig. 3.3).

4. Stars which appear as negative point sources in the H_2-K images (and green in the JKH_2 images) can indicate strongly reddened and / or variable stars. These could be YSOs or giant stars. Investigation of the near- and mid-infrared magnitudes is required before they can be selected as potential driving sources. Stars with large J-H and small H-K colours in the NIR colour-colour diagram, or with negative slopes in their SEDs across the mid-infrared are likely to be main sequence stars and automatically excluded as potential driving sources.

5. If several potential driving sources still remained after using the above selection criteria, the star with the largest H-K colour was selected. As a very last resort, if the stars all have the same degree of reddening, the candidate with the greatest $K_2 - K_1$ variability was chosen.

There is an argument to be made that a selection bias exists in this assignment of driving sources, and it is certainly the case that the method is highly subjective. Any star that would be considered too "evolved" is excluded in order to avoid contamination by, for example, AGB stars. The least "evolved" candidate is always given preference, on the basis of the assumption that outflows are preferentially driven at earlier stages of stellar development.

No correction was made for extinction or inclination, but the slope of the SED is sensitive to both. Protostars are not simply projected onto a flat plane, so they experience increased reddening if they are projected further away (or more deeply) into the parental cloud when compared to neighbours that are situated toward the front of the cloud or on the edges where the column density of material

is lower. This means that even where several candidates exist, the "true" driving source may be totally embedded and undetected in any surveys.

Using variability as a decider between potential driving sources could bias the selection against the "true" driving source. If a driving source undergoes rare periodic accretion events that feed the outflow, but has relatively small variations over longer timescales, it could be overlooked if, at the time of imaging, it was not actively ejecting material. The only way to determine the real driving sources of outflows would be to obtain follow-up observations at longer wavelengths, preferably in conjunction with proper motion studies on the knots themselves.

Due to this general uncertainty in the correctness of the assigned driving sources, and the acknowledgement of the high chance of making incorrect assignments, all selected driving sources were given a percentage "probability" value to weight them by the likelihood of a correct assignment. This shall be referred to hereafter as the "confidence level", and is calculated based on, e.g, the number of other candidate driving sources, the presence of any nearby clusters, and so on. In other words, if three additional possible driving sources exist, the confidence level in the selected driving source will be, at most, 25 %. If the star seems to originate from any sort of clustered environment, this percentage will be even lower. Outflows in isolated environments where only one good candidate driving source exists will have a much higher percentage, but none has 100 %.

3.2.5 Measuring properties

3.2.5.1 Driving source properties

Once the most likely driving source for an outflow was established, the properties of that driving source were measured. The driving source was labelled with the identifier and coordinates of the shortest-wavelength survey in which it is detected, since this typically corresponds to higher resolutions. The ID number of the source was logged from every other catalogue in which it was detected. For the near- and mid-infrared surveys, the magnitudes in each filter were also recorded. Any other detections from SIMBAD were also included, such as the identifiers of nearby clusters, HII regions or other star forming regions. If the outflow was already known as a Herbig-Haro (HH) object or at radio wavelengths in, e.g., Gottschalk et al. (2012), this information was also gathered from the SIMBAD catalogue. In Cygnus-X, the YSO catalogues of Rebull et al. (2011) and Kryukova et al. (2014) partly covered the survey area; in the cases where a driving source coincided with the location of one of their known YSOs, the identifier was recorded.

In a number of cases it was not possible to assign a driving source at all. For chains of knots where the most probable location of a driving source could be implied by the morphology of the outflow knots, or by the presence of a filament of cloud crossing the outflow axis, this location was marked with a circled and labelled "*noname*". These coordinates are used as the outflow coordinates.

However, if the location of the driving source cannot be implied by the morphology of the knots, and there are no other indicators, a position was marked along the outflow axis to act as a temporary source which is labelled "*unknown*". If a reliable driving source position cannot be obtained

then the lengths and luminosities of each lobe are also unreliable and cannot be permitted to contaminate the distributions. For this reason, they were given an extremely low confidence level ($0-10\%$), in order to fully exclude them from the analysis. They were, however, included in the catalogue and the fluxes of each knot were measured for the benefit of future studies.

Similarly, for individual, isolated knots with no implied direction of travel, or groups of mis-aligned knots, the identification of potential driving sources was almost impossible. In these cases, a marker was placed in the centre of the group to record the coordinate position, and labelled with "*unknown*". These groups were also given a confidence level of $0-10\%$ and excluded from the analysis. However, they were included in the catalogue and the fluxes of the knots were measured.

3.2.5.2 Environment

Even in cases where a good candidate driving source cannot be identified, it is still possible to estimate whether or not the outflow appears to originate from a cluster of stars, or if it is in a more isolated environment. Traditionally, "cluster" refers to either Open Clusters (OpC) or Galactic Clusters (GC). In the context of this work, the term "cluster" is used rather more loosely and encompasses any local over-density of stars irrespective of the number of members. This includes reddened clumps of YSOs, huge star forming regions (SFRs), HII regions, ultra compact HII (UCHII) regions and so on. Collections that are more filamentary are referred to as "groups".

Where any such cluster or group was identified in the JKH_2 images, the location was marked with a circle whose size encloses the apparent extent of the cluster. The coordinate position and radius were recorded for every such cluster, irrespective of whether or not it was associated with an outflow. SIMBAD was checked for known clusters in the surrounding area and any identifiers were recorded. An exhaustive search in the survey area was not performed, and so there may still be more clusters to be found. The newly discovered candidate clusters, with JKH_2 images, positional data and further comments about each cluster, can be found online (see Froebrich and Makin (2016) for Auriga and Cassiopeia (hereafter F16), and Makin and Froebrich (2018) for Cygnus-X (hereafter M18)).

3.2.5.3 Outflow lobe lengths

In order to allow for greater flexibility in analysing the outflows, and to ensure that the outflow sample can be most fully investigated, the properties of each outflow lobe were measured separately. The number of visible lobes for each outflow were recorded.

The length of each lobe was measured manually using vectors, as shown in Fig. 3.9 (a). They were drawn from the central coordinates of the driving source, out to the farthest end of the most distant knot from the source. All of the lengths are measured in units of degrees, and can be converted into projected physical lengths if the distance toward the outflow is known. The topic of distances shall be covered in detail in Chapter 3.3.1, where the method for converting the lengths from units of degrees into parsec will also be shown. For the purposes of the results for Auriga and Cassiopeia

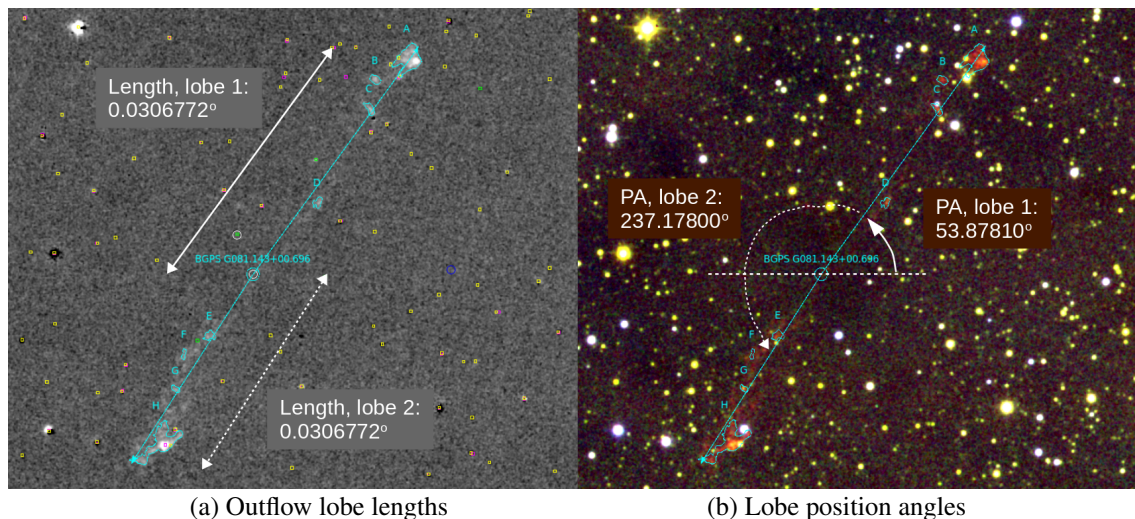(a) Outflow lobe lengths   (b) Lobe position angles

FIGURE 3.9: A demonstration, using an image of OF 197 (MHO 3878) in Cygnus-X, of the measurement of outflow properties. Outflow lobe lengths are measured in degrees, separately, from source to tip (a) after the most likely driving source is identified. The position angles are measured in degrees from west towards north due to a peculiarity of the software, then converted to be from north towards east.

presented in Chapter 4 and for Cygnus-X in Chapter 5, the distances used toward each object were taken as the most commonly used literature values (2 kpc and 1.4 kpc respectively). These distances are well-used and should be more than sufficient for an initial and general overview of the outflow statistics. Nevertheless, their validity will be tested in Chapter 6 when individualised distances shall be applied to each outflow for which a distance can be found.

3.2.5.4   Outflow position angle

The length vectors were used to measure the position angle of each outflow lobe, as shown in Fig. 3.9 (b). Traditionally, position angles are measured from north towards east, but the DS9 software records the position angles as measured from west towards north. The measured values were therefore converted afterwards to be shown in the usual way, from north toward east. Only in the rare cases of a few well-studied objects in the literature are there spectroscopic data that can provide the real outflow inclination with respect to the observer. Therefore, this study only works with the position angles in two dimensions and not the 3-D orientation. Although care will be taken to avoid using these terms interchangeably, it should be noted that any references to "orientation" in later chapters will be referring to the 2-D position angle, uncorrected for inclination.

The opening angle of the outflow cavity was not measured since it is difficult to measure this reliably using only the H_2 data. If an outflow displayed obvious signs of precession, for instance, if it showed S-shaped symmetry about the driving source, this was recorded since it can help to provide an estimate of the fraction of driving sources that are likely to be binary systems. Since many of the apparently precessing outflows did not appear to have completed a full "rotation" at the time of measuring, the lobe position angles were not measured along the outflow axis. There

was too much uncertainty in where the outflow axis actually lay, particularly if the outflow was too short to have completed an apparent rotation.

It was also noted during this stage of the analysis of jet groups that some outflows appear to originate from "multi-polar" systems, i.e., those where the axes of two outflows appear to cross each other forming an X-shaped configuration. As with the precessing outflows, this can be an indicator of potential binary or multiple star formation, so this was also recorded.

3.2.5.5   Labelling of sub-features

Each knot in an outflow is given a separate label. If the lobe with the smallest position angle is taken to be "lobe 1", then labelling of the knots begins at the farthest tip of lobe 1 with "A" and continues alphabetically for each knot in turn until the end of lobe 2 (or terminates at the driving source for outflows with only one lobe visible). Collections of knots were labelled in no particular order. After the knots were labelled and the lobes measured, an image was captured for the catalogue and these regions, vectors, and other measured objects were saved into an individual region file for later compilation into the final catalogue (see Fig. 3.10 (b)).

3.2.5.6   Manual re-drawing of region contours

In preparation for measuring the fluxes in each knot, the contours were manually redrawn around the emission in the H_2-K difference image. This was necessary in order to ensure that as much of the H_2 emission generated by the outflows was captured as possible. It also allowed the separation of contiguous knots that were conjoined by the automatic detection algorithm, whilst excluding contributions from bright stars and cloud edges. Therefore, where individual knots could be resolved in an image, manual contours were drawn around each of them separately. In order to be able to correct for the local background flux, a contour was also drawn around a nearby, relatively homogeneous region in the image that contained no H_2 emission, residual stars or artefacts. This was done for every outflow.

In Auriga and Cassiopeia, the labelling of these knots matched the labelling method as described in Section 3.2.5.5. With a relatively small number of knots, it was possible to measure the surface brightnesses and perform the conversion into fluxes using a spreadsheet set up for this purpose. However, with the considerably larger number of knots in Cygnus-X this would not have been feasible and thus needed to be done automatically. To accomplish this, a change was made to the labelling of the manually-drawn regions in Cygnus-X. Each lobe was treated separately, as demonstrated in Fig. 3.10 (a), with the knots labelled sequentially from "A" at the ends towards the driving source. The letters are appended with a number indicating the lobe to which it belongs.

3.2.5.7   Gaps between knots

The length of the gaps between subsequent knots can tell us something about the accretion history of the outflow, the density and structure of the medium into which it propagates, or both. Lines

(a) Manually re-drawn contours   (b) Original contours from F15 catalogue
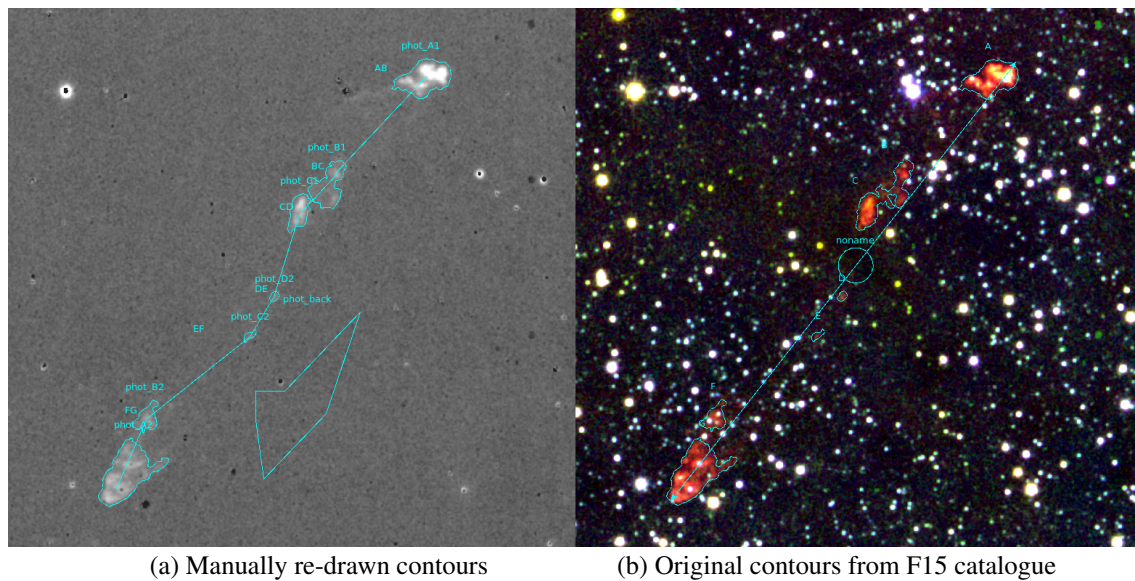
FIGURE 3.10: An image of outflow OF 085 (MHO 4005) to show examples of the two types
of region files produced during the analysis; (a) demonstrates the separation and labelling of
individual knots in preparation for photometry, and the lines measuring the gaps between se-
quential knots; (b) shows the original contours, with the vectors used for measuring the length
and position angle of each lobe, and the positional marker of the most likely driving source.

were drawn between the approximate peak in intensity values for sequential pairs of knots, and the
length of the line measured as the "gap" (in units of degrees). This was only done for bipolar and
single-sided outflows; single knots and those forming loose collections were excluded from these
measurements. Once completed, the manually-drawn contours, background region contours and
lines measuring the knot gaps were saved into a region file, one for each outflow. These region
files were then used to measure the integrated flux inside each contour in the same way as was
done in F15 (described in Section 3.2.6).

3.2.6   Photometry

The integrated fluxes were measured using the H_2-K difference images, in which the H_2 flux is
conserved by scaling only the K-band continuum fluxes. The program used to measure the fluxes
was implemented by Nicholas (2016) and was used for the measurement of fluxes in the F15
catalogue, and the Auriga and Cassiopeia (F16) and Cygnus-X (M18) outflow catalogues. The
contours themselves can be read as pairs of vertices with x and y pixel coordinates. From these,
the program determines the area, A, enclosed by the shape, and the central coordinates. For every
contour in turn, the minimum and maximum coordinate values are used to construct a box that
fully surrounds it. This is represented as an example in Fig. 3.11 (a), with a H_2 emission feature
enclosed by a cyan contour, and the constructed box as a dashed red line. The scale of a single
pixel is marked with the green cross.

Each pixel within the box is tested in turn, and if it is inside the contour boundary then the pixel
intensity is counted toward the total. Fig. 3.11 (b) demonstrates the method by which the routine
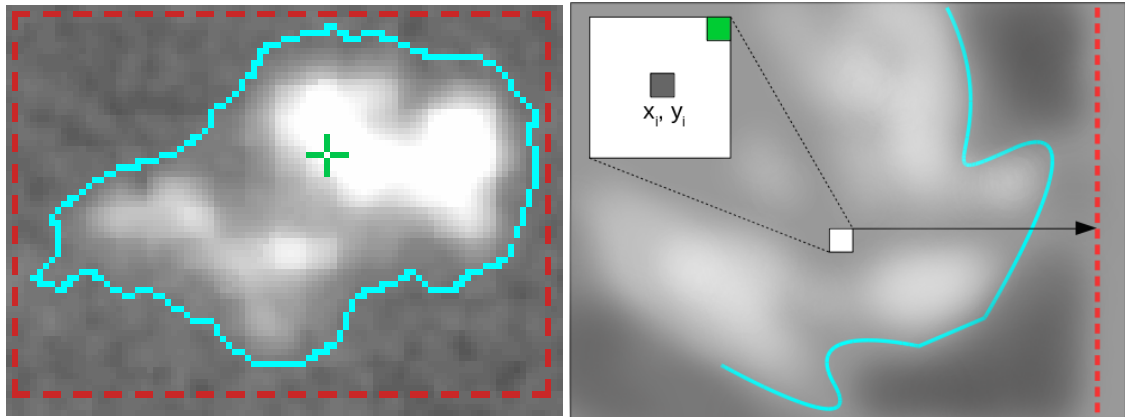
(a) An overview of the first step of photometry   (b) Close-up of a pixel at position x_i, y_i

FIGURE 3.11: A schematic showing the method of determining whether or not a pixel belongs inside the boundary of a contour around H_2 emission. In both (a) and (b) the contour is indicated with cyan lines and the "box" that encloses it is shown with a red dashed line.

decides if a pixel is inside the boundary or not, since individual pixels at the edge of the contour may be bisected by it and thus only contribute part of their flux. Each pixel, whose notional centre is at position x_i, y_i, is moved linearly to the right from its initial position until it meets the edge of the box. Depending on its location, it will cross the contour boundary a number of times, and the number of intersections between the pixel's path and the boundary determines the pixel location. If the pixel is located inside the contour it will cross the boundary an odd number of times (including zero), whilst if it crosses an even number of times then the pixel is outside the boundary and the pixel intensity is not included. The coordinates of all pixels deemed to be inside the contour were output to a text file.

In the next step, the program opens the relevant H_2-K FITS image and, for every pixel coordinate position stored in the text file, retrieves the intensity value at that position and stores it with those coordinates. Using these pixel intensities, the mean, median, maximum and total number of counts are calculated, which are then corrected using the median background counts. This process was repeated for every individual knot in the survey field. However, the values in terms of counts are not particularly useful, so it was necessary to convert the counts into fluxes with units of $W\,m^{-2}$. This was done in two steps, with the first being to convert the counts into magnitudes, and the second being to convert the magnitudes into fluxes.

The conversion of counts into magnitudes is performed on an image-by-image basis using Equation 3.2 since it utilises terms obtained from the FITS header of each image. This means that each image has a conversion factor that is the same for all H_2 emission features in the image.

$$m = m_{zp} - 0.05\,(X\,-\,1) - 2.5\,log_{10}\left(\frac{counts}{t_{exp}}\right) - m_{ap} \tag{3.2}$$

Where m_{zp} is the magnitude zero point, which will calibrate the magnitudes into the 2MASS K-band, and includes corrections that must be made due to the $0''.2$ pixel size; X is the airmass, which is always between 1 and 2 and is of the same (or smaller) order of magnitude as the m_{zp}

uncertainty (shown in Fig. 3.6 (c)); the exposure time, t_{exp} is always 720 seconds per pixel; and m_{ap} is the aperture correction. Since only extended sources are considered, as opposed to point sources, m_{ap} can be set to zero. The conversion of magnitudes m into fluxes is achieved by:

$$F = F_0^{H_2} \times 10^{-\left(\frac{m}{2.5}\right)} \tag{3.3}$$

The flux zero point $F_0^{H_2}$ is calculated using the 2MASS K-band flux zero point from Cohen, Wheaton, and Megeath (2003), being $4.283 \times 10^{-10}\,\mathrm{W\,m^{-2}\,\mu m^{-1}}$, and the K-band filter width, being $0.262\,\mu m$. This yields a flux zero point value of $F_0^{H_2} = 1.122 \times 10^{-10}\,\mathrm{W\,m^{-2}}$. By substituting Equation 3.2 into Equation 3.3 we can obtain the conversion factor for the flux, in terms of the number of counts, for every H_2 feature in a particular image:

$$F = F_0^{H_2} \times \left(\frac{counts}{t_{exp}}\right) \times 10^{-\left(\frac{m_{zp} - 0.05\,(X\,-\,1)}{2.5}\right)} \tag{3.4}$$

$$F = counts \times \left(\frac{1.122 \times 10^{-10}\,\mathrm{W\,m^{-2}}}{720\,\mathrm{s}}\right) \times 10^{-\left(\frac{m_{zp} - 0.05\,(X\,-\,1)}{2.5}\right)} \tag{3.5}$$

The fluxes can be further converted into surface brightness by accounting for the $0''.04$ squared pixel size (with units of $\mathrm{W\,m^{-2}\,arcsec^{-2}}$). This was done for Froebrich et al. (2015) to take account of the potential for including residual stars (since any odd peaks in emission will be spread across the area of the contour). However, since care was taken to avoid the inclusion of residual stars within the redrawn contours, it is acceptable to discuss the brightness of H_2 features in terms of their fluxes for the photometry performed in Chapters 4 and 5.

3.2.7   MHO catalogue

The methods used for analysing the outflows from UWISH2 are consistent with those described in Davis et al. (2010) to identify Molecular Hydrogen emission-line Objects (MHOs, see Chapter 2.8). Therefore, each of the outflows can be included in the MHO catalogue[4]. Each outflow was assigned an "MHO ID" number in the format [MHO XXXX]. For new discoveries, a one-to-one correspondence exists between the outflow ID numbers and MHO ID numbers. In Cygnus-X however, there are 147 already-known MHOs within the survey area. During the "second pass", the configurations of the already-known MHO numbers were checked in order to compare solutions. Where possible, the existing MHO ID was adopted, to minimise the number of ID numbers generated. This was straightforward for the cases where the UWISH2 solution matched the existing outflow exactly, or where new knots could be included in the existing solutions. In the less straightforward cases, two lobes of the same outflow had been given separate MHO ID numbers,

---

[4] The MHO Catalogue; http://astro.kent.ac.uk/~df/MHCat/index.html

and some outflows are composed of multiple MHO numbers. In these cases, rather than assigning a new MHO ID, all existing ID numbers are associated with the corresponding outflow ID.

To provide correspondence with the published literature, comments are included for every outflow in the image set published in M18 which detail the breakdown of the labelled knots in the image and which MHO number they belong to from the existing MHO catalogue. Since photometry was performed individually for each knot, this allows interested parties to follow up on the work done, e.g. for proper motion studies, etc. In the analysis performed in Chapters 5 and 6 which pertain to Cygnus-X, it should be noted that the outflow configurations determined by the author are used wherever there is a conflict between these and the already-known MHO catalogue entries.

3.3   Part III: Corrected-distance statistical analysis

3.3.1   Distances

For the outflow catalogues (F16 and M18), standard distances toward every outflow were used. In Auriga and Cassiopeia the assumed distance was 2 kpc, whilst 1.4 kpc was used towards the outflows in Cygnus-X. This is a common practice, particularly in Cygnus-X, since the accurate measurement of distances is not a trivial problem to solve. Most of the objects in Auriga and Cassiopeia should be located in the Perseus spiral arm, so the distance used is based on the distance from the Sun to the Perseus arm. This was measured via trigonometric parallax to be $2.0 \, \text{kpc} \pm 0.2$ in the Galactic anti-centre direction (Choi et al., 2014) and represents the best general distance towards the region. The Cygnus-X distance is based on the maser parallax study of Rygl et al. (2012), which suggested a general distance of $1.40 \, \text{kpc} \pm 0.08$. This value is being commonly used in the literature (see e.g. Varricatt et al. (2010), Lumsden et al. (2013), Kryukova et al. (2014), Rivera-Gálvez et al. (2015), etc).

Determining distances toward the outflows is important since this allows the lengths (as measured in degrees) to be converted into projected lengths in parsec and for the fluxes to be converted into luminosities. With a large enough sample, it is then possible to investigate the length and luminosity distributions, and the dynamical timescales, in order to constrain the results of numerical simulations. In Serpens and Aquila, it was discovered in IF12b that the outflows could be up to 2 kpc further away than the 3 kpc assumed distance used in IF12a. Since the luminosity scales with the distance squared, differences of this magnitude can significantly distort the distributions with a high enough frequency. Therefore, individualised distances need to be obtained toward each outflow in order to most accurately present the nature of the parameter distributions.

3.3.1.1   Common methods for measuring distances

Cluster distances can be estimated by plotting the cluster members on a Hertzsprung-Russell (HR) diagram and fitting an isochrone to them. However, non-member stars cannot be easily distinguished from member stars and are often included, which introduces scatter that renders the estimate highly uncertain. In addition, although stars tend to form in clusters (Lada and Lada, 2003), it was found that many outflows originate from isolated environments where, if there is a cluster, it cannot be seen in the near-infrared images (F16, M18). In previous outflow studies, e.g. Varricatt et al. (2010), distances were obtained from the existing literature where different cluster-fitting methods were used for each object.

Distances can be obtained for an individual object (stars, SNRs, clouds, etc) by measuring the radial velocity (via the Doppler shift in the spectral lines it emits). The paths of objects around the Galaxy can be approximated as circular, and the Galactic rotation curve has been modelled (e.g., Brand and Blitz 1993; Clemens 1985; Reid et al. 2009, 2014; Schmidt 1965). Given an object at Galactic longitude l, with a particular radial velocity, a unique distance solution can generally be obtained by fitting it to the Galactic rotation curve. This method is known as the kinematical
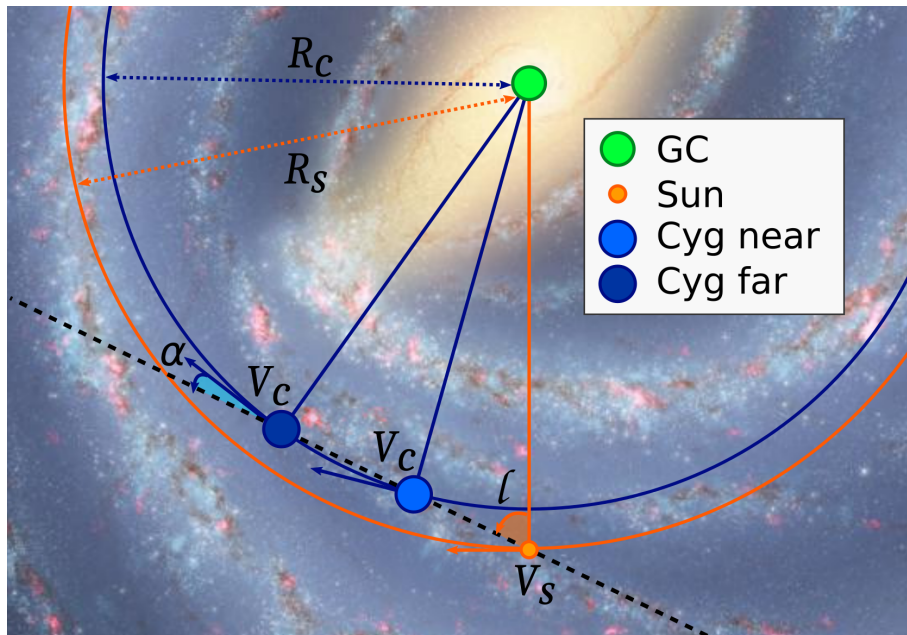
FIGURE 3.12: A schematic diagram demonstrating the difficulty with measuring kinematic distances toward Cygnus-X. The distances R_c and R_s represent the Galactocentric radii of Cygnus-X and the Sun respectively. The dashed line represents the line of sight from the Sun towards Cygnus-X ($l \sim 80°$). Background image (not to scale) is an artist's impression, courtesy of NASA / JPL – Caltech / R. Hurt (SSC / Caltech).

distance method, and has been widely used (see e.g., Caswell et al. 1975; Ilovaisky and Lequeux 1972; Roman-Duval et al. 2009; Urquhart et al. 2012; Whitaker et al. 2017; Wienen et al. 2015). However, there is a significant problem in the Cygnus-X region, demonstrated in Fig. 3.12 (not to scale). The line of sight from the Sun towards Cygnus-X (represented by the black dashed line) is projected along the Orion spur, and also includes objects from the more distant Perseus arm, as well as objects from the outer Galaxy. This means that there is a complex interlayering of material that ranges from about 1 kpc up to 10 kpc (Rygl et al., 2012) in distance from us.

The problem is further compounded by the fact that Cygnus-X is located in the inner Galaxy, i.e., the Galactocentric radius of Cygnus-X (R_c) is smaller than that of the Sun (R_s). In the outer Galaxy ($R_s < R_{object}$), the radial velocity of an object yields a unique kinematic distance, but in the inner Galaxy there are two potential solutions for a given radial velocity v_c that both have the same Galactocentric radius. This is known as the kinematic distance ambiguity (KDA), and is difficult to resolve (certainly beyond the scope of this work). The difference in v_s (the radial velocity of the Sun) and v_c is small along this line of sight, especially near the Galactic tangent at $l \sim 90°$ where $\alpha \simeq 0°$. As pointed out by Rygl et al. (2012), these velocities are similar to the typical velocity dispersion found in interstellar gas in high-mass SFRs (which is between $1 - 7 \, \mathrm{km \, s^{-1}}$ according to Moscadelli et al. 2002). This degeneracy along the line of sight makes kinematical distances toward Cygnus-X highly unreliable.

The most accurate distance measurements are obtained via parallax, and particularly via maser parallax. However, it is not feasible to obtain these for even a small fraction of the outflows in the UWISH2 sample. Therefore, since main-sequence fitting cannot be performed for isolated

outflows, and kinematical distances are only suitable for the Auriga and Cassiopeia region, and since maser parallax measurements have only been done for a tiny fraction of outflows, another method must be used in order to ensure that distances toward outflows in both regions are obtained in a consistent and unbiased fashion.

3.3.1.2 Distance estimation: Bayesian method

In order to ensure the greatest consistency possible for the largest number of objects, the Bayesian distance calculator of Reid et al. (2016) was used to recalibrate the distances for any object for which the local standard of rest velocity (v_{LSR}) has been measured in the literature. For each outflow, the literature was searched for nearby (i.e., those within $4'$ of the outflow driving source) v_{LSR} measurements. The v_{LSR} of objects that are spatially related should be similar, so if all objects within the $4'$ radius have a similar v_{LSR}, then the outflow is probably related to the same group. In that case, the nearest object (if it is not the outflow driving source) is the one whose v_{LSR} was adopted. If there were two "sets" of v_{LSR} measurements within $4'$, or if the nearest measurement was over $1'$ from the driving source, then the v_{LSR} of the most proximate object was adopted. However it must be stated that apparent proximity in our images is no guarantee of actual proximity, and that objects that appear to be close together may, in fact, be kiloparsecs apart as projected along the line-of-sight, as discussed above. This is an issue that could reasonably affect any individual outflow in the sample, but in a sufficiently large sample this should not present a significant problem.

The Reid et al. algorithm includes contributions from kinematic distances. However, as discussed previously these are unreliable in Cygnus-X and hence the contribution from kinematical distances was zero-weighted. The results were weighted in favour of contributions from parallax (being the trigonometric parallax of GMCs) and the contribution from spiral arms was only considered if there was no parallax component for the given inputs, in which case it is given precedence. Since resolving the near/far kinematic distance is beyond the scope of this work, no weighting in favour of one or the other was applied. The algorithm then provides one (or more) distance estimates for the object in question, as well as the errors, the probability of the distance being correct and the most likely spiral arm association.

3.3.1.3 Distance by association

In the F15 catalogue, H_2 emission knots of the same type were "grouped" together if they were located within $0°.1$ of each other, because it can be assumed that they are spatially related. In the same spirit, if the distance toward an outflow in a given group can be estimated, it is assumed that any other outflows in the group are part of the same complex, and thus that distance was adopted toward all outflows in that group. This was particularly applied to the groups containing the DR 20, DR 21, W 75 N and AFGL 2591 objects in Cygnus-X. The maser parallax study of Rygl et al. (2012) provides accurate distances toward these specific objects (their fifth object, IRAS 20290+4052, had no H_2 emission associated with it in the UWISH2 survey):

- DR 20, $d = 1.46\,\mathrm{kpc}\,^{+0.09}_{-0.08}$

- DR 21, $d = 1.50\,\mathrm{kpc}\,^{+0.08}_{-0.07}$

- W 75 N, $d = 1.30\,\mathrm{kpc} \pm 0.07$

- AFGL 2591, $d = 3.33\,\mathrm{kpc} \pm 0.11$

These distances were applied towards all of the outflows that are part of the same group (i.e., those within $0°.1$). The Rygl et al. study suggested that the DR 17, DR 22, DR 23, and AFGL 2620 regions can be assumed to be part of the same complex and thus held at a distance of $1.40\,\mathrm{kpc} \pm 0.08$. However, this was based on the earlier work of Schneider et al. (2006), and not on maser parallax measurements, so this distance was not universally adopted for these regions.

Some of the outflows in the regions where maser parallax distances can be applied also have distances estimated via the Bayesian model. If the distances from the two sources are compared, it can be determined that the Bayesian-derived values tend to overestimate the distances, and the typical amount of overestimation varies from region to region. In DR 21 the discrepancy is small, with an average difference of 2 % between the distances obtained by the two methods. In W 75 N the discrepancy is greatest, with an average of 13 % difference between the two methods. The only exception is for AFGL 2591, where the Bayesian distance is 52 % lower than the 3.33 kpc distance found by Rygl et al.

3.3.2   Distinct sub-regions in Cygnus-X

The Cygnus-X region contains sub-regions that have been identified in previous studies as having different properties than elsewhere in the region (such as cloud masses, morphologies, etc). The properties of the outflows in each of these sub-regions can be compared and contrasted, and also compared to those from Auriga and Cassiopeia, in order to investigate if the outflow propagation has any dependence upon those environmental properties. The sub-regions that shall be investigated are Cygnus-X north, Cygnus-X south, W 80, and the "remainder". The particular characteristics of each of these sub-regions were discussed in Section 2.9.

The Cygnus-X north and Cygnus-X south regions were defined in Schneider et al. (2006), and the same definitions were later used in the YSO survey of Kryukova et al. (2014), which identified 1800 YSOs and YSO candidates. In line with the existing definitions, the region designated as Cygnus-X north in this Thesis is a $3.3\,\mathrm{deg}^2$ area around DR 17 – DR 23 (RA: 308.531 – 311.344, Decl: 40.968 – 43.032). Cygnus-X south is designated as a $7.5\,\mathrm{deg}^2$ area around DR 4 – DR 15 (RA: 307.125 – 309.657, Decl: 37.968 – 40.600).

Similarly, the nearby HII region W 80 was identified by Wendker, Benz, and Baars (1983) as being approximately $3°$ in diameter and encompassing the North American nebula (NGC 7000) and the Pelican nebula (IC 5070). These two nebulae are separated by the giant molecular cloud L 935. The extent of this region is difficult to precisely define since the surrounding region may be up to 10 pc in diameter. However, based on the work of Rebull et al. (2011), which covered a $7\,\mathrm{deg}^2$ area, and Bally et al. (2014), the active star formation occurs over an area that approximately covers

Galactic latitudes $84° - 86°$, and longitudes -2° to 0°.5. For the sake of simplicity, an outflow is positively identified as being part of the W 80 complex if; (a) the driving source is detected in the Rebull et al. catalogue, (b) if the outflow is already known as an MHO in the Bally et al. catalogue, or (c) if the outflow is part of the same group as an object from (a) or (b).

3.3.3 Outflow and knot luminosities

The measured fluxes of the outflows and knots can be converted into luminosities if the distance, d, toward them is known. The relation between the flux, F, and the luminosity of an object, L, is:

$$F = \frac{L}{4\pi d^2} \longrightarrow L = 4\pi d^2 F \tag{3.6}$$

The distances are initially recorded in units of parsecs, and thus must be converted into units of meters. The fluxes, as returned by the photometry calculations, are in units of $10^{-19}\,\mathrm{W\,m^{-2}}$.

$$L = 4\pi \times \left(3.086 \times 10^{16}\,\mathrm{m\,pc^{-1}} \times d_{pc}\right)^2 \times \left(1 \times 10^{-19}\,\mathrm{W\,m^{-2}} \times F\right) \tag{3.7}$$

Finally, in order that the luminosity values L (in W) should be converted to the more convenient units of Solar luminosity ($L_\odot$), the returned values from Equation 3.7 are divided by 3.828×10^{26} W.

3.3.4 Outflow lengths and gaps between knots

The length of an outflow can be converted into a projected length (in parsecs) l_{pc} using the measured length (in degrees) and the estimated distance d toward it (also in parsecs). Since the parsec is defined as the distance at which one astronomical unit (AU) subtends an angle of one arcsecond, the measured length is first converted from units of degrees to arcseconds.

$$l_{AU} = \left(l_{deg} \cdot 60\,['] \cdot 60\,['']\right) \cdot d_{pc} \tag{3.8}$$

Then, given that the distances toward the outflows are already in units of parsecs, the length is returned in units of AU. Dividing this value by the number of AU in one parsec will therefore convert the length from AU to parsec.

$$l_{pc} = \frac{l_{AU}}{206264.80622} \tag{3.9}$$

The same process can also be repeated for the lengths of the gaps between subsequent knots in an outflow. Since these gaps can represent a "fossil record" of the accretion and ejection history of an outflow, it is also possible to convert these gaps (in parsec) into measurements of the dynamical time between these accretion events. For this, a projected transversal speed of $80\,\mathrm{km\,s^{-1}}$ is assumed. Although atomic jets can reach velocities of up to $1\,000\,\mathrm{km\,s^{-1}}$, the molecular shocks

traced by the $1-0\,S(1)$ line of H_2 typically occur through much slower interactions with the ambient medium, with velocity ranges between 10 and $100\,\text{km}\,\text{s}^{-1}$ being more typical of the types of objects represented in this work (see e.g. Frank et al. (2014) and references therein).

Clearly, there is a large scope for variation in the outflow ejection velocities, and these can also vary depending on a range of factors including the evolutionary stage of the driving source, the distance of the outflow knots from the driving source and the density of the ambient medium. Therefore, the values calculated in Chapter 6 for the dynamical timescales should be taken as order-of-magnitude estimates and not as precise values.

3.3.5   Statistical correction

The relatively small sample from Auriga and Cassiopeia is a problem from the point of view of statistical analysis. In Cygnus-X the Bayesian distances may tend to be overestimated based on comparison with the parallax distances, but since we do not have maser parallax distances for the vast majority of specific objects, the uncertainties in the distance are generally high. These must be compensated for before fits can be determined to the length and luminosity distributions. The statistical correction method that shall be used was successfully implemented to correct the distributions in Serpens and Aquila (IF12b).

Chapter 6 only includes outflows with an individual distance estimate, and each of these distances has an associated error as a fraction of that distance. It is assumed that each outflow is most likely to be found near the given distance. Therefore, for every outflow a standard normal distribution was created at the given distance, with $N = 10\,000$ and σ being the associated distance error. Each of these normal distributions were then pooled together for each of the two regions to create the final statistical populations, which are then each divided by $10\,000$.

However, it should be noted that although IF2012b included an additional error in this calculation to account for the approximate local extinction, this has not been included as a step. It would be possible to make the same assumption in the Auriga and Cassiopeia regions as were made in Serpens and Aquila; i.e. that the optical extinction increases by $A_V = 0.7$ mag per kpc (Froebrich et al., 2010) and that A_V can be converted to K-band extinction using the Mathis (1990) relation of $A_V = 9.3 \times A_K$. However, the amount of optical extinction can vary greatly in Cygnus-X, for example up to 25 mag around DR 21 (Nadeau, Riopel, and Geballe, 1991) and 100 mag in the gap between the two lobes. In the W 80 region, optical extinction varies from $A_V = 0.2$ up to ≈ 4 (Straizys et al., 1989) in a region that is only around 600 pc from the Sun. Since we cannot apply the standard assumptions in Cygnus-X, for the sake of consistency, no corrections are made for extinction in either region.

3.4   Non-parametric testing

In Chapters 4, 5, and 6, two non-parametric (i.e., not required to follow a normal distribution) tests were used in order to investigate the degree of similarity or difference between sub-samples

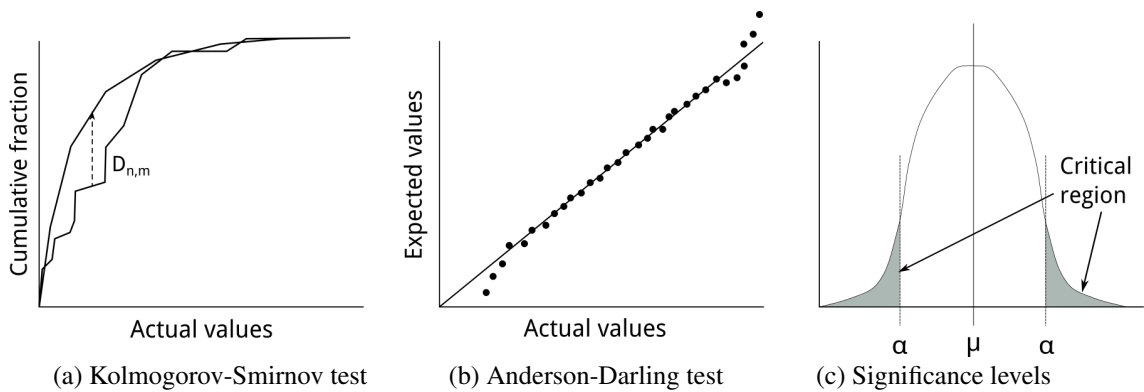(a) Kolmogorov-Smirnov test   (b) Anderson-Darling test   (c) Significance levels

FIGURE 3.13: Demonstration of the differing methods of calculating test statistics in (a) the Kolmogorov-Smirnov (KS) test which returns the absolute maximum distance between two CDFs, and (b) the Anderson-Darling (AD) test which calculates the weighted least squares difference between the samples. The significance levels (α) bound the critical region for each test (c).

of outflow populations. The first of these was the 2-sample Kolmogorov-Smirnov (KS) test, and the second was the k-sample Anderson-Darling (AD) test. These tests, when applied to continuous data, are both two-tailed and assume the null hypothesis (H_0) that the samples being tested are drawn from the same parent distribution. Although the methodology underlying each test is different, both of them provide a measure of the distance between the cumulative distribution functions (CDFs) of the given samples. This pair of tests each has their own complementary merits and limitations, so by using both concurrently, the nature of the distributions can be more clearly understood. Both tests were run using statistics modules from scipy.stats in Python 3 [5].

3.4.1 Kolmogorov-Smirnov test

In the KS test, the supremum, or absolute maximum distance between the two CDFs is returned as the test statistic $D_{n,m}$, where n and m are the respective samples (see Fig. 3.13 (a) for a visual representation). This distance is typically greatest in the central part of the CDF, and it also tests other parameters (such as median, shape, and variance) for deviations from the null hypothesis. The KS test is therefore most powerful at determining differences in the central region of the CDF where most of the data lies. It should be noted that the tails of the distributions coverge to the same values on a CDF, meaning that the KS test is weak at highlighting differences in the tails.

3.4.2 Anderson-Darling test

The AD test, instead of using the absolute maximum distance between CDFs, instead calculates the test statistic (A^2) by using the doubly weighted sum of integrated squared differences between the given samples (Scholz and Stephens, 1987). In the standard implementations of the AD test, this is done by calculating the expected values for a given distribution family, and then casting the CDF of those expected values against the actual values being tested. If the distributions are the

---

[5]Scipy: https://www.scipy.org/

same, the results should be uniform. Hence, the AD test measures the distance from uniformity (as shown in Fig. 3.13 (b)). The k-sample version of this test follows the same principle but does not require a family of distributions be specified.

In this test, greater weight is provided to the tails of the distributions, making a useful counterpoint to the KS test. However it should be noted that the critical values depend greatly on the number of objects in each sample, i.e., small samples are not suitable for analysis with the AD test and samples should be larger than about 10. In addition, the p-values as generated by scipy.stats are often calculated by extrapolation and can thus be less accurate than in the KS test if the populations are small.

3.4.3   Statistical significance

Each test returns both the test statistic and the p-value. If the test statistic is small (i.e. close to zero) then the null hypothesis that the two samples are drawn from the same parent distribution cannot be rejected. A test statistic of exactly zero would signify that there is no distance between the distributions of the two tested samples, and that they are therefore identical.

The null hypothesis also cannot be rejected if the p-value is very high. The p-value represents the probability of obtaining the observed test statistic if one assumes that the null hypothesis is true. In Fig. 3.13 (c) a high p-value would fall into the unshaded region. The lines bounding the critical regions (the shaded areas of the graph) represent the significance level, α. Any given α will have an associated critical value C(α) which depends on the sample sizes being tested. If the p-value is smaller than α, or the test statistic is larger than the critical value (thus falling into the critical region), the result can be said to be statistically significant.

Care must be taken with interpreting results from these tests, however. It must be recognised that as sample sizes increase, the p-values will tend to decrease. It is therefore possible to make p-values arbitrarily small by gathering sufficient data. Under such circumstances, even small differences in samples can appear to be significant (even if they are not). Samples that are too small will yield unreliable results.

Further, and most importantly, there is no non-arbitary method for deciding on the significance level cut-off. By convention, α is usually chosen to be around 5 % (2 σ), but such a generous cut-off increases the type I error rate (the chance of rejecting H$_0$ when it is actually true). With a more stringent limit, such as 3 σ ($\alpha = 0.3$ %) the chance of a type II error is increased (i.e., the probability of accepting H$_0$ when it is actually false). Employing hard cut-offs also means that test statistics or p-values close to the limit can not be accepted with any certainty, simply because the limits are so arbitrary.

With this in mind, a limit of 1 % has been chosen for two reasons. Firstly, the AD test as implemented in Scipy calculates critical values for significance levels of 25 %, 10 %, 5 %, 2.5 % and 1 %, so utilising a strict 3 σ cut-off in the AD test results would not be possible under these conditions, particularly as the p-values in this test can be unreliable. For the sake of consistency

between the two tests, the same cut-off should be used. Secondly, a value of 1 % would strike a more acceptable balance between the opportunity for type I and type II errors.

Therefore, if $A^2 >$ the critical value at $\alpha = 1\%$ (which will be 3.752 unless otherwise stated) for the AD test, or if the p-value $< 5 \times 10^{-3}$ (for the two-tailed test) then the result is statistically significant and the null hypothesis can be rejected. In this case, the two samples can be considered to be drawn from different parent distributions. Otherwise, the null hypothesis cannot be rejected. Values close to the cut-off will be highlighted, since their statistical significance (or not) depends heavily on where the cut-off is chosen. In subsequent chapters, hypothesis test values will be presented with the p-value first, followed by the AD test statistic A^2. For statistically significant results, the significance level will follow the p-value, and the critical value at a 1 % significance level will follow the A^2 value, both in parentheses.

Chapter 4

Results, part I: Outflows in Auriga and Cassiopeia

4.1 General results

In Auriga and Cassiopeia there were 51 groups from F15, containing H_2 features originally described as "jet", i.e. being shock-excited emission most likely from a jet or outflow from a YSO. When these groups were analysed, 46 of them were indeed found to contain shock-excited H_2 emission, and 98 individual Molecular Hydrogen emission-line Objects (MHOs) were identified out of the emission-line features. Seventy-four of the MHOs are clearly recognisable as outflows, with 57 being bipolar (having two lobes visible) and 17 being single-sided (having only one lobe visible). The remainder of the MHOs are either individual knots of H_2 emission, or are composed of groups of knots with no clear and convincing driving source candidate. The 5 groups from which no MHOs were identified contained 15 individual H_2 detections. However, 12 of these (6%) were found to be the fluorescently-excited edges of molecular clouds, and 3 (1.6%) are image artefacts or variable stars, and all of these false-positives have been rejected.

The positions of all the outflows identified in Auriga and Cassiopeia are shown in Fig. 4.1. There is a clear correlation between the positions of the outflows (marked by black triangles) and high column-density CO regions (darker grey areas in the background intensity plot), and the outflows tend to be clustered in small groups of a few members. All 74 outflows (bipolar and single-sided) have candidate driving sources associated with them. Twelve of the 98 outflows (12%) appear to form X-shaped pairs of outflows whose axes are roughly perpendicular to each other, and each pair
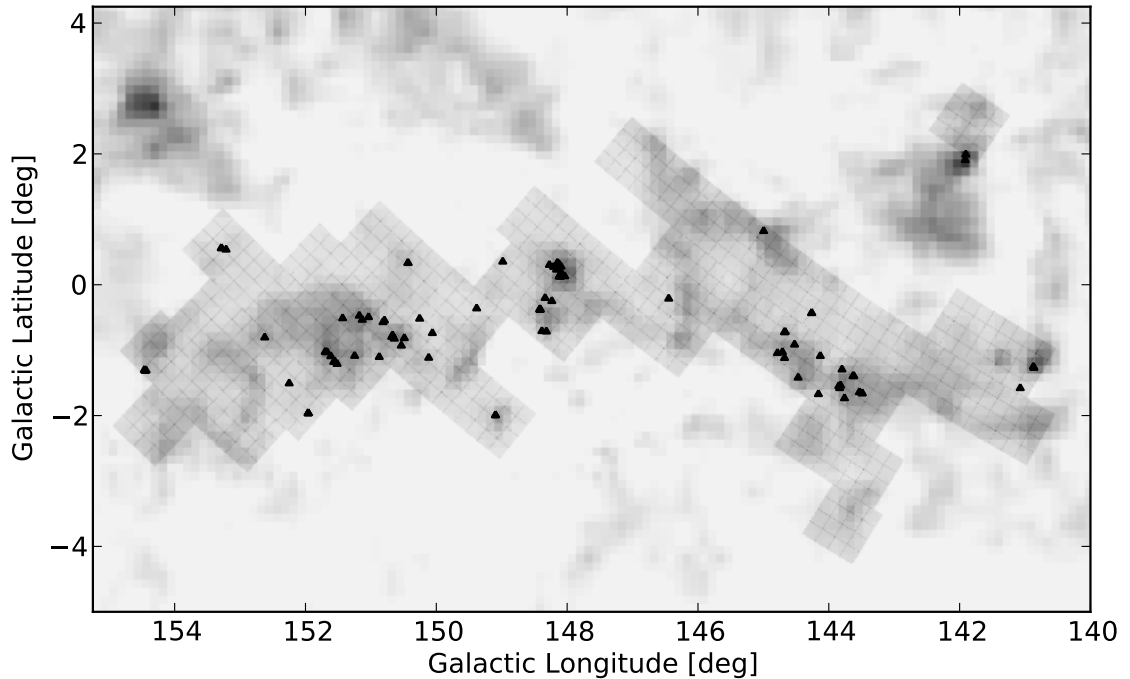
FIGURE 4.1: A map in Galactic coordinates demonstrating the coverage of the UWISH2 survey in the Auriga and Cassiopeia regions. The background image is a ^{12}CO (J = 1 → 0) intensity map from Dame, Hartmann, and Thaddeus (2001), where darker grey hues correspond to areas of increased CO emission. The UWISH2 observations are indicated by the overlaid grid, where each 4×4 set of squares corresponds to one UWISH2 tile. The black triangles show the positions of every MHO detected in the survey area.

of outflows typically appears to originate from the same driving source. According to Lee et al. (2016), it is possible that these systems of outflows represent binary or multiple systems, which tend to produce outflows that are oriented either randomly, or preferentially perpendicular, with respect to each other. This claim is perhaps supported by the fact that two of the four outflows that show clear signs of precession are found in these X-shaped systems, suggesting that precession (a typical signpost of binary star formation) may be over-represented in these systems.

On the subject of multi-star systems, 41 % (40) of the candidate driving sources are located in or nearby to a cluster or group that is visible in our NIR images. This means that the majority of the driving sources (59 %) are found in more isolated environments, which was also found in Orion A (Davis et al., 2009). This may be counter-intuitive, since most stars form in clusters (Lada and Lada, 2003) and the majority of young protostars and CTT stars are found in clusters. One might reasonably expect then that if protostars and CTTSs drive outflows, we should find more outflow driving sources in clusters. It is unclear why the opposite result is found, but this will be discussed further in Chapter 6 in light of the results from Cygnus-X.

Figure 4.2 shows a colour-colour diagram representing the J-H versus H-K colours of each candidate driving source that has a detection in the NIR catalogues of 2MASS (23 driving sources (31 %)), UGPS (35 driving sources (47 %)), or both (23, i.e. all 2MASS-detected driving sources had UGPS counterparts). The stars are all clustered near the bottom of, or to the right of, the reddening band. This suggests that all of the candidate driving sources are CTTSs and protostars.
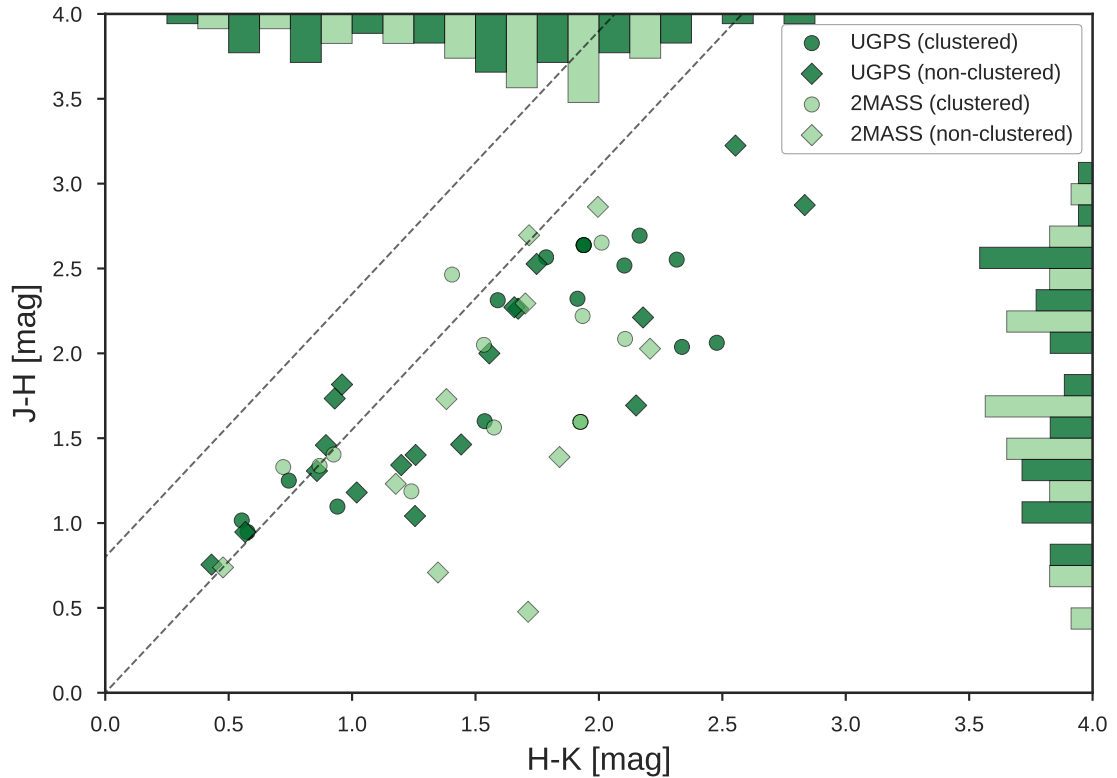
FIGURE 4.2: NIR colour-colour diagram of the candidate driving sources for each outflow. The scatter points show the J-H vs H-K colours of the driving sources, with either dark green for UGPS detections or pale green for 2MASS. The circular icons represent those outflows from a clustered environment, whilst diamonds denote that the source is more isolated. The overlaid dashed lines represent the standard reddening band for normal stellar photospheres. The histograms show the overall/total distribution of these points, with dark green bars for UGPS and pale green for 2MASS.

When investigating the variability of the candidate driving sources, the magnitudes from the UGPS and 2MASS surveys must be compared since most of the area of Auriga and Cassiopeia has only been imaged once in the UGPS K-band (by comparison, most of Cygnus-X has been imaged twice in the UGPS K-band). Only four of the candidate driving sources that were detected in UGPS have magnitudes from two epochs for comparison, and none of those are more variable than 0.1 mag over the several-years timescale. Of the candidate driving sources detected in UGPS, 23 of them (65%) have corresponding detections in 2MASS. Of these 23, 16 (70%) are more variable than 0.1 mag between the two epochs, and 4 (17%) of them by more than 0.5 mag.

However, it should be noted that whilst 50% of the UGPS $(K_2 - K_1)$ magnitudes show an increase in brightness, the other 50% show a decrease. From UGPS to 2MASS $(K_1 - K_S)$ however, 70% of the 2MASS magnitudes are brighter than those from UGPS, suggesting a systematic bias. The most likely reason for this is the improved spatial resolution of the UGPS survey. In other words, the UGPS survey is able to resolve stars separately which appear as a single star in 2MASS. Therefore, since only four candidate driving sources have two detections in UGPS, this is too small a sample from which to draw any conclusions regarding the variability of the driving sources.

The WISE catalogue was used to obtain magnitudes in the mid-infrared for 59 (80%) of the
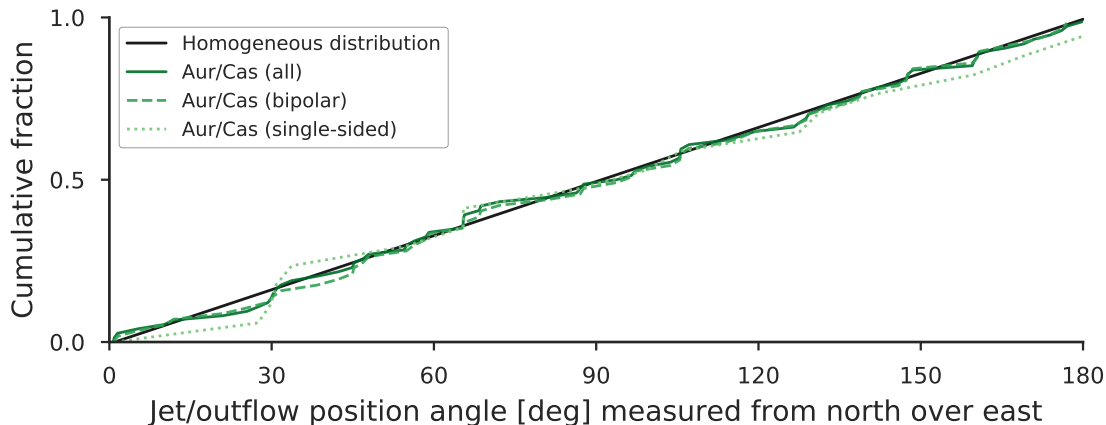
FIGURE 4.3: A cumulative distribution function demonstrating the distribution of outflow position angles for all outflows (i.e., bipolar and single-sided) in Auriga and Cassiopeia. The bipolar and single-sided outflow distributions are shown separately, and for the bipolar outflows the average lobe position angle is used. These distributions are compared to a homogeneous "test" distribution.

candidate driving sources. By using all four filters from WISE it is possible to classify the driving sources by evolutionary stage. This is done by reconstructing the Spectral Energy Distribution (SED) between those wavelengths and then calculating the slope (α) for each of them to determine whether they are protostars ($\alpha < 0$) or CTTS ($\alpha > 0$). This was done following the method of Majaess (2013) as described in Chapter 3.2.3. In F16 it was reported that 10 (17 %) of the candidate driving sources had SEDs with negative slopes (i.e., were CTTSs) and 49 (83 %) had positive slopes (were protostars) over the WISE wavelength range. An arbitrary value was then used to split the population into "young" and "old" such that half of the population was in the former category and half in the latter. This meant that there were as many "young" driving sources in the "old" category as there were "old" driving sources. An error was later discovered in the calculation of the α values; once this was corrected, the disparity between the number of protostars and CTTS became greater, with only 2 (3 %) having negative slopes and 57 (97 %) having positive slopes, meaning that the majority of the candidate driving sources are likely to be protostars.

4.2 Outflow properties

4.2.1 Outflow position angles

In Fig. 4.3 the distributions of the outflow position angles are shown. The whole population (i.e., the bipolar and single-sided outflows together) is shown with a dark green solid line, and the bipolar (mid-green dashed) and single-sided (light green dotted) populations are shown plotted over the top. As described in Chapter 3.2.5.4 the position angle of each lobe is measured from north over east, and 180 is subtracted from all position angles over 180° so that every position angle lies between 0° and 180°. Each bipolar lobe pair has their position angles averaged so that for each outflow there is only one position angle measurement.

Since the distributions each appear to be roughly homogeneous between $0°$ and $180°$ a "test" distribution was created in order to determine if the outflow position angles are indeed random (shown with a solid black line). The two-sample Kolmogorov-Smirnov (KS) test and the k-sample Anderson-Darling (AD) test were used for each sample, with a null hypothesis that they are each drawn from the same parent sample as the homogeneous distribution. In every case, the position angle distributions and the test distributions were drawn from the same parent sample:

Bipolar outflows: $p = 0.999$, $A^2 = -1.19$

Single-sided outflows: $p = 0.986$, $A^2 = -0.988$

All outflows: $p = 0.998$, $A^2 = -1.14$

Additionally, when the bipolar and single-sided outflow distributions are KS-tested against each other, the bipolar and single-sided outflows are drawn from the same parent sample ($p = 0.988$, $A^2 = -1.07$). Most of the bipolar outflows in Auriga and Cassiopeia are also straight, with a median position angle difference of less than $5°$ between each pair of bipolar lobes. Only 8 of the 57 (14 %) bipolar outflows have a position angle difference between their lobes of over $10°$ and none of these have a position angle difference greater than $20°$.

4.2.2   Outflow lengths

As discussed in Chapter 3.2.5.3, outflows are traditionally measured in terms of their "total length", i.e., from end-to-end. However, no distinction is made between bipolar and single-sided outflows so that all outflows tend to be mixed into a common distribution, irrespective of whether both sides of the outflow are visible or not. Figure 4.4 demonstrates that this is problematic. In both cases, the bipolar and single-sided outflow populations are shown separately. The top panel of the figure shows the projected lobe lengths, and while the outflow lobes are typically short, the bipolar and single-sided outflow lobe length distributions seem not to be too dissimilar. In the bottom panel the projected total lengths are shown, and clearly the peak of very short outflows disappears for the bipolar flows, meaning that the two distributions are significantly different from each other.

To quantify this result, KS and AD tests were performed. For the lobe length samples, the bipolar and single-sided outflows are clearly drawn from the same parent distribution ($p = 0.534$, $A^2 = -0.073$) even if the bipolar outflow lobes appear to be slightly shorter than for the single-sided ones. For the total length distributions, the KS-test shows that the null hypothesis can also not be rejected although the samples have less similar distributions ($p = 0.180$, $A^2 = 1.596$). The reason for this is perhaps obvious, i.e., that for the single-sided outflows the lobe length is the same as the total length. However, this is definitely not the case for the bipolar outflows where the lobes and total lengths are drawn from different parent distributions ($p = 4.644 \times 10^{-4}$, $A^2 = 12.970$). Therefore, if the outflow total lengths are measured, the bipolar and single-sided objects should not be mixed into a common distribution.

In order to begin to investigate what factors might be responsible for the manner in which the outflows are propagated, various indicators are used to split the population of outflow lobe lengths.
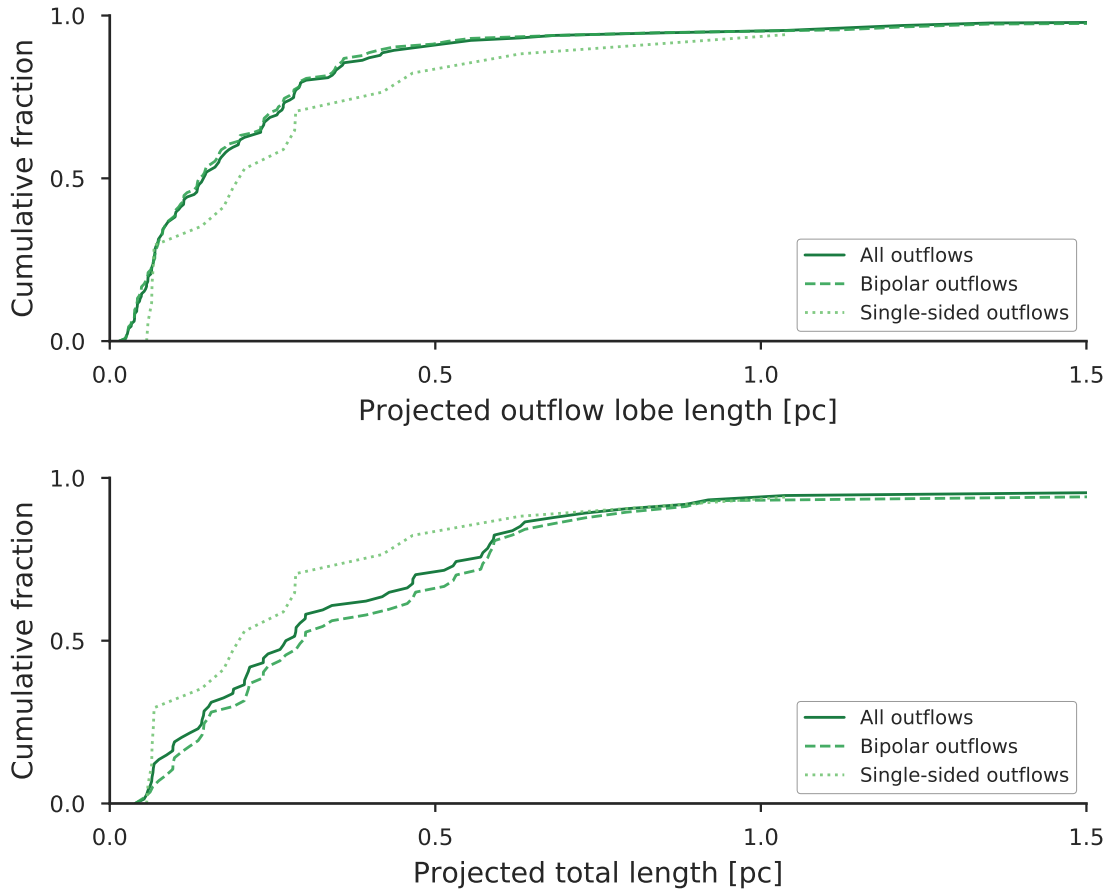
FIGURE 4.4: Cumulative distributions for (top) projected outflow lobe lengths and (bottom) projected total (end-to-end) outflow lengths. The populations are each split between bipolar (dashed mid-green lines) and single-sided outflows (dotted pale green lines). The total populations are shown with dark green solid green lines for reference.

In the top row of Fig. 4.5, all single-sided and bipolar lengths are used to create cumulative distribution functions showing the distribution of projected lobe lengths. On the bottom row only the bipolar outflows are shown in order to investigate the degree of symmetry between the lobe lengths of a given outflow. This is calculated in terms of the length ratio, i.e. of the length of the short outflow lobe divided by the length of the longer lobe in each bipolar pair of lobes:

$$R_L = \frac{L_{short}}{L_{long}} \tag{4.1}$$

All values are therefore between 0 (highly asymmetrical) and 1 (highly symmetrical). $R_L = 0.5$ indicates that the longer lobe of the pair is twice as long as the short one. The projected lobe length distribution (top row) and corresponding length ratio distribution (bottom row) are each split in two different ways; firstly, by whether or not the outflow originates from a clustered environment, and secondly, by the confidence level (p) that the selected driving source is the correct one.

As can be seen in the left-hand panels of Fig. 4.5, outflows associated with a more isolated environment have a larger fraction of very short objects. The median lobe length for clustered outflows
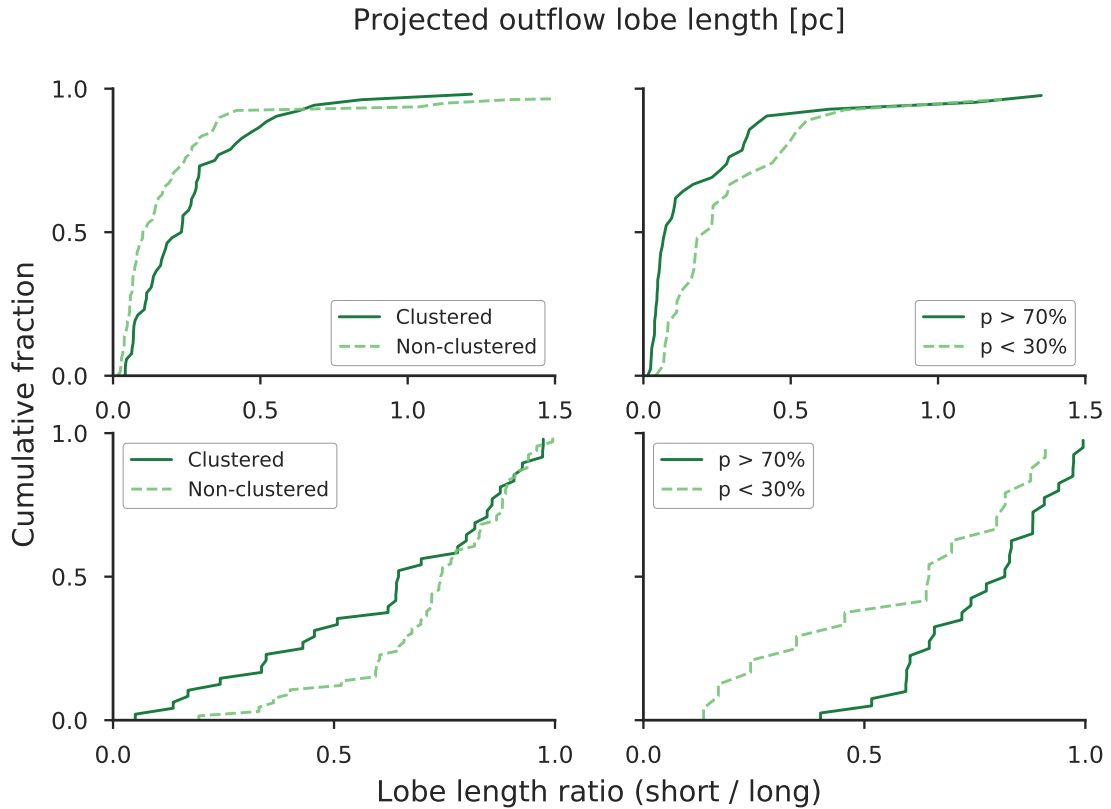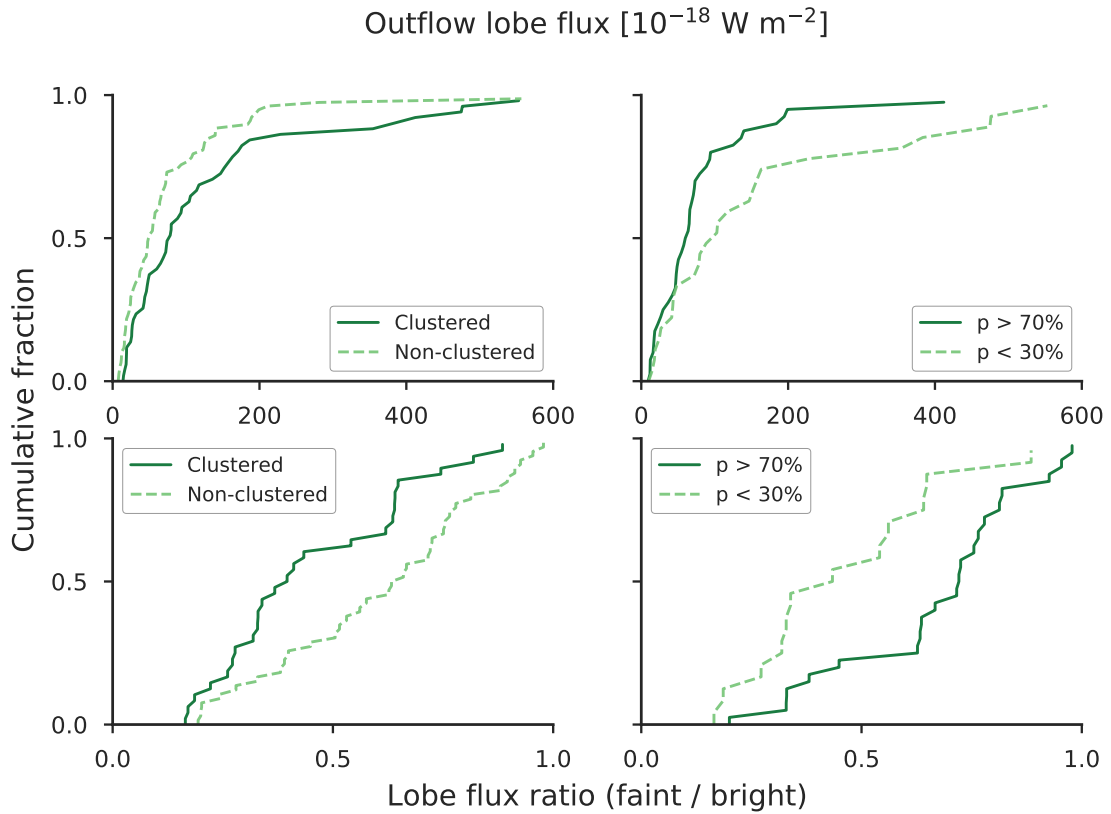
FIGURE 4.5: (Top row) Projected lobe length and (bottom row) lobe length ratio distributions. These pairings are each split by (left) whether or not the outflow is associated with a clustered environment, and (right) whether the candidate driving source is likely ($p > 70\%$) or unlikely ($p < 30\%$) to be correctly assigned.

is $0.22\,\mathrm{pc}$, whilst for the isolated outflows the median lobe length is less than half that length, with $0.10\,\mathrm{pc}$. The KS test results give $p = 8.40 \times 10^{-3}$, which is close to the significance level of $\alpha = 5 \times 10^{-3}$, so although the null hypothesis cannot be rejected at the given significance level it is not a decisive result. The AD test suggests the two samples are drawn from different populations, with $A^2 = 5.440\,(> 3.752)$. The median length ratio for bipolar outflows is 0.72, suggesting that outflows tend to be somewhat asymmetrical, with the distribution of length ratios between 0.6 and 1 being almost homogeneous. When this is split for clustered and non-clustered outflows, the median length ratios are 0.78 and 0.74 respectively. Similarly, the KS and AD tests suggest the ratio populations are drawn from the same parent distribution ($p = 0.135$, $A^2 = 0.727$). However, the fraction of highly asymmetric outflows ($R_L < 0.5$) is lower from isolated outflows.

In the right-hand column of Fig. 4.5 only those outflows with a high ($p > 70\%$) or low ($p < 30\%$) confidence level are shown. The lobe length samples are likely drawn from different distributions ($p = 1.036 \times 10^{-3}$, $A^2 = 5.861$) but again, the p-value is close to the 1% significance level and is therefore not a decisive result. For the length ratios, however, the null hypothesis cannot be ruled out ($p = 0.208$, $A^2 = 2.155$). It can be seen that the higher-confidence sources rarely drive highly asymmetrical outflows, and that the isolated outflows, where the confidence levels are typically higher, tend to be shorter than those from clusters. The over-abundance of highly asymmetric, outflows with low-confidence sources coincides with those originating from clusters.
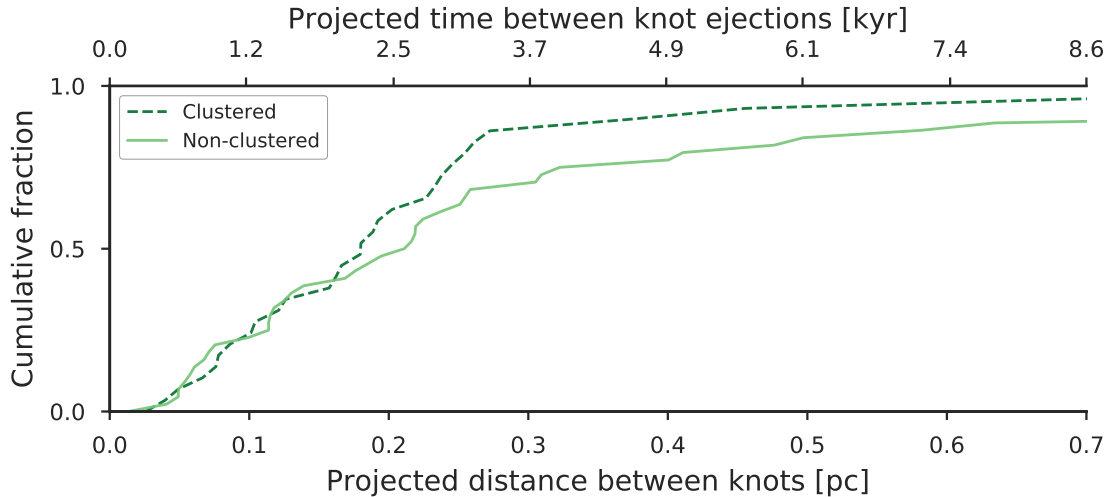
FIGURE 4.6: Cumulative distribution function showing the distribution of projected distance (gaps) between consecutive knots in outflow lobes, with the projected timescale corresponding to these gaps along the top axis assuming a transversal speed of $80\,\mathrm{km\,s^{-1}}$. The distribution of knot gaps is split between those from outflows in clustered vs. non-clustered environments. Five gaps are excluded from the right-hand side of the figure as the axis is truncated to 0.7 pc.

It would be uncontroversial to conclude from this that the lower-confidence sources are associated more frequently with clusters. Although the incidence of highly asymmetric ($R_L < 0.5$) outflows is fairly infrequent ($\sim 20\,\%$ of bipolar flows), they are mainly associated with mid- or low-confidence level driving sources.

4.2.3 Gaps between H_2 knots

In F16 the distribution of gaps between large H_2 emission knots was shown in Fig. 6, which demonstrated that the vast majority of the gaps were shorter than 0.5 pc, with only a very small number of gaps being longer than that. In Fig. 4.6 this figure has been replicated using the cumulative distribution. The x-axis is truncated to 0.7 pc in order to investigate the distribution over this range of interest where most of the gaps are situated. This excludes five gaps from the right-hand side of the figure. In addition, the distribution is split into those gaps found in outflows from clustered environments and those from isolated environments. It can be seen that the distribution of knot gaps appears almost homogeneous between 0.025 pc and 0.275 pc, with little difference between the clustered and non-clustered distributions. Assuming a constant transversal speed of $80\,\mathrm{km\,s^{-1}}$, this corresponds to timescales between large H_2 knots of $0.3 - 3.4\,\mathrm{kyr}$.

KS and AD tests suggest that the clustered and non-clustered samples are likely drawn from the same parent distribution ($p = 0.495$, $A^2 = -0.110$) despite the long tail of knot gaps longer than 0.7 pc (with the maximum being 1.24 pc). Once again, the small population size is a problem, with fewer than 80 knot gaps in total. Therefore, this will be revisited in Chapter 5 when the results from Cygnus-X are presented, and will be discussed in more depth in Chapter 6. However, it should be noted that the results obtained for Auriga and Cassiopeia are very similar to those

FIGURE 4.7: (Top row) Projected lobe flux and (bottom row) lobe flux ratio distributions. These pairings are each split by (left) whether or not the outflow is associated with a clustered environment, and (right) whether the candidate driving source is likely ($p > 70\%$) or unlikely ($p < 30\%$) to be correctly assigned.

found in Serpens and Aquila (IF12b) who found that the projected time between large H_2 knots is between $1 - 2$ kyr.

4.2.4 Outflow fluxes

In the same way as was done in Fig. 4.5, the distribution of fluxes in the outflow lobes has been split using the same indicators. The lobe flux distributions are shown in Fig. 4.7 (top), which includes all single-sided and bipolar lobes. The flux ratio R_F distribution (bottom) is shown for the bipolar outflows as the ratio of the flux of the faint lobe divided by the bright lobe in each pair of lobes. Again, all ratios are between 0 and 1, and values toward 1 indicate that the two lobes have the same brightness, whilst values toward 0 indicate a large degree of asymmetry.

$$R_F = \frac{F_{faint}}{F_{bright}} \tag{4.2}$$

Referring to Fig. 4.7 (left panels), the brightest outflow lobes are preferentially driven by sources in clustered environments, whilst there is a slight preference for outflow lobes that do not originate from clustered environments to be fainter. KS and AD testing is inconclusive about whether they

are drawn from the same parent sample ($p = 1.068 \times 10^{-2}$, $A^2 = 4.533$). There is a preference for outflows driven by sources located in clustered environments to be more asymmetrical, whilst the opposite is true for the non-clustered outflows. Here, the null hypothesis cannot be rejected, although the results are also not decisive ($p = 2.926 \times 10^{-2}$, $A^2 = 2.929$). If the brighter lobes also tend to be highly asymmetrical, and also tend to be from clustered environments whilst more isolated outflows are fainter and symmetrical, it is possible that this could represent an environmental effect. This will be investigated in Chapter 5 to see if the same result is found in Cygnus-X.

As was seen in Fig. 4.5, the right-hand panel showing the distributions split between high-confidence (p > 70 %) and low-confidence (p < 30 %) driving sources in Fig. 4.7 mirrors the clustered and non-clustered splits in the left-hand panels reasonably well. For the lobe fluxes, the high and low-probability samples are likely drawn from the same parent distribution ($p = 0.189$, $A^2 = 0.304$). However, the flux ratio samples are drawn from different distributions ($p = 2.826 \times 10^{-4}$, $A^2 = 8.832$). As with the length distributions, the high-probability outflows seem to be generally more symmetrical, and the low-probability outflows are more similar to the distribution of those from clustered environments.

4.2.5 Outflow asymmetry

Since there appears to be some connection between clustered and non-clustered environments and the ratios of the lengths and fluxes, Fig. 4.8 shows the length ratios (short over long) plotted against the flux ratios (faint over bright) for all bipolar outflows. If we take "symmetry" in either lengths or fluxes to mean those outflows where $R_L > 0.5$ or $R_F > 0.5$, and "asymmetry" to mean those where $R_L < 0.5$ and $R_F < 0.5$, then the dashed lines in the figure denoting $R_L = 0.5$ and $R_F = 0.5$ are useful for demarcation purposes. The lobes from clustered environments are shown with darker green squares, whilst isolated lobes are denoted with pale green circles. The size of each point corresponds to the confidence level that the driving source is correctly assigned (larger points correspond to higher confidence). The number of objects in each "box" is summarised in Table 4.1.

TABLE 4.1: Table showing the breakdown of clustered and non-clustered bipolar outflows corresponding to Fig. 4.8.

(a)	Clustered: 8	(b)	Clustered: 8
	Non-clustered: 9		Non-clustered: 20
	Total: 17		Total: 28
(c)	Clustered: 7	(d)	Clustered: 1
	Non-clustered: 1		Non-clustered: 3
	Total: 8		Total: 4

It can be very quickly seen that there is no direct correlation between the length ratio and flux ratio for any given outflow. In general, most of the outflows are more symmetrical than not in terms of their lengths (45 > 0.5 versus 12 < 0.5), while the flux ratios are more evenly spread (32 > 0.5 versus 25 < 0.5). This may be a selection effect, and that the outflows with highly asymmetrical
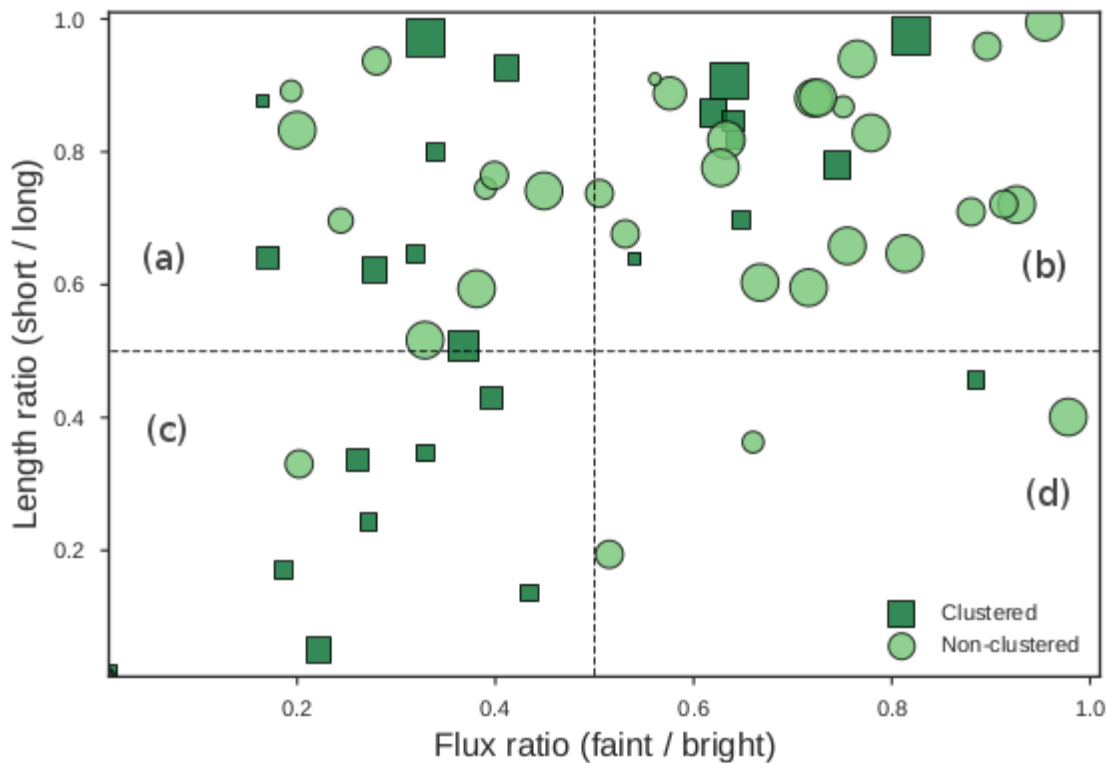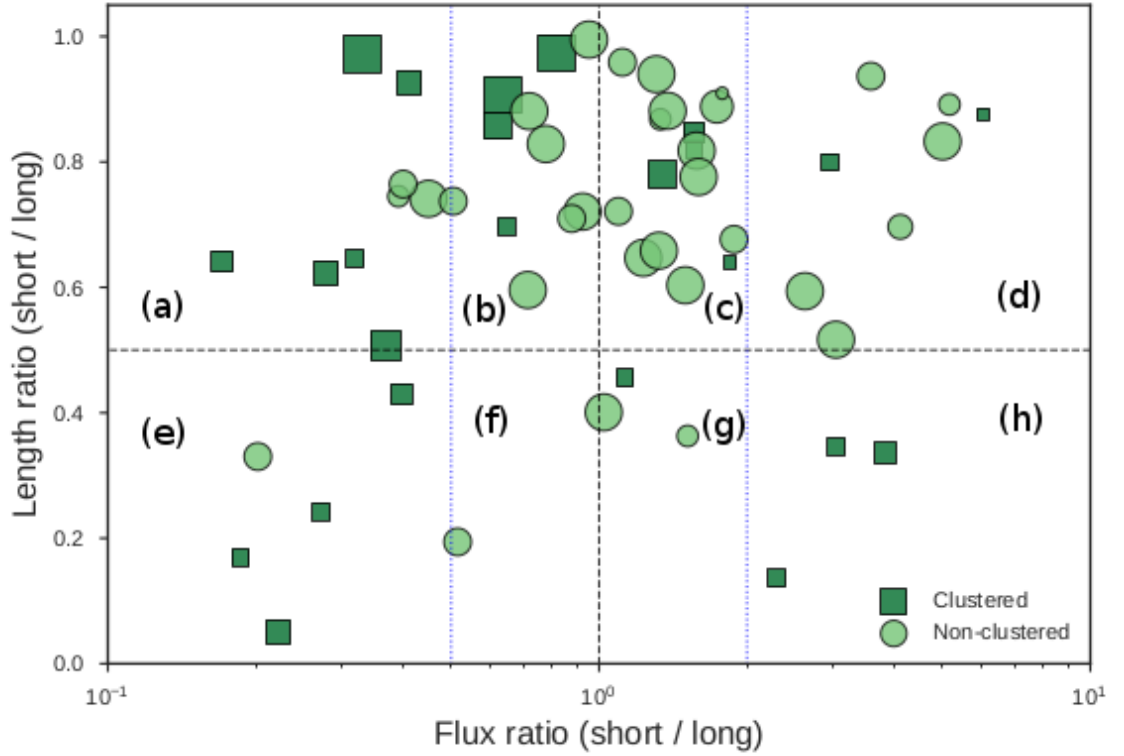
FIGURE 4.8: A scatter plot showing the ratio of lobe lengths (short side over longer side) against the ratio of fluxes (faint side over brighter side) for all bipolar outflows. The horizontal dashed line indicates $R_L = 0.5$ and the vertical dashed line shows $R_F = 0.5$. The breakdown of objects in each "box" is shown in Table 4.1.

lengths are simply more likely to be counted amongst the single-sided outflows. Of the 45 outflows with mostly symmetrical lengths, a small majority (28) also have symmetrical lobe fluxes with most of these being from isolated environments, while the remaining 17 that have asymmetrical fluxes are evenly split in terms of the environment they originate from. Out of the 32 outflows with symmetrical fluxes, a large majority 87.5 % are also symmetrical in terms of their lengths and 20 of these highly-symmetrical objects are also found in isolated, non-clustered environments. The isolated outflows, then, may tend to be more symmetrical.

Overwhelmingly, the highly asymmetrical outflows (i.e., those that are asymmetrical in both their length and flux ratios) are found in clustered environments. It is not clear if this is a real effect, or if the generally higher uncertainty in the driving sources from outflows located in clusters is the main factor in this result. In other words, if the driving sources in clusters are systematically misidentified, this could lead to large asymmetries in the measured lobes. In the next Chapter, this will be investigated further with the larger sample from Cygnus-X. Although interesting, this does not shed light onto the relationship (if any) between the length and flux in any given outflow lobe pair. We can therefore try to relate the two parameters by plotting the flux ratio as the flux in the short side over the flux in the long side, $R_F(^S/_L)$. This then relates the lengths and fluxes using the same lobe, and is demonstrated in Fig. 4.9.

The y-axis is the same as in Fig. 4.8, where the dashed black line denotes a length ratio of 0.5 (i.e.

FIGURE 4.9: A scatter plot showing the ratio of the lobe lengths (short side over longer side) against the ratio of fluxes (flux of the short side over the flux of the long side) for all bipolar outflows. This relates the flux ratios to the length ratios. The dashed horizontal line indicates a length ratio of $R_L = 0.5$, while the dashed vertical line indicates a flux ratio of $R_F(^S/_L) = 1$. The blue dotted lines mark $R_F(^S/_L) = 0.5$ and $R_F(^S/_L) = 2$. The point sizes represent the confidence level in the chosen driving source, with larger points for higher confidence levels.

TABLE 4.2: Table showing the breakdown of clustered (CL) and non-clustered (NC) bipolar outflows corresponding to Fig. 4.9.

(a)	(b)	(c)	(d)
Clustered: 6	Clustered: 4	Clustered: 4	Clustered: 2
Non-clustered: 3	Non-clustered: 7	Non-clustered: 13	Non-clustered: 6
Total: 9 (16 %)	Total: 11 (19 %)	Total: 17 (30 %)	Total: 8 (14 %)
(e)	(f)	(g)	(h)
Clustered: 4	Clustered: 0	Clustered: 1	Clustered: 3
Non-clustered: 1	Non-clustered: 1	Non-clustered: 2	Non-clustered: 0
Total: 5 (9 %)	Total: 1 (2 %)	Total: 3 (5 %)	Total: 3 (5 %)

where the longer of the two lobes is twice as long as the shorter lobe) and perfectly symmetrical outflows have a length ratio of 1. On the x-axis, the black dotted line shows where the flux ratio is 1 (i.e. where the long and short lobes both have the same surface brightness). The two blue dotted lines indicate where the flux ratios are equal to 0.5 (where the longer lobe is also twice as bright as the shorter lobe) and to 2 (where the longer lobe is half as bright as the shorter lobe).

As was established from Fig. 4.8, 45 (79 %) of the 57 bipolar outflows are more symmetrical

($R_L > 0.5$) and 12 of them (21 %) are asymmetrical in terms of their lengths, and so this does not change in Fig. 4.9. The most symmetrical outflows, i.e. those which are symmetrical in both their lengths and fluxes, are found in boxes (b) and (c), and these objects comprise 49 % of the total number of outflows. The population of bipolar outflows has been split into those originating from clusters (24 of the bipolar flows) and those not originating from clusters (33 of the bipolar flows). In segments (b) and (c), there are only 8 out of 24 (33 %) clustered outflows, but there are 20 out of 33 (61 %) isolated outflows. This suggests that the more isolated outflows are most likely to be more symmetrical in both their lengths and fluxes. This is also somewhat supported by the fact that of the 12 outflows with asymmetrical lengths, 75 % originate from clusters, and these are split rather evenly between boxes (e) and (h) where one lobe is more than twice as bright as the other (hence representing the most asymmetrical objects).

The clustered outflows have a slight preference for the longer lobe to be the brighter one (58 % of clustered outflows have a flux ratio of $R_F(^S/_L) < 0.5$), whilst the opposite is true for the non-clustered outflows, where the majority (64 %) have a flux ratio of $R_F(^S/_L) > 0.5$. This suggests that the asymmetry in the fluxes can depend on whether or not the source originates in a cluster or is isolated. If this result is also found with the much larger sample in Cygnus-X, it may indicate that isolated environments produce outflows where the shorter lobe is brighter than the longer lobe.

Summary of key results

- A total of 98 MHOs were identified in the Auriga and Cassiopeia region, and all of them are new discoveries. Of these, 57 are bipolar and 17 are single-sided outflows.

- Most of the outflows (59 %) are located outside of clusters or co-forming groups.

- The vast majority are driven by protostars (97 % of 57 bipolar or single-sided outflows with an identified driving source).

- The distribution of outflow position angles is homogeneous.

- Most of the bipolar outflows (86 %) are straight, having a position angle difference of less than 10° between pairs of lobes. Of the remainder, none have a position angle difference greater than 20°.

- Single-sided and bipolar outflows should not be mixed into a common distribution when measuring the total lengths.

- Outflows from clusters tend to be longer and brighter than isolated outflows. Isolated outflows are more symmetrical.

- Results for the low-confidence outflows mirror those of the outflows from clusters. This is unsurprising since the outflows from clusters have a much higher uncertainty regarding the correct driving source.

- The projected lengths of gaps between subsequent knots suggest typical timescales between large ejection events of 0.3 to 3.4 kyr. There is no statistical difference between gaps from outflows originating in clusters versus those in isolated environments.

- The isolated outflows are the most likely to be symmetrical in both their lengths and fluxes.

Chapter 5

Results, part II: Outflows in Cygnus-X

> Author's note: In this chapter, I present the general results of the outflow survey undertaken in the Cygnus-X region. The work presented here was peer-reviewed and published in the Astrophysical Journal Supplement series (Makin and Froebrich, 2018) hereafter referred to as M18. This work was undertaken in collaboration with Dirk Froebrich at the Centre for Astrophysics and Planetary Science, at the University of Kent, between 2015 and 2017. The catalogue data can be obtained from the Vizier database[a]. The images can be obtained from the online journal.
>
> ---
> [a]ADS link to Vizier catalogue: http://adsabs.harvard.edu/abs/2018yCat..22340008M

5.1 General results

In the Cygnus-X region, there were 210 groups of H_2 features classified as "jet" emission from the F15 catalogue. Out of these groups, 200 were found to contain genuine shock-excited H_2 emission, with the remaining 10 groups only composed of fluorescently-excited cloud edges or other image artefacts. From these 200 groups, 572 outflows were identified. The average group therefore contained 2.8 outflows and the median number of outflows per group was 1, although some of the larger and better known regions contain many more than the average. The DR 21 region for example, contains 38 outflows, the majority of which are already known in the MHO catalogue (Davis et al., 2010). Out of the 572 outflows identified, almost half are bipolar (261 outflows, 46 %), a quarter are single-sided (152 outflows, 27 %) and the remaining quarter are individual knots or groups of knots without a clear driving source (159 objects, 28 %).

Some outflows are composed of one or more already-known MHOs; there were 147 known MHOs falling inside the survey area and these correspond to 107 of our outflows (19 % of the total of 572). This means that 465 of the outflows from the survey in Cygnus-X are totally new discoveries (an increase of 435 % inside the survey area). This represents the largest collection of H_2 outflows published in a single paper to date. The only already-known outflow falling within the survey area that was not included in this list of outflows is MHO 3411. It appears in the UWISH2 JKH$_2$ images as a point source, rather than an extended H_2 emission-line feature. In the original image from Bally et al. (2014) (as shown in the MHO catalogue) it appears to be a point source which may have some extended emission around it. However, since it is not clear from either set of images
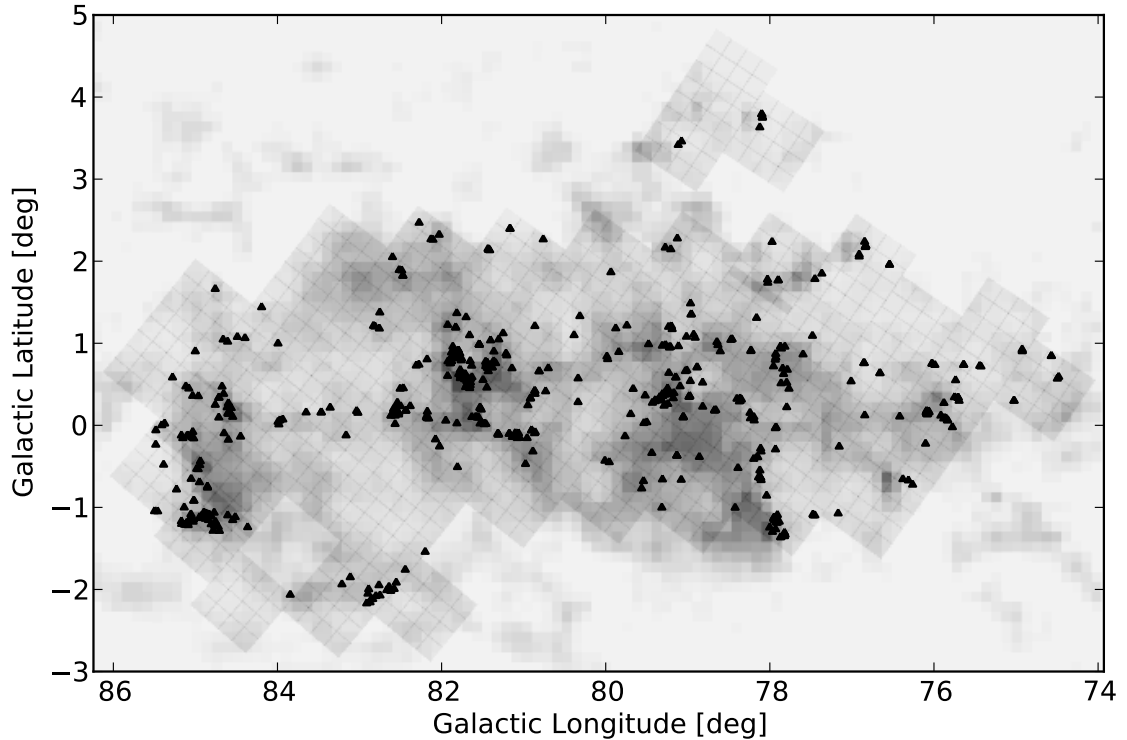
FIGURE 5.1: A map in Galactic coordinates demonstrating the coverage of the UWISH2 survey in the Cygnus-X region. The background image is a ^{12}CO (J = 1 → 0) intensity plot from Dame, Hartmann, and Thaddeus (2001), where darker grey regions correspond to areas of increased CO emission. The UWISH2 observations are indicated by the overlaid grid, where each 4×4 set of squares corresponds to one UWISH2 tile. The black triangles show the positions of every outflow detected in the survey area.

if this MHO is really a H_2 knot, or a point source with some associated reflection, it is excluded from our list and analysis, but its removal from the MHO catalogue is not recommended.

The spatial distribution of the outflows identified in Cygnus-X is shown in Fig. 5.1, where each is marked with a black triangle. As with the Auriga and Cassiopeia coverage map, the grid represents the UWISH2 survey tiles that cover the region and the background image is a CO intensity map using the ^{12}CO (J = 1 → 0) transition from Dame, Hartmann, and Thaddeus (2001). It is clear that many of the outflows are clustered in groups throughout regions of high CO column density, as was noted in Auriga and Cassiopeia.

Candidate driving sources have been identified for 215 (82 %) of the bipolar outflows and 146 (96 %) of the single-sided outflows. For a further 27 bipolar outflows (10 %) the most likely location for the driving source has been identified. The "most likely location" refers to cases where no detections exist in the selected catalogues, but the most reasonable location for an embedded driving source can be estimated by, e.g. the morphology of the emission knots (where two opposing bow shocks appear to be curved away from each other the source should lie between them) or by the presence of dark regions in the JKH_2 images (indicating the presence of filaments of cloud crossing the outflow axis). In Cygnus-X the amount of extinction caused by dust can be very large (up to $A_V \sim 25$ mag in regions such as DR 21 (Nadeau, Riopel, and Geballe, 1991))
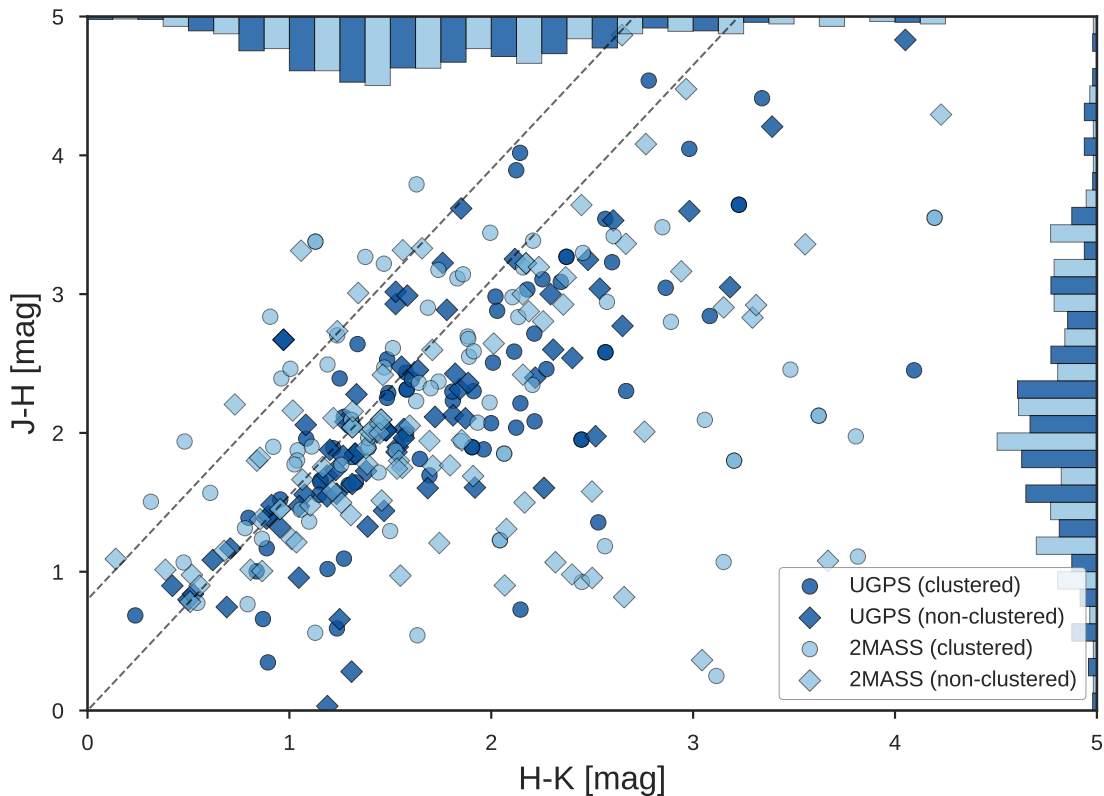
FIGURE 5.2: NIR colour-colour diagram of the candidate driving sources using data from both UGPS (dark blue) and 2MASS (pale blue). The circles represent sources located in clustered environments, whilst diamonds signify sources that are more isolated. The dashed lines represent the standard reddening band for normal stellar photospheres. The projected histograms show the distributions of all of these points, with dark blue corresponding to the UGPS points, and pale blue for 2MASS.

and varies greatly across the region, which can make identifying the correct driving source even more difficult than in Auriga and Cassiopeia.

Even where a potential driving source cannot be identified, it is still clear whether or not the outflow is associated with, or originates from, a clustered environment. Since most stars form in clusters (Lada and Lada, 2003) one might expect that most of the outflows originate from clustered environments. However as was found in Auriga and Cassiopeia, most of the outflows (334, 58 %) are found in isolated environments, whilst 238 (42 %) are found in clusters.

Out of the 413 outflows that are bipolar or single-sided, 294 (71 %) have detections in either 2MASS, UGPS, or both. This allows the calculation of the NIR colours as shown in Fig. 5.2. There is a considerable amount of scatter in this figure, which suggests that there could be contamination from non-YSO sources. This is particularly the case for the sources situated above the reddening band. However, most of these sources have their magnitudes taken from 2MASS - the single UGPS source above the reddening band is a potential binary object. This suggests that the cause of this scatter could be the poorer resolution in 2MASS being unable to resolve two or more nearby stars that are resolved in UGPS, particularly as around half of the objects inside or above the reddening band are known YSOs or potential binaries, and the magnitudes are not corrected for extinction.

Most of Cygnus-X has been imaged twice in the UGPS survey. This means that for 294 drivings sources there are three K-band magnitudes available; K_1 and K_2 from UGPS, and K_S from 2MASS. Between 2MASS and UGPS (K_1 and K_S) there are 168 driving source candidates with detections in both, of which 121 (72 %) are variable by more than 0.1 mag, 52 (31 %) are variable by more than 0.5 mag, and 34 (20 %) are more variable than 1.0 mag. Between the two epochs of UGPS there are 267 driving source candidates detected in both epochs, of which 166 (62 %) are variable by more than 0.1 mag, 50 (19 %) are variable by more than 0.5 mag, and 24 (9 %) are variable by more than 1 mag. However, as was found in Auriga and Cassiopeia, the K_S magnitudes are systematically brighter than those from K_1, whilst the magnitudes between K_1 and K_2 are equally split between brighter and fainter objects. It is unsurprising then, that the sources appear more variable when comparing UGPS to 2MASS than in the two UGPS epochs. This systematic bias implies that the variability should not be measured using a combination of 2MASS and UGPS.

In addition to this, only five of the candidate sources with more than 1.0 mag of variability were also detected in the UGPS surveys for variable stars (Contreras Peña et al., 2014; Lucas et al., 2017). Since stars that show nebulosity around them were not excluded (indeed, using these objects as preferable driving sources where the nebulosity extends in the same direction as the outflow knots), or those with K > 16 mag as Lucas et al. did, the photometry is rather unreliable and so many (or even most) of our suggested driving sources are unlikely to be genuine variable stars. The five objects which were successfully matched against the Lucas et al. catalogue are:

OF 020 (MHO 4016): V110 (separation $0''.27$)

OF 031 (MHO 3929): V93 (separation $0''.06$)

OF 090 (MHO 3872): V80 (separation $0''.055$)

OF 114 (MHO 3840): V40 (separation $0''.08$)

OF 324 (MHO 4002): V109 (separation $0''.006$)

In the mid-infrared, 269 of the bipolar and single-sided outflows have detections in all four of the filters of WISE. When the slopes of their SEDs are calculated, 54 (20 %) have $\alpha < 0$ and 215 (80 %) have $\alpha > 0$. This means that the majority of the outflow driving sources are likely to be protostars. It is therefore possible to perform K-S testing on the basis of the evolutionary stage of the driving sources, unlike in Auriga and Cassiopeia. It should be noted, however, that α is sensitive to local extinction, and we have not performed any corrections to account for this. Therefore, we use this measure as a statistical indicator of approximate evolutionary stage on the assumption that variations over a large enough sample will not be significant on average.
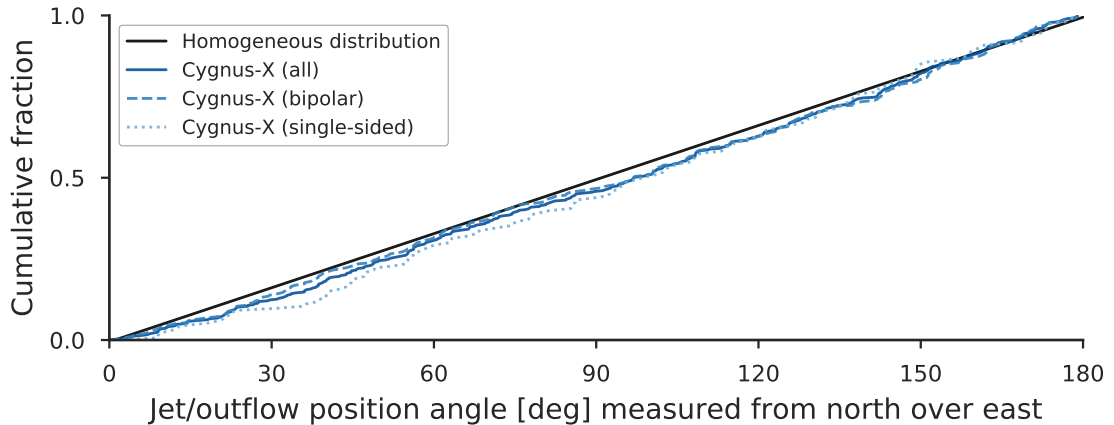
FIGURE 5.3: Cumulative distribution function demonstrating the distribution of outflow position angles for all outflows (i.e., bipolar and single-sided) in Cygnus-X. The bipolar and single-sided outflow distributions are shown separately, and for the bipolar outflows the average lobe position angle is used. The homogeneous "test" distribution is shown in black.

5.2 Outflow properties

5.2.1 Outflow position angles

As in Auriga and Cassiopeia, the distribution of position angles in Cygnus-X (shown in Fig. 5.3) appears to be homogeneous between $0°$ and $180°$. The homogeneous "test" distribution is again shown with a solid black line. The bipolar outflows are shown with a dashed mid-blue line, the single-sided outflows with a dotted pale blue line, whilst the total population (bipolar and single-sided outflows together) is denoted by the dark blue line. All three samples have a good correlation with the homogeneous distribution, confirming that the outflows are oriented randomly across the whole of the Cygnus-X region, and both the KS and AD test agree that they are drawn from the same parent sample:

Bipolar outflows: $p = 0.964$, $A^2 = -0.730$

Single-sided outflows: $p = 0.363$, $A^2 = 0.083$

All outflows: $p = 0.802$, $A^2 = -0.286$

It should be noted, however, that the p-value for the single-sided outflows is much lower than for the other samples, and the A^2 value higher. In Davis et al. (2007), the brightest outflows in the DR 21 region were found to be perpendicular to the dusty filament that forms the DR 21 ridge, whilst the fainter outflows were oriented randomly. When the single-sided sample is investigated, it does appear that these objects are preferentially located in the DR 21, DR 15 and North American Nebula regions. This suggests that there may be some preferential orientations on the scale of these active star-forming regions. In DR 15 for example, there are 9 single-sided outflows and only 3 bipolar outflows, and most of these outflows appear in the NIR images to be oriented either parallel or perpendicular to each other. This suggests that locally there may indeed be some sort
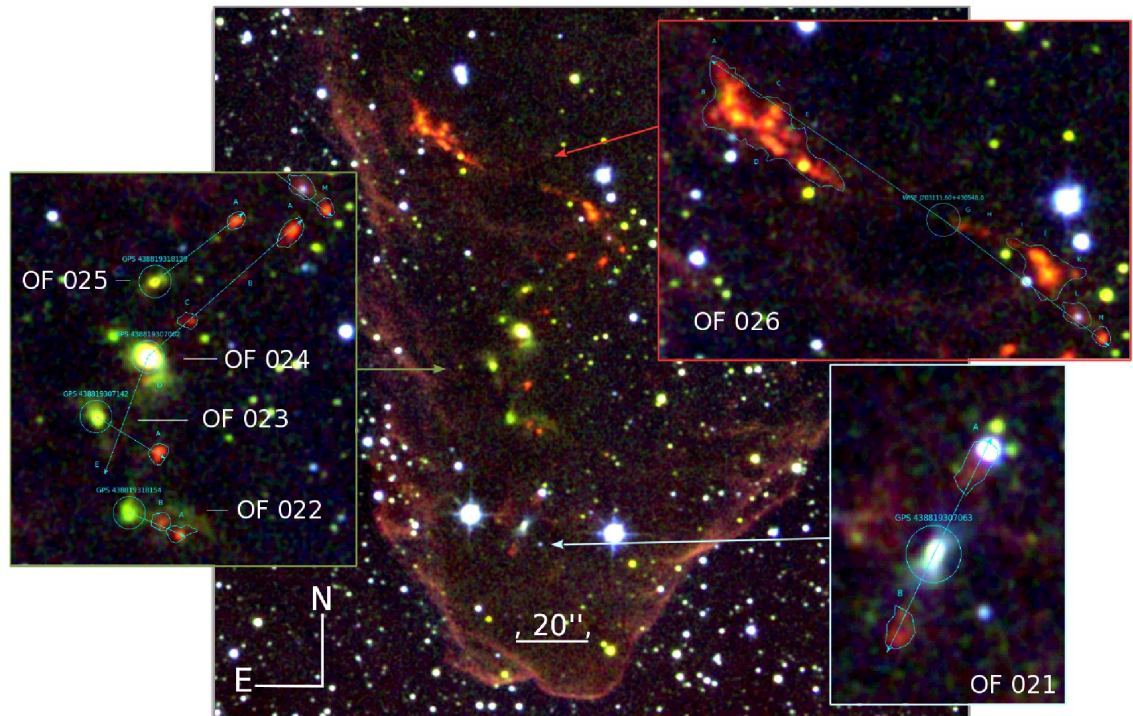
FIGURE 5.4: A bright-rimmed cloud, illuminated from the south, near IRAS 20294+4255. A chain of outflows have been identified within this cloud whose assigned driving sources imply an evolutionary progression from the oldest in the south to the youngest in the north.

of preferential orientation, but whether or not this is related to the local filament (as is suggested to be the case in DR 21) is unclear and requires further study.

In order to test if the outflows from these regions are the ones that are inhomogeneous, the population was separated into two samples: those from the major star forming regions in Cygnus-X in which most of the already-known outflows were found (DR 15, DR 21, W 75 N, L 906 E, Gulf-of-Mexico and the Pelican Nebula), and those that are not from those regions. Outside of these regions there are 108 single-sided outflows, which are found to be homogeneously distributed once the outflows from the large star-forming complexes are excluded. The bipolar flows in these regions are homogeneously distributed overall, but are inhomogeneous within each sub-region's apparent boundaries, suggesting that there may be preferences on local levels in the position angles of the outflows. Outside of these large regions, then, it can be concluded that there is no preference in the outflow position angles on the large scales of the general population, which supports the findings of Davis et al. (2009) who found that outflows (in Orion A) were randomly oriented. No preference is found for outflows to be oriented perpendicular to the Galactic plane, which contradicts the results found in Serpens and Aquila (IF2012a).

In addition, there are smaller regions of low-mass star formation that seem to contain outflows with a preferentially perpendicular or parallel orientation with respect to each other. One clear example is the bright-rimmed cloud near IRAS 20294+4255, which lies at the tip of a dusty pillar and seems to represent a textbook example of triggered star formation (Deb, Kothes, and Rosolowsky, 2018), where six outflows are identified in a chain from south to north (shown in Fig. 5.4). Follow-up observations are likely needed in order to confirm the driving sources, and thus the orientations,

of each apparent outflow. However, an approximate age progression can be inferred for the driving sources based on their appearances and α values from WISE. The cloud itself appears to be illuminated from the south (probably by an O or B-type star, given the fluorescent emission outlining the cloud edge). OF 021 appears to be the most evolved driving source and is located at the southernmost tip of the cloud; since it appears blue in the JKH_2 images it includes contributions from the shorter-wavelength J-band, as do the "wings" of reflected light that align with the two faint knots. The UGPS and 2MASS colours imply that this is the least reddened of the driving sources here, and it has no WISE detection. OF 022 (MHO 3569), OF 023 (MHO 3571), and OF 024 (MHO 3568) are cautiously assigned as driving sources; each of them is reddened, with K-band reflection nebulae in directions either perpendicular or parallel to OF 021. All three are known YSOs in Kryukova et al. (2014) and their Spitzer α values are all positive, as are those from WISE ($\sim +1$) suggesting at least Class I protostars. The two most northerly driving sources, those for OF 025 (MHO 3566) and OF 026 (MHO 3564), have $\alpha \sim +2$, implying that they could be even less evolved. OF 026 is not visible at shorter wavelengths than 3.6 μm, and the outflow itself is precessing, suggesting a binary source. It was already detected as an outflow using CO (Gottschalk et al., 2012).

Multi-outflow systems are found in Cygnus-X in the same proportion as in Auriga and Cassiopeia. A total of 50 (9 %) of the outflows form such systems in Cygnus-X, and of these, 42 % show signs of precession compared to only 22 % of the outflows in the rest of the Cygnus-X population which closely mirrors the results from Auriga and Cassiopeia. Interestingly, some of these systems in Cygnus-X are composed of more than two outflows. It may be the case that multiplicity of forming stars, and triggering by means of local feedback, has more of an effect on the relative orientation of nearby outflows than the structure of the host filament or cloud.

5.2.2 Outflow lengths

In Cygnus-X, 41 of the bipolar outflows (16 %) are over a parsec in length (parsec-scale) using the assumed distance of 1.4 kpc, and the median total length is 0.45 pc. In Fig. 5.5 the lobe length and total length distributions of the bipolar and single-sided outflows are compared to each other. In the top sub-figure, the lobe length distributions are shown, with the total length distributions on the bottom. With the larger sample size, the difference between the single-sided and bipolar total lengths becomes even more apparent, with an even spread of outflows between 1.2 and 2.0 pc. This "tail" of very long outflows in the total length panel ends just under 4.0 pc owing to some extreme outliers such as the DR 21 and W 75 N outflows. These, and five additional outflows are not shown in the top panel due to the truncation of the x-axis at 2.0 pc, and two outflows are not shown on the bottom panel for the same reason.

The bipolar and single-sided lobe distributions (top panel) are more similar to each other than was found in Auriga and Cassiopeia, and are most likely drawn from the same parent distribution ($p = 0.674$, $A^2 = -0.395$). Conversely, the total length distributions (bottom panel) are clearly different from each other as can be clearly seen in the poor correlation between their cumulative distribution functions ($p = 8.24 \times 10^{-8}$, $A^2 = 27.615$). This is further evidence that mixing the
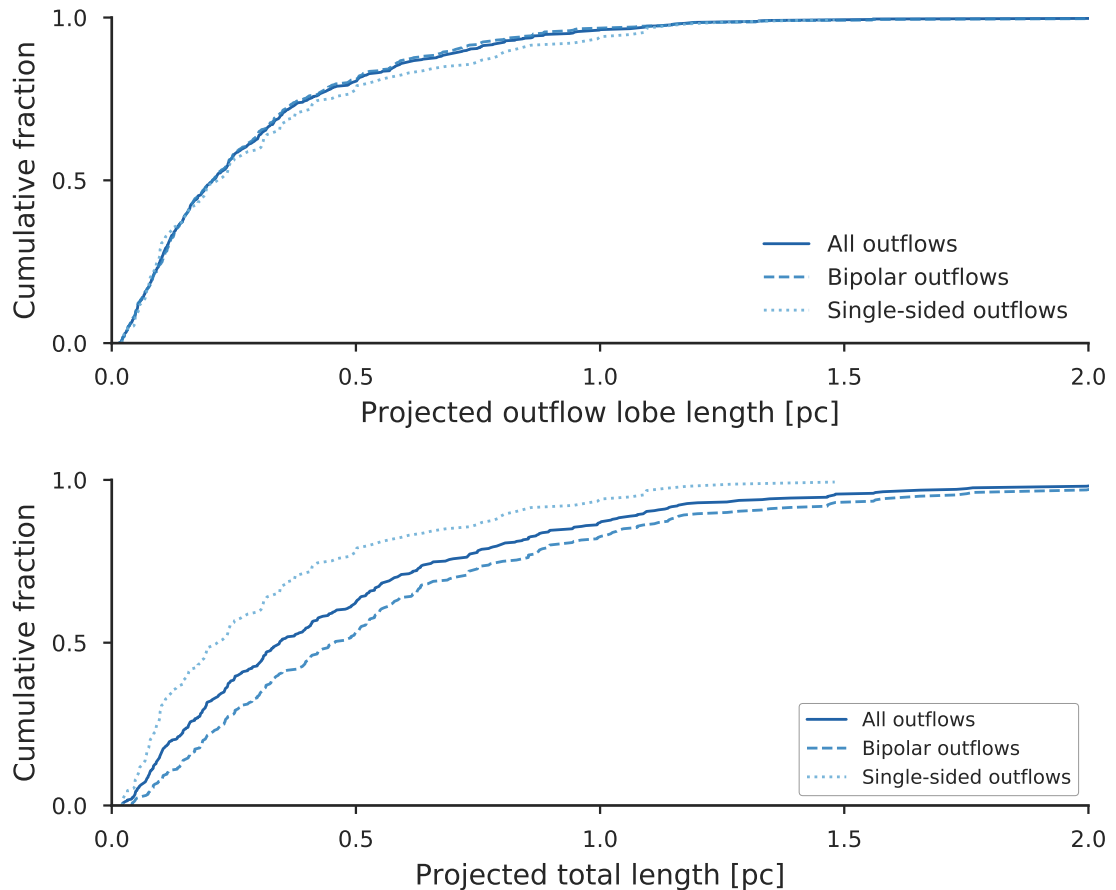
FIGURE 5.5: Cumulative distributions for (top) projected outflow lobe lengths and (bottom) projected total (end-to-end) outflow lengths. The populations are each split between bipolar (dashed mid-blue lines) and single-sided outflows (dotted pale blue lines). The total populations are shown with dark blue solid lines for reference.

bipolar and single-sided outflows into the same total length distribution should be avoided. As in Chapter 4 the total lengths will therefore be avoided and instead, the lobe lengths of the bipolar and single-sided outflows will be presented together.

In order to investigate some of the parameters that may affect the outflow lengths, Fig. 5.6 splits the lobe length (top row, bipolar and single-sided outflows together) and lobe length ratios (bottom row, for all bipolar outflows) in the same way as was done in Fig. 4.5 for Auriga and Cassiopeia. The plots appear visually similar to the Auriga and Cassiopeia version of the same panel graph, with the main differences being a slightly higher proportion of long outflows in Cygnus-X, and the length ratios in Cygnus not being homogeneous between 0.6 and 1. Statistical testing was done for each of the sub-populations and these results are summarised in the following discussion. The length ratios are homogeneously distributed between 0.5 and 1, apart from the sharp peak at 0.75 which suggests that most of the bipolar outflows are somewhat asymmetrical in their lobe lengths, but with a relatively small fraction of outflows being highly asymmetrical. Overall, this is the same result as was found for Auriga and Cassiopeia.

In the left-hand panels of Fig. 5.6 the lobe length distributions appear similar, apart from the dearth
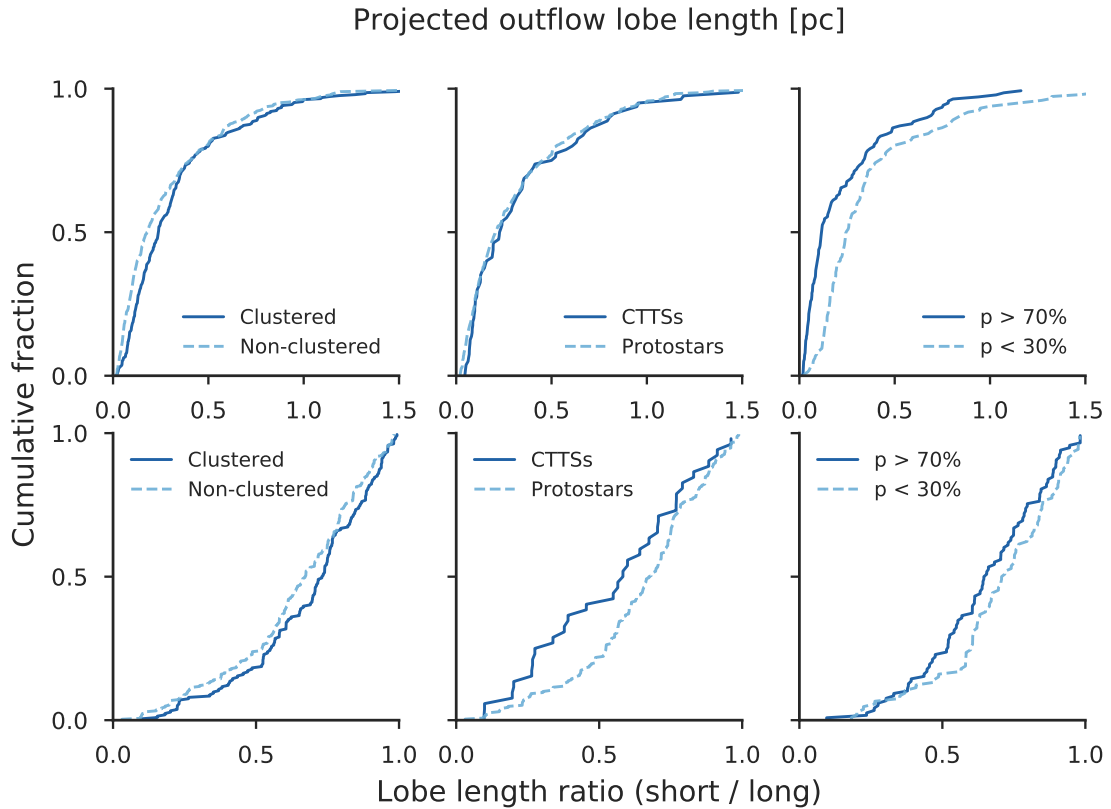
FIGURE 5.6: (Top row) Projected lobe length and (bottom row) lobe length ratio distributions. These pairings are each split by (left) whether or not the outflow is associated with a clustered environment, (centre) whether or not the candidate driving source is a protostar or CTT star, and (right) whether the candidate driving source is likely (p > 70 %) or unlikely (p < 30 %) to be correctly assigned.

of very short lobes originating from clustered environments. This similarity is superficial since the KS and AD tests show that the clustered and non-clustered lobe lengths are drawn from different distributions ($p = 8.62 \times 10^{-4}$, $A^2 = 7.794$). Conversely, there is little difference between the length ratio distributions of clustered and non-clustered outflows ($p = 0.0195$, $A^2 = 1.837$). The median length ratios for the clustered and non-clustered distributions are not significantly different (0.73 versus 0.67, respectively) but it suggests that outflows originating from clusters may be slightly more symmetrical in their lengths than those from more isolated locations.

In the central panels of Fig. 5.6 the lobe lengths of outflows driven by CTTSs and those from protostars are most likely drawn from the same parent distribution ($p = 0.452$, $A^2 = -0.171$). The length ratios, by contrast, are more than likely drawn from different distributions ($p = 9.00 \times 10^{-3}$, $A^2 = 4.289$). The KS test p-value in this case is close to the 1 % significance level and thus not a convincing result. It is therefore clear that protostellar sources drive more symmetrical outflows, whilst the CTTSs have an almost homogeneous distribution of length ratios.

In the right-hand panels of Fig. 5.6, the lobe lengths are drawn from very different populations ($p = 6.55 \times 10^{-12}$, $A^2 = 23.236$), whilst the lobe length ratios are far more similar ($p = 0.0363$, $A^2 = 2.050$). The driving sources in which we have a higher confidence level drive shorter outflows, whilst the lower-confidence driving sources are missing this peak of very short
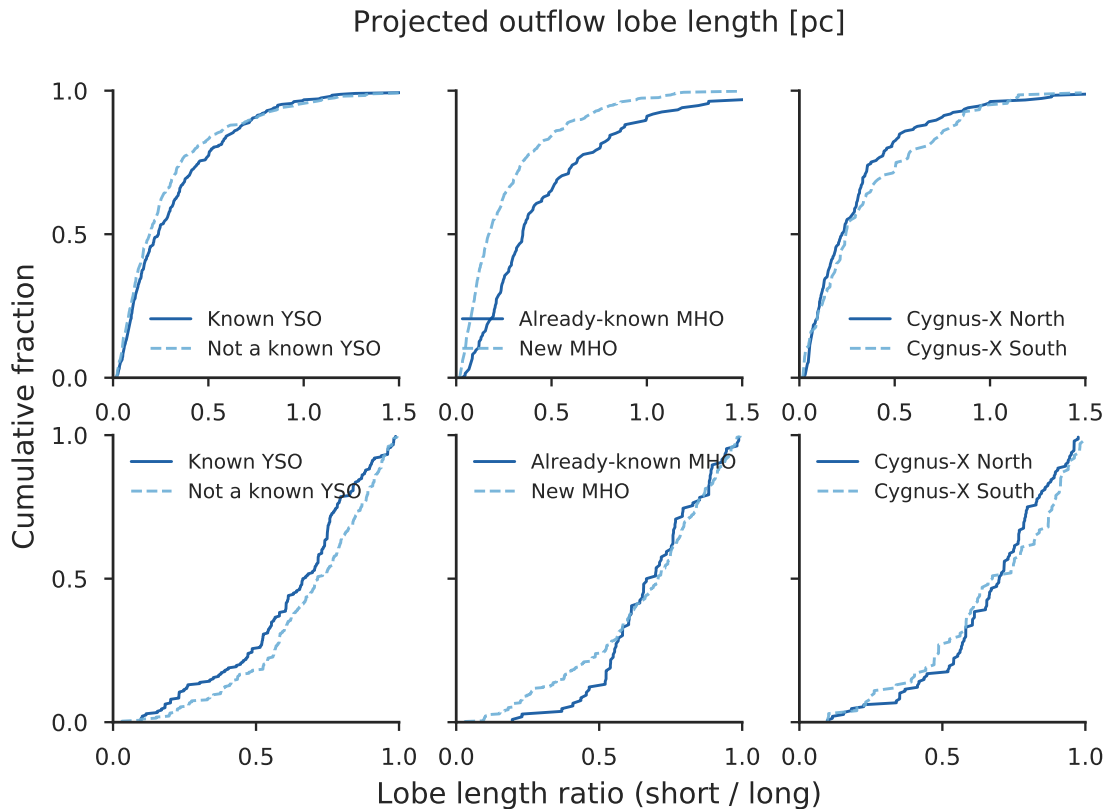
FIGURE 5.7: (Top row) Projected lobe length and (bottom row) lobe length ratio distributions. These pairings are each split by (left) whether or not the candidate driving source is known to be a YSO, (centre) whether the outflow was already known as an MHO or is a new discovery, and (right) whether the outflow is located in Cygnus-X north or Cygnus-X south.

outflows. In Cygnus-X generally, the confidence level in the driving sources tends to be lower than in Auriga and Cassiopeia due in large part to the increased column density of dust obscuring the driving sources and the more crowded field which leads to an increased number of potential driving sources for any given outflow.

Since the Cygnus-X region is well studied, it is also possible to split the lobe length and length ratio distributions according to additional parameters. For about half of the outflows the driving source has been identified as a YSO in either the Gulf-of-Mexico and Pelican Nebula (Rebull et al., 2011) or in Cygnus-X north and Cygnus-X south (Kryukova et al., 2014), so we can test if there is a difference between the outflows driven by known YSOs and the remainder of the population that are unclassified. Additionally, about a fifth of the outflows were already known in the MHO catalogue, so differences between the known sample of outflows, and those newly discovered, can be examined. Similarly, the difference between the outflows located in the Cygnus-X North region and those in Cygnus-X South can be investigated, since Kryukova et al. (2014) found that the luminosity distributions of the YSOs in each of those regions are different, with the Cygnus-X North YSOs being brighter than those in the South. These splits are shown in Fig. 5.7.

In the left-hand panels of Fig. 5.7 it can be seen that the outflow lobes from unclassified driving sources are slightly shorter than those from known YSOs, but they are probably drawn from the

same parent distribution ($p = 0.0329$, $A^2 = 2.316$). The unclassified driving sources also drive more symmetrical outflows, with the asymmetrical outflows being slightly preferentially driven by the known YSOs. In this case, the samples are drawn from different distributions ($p = 2.38 \times 10^{-4}$, $A^2 = 6.394$). Since the coverage of the YSO surveys does not correspond exactly with the UWISH2 survey area, and includes a mix of YSOs (CTTSs and WTTSs) and Class I protostars, it is not clear if the difference is due to the slightly biased coverage or the mixing of various evolutionary stages into a common distribution.

By far the clearest difference in lobe length distributions comes from those outflows that were part of the already-known sample and those that are newly discovered, as shown in the central panels of Fig. 5.7. It is very clear that there is a dearth of very short outflows in the already-known sample, and that the very longest outflows are preferentially those that are already-known. KS and AD testing confirms that these are drawn from very different distributions ($p = 2.35 \times 10^{-11}$, $A^2 = 31.707$). This suggests a bias in the known sample, perhaps due to the historical focus on high-mass star formation regions for more targeted observation campaigns. The lobe length ratios, however, are likely drawn from the same parent distribution ($p = 0.119$, $A^2 = 1.233$).

Although Kryukova et al. (2014) showed that the MIR bolometric luminosities of the YSOs from Cygnus-X north versus Cygnus-X south form different distributions, the outflow lobe length distributions from these two regions appear to be rather similar (right-hand panels in Fig. 5.7). It could be argued that there is a slight preference for the outflows from Cygnus-X south to be longer than those from the north, however testing suggests that despite visible differences in the CDFs of both the lengths and the length ratios, in both cases they are drawn from the same parent distribution (lengths: $p = 0.299$, $A^2 = 1.131$, length ratios: $p = 0.0921$, $A^2 = 1.009$).

5.2.3   Gaps between H$_2$ knots

When the gaps between subsequent H$_2$ emission knots in each outflow lobe are measured, 858 in total are found in Cygnus-X. This represents a far larger sample size than in Auriga and Cassiopeia. The distribution of the gap lengths is shown in Figure 5.8, split between those gaps belonging to outflows originating in clusters, and those from isolated environments. The mean gap length is 0.12 pc, and the median is 0.07 pc. At the assumed common distance of 1.4 kpc in Cygnus-X, and assuming a common transversal speed for all outflows of 80 km s^{-1}, the typical range of gap lengths ($0.025 - 0.1$ pc) corresponds to dynamical timescales of $0.3 - 1.2$ kyr.

There is no difference when the distribution of knot gaps is split between outflows from clustered and non-clustered environments ($p = 0.571$, $A^2 = -0.081$), or when the distribution is split between protostellar and CTTS driving sources ($p = 0.748$, $A^2 = -0.548$). This will be revisited in Chapter 6 to see if this result persists once the projected gap lengths are corrected for individualised distances to the outflows. It can be noted, however, that unlike in Auriga and Cassiopeia, the knot gaps do not have a homogeneous distribution between 0 and 0.26 pc, instead having a tall peak between 0.02 and 0.10 pc.
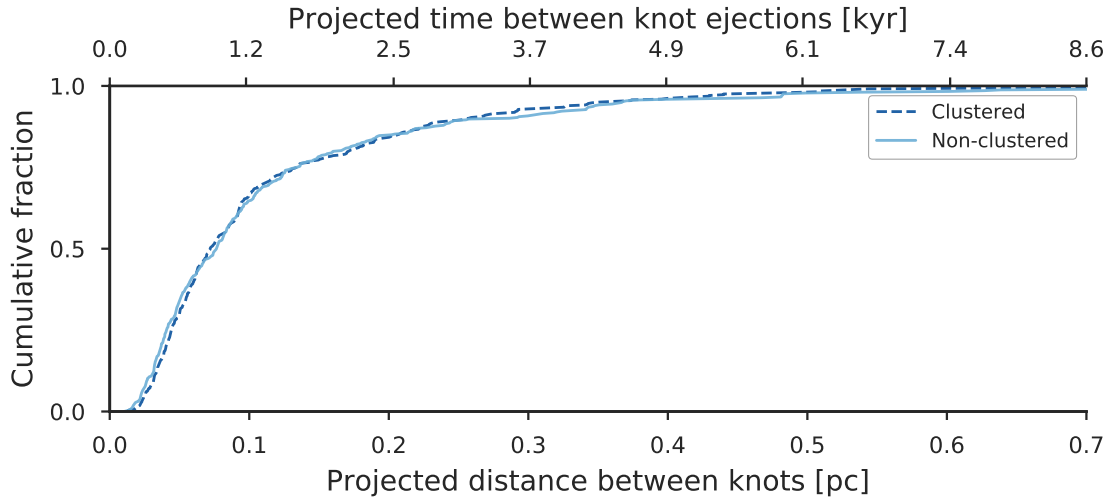
FIGURE 5.8: Cumulative distribution function showing the distribution of projected distance (gaps) between consecutive knots in outflow lobes, with the projected timescale corresponding to these gaps along the top axis assuming a transversal speed of $80\,\mathrm{km\,s^{-1}}$. The population of knot gaps is split into those from outflows in clustered vs. isolated environments. The x-axis is truncated at $0.7\,\mathrm{pc}$, with five objects not shown.

5.2.4 Outflow fluxes

The median total flux is found to be $18 \times 10^{-18}\,\mathrm{W\,m^{-2}}$ suggesting that the typical bipolar outflow is faint in H_2 (corresponding to a total luminosity of $1.1 \times 10^{-3}\,\mathrm{L_\odot}$ at a distance of $1.4\,\mathrm{kpc}$). The average total flux for bipolar flows, however, is $111 \times 10^{-18}\,\mathrm{W\,m^{-2}}$ ($6.8 \times 10^{-3}\,\mathrm{L_\odot}$ at $1.4\,\mathrm{kpc}$) as a result of extreme outliers such as the DR 21, AFGL 2591, and W 75 N outflows. Indeed, the DR 21 main outflow has by far the highest H_2 flux in the sample, representing $42\,\%$ of the total H_2 flux. This corresponds to a luminosity in the $1-0\,S(1)$ line of H_2 of $0.93\,\mathrm{L_\odot}$ (using the common distance of $1.4\,\mathrm{kpc}$). The next four highest-flux objects in the sample each account for about $3\,\%$ of the total, but the vast majority of objects are considerably fainter than this. The median flux ratio of the faint lobe over the bright one is 0.5 suggesting that in the typical bipolar outflow, one lobe is twice as bright as the other. In Fig. 5.9 and Fig. 5.10 it should be noted that around 60 of the very brightest outflows (those with a flux greater than $600 \times 10^{-18}\,\mathrm{W\,m^{-2}}$) are excluded from the right side of the plots on the top row where the x-axes have been truncated.

The top row of Fig. 5.9 shows the distribution of outflow lobe fluxes along the top row, and the lobe luminosity ratios (faint lobe over bright lobe) along the bottom row. Each distribution is split for clustered and non-clustered outflows (left-hand panels), CTTS and protostars (central panels) and high/low confidence levels (right-hand panels). It can be immediately noted that unlike in Auriga and Cassiopeia, the flux ratio distribution in Cygnus-X appears almost homogeneous. The reasons for this may not be entirely related to the small sample size in Auriga and Cassiopeia.

In the top left panel of Fig. 5.9 the fainter lobes tend to be driven by outflows from isolated environments, whilst the brightest outflows are found in high-mass star forming regions and clusters. Certainly they are drawn from very different distributions ($p = 9.88 \times 10^{-5}$, $A^2 = 14.818$). The
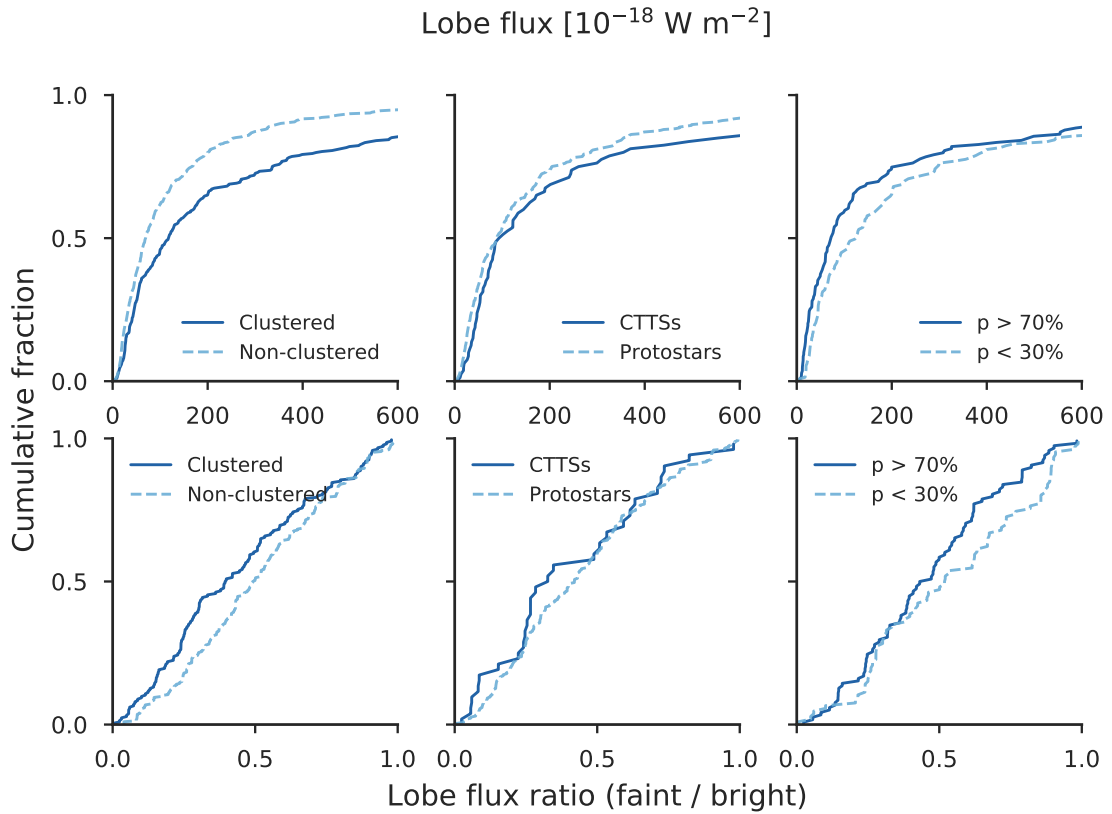
FIGURE 5.9: (Top row) Projected lobe flux and (bottom row) lobe flux ratio distributions. Each pairing is split by (left) whether or not the outflow is associated with a clustered environment, (centre) whether or not the candidate driving source is a protostar or CTT star, and (right) whether the driving source is likely (p > 70 %) or unlikely (p < 30 %) to be correctly assigned.

outflows from clusters are also more asymmetrical than those that are isolated (bottom left panel), and the flux ratios are also drawn from different distributions ($p = 2.401 \times 10^{-4}$, $A^2 = 6.791$).

There is little difference between the flux distributions of the lobes driven by protostars and those by CTTSs as shown in the top central panel of Fig. 5.9 ($p = 0.350$, $A^2 = 0.674$), although the protostellar lobes are slightly fainter on average. Similarly, the bottom central panel shows that the most asymmetrical outflows are more likely driven by CTTSs compared to the protostars, whose distribution is more homogeneous. However, this difference is not significant and most likely due to the smaller sample size of CTTS outflows, since testing shows that the flux ratio distributions are also drawn from the same parent distribution ($p = 0.246$, $A^2 = 0.509$).

The outflows with the highest confidence level in the selected driving source drive fainter outflows than those with the lowest confidence, and the KS and AD tests disagree about whether or not they are drawn from the same parent sample ($p = 0.035$, $A^2 = 4.847$). That the lowest-confidence sources drive brighter outflow lobes can probably be accounted for if one considers that outflows from high-mass star forming regions and clusters have a much lower confidence level than those which are more isolated. One might also expect that the lower confidence sources would drive more asymmetrical outflows due to the typically larger number of potential sources (as was found
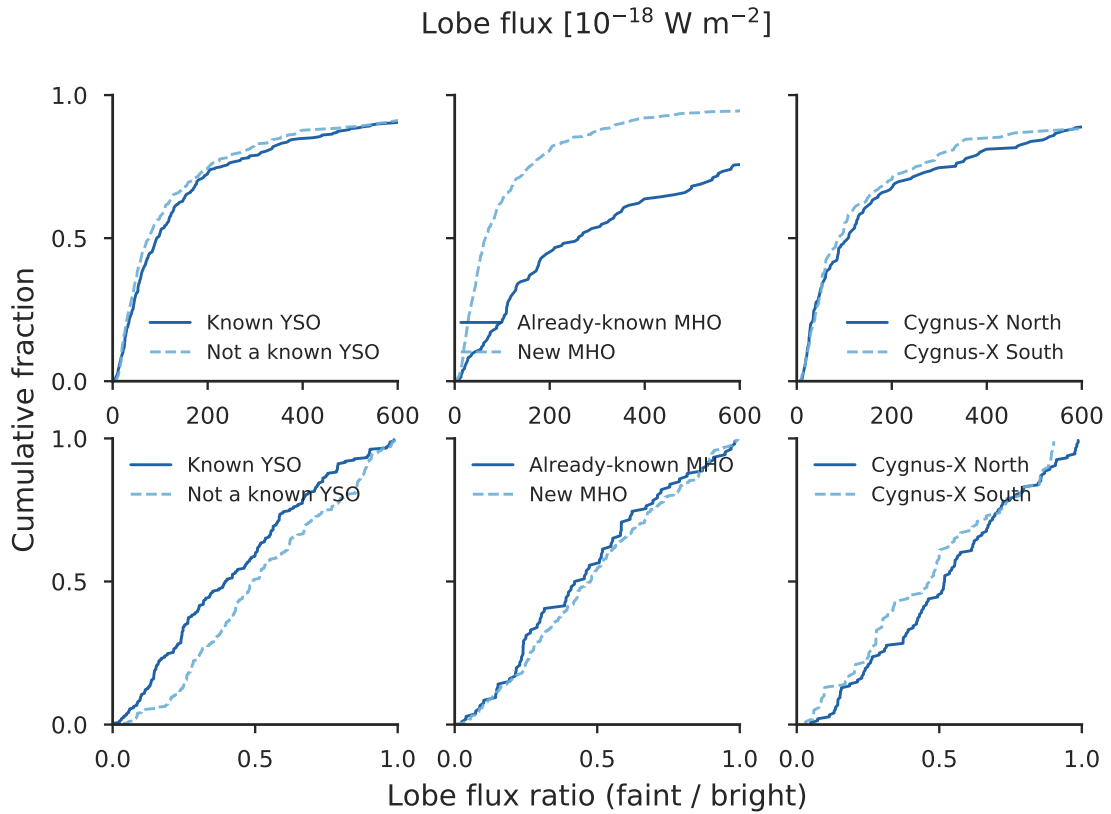
FIGURE 5.10: (Top row) Lobe flux and (bottom row) lobe flux ratio distributions. Each pairing is split by (left) whether or not the candidate driving source is known to be a YSO, (centre) whether the outflow was previously known as an MHO or is a new discovery, and (right) whether the outflow is located in Cygnus-X north or Cygnus-X south.

in Auriga and Cassiopeia), but instead it is the highest-confidence sources that seem to drive more asymmetrical outflows. The distributions, however, are both drawn from the same parent sample so the difference is not significant ($p = 0.010$, $A^2 = 2.629$).

In the left-hand panels of Fig. 5.10 the lobe fluxes appear from a visual inspection to be similar, and testing confirms that the outflows from known YSOs and those from unidentified YSOs are drawn from the same parent distribution (0.261, $A^2 = 0.877$). In the same way as for the length ratio distributions, the known YSOs preferentially drive asymmetrical outflows in terms of their fluxes, and the flux ratio distributions are drawn from different parent samples ($p = 1.79 \times 10^{-5}$, $A^2 = 14.126$). As with the lobe lengths showing that the newly discovered outflows are considerably shorter than the previously-known sample, the central panels of Fig. 5.10 show that the newly discovered outflows are also overwhelmingly fainter. The already-known outflows account for most of the very bright outflow lobes and the KS-test shows they are drawn from totally different distributions ($p = 6.68 \times 10^{-18}$, $A^2 = 58.599$). Conversely, the flux ratios are drawn from the same distribution ($p = 0.213$, $A^2 = 0.047$).

The luminosity distributions of the YSOs from Cygnus-X north and Cygnus-X south were found to be different in each region, with the YSOs in the north being typically brighter than in the south (Kryukova et al., 2014), assuming a common distance for all objects of 1.4 kpc. If the outflow

luminosity is correlated with the source luminosity (Caratti o Garatti et al., 2006), then one would expect to see the outflows in the north being brighter than those in the south. In fact, what is found in the right-hand panels of Fig. 5.10 is that the flux distributions in the two regions are the same ($p = 0.596$, $A^2 = -0.593$), implying that their luminosities at a common distance scaling of 1.4 kpc are also the same. This may suggest that either the source and outflow luminosities are not actually correlated, or that there is something different about the driving sources of outflows when compared the (much larger) population of YSOs that do not drive outflows. This will be investigated in more detail in Chapter 6. Similarly, although the flux ratios appear to be slightly different, with the outflows in Cygnus-X north being slightly more symmetrical, the difference is superficial and they are both drawn from the same parent sample ($p = 0.0828$, $A^2 = 1.512$).

5.2.5   Outflow asymmetry

In the same way as the asymmetry of outflow lobes was investigated in Chapter 4, Fig. 5.11 shows the length ratios R_L against the flux ratios R_F. The dashed lines take the same meaning as before, i.e., marking $R_L = 0.5$ and $R_F = 0.5$, with values closer to 1 representing more symmetrical outflows and values closer to 0 being the least symmetrical. In this plot, outflows from clustered environments are represented by darker blue squares, isolated outflows are shown with pale blue circles, and the larger the point, the greater the confidence level in the assignment of the driving source. In Table 5.1 the breakdown of the populations in each "box" is shown.

TABLE 5.1: Breakdown of the length (short over long) vs. flux (faint over bright) ratios for clustered vs. non-clustered bipolar outflows (corresponding to Fig. 5.11).

(a)	Clustered: 50	(b)	Clustered: 37
	Non-clustered: 60		Non-clustered: 56
	Total: 110		Total: 93
(c)	Clustered: 15	(d)	Clustered: 5
	Non-clustered: 18		Non-clustered: 19
	Total: 33		Total: 24

As was seen in Auriga and Cassiopeia, there is no direct or apparent correlation between the length and flux ratios for any given outflow. Most of the outflows are more symmetrical in their lengths, whilst the flux ratios are fairly homogeneously spread. Indeed, the proportion of outflows with $R_L > 0.5$ is the same in Cygnus-X (78 %, 203 objects) as in Auriga and Cassiopeia, so this could be universal. However, of those outflows with symmetrical lengths there is a slight preference for the fluxes in Cygnus-X outflows to be asymmetrical (55 % versus 45 %). This contradicts the findings in Auriga and Cassiopeia where the same majority of outflows have symmetrical fluxes.

In Fig. 5.12 the length ratio (short over long) against the ratio between the flux of the short lobe over the flux of the longer lobe is shown, in the same way as was done in Chapter 4 for Auriga and Cassiopeia with Fig. 4.9. The dashed and dotted lines take the same meaning as before, and again, the darker blue squares represent outflows from clustered environments whilst the pale
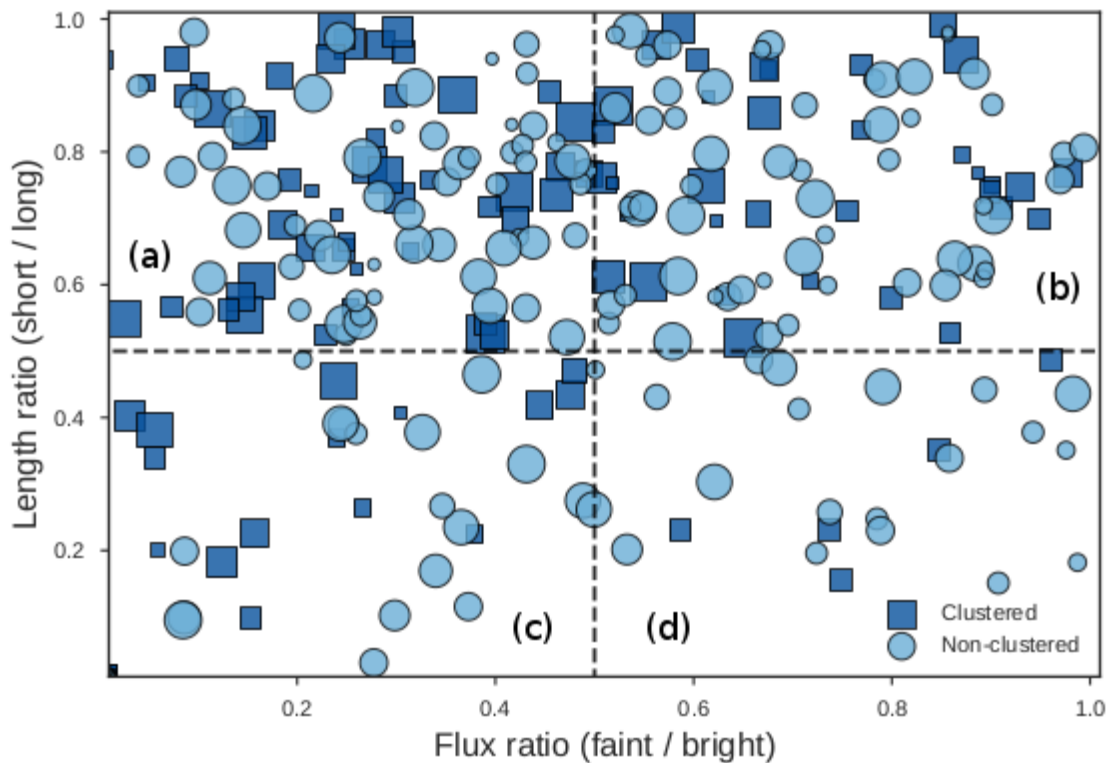
FIGURE 5.11: The ratio of lobe lengths (short side over longer side) against the ratio of fluxes (faint side over brighter side) for all bipolar outflows. The horizontal dashed line indicates $R_L = 0.5$ and the vertical dashed line shows $R_F = 0.5$.

circles denote more isolated outflows. Immediately it can be seen from this figure and the accompanying breakdown in Table 5.2 that there are many more outflows (66 %) with $R_F(^S/_L) < 0.5$ suggesting that a majority of the longer lobes are also the brighter ones. This is the opposite result to what was found in Auriga and Cassiopeia. Although there are more non-clustered outflows than clustered ones, the proportions are the same (68 % clustered and 65 % non-clustered with $R_F(^S/_L) < 0.5$). This is also in contradiction to what was found in Auriga and Cassiopeia, where the clustered and non-clustered outflows were segregated with a majority of clustered outflows having $R_F(^S/_L) < 0.5$ (58 %) and the majority of non-clustered outflows having $R_F(^S/_L) > 0.5$ (64 %). Considering that the clustered and non-clustered outflows are found in the same proportions in both regions, this is a curious result that will be discussed further in Chapter 6.

Of the most symmetrical outflows, i.e. those found in boxes (b) and (c), only 35 % are symmetrical in both length and flux, compared to the 49 % found in Auriga and Cassiopeia. Of the total number of outflows from clusters (being 107 objects), 35 % are in these two boxes (33 % in Auriga and Cassiopeia) but of the 153 isolated outflows, only 36 % are in these boxes (compared to 61 % in Auriga and Cassiopeia). By contrast, the most asymmetrical boxes, (e) and (h), contain the same proportion of outflows as in Auriga and Cassiopeia (13 %) but the split between clustered and isolated outflows is very different. In Cygnus-X, 14 % of the clustered outflows and 12 % of the isolated outflows are found in these two boxes, whilst in Auriga and Cassiopeia there was a far stronger preference for clustered outflows to be found than the isolated (29 % versus 3 %).
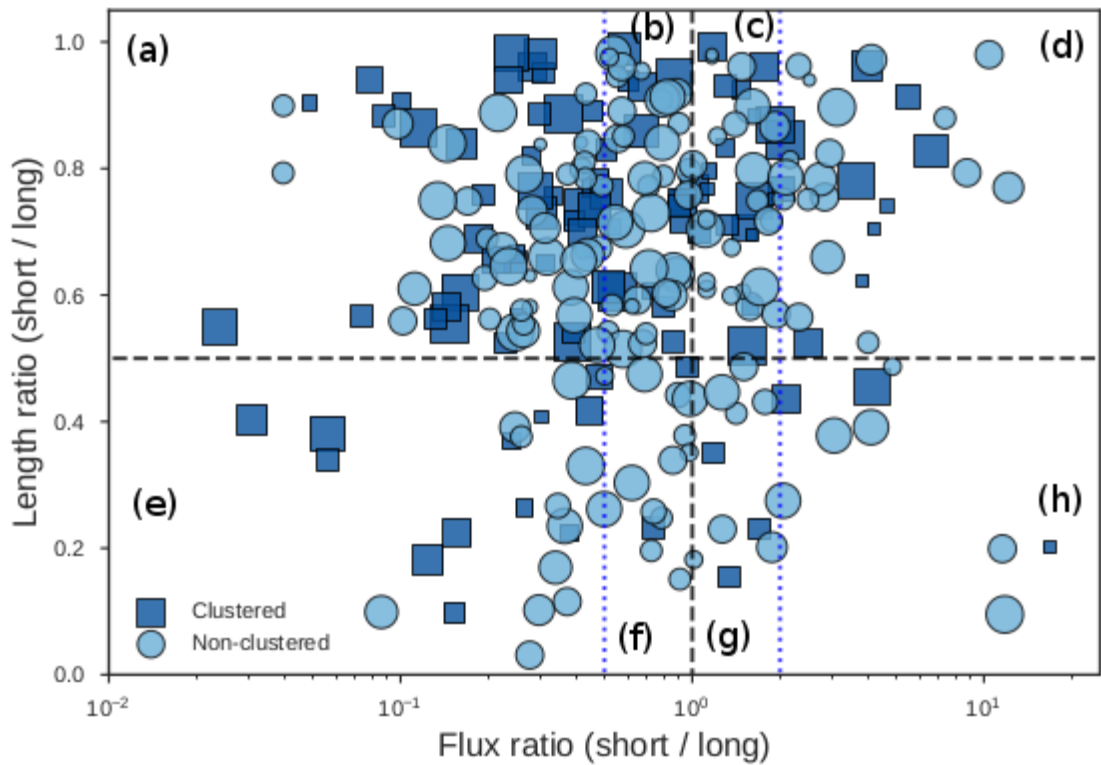
FIGURE 5.12: The ratio of the lobe lengths (short side over longer side) against the ratio of fluxes (flux of the short side over the flux of the long side) for all bipolar outflows. This relates the flux ratios to the length ratios. The dashed horizontal line indicates a length ratio of $R_L = 0.5$, the dashed vertical line a flux ratio of $R_F(^S/_L) = 1$. The blue dotted lines mark $R_F(^S/_L) = 0.5$ and $R_F(^S/_L) = 2$. The point sizes represent the confidence level in the chosen driving source, with larger points for higher confidence levels.

TABLE 5.2: Breakdown of length ratio (short over long) vs. flux ratios (short over long) for clustered vs. non-clustered bipolar outflows (corresponding to Fig. 5.12).

(a)	(b)	(c)	(d)
Clustered: 40	Clustered: 19	Clustered: 18	Clustered: 10
Non-clustered: 41	Non-clustered: 34	Non-clustered: 22	Non-clustered: 19
Total: 81 (31 %)	Total: 53 (20 %)	Total: 40 (15 %)	Total: 29 (11 %)
(e)	(f)	(g)	(h)
Clustered: 12	Clustered: 2	Clustered: 3	Clustered: 3
Non-clustered: 12	Non-clustered: 12	Non-clustered: 7	Non-clustered: 6
Total: 24 (9 %)	Total: 14 (5 %)	Total: 10 (4 %)	Total: 9 (3 %)

Summary of key results

- A total of 572 MHOs were identified in the Cygnus-X region, 465 of which are totally new discoveries. The remaining 107 MHOs are composed of 147 previously discovered objects.

- Of the 572 MHOs in Cygnus-X, 261 are bipolar and 152 are single-sided for a total of 413 outflows.

- The same proportion of MHOs are found in isolated locations (58 %) or clusters (42 %) as in the Auriga and Cassiopeia region.

- Fewer definitive driving sources were identified in Cygnus-X due to the relatively crowded field and higher extinction, but 82 % of the bipolar and 96 % of the single-sided outflows have candidate driving sources.

- No correlation was found between driving source variability and any other parameters in the two available epochs of the UKIDSS Galactic Plane Survey. It was shown that the variability cannot be determined between 2MASS and UGPS due to the difference in resolution between the two surveys.

- Of the 269 candidate driving sources whose SED slopes could be calculated using WISE, 20 % were found to have negative slopes (most likely YSOs) whilst 80 % had positive slopes (likely to be protostars)

- As in Auriga and Cassiopeia, the position angles are in agreement with a homogeneous distribution. However, this is not the case on the scales of individual star forming regions such as DR 21 and DR 15.

- The same proportion of outflows were located in multi-outflow systems (around 10 %). Outflows in Cygnus-X tend to be less straight than those found in Auriga and Cassiopeia.

- Cygnus-X also shows that single-sided and bipolar outflows should not be mixed into a common total length distribution.

- The typical outflow has a total length of 0.45 pc, and only 16 % of outflows are over a parsec in length. The typical outflow is also faint, with a total luminosity of $1.1 \times 10^{-3} \, \mathrm{L_\odot}$ at a distance of 1.4 kpc.

- Most outflows are slightly asymmetrical in their lengths, with a typical length ratio (short over long) of around 0.7, whilst the luminosity ratios (faint over bright) are more homogeneously distributed.

- Outflows from clusters tend to be longer and brighter than their more isolated counterparts.

- There is a bias in the sample of already-known MHOs showing that the vast majority of objects discovered in this work are considerably shorter and fainter than those that were previously known.

- There are 858 knots in the bipolar and single-sided outflows. Most of the gaps between subsequent knots are around 0.1 pc in length (1.2 kyr timescale at an assumed velocity of $80 \, \mathrm{km \, s^{-1}}$).

Chapter 6

Results, part III: Corrected distributions and multi-region comparison

> Author's note: In this Chapter, I present a more comprehensive analysis of the data obtained from the UWISH2 survey, and compare the results to those from earlier surveys. This work was undertaken in collaboration with Dirk Froebrich at the Centre for Astrophysics and Planetary Science, at the University of Kent and was carried out from 2016 – 2018. The methods used to obtain the results are discussed in Chapter 3.3 while the discussion of the results will be presented in Chapter 7. This work will be published in Makin and Froebrich (2018b) (*in preparation*).

6.1 Distance correction

In order to investigate whether or not the common distances used in Chapter 4 and Chapter 5 were reasonable, it was first necessary to determine more accurate distances toward as many of the outflows as possible. Estimated distances toward 341 outflows (bipolar and single-sided, being 82 % of 413) and 105 individual knots (66 % of 159) were obtained in Cygnus-X, and towards 49 outflows (66 % of 74) and 11 individual knots (46 % of 24) in Auriga and Cassiopeia. Table 6.1 shows the breakdown of the distances obtained for each region. The distribution of these estimated distances is shown as a function of position in the Galactic plane in Fig. 6.1, and summarised as a histogram in Fig. 6.2. In both regions, almost none of the outflows are found at the common distances we originally used, although most are located within 20 % of them. There is a significant fraction of outflows in both regions (about one-fifth) that are most likely found considerably closer to us than those distances (marked with pale triangles in Fig. 6.1).

In Auriga and Cassiopeia, the majority (82 %) of outflows have Bayesian distances larger than, but within 15 % of, 2 kpc. The maximum Bayesian distance in this region was a single object at 2.3 kpc, while the median at that range is 2.16 kpc. The 18 % of outflows closer than 2 kpc are all found at around 0.5 kpc. With the exception of this unexpected minority, the initial estimate of 2 kpc was a good one, particularly given the $\sim 5 - 10$ % overestimations in the Bayesian model.
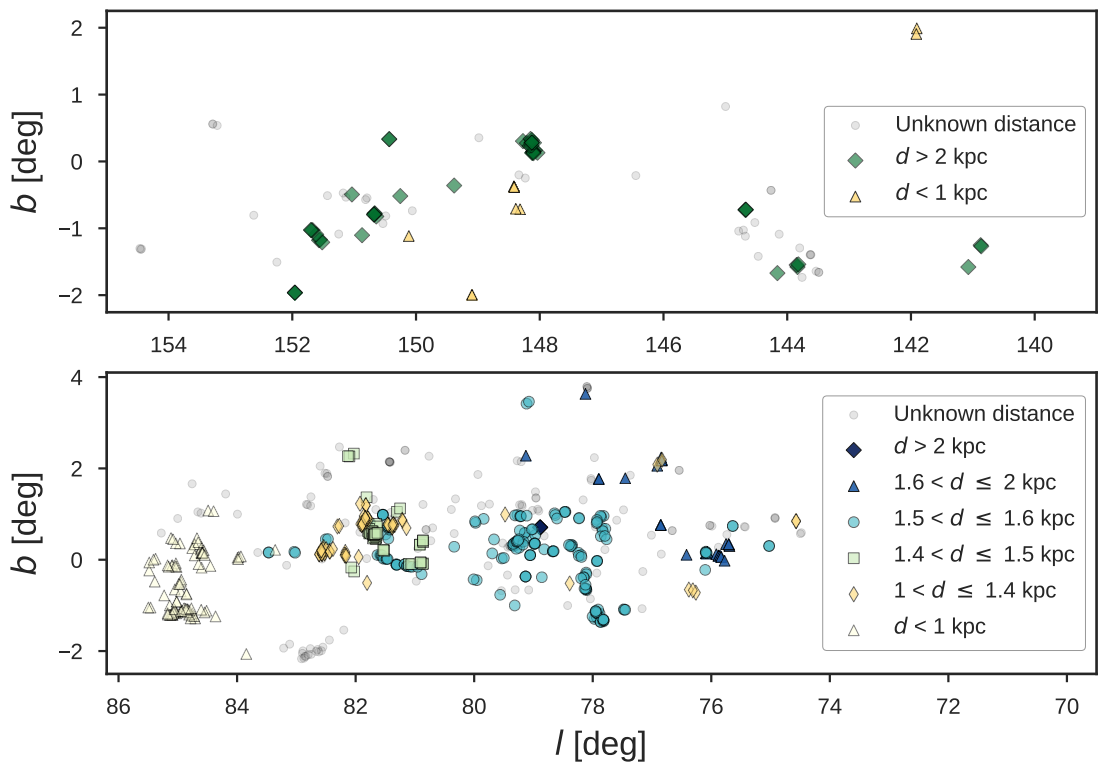
FIGURE 6.1: Outflow distances as a function of position in the Galactic plane for Auriga and Cassiopeia (top) and Cygnus-X (bottom). Both panels include bipolar and single-sided outflows, and individual knots where a distance could be assigned by association. Outflows with no estimated distance are denoted by light grey circles.
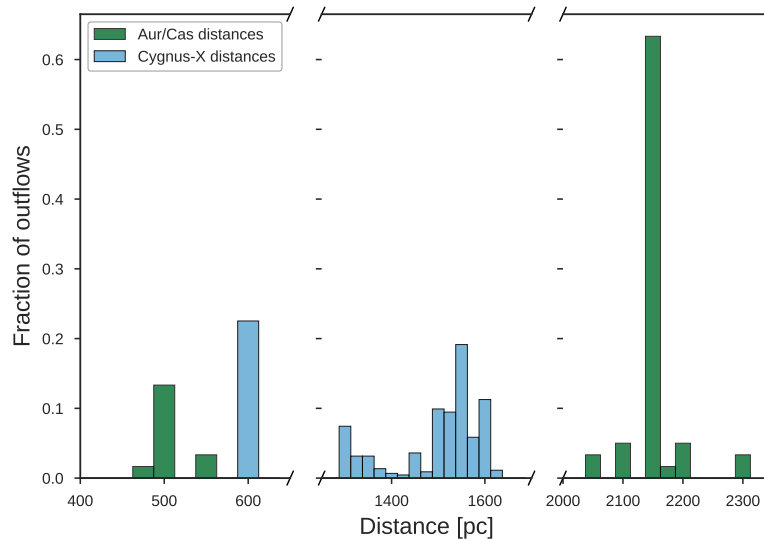
FIGURE 6.2: Histogram showing the distribution of estimated outflow distances in Auriga and Cassiopeia (dark green) and Cygnus-X (light blue). Both sets of data are normalised to the same total number of objects. The discontinuous x-axis excludes regions where there are no outflows. The two outflows from AFGL 2591 (Cygnus-X) at 3.33 kpc are not shown.

However, the fraction of objects located at this nearby distance is large enough to significantly influence the results that depend on the distance, given the small size of the sample. Similar results are found in Cygnus-X, where 21 % of the outflows are located in the well-studied HII region

W 80, which spans $\sim 3°$ on the sky. This region includes the North America nebula (NGC 7000), the Pelican nebula (IC 5070), and the Lynds dark cloud L 935 that separates them and obscures the stars responsible for the ionization of the region (Bally et al., 2014). A further group of 17 outflows around $l \sim 83°$, $b \sim -2°$ (shown as a clustering of grey circles in the lower left of Fig. 6.1) may also be associated with this region and located at a similar distance. The entire region suffers from high extinction, as found in the rest of W 80, and most of these 17 outflows are either very short, or are individual knots of emission, and all of them are excluded from the analysis.

TABLE 6.1: A breakdown of the distances (in kpc) toward outflows in the Auriga and Cassiopeia (left columns) and Cygnus-X (right columns). The numbers include all bipolar and single-sided outflows, but individual knots are excluded.

Auriga and Cassiopeia			Cygnus-X		
Distance (kpc)		No. of outflows	Distance (kpc)		No. of outflows
$d \leq 1.00$		9 (18.4 %)	$d \leq 1.00$		71 (20.8 %)
$1.95 < d \leq 2.05$		1 (2.0 %)	$1.00 < d \leq 1.35$		43 (12.6 %)
$2.05 < d \leq 2.15$		14 (28.6 %)	$1.35 < d \leq 1.45$		15 (4.4 %)
$2.15 < d \leq 2.25$		24 (49.0 %)	$1.45 < d \leq 1.55$		91 (26.7 %)
$2.25 < d \leq 2.35$		1 (2.0 %)	$1.55 < d \leq 1.65$		119 (34.9 %)
$2.35 < d$		0 (0.0 %)	$1.65 < d$		2 (0.6 %)
Total:		49 (100 %)	Total:		341 (100 %)

A handful of objects in W 80 have atypically large V_{LSR} measurements which results in distance estimates that are inconsistent with the images of the outflows (OF 064, $d = 9.05$ kpc; OF 206, $d = 5.30$ kpc; and OF 310, $d = 5.43$ kpc). In Fig. 4 of IF12b it was shown using the example of HH 211, scaled to different distances, that even a bright ($3.1 \times 10^{-3} L_\odot$ in the $1-0$ S(1) line of H_2) bipolar outflow becomes faint and hard to recognise as an outflow when placed at greater distances than $4-5$ kpc. The H_2 knots of these three objects appear bright and well defined, and the surrounding fluorescent material would not be visible in the NIR images at such large distances. Therefore, where the Bayesian distance is greater than 4 kpc but the outflow appears well-defined and bright in the NIR images, it is assumed that the V_{LSR} measurement "belongs" to an object unrelated to the outflow driving source, and the same distance as for the rest of the objects in W 80 (being 600 pc ± 12 %) is used instead.

When the distances are used to correct the lobe lengths, the fraction of very short objects (< 0.1 pc) increases in Auriga and Cassiopeia. Some of the longest outflow lobes were originally found in this region, but these are the objects that are in fact located much nearer to the Sun (at around 0.5 kpc) so the "tail" of very long outflow lobes disappears in the distance-corrected population. The same result is true for the 21 % of outflows located in the W 80 region of Cygnus-X. However, these shortened outflows are largely offset by the increase in length that results from most of the other outflows in the sample being projected further away from us. On the largest scale then, correcting the distances in Cygnus-X produced little observable effect, such that it is arguably justifiable to use a common distance toward all of the outflows. However, the effects of correcting the distances becomes more obvious when the Cygnus-X population is divided into sub-samples.
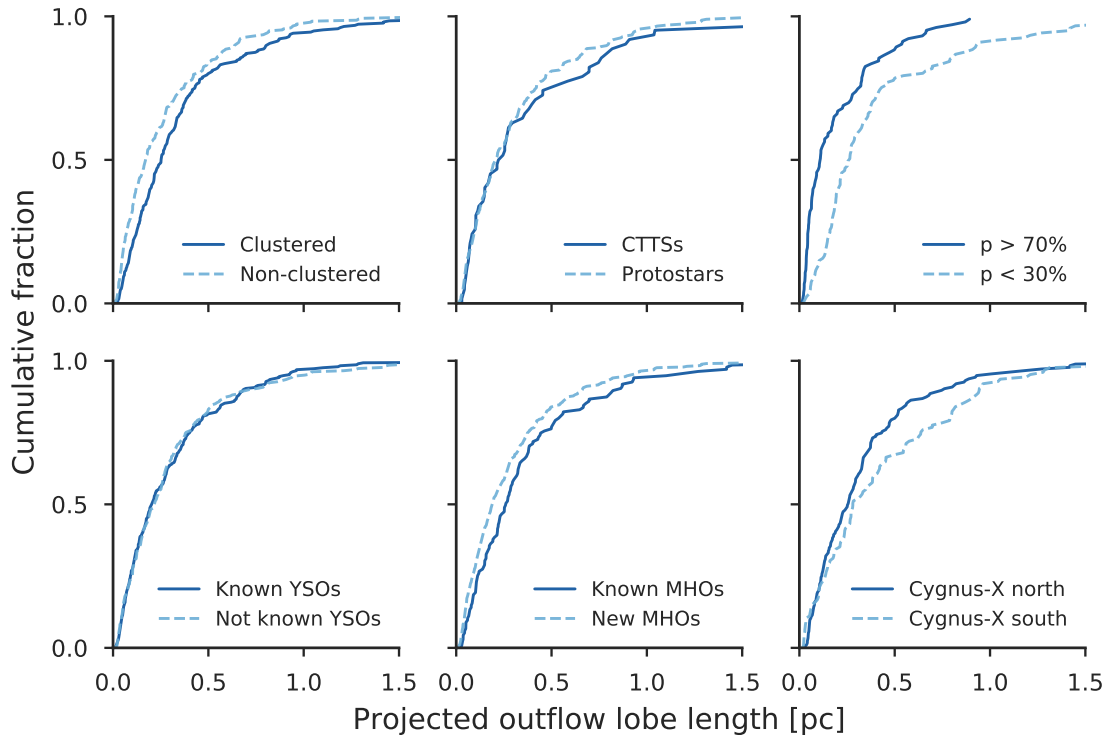
FIGURE 6.3: Projected lobe lengths, corrected with individual estimated distances. The splits used are the same as in Fig. 5.6 and Fig. 5.7.

Now that these distances have been obtained, the outflow length and luminosity distributions can be investigated and compared to those obtained from previous works.

6.1.1 Outflow lobe lengths revisited

In Fig. 6.3, the outflow lobe length distributions are plotted following correction for the individualised distances. The splits used are the same as those from Fig. 5.6 and Fig. 5.7. It can be clearly seen that although the figures appear superficially similar, there are some key differences. Following distance correction, there is no change in the result that the clustered and non-clustered outflows are drawn from different distributions ($p = 4.09 \times 10^{-4}$, $A^2 = 9.125$), and as before, the outflows from clusters are longer than those from isolated environments. The CTTSs and protostars are still most likely drawn from the same parent distribution ($p = 0.840$, $A^2 = -0.743$). Similarly, the outflows driven by known YSOs and objects not known as YSOs are also all drawn from the same parent distribution ($p = 0.977$, $A^2 = -0.922$), suggesting that the vast majority of the driving sources are young stars, even if they have not been identified as such. This is a more decisive result than was found using a common distance of 1.4 kpc. In Cygnus-X north versus Cygnus-X south, the samples were originally from different distributions, but now appear to be drawn from the same parent distribution ($p = 0.0425$, 2.993). However, it should be noted that the p-value is low and the A^2 value high, so this is not a decisive result.

Unlike the results of Chapter 5 where the greatest difference was in the sample of previously-known versus newly-discovered MHOs, the difference in the two samples has been greatly reduced
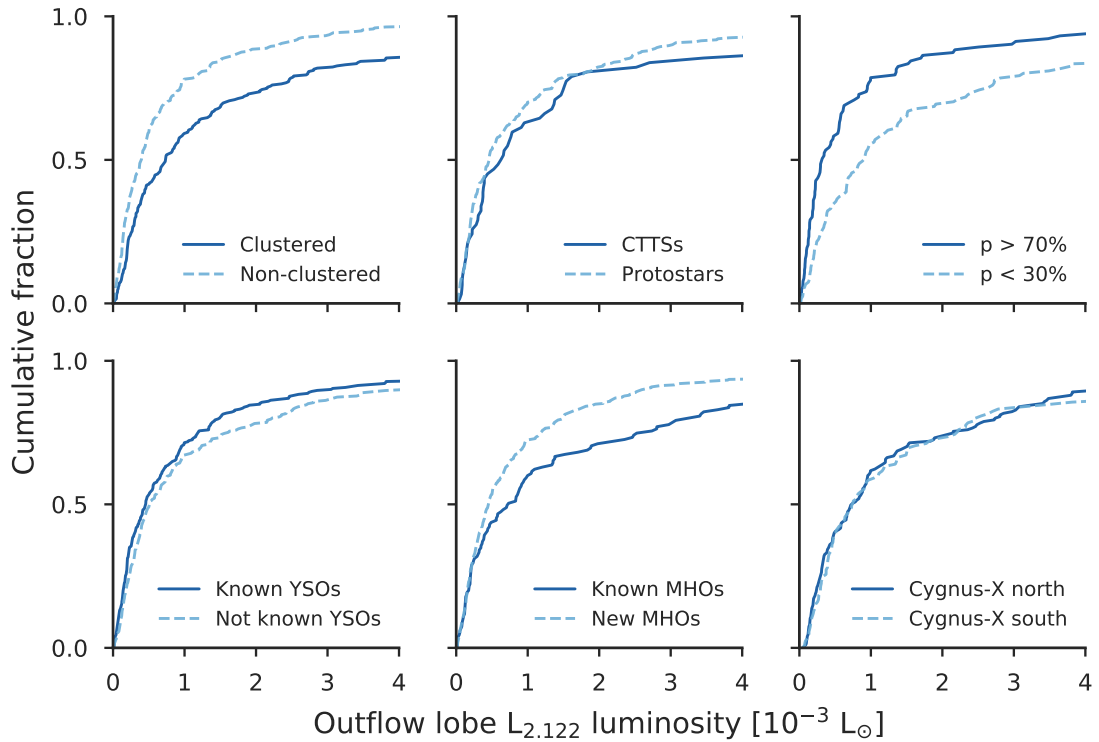
FIGURE 6.4: Outflow lobe luminosity distributions, corrected with individual distances. The splits used are the same as in Fig. 6.3. The x-axis excludes 46 outflow lobes from the right-hand side of each panel that are more luminous than $4 \times 10^{-3}\,\mathrm{L_\odot}$.

following distance correction ($p = 0.0138$, $A^2 = 3.348$). This is largely due to outflows in the nearby region of W 80 no longer being projected toward a much greater distance. However, for both the KS and AD tests, although the null hypothesis cannot be rejected, the results are close to the significance limits and thus do not represent convincing results. The non-clustered outflows and the newly discovered MHOs each have a peak of very short ($l < 0.2\,\mathrm{pc}$) lobes. These two sub-samples are most likely drawn from the same parent population with a probability of $p = 0.651$, $A^2 = -0.289$. The clustered outflows and previously known MHOs are likely also drawn from the same parent sample, with $p = 0.998$, $A^2 = -1.177$. This confirms that the newly discovered outflows tend to be found in isolated environments, and that they tend to be shorter than the previously discovered outflows. The greatest difference in the sub-sample splits now arises from the high- versus low-confidence samples ($p = 3.38 \times 10^{-9}$, $A^2 = 20.038$). However, this result mirrors the findings in Chapter 5 where this pairing was also found to be drawn from very different distributions. The low-probability outflow lobes are largely unchanged, except that the fraction of lobes shorter than $l < 0.1\,\mathrm{pc}$ has increased. Nevertheless, the high probability outflows are still overwhelmingly shorter than the low probability ones, and this has not changed.

6.1.2 Outflow lobe luminosities revisited

In Fig. 6.4 the outflow lobe luminosity distributions are plotted, using the individual distance estimates. The splits in this figure are the same as those used in Fig. 5.9 and Fig. 5.10. As with the

lobe length distributions, there are some changes following distance correction. There is even less of a statistical difference between the CTTS-driven and protostar-driven outflow lobe luminosities, with $p = 0.569$ and $A^2 = -0.020$ that they are drawn from the same parent sample. This adds further weight to the argument that the outflow properties do not depend on the evolutionary stage of the driving source. The highest p-value is found when comparing the outflow lobe luminosities from Cygnus-X north and Cygnus-X south, with $p = 0.786$ and $A^2 = -0.847$ that they are drawn from the same parent sample. Since Cygnus-X north is slightly further away than Cygnus-X south, correcting the distances has slightly increased the brightness of the very faint outflows from Cygnus-X north, and decreased the brightness of those in Cygnus-X south.

As with the lobe lengths, the distance-corrected lobe luminosities show that the outflows driven by confirmed YSOs and those not driven by confirmed YSOs are likely drawn from the same parent distribution ($p = 0.137$, $A^2 = 1.761$). This is the same result as was found in Chapter 5. As with the outflow lengths, correcting the distances toward individual outflows has greatly reduced the difference between the previously known MHOs and the newly discovered sample ($p = 6.64 \times 10^{-3}$, $A^2 = 6.031$). However, the although we cannot reject the null hypothesis in the KS test, the p-value is close to the significance level, and the A^2 value is greater than the critical value and the null hypothesis can be rejected for the AD test. Therefore, this is not a conclusive result, and vast majority of the newly discovered outflows are considerably fainter than in the previously-known sample. The outflows from clusters are still much brighter than those from isolated environments, and correcting the distances towards them does not change the fact that they are drawn from different parent samples ($p = 4.92 \times 10^{-6}$, $A^2 = 18.477$). The outflows from clusters coincide with the outflows with the lowest confidence in the correctly assigned driving source, and so it is unsurprising that the high- and low-confidence driving sources also produce outflows with distributions drawn from different parent samples ($p = 2.94 \times 10^{-5}$, $A^2 = 12.193$). This is unsurprising, but a more decisive result than when using the common distance of 1.4 kpc.

6.2   Comparison with previous works

6.2.1   Outflow total lengths and luminosities

Earlier studies historically measured outflows in terms of their total properties, i.e. the length from end-to-end for bipolar flows and from source-to-end for single-sided flows. It was shown in both Chapter 4 and Chapter 5 that the bipolar and single-sided outflows produce entirely different total length distributions, and that mixing them into a common distribution should be avoided. However, in order to compare the results from Cygnus-X and from Auriga and Cassiopeia with these older surveys, this is a necessity. Previous studies also made no corrections for the outflow inclinations, so this will also not be done for the results presented in this Chapter.

Figure 6.5 shows the total length against total luminosity in the $1-0\,S(1)$ line for outflows from Cygnus-X (pale blue circles), Auriga and Cassiopeia (green diamonds), Serpens and Aquila (from IF12b, purple triangles), and Orion A (from Stanke, McCaughrean, and Zinnecker (2002), gold
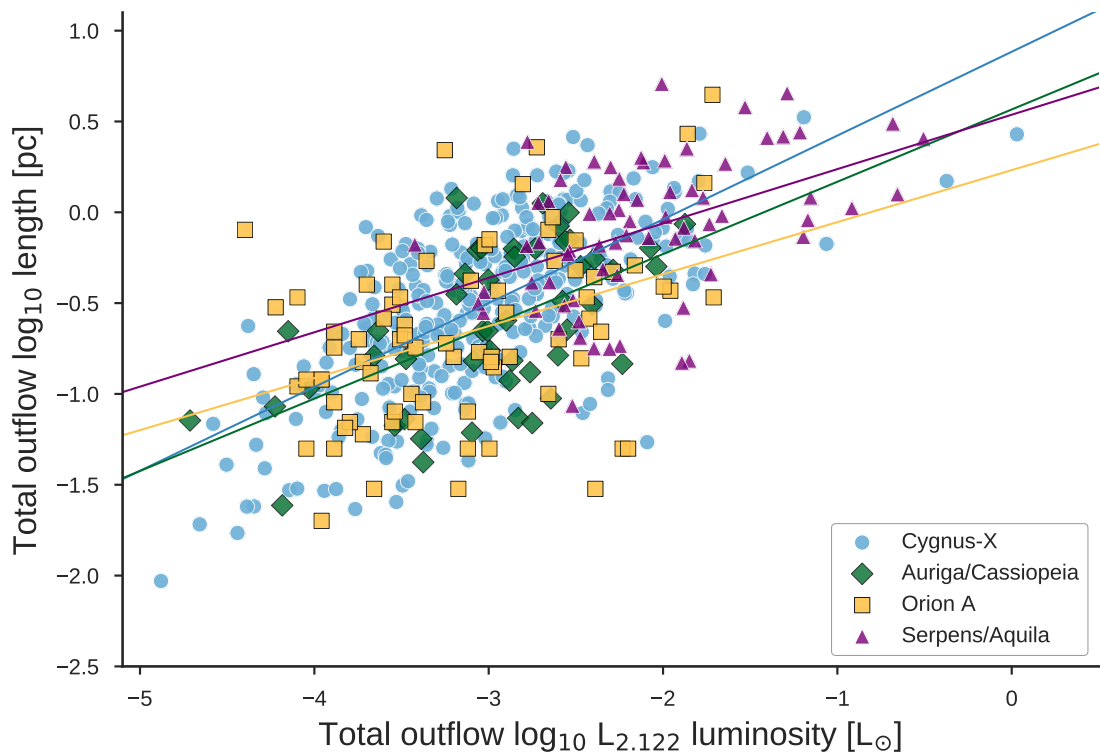
FIGURE 6.5: A plot of total outflow length against total outflow luminosity for Cygnus-X (pale blue circles), Auriga and Cassiopeia (dark green diamonds), Serpens and Aquila (purple triangles, data from IF12b), and Orion A (gold squares, data from Stanke, McCaughrean, and Zinnecker (2002)). The coloured lines represent the respective fits to each scatter plot.

squares). From Auriga and Cassiopeia, and Cygnus-X, the outflows without an individual estimated distance are excluded. In Serpens and Aquila, individual distances were determined toward each outflow using the reddening of local field stars (IF12b). These distances typically ranged from 3 to 5 kpc. In Orion A a common distance of 450 pc was used toward the outflows. Although later parallax measurements put the distance toward Orion A at closer to $389 \, \text{pc}^{+24}_{-21}$ (Sandstrom et al., 2007), this makes an insignificant difference to the distribution of the lengths and luminosities of the outflows in the region. Individualised distances were not used for Orion A. It can be seen that there is a weak linear correlation between the outflow total length and the outflow total luminosity. In Cygnus-X, the slope is 0.46 (correlation coefficient $R = 0.65$), and in Auriga and Cassiopeia the slope is 0.40 ($R = 0.56$). The slope is 0.30 in Serpens and Aquila ($R = 0.46$), and in Orion A it is 0.29 ($R = 0.40$). This suggests a power-law relationship between these two parameters of the form:

$$\text{length}_{(pc)} \propto L_{2.122}^{0.3...0.46} \tag{6.1}$$

In general, the scatter is significant, most likely due to the general uncertainty applicable to the obtained distances. Interestingly, there seems to be a maximum length, but not a maximum luminosity, for the outflows in this line of H_2 since the points turn off to form a plateau at the top right of the figure. However, as evidenced by the fact that HH objects can reach tens of parsec in length, clearly this is not the maximum outflow length that a forming star can produce. This will

be discussed further in Chapter 7.

The Serpens and Aquila outflows appear to be preferentially longer and brighter than those in the other regions. This is most likely due to the much greater distance at which the outflows are projected. Any fainter, shorter objects would simply be beyond our ability to detect as outflows at that distance. Thus, these outflows must represent a selection of the most luminous objects in that region. Perhaps then, the difference in the slopes is due to a real physical effect, and that relationship between length and brightness changes as the outflow grows. This shall be explored further in Chapter 6.3, but likely requires better-constrained distances in order to tighten the correlation and determine the precise nature of the relationship between these outflow parameters. One might also have expected the Orion A sample, being projected at the same distance as W 80 in Cygnus-X, and the nearby outflows in Auriga and Cassiopeia, to contain a sizeable fraction of faint, short outflows than are found, but these also seem to be largely missing from the sample.

6.2.2 Total length distributions

IF12b found the total length distribution to be governed by an exponential behaviour, following:

$$N \propto 10^{\,length\,[pc]\,\times\,\gamma} \tag{6.2}$$

Where N is the number of outflows, and γ varies depending on the width of the bins and the statistical correction applied. The same result is found for Cygnus-X and Auriga and Cassiopeia where the value of γ varies by region, and with the size of the errors applied to the distance. The fact that the length distributions are better fit by exponentials was also noted in F16 and M17 using common distances. Every region seems to contain a significant enough minority of long outliers that power-law fits are disfavoured.

In Fig. 6.6, the fit to the distribution for each region is plotted. In general, the Perseus west, Auriga and Cassiopeia and Cygnus-X populations have similarly steep distributions, suggesting a relatively high fraction of very short outflows (typically these are the single-sided outflows). Serpens and Aquila has the shallowest slope, and the fact that the Davis et al. (2009) sample in Orion A has a slightly steeper slope than the Stanke, McCaughrean, and Zinnecker (2002) sample suggests that the dearth of very short objects originally found by Stanke et al. was due mainly to the sensitivity of the survey. Correcting the distances toward individual outflows does not affect whether or not the distributions are governed by exponentials or power laws. However, the slope of the distribution depends heavily on the maximum boundary of the distribution, i.e., how many outliers are included that may skew it. It should be noted that up to 1 pc in length, the distributions have slopes in the region of -1.2 $\pm$ 0.2 (with the exception of Serpens and Aquila, whose slope is $\sim$ -0.5 in this range due to the lack of very short objects).

The fractions of outflows over 1 pc in length varies from region to region, and so does their influence on the slopes. In Orion A, 8 –9 % (Davis et al., 2009; Stanke, McCaughrean, and Zinnecker, 2002) of the outflows were parsec-scale. The Perseus west complex had 12 % (Davis et al., 2008), and in Serpens and Aquila the fraction was initially 10 % (IF12a) and up to 15 – 18 % following
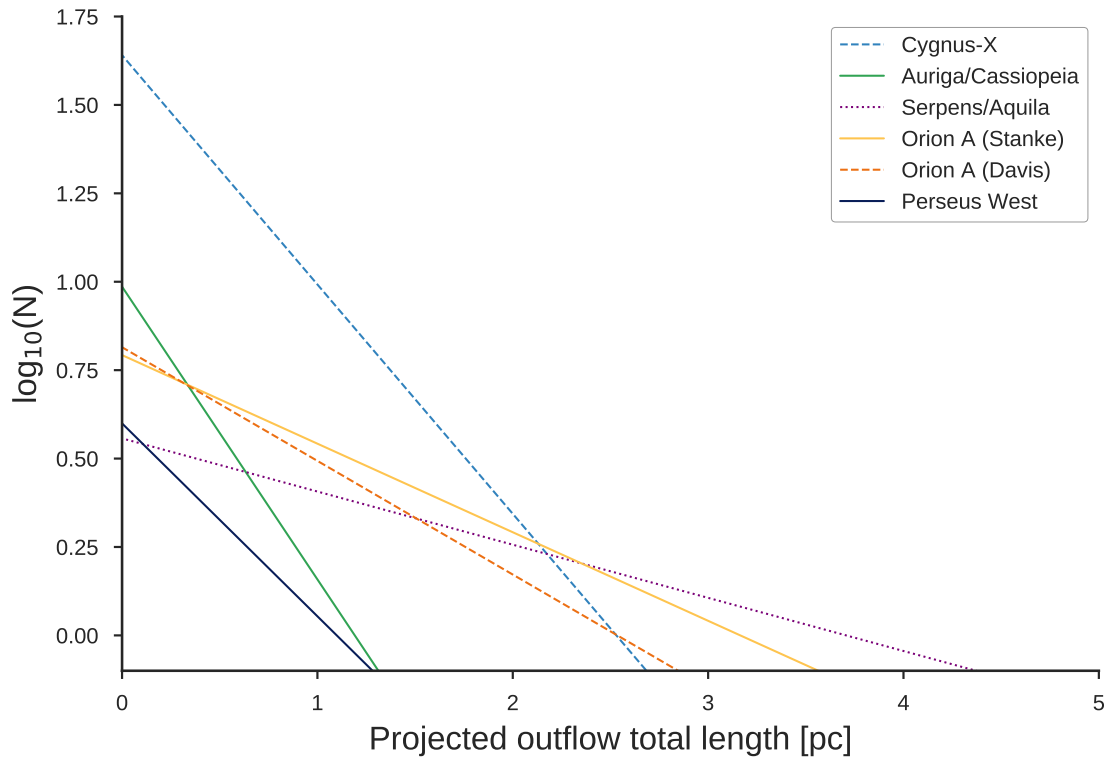
FIGURE 6.6: Total outflow length distributions. Bipolar and single-sided outflows are mixed together, and no corrections are made for outflow inclination. The Cygnus-X, Auriga and Cassiopeia, and the Serpens and Aquila lengths are all corrected for the individual outflow distances. The Orion A data used common distances of 450 pc (data from Davis et al. (2009) and Stanke, McCaughrean, and Zinnecker (2002)), and in Perseus west a common distance of around 350 pc was used (data from Davis et al. (2008)). The bins were 0.1 pc in width.

distance-correction (IF12b). In Auriga and Cassiopeia, the distance-corrected fraction of parsec-scale flows reduces to 4 % from the 5 %, due to the ~ 18 % of outflows located at 0.5 kpc (F16). The same was found in Cygnus-X, where originally 16 % of the outflows were found to be parsec-scale (M18), which is now revised to 13 % due to the correction of the W 80 sub-population.

TABLE 6.2: A table showing a comparison of total outflow length values for each region; (1) average slope value for the total length distributions in each region, and the 1σ error; (2) fraction of outflows in the region that are parsec-scale; (3) median outflow length in parsec. The historical data was obtained from: (a) IF12b, (b) Stanke, McCaughrean, and Zinnecker (2002), (c) Davis et al. (2009), and (d) Davis et al. (2008).

Region	Mean distribution slope $\bar{\gamma}$	Parsec-scale fraction	Median length [pc]
Serpens and Aquila[a]	-0.15 ± 0.06	15 − 18 %	0.89
Orion A (2002)[b]	-0.27 ± 0.06	8 %	0.20
Orion A (2009)[c]	-0.32 ± 0.04	9 %	0.22
Perseus West[d]	-0.52 ± 0.20	12 %	0.23
Cygnus-X	-0.63 ± 0.08	13 %	0.35
Auriga and Cassiopeia	-0.81 ± 0.25	4 %	0.22
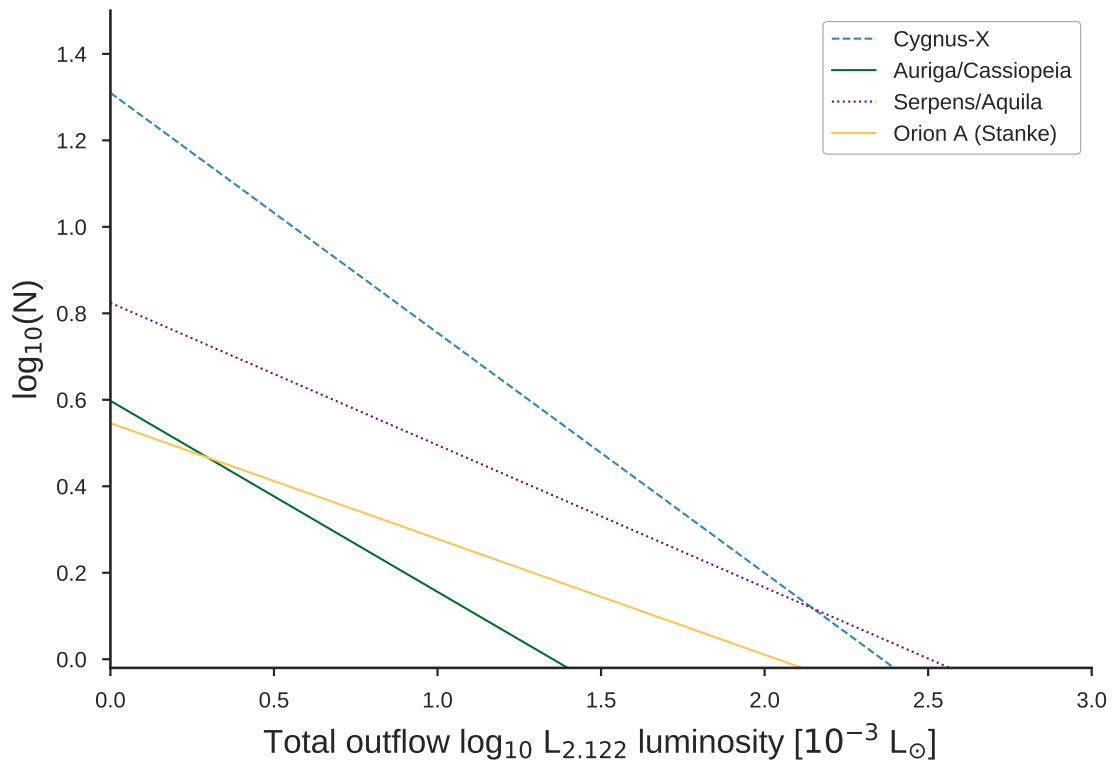
FIGURE 6.7: Total outflow luminosity distributions, composed of bipolar and single-sided outflows. The Cygnus-X, Auriga and Cassiopeia, and the Serpens and Aquila lengths are all corrected for the individual distances of the outflows. The Orion A data used common distances of 450 pc (data from Stanke, McCaughrean, and Zinnecker (2002)). The bin width is 0.1.

Fitting over a range of parameters allows us to constrain the typical distribution for each region. Since the slopes are largely dependent upon the bin width used, the distribution slope γ of each region was recorded across a range of bin widths, from 0.025 pc to 0.2 pc, in steps of 0.025 pc. These calculated γ values are averaged for each region and shown in Table 6.2 with the 1 σ errors.

6.2.3   Total luminosity distributions

In the Serpens and Aquila sample of IF12b, the outflow luminosities were found to follow a power law distribution of the form:

$$N \propto L_{2.122}^{\beta} \tag{6.3}$$

Where N is the number of outflows, and β varies depending on the width of the bins used and the statistical correction applied. Figure 6.7 shows the distributions of the total outflow luminosities for the four regions in which the outflow luminosities have been measured. The faintest outflows in Serpens and Aquila are of the order of $0.001\,L_{\odot}$, whilst in both Cygnus-X and in Auriga and Cassiopeia, there is a sizeable fraction of outflows that are up to two orders of magnitude fainter than this. This was demonstrated clearly in Fig. 6.5. The luminosity distributions form a straight line on a log-log plot where the values for β are relatively similar, ranging from $\sim$ -0.3 to -0.5.

TABLE 6.3: A table showing a comparison of total outflow luminosity values for each region; (1) average slope value for the total luminosity distributions in each region, and the 1σ error; (2) median outflow luminosity in units of $10^{-3}\,\mathrm{L}_\odot$. The historical data was obtained from: (a) IF12b, and (b) Stanke, McCaughrean, and Zinnecker (2002).

Region	Mean distribution slope, $\bar{\beta}$	Median $L_{2.122}$ [$10^{-3}\,\mathrm{L}_\odot$]	Range $L_{2.122}$ [$10^{-3}\,\mathrm{L}_\odot$]
Serpens and Aquila	-0.34 ± 0.12	5.96	0.38 − 311.97
Orion A (2002)	-0.29 ± 0.16	0.65	0.04 − 19.52
Cygnus-X	-0.53 ± 0.10	0.86	0.01 − 1071.11
Auriga and Cassiopeia	-0.51 ± 0.29	1.32	0.02 − 13.36

In the same way as was done for the outflow lengths, the slopes of the distributions (β) were calculated using a range of bin widths from 0.025 to 0.2 in steps of 0.025, and averaged for each region. The average slopes, $\bar{\beta}$ are listed in Table 6.3, along with the median, minimum and maximum luminosities for each region. It can be seen from these results that although Cygnus-X contains the outflows with the highest $L_{2.122}$ luminosity, the typical outflow in the region is relatively faint. The median luminosity seems to scale with the distance, such that the most distant region (Serpens and Aquila) has the brightest population of outflows, whilst the most nearby region (Orion A) contains the faintest. In Cygnus-X and Auriga and Cassiopeia, the minimum luminosities are so low due to the fraction of outflows located relatively nearby to us. It has been suggested previously that the total outflow H_2 luminosity is correlated with the bolometric luminosity of the driving source. In Stanke (2000), there appeared to be a correlation, if the Class I and Class 0 sources were considered separately. Froebrich et al. (2003) found no statistically significant correlation using Class 0 sources. However, Caratti o Garatti et al. (2006) found an empirical relation for Class 0 (and some Class I) sources of the form:

$$\log\left(L_{H_2}[L_\odot]\right) = (0.58 \pm 0.06)\log\left(L_{bol}[L_\odot]\right) - (1.40 \pm 0.04) \tag{6.4}$$

This relationship was derived using a small sample, and the assumption that the $1-0\,S(1)$ line of H_2 accounts for $10\,\%$ of the total H_2 luminosity. Therefore, in order to see if the relation holds for a larger statistical sample, the outflow vs. source luminosity plot from Caratti o Garatti et al. (2006) can be recreated for the Cygnus-X sample, as shown in Fig. 6.8.

In this case, the outflows plotted are those that have individual distances, and are associated with a known YSO from the Kryukova et al. (2014) sample ("KMH sources") so that the bolometric luminosities are obtained in a consistent manner. It should be noted that these bolometric luminosities have been obtained from the MIR magnitudes, corrected with the same distance as was applied to each corresponding outflow, and that whilst the bolometric luminosities have been corrected for extinction, the outflow luminosities have not. The outflows that do not have a source detected in the KMH 2014 catalogue, but are detected in Lumsden et al. (2013), are included on the plot ("MSX sources") and are corrected for the distances in the same way. The red line corresponds to the Caratti o Garatti et al. model (Equation 6.4). For consistency between the two samples, only
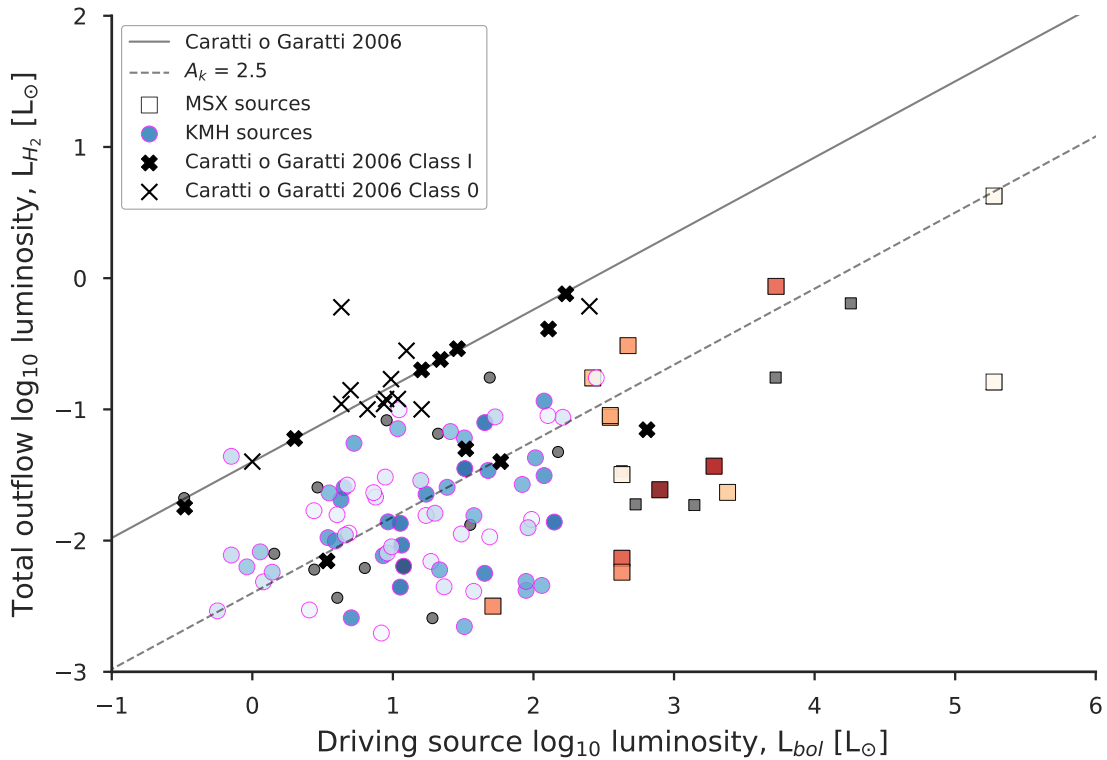
FIGURE 6.8: Outflow total H_2 luminosity vs. driving source mid-infrared bolometric luminosity for Cygnus-X. The solid red line shows the empirical relationship found by Caratti o Garatti et al. (2006), whose data points are shown with black crosses. Reddening has not been applied to the outflow luminosities; to effect an order of magnitude shift in the outflow luminosity would require an extinction in the K-band of $A_k \sim 2.5$ mag. The red dashed line therefore indicates where an outflow in agreement with the empirical model would lie if extincted by $A_k = 2.5$ mag. The square points are those outflows associated with objects in the MSX catalogue and circles represent known YSOs from the KMH catalogue (Kryukova et al., 2014). In both cases, the colours are represented from oldest (white) to youngest (red or blue respectively).

those outflows whose sources have detections in WISE have been shown.

It is clear that the degree of scatter in Fig 6.8 is significant, and cannot be accounted for simply by applying reddening to the outflows. Kryukova et al. applied a selection criteria of $A_V > 3$ towards all of their YSOs, but in the near-infrared this corresponds to an extinction of only ~ 0.3 mag (assuming the Mathis (1990) relation of $A_V = 9.3\, A_K$). This is not sufficient to shift any of the outflow luminosities into agreement with the empirical relation found by Caratti o Garatti et al. To effect an order of magnitude shift in the luminosity of the outflows would require $A_K = 2.5$ mag ($A_V \sim 25$ mag, as found e.g. in DR 21), and the majority of outflows would require an even higher A_K than this. The dashed line in the figure shows where objects in agreement with the empirical relationship would lie on the graph if an extinction of $A_K = 2.5$ mag were applied to them. In other words, objects below this line would require an $A_V > 25$ mag be applied to the outflow luminosity in order to shift it into agreement with the Caratti o Garatti et al. model. Clearly this would not be possible, since the outflows would be so heavily extincted that they would hardly be observable. The same scatter was also found in Serpens and Aquila (IF12b).

It should also be considered that points may be scattered along the horizontal axis if the driving source is part of a binary or a small cluster, or if it is a variable object that was undergoing an outburst event during imaging. If the luminosity of the driving source is overestimated because of these factors, then the points could be scattered to the right of the line showing the Caratti o Garatti et al. model. It is most likely, given the general crowding in the Cygnus-X field, and the often large variations in extinction across the region, that most of the points should be scattered below and to the right of the line. However, discovering the extent to which the points are scattered and for which reasons would require follow-up observations of individual objects, and thus is beyond the scope of this work to determine. Since the driving sources in the Caratti o Garatti et al. study were typically younger (i.e., mainly Class 0) it was possible that the fact that the majority of driving sources and outflows are not in agreement with the empirical model could represent an evolutionary trend. However, it can be seen from the homogeneous mixture of older and younger stars in the KMH and MSX samples that there is no visible correlation between the evolutionary stage of a protostar and the luminosity of its outflow.

6.3 The outflow length-luminosity relationship

As has already been shown, there is a linear relationship between the $\log_{10}$ length of an outflow (in parsec) and its $L_{2.122}$ luminosity. However, the causes for this are not clear. The relative dependence of outflow lengths and luminosities upon other parameters can therefore be investigated.

6.3.1 Driving source evolution

Stanke (2003) proposed that Class 0 protostars drive outflows that quickly grow to parsec-scales, and then become shorter and fainter over time as the driving source evolves. It was therefore expected that longest (parsec-scale) and brightest of outflows would be driven by Class 0 sources, that CTTSs would drive the shortest, faintest outflows, and that Class I sources would drive the outflows of intermediate lengths and brightness. However, this was not reflected in the results from either the Cygnus-X, or the Auriga and Cassiopeia samples.

Figure 6.9 plots the outflow lobe luminosities and projected lobe lengths against each other as a function of evolutionary stage. In order to be able to consider the Auriga and Cassiopeia sample, a more detailed split of the population using α is used than simply splitting into protostars / YSOs:

- Class II objects, where $\alpha < -0.3$,

- Flat spectrum objects, where $-0.3 < \alpha < 0.3$ (Greene et al., 1994),

- Class I objects, where $\alpha > 0.3$,

- Potential Class 0 objects.

If there were indeed an evolutionary trend to be found, the flat spectrum sources should lie between the Class I and Class II objects in length and luminosities. It should be noted that very few of the

(a) Auriga and Cassiopeia   (b) Cygnus-X
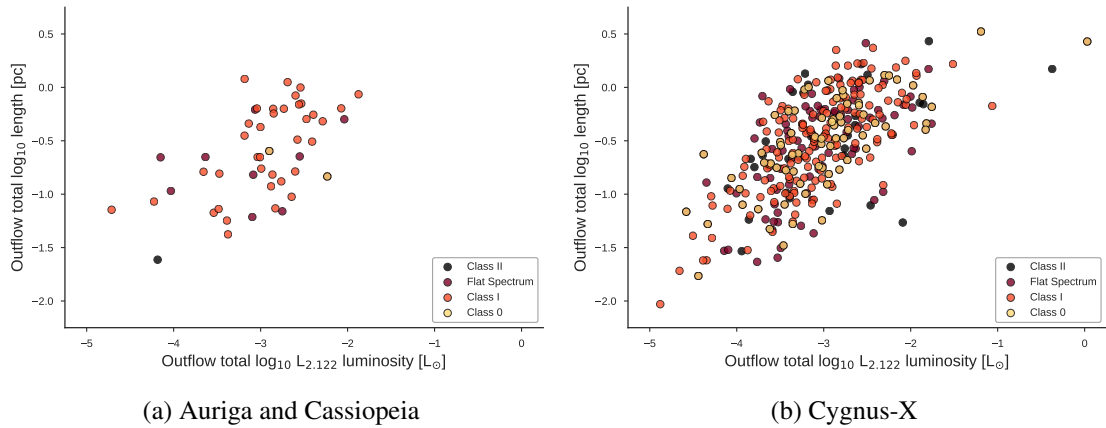
FIGURE 6.9: A scatter plot showing the $\log_{10}$ total outflow luminosities against the $\log_{10}$ projected total outflow lengths. The scale of both plots is the same in order to highlight the difference between the two regions. The scatter point colours correspond to the evolutionary stage of the driving source as determined from WISE data.

driving sources are confirmed to be Class 0 sources, thus "Class 0 sources" for the purposes of these plots are approximated as those which are undetected in the near-infrared or WISE, but have point-source detections in AKARI FIR and/or BGPS.

The Orion A sample of outflows is comparable in size to the Auriga and Cassiopeia population. However, it is inconclusive if the results from these two regions are in agreement with each other, as summarised in Table 6.4 where the average total properties of the outflows in each region are presented. It can be clearly seen in the Orion A column that there is a tendency for outflows to decrease in length and luminosity as the driving source evolves. However this result is not seen in Auriga and Cassiopeia, where few outflows reach parsec-scales (all of which are driven by Class I sources) and the brightest outflows tend to be driven by Class I sources, not Class 0. It is also not reflected in Cygnus-X, where the Class II sources drive, on average, brighter and longer outflows than their less evolved counterparts. Given the number of outflows driven by Class II sources that are longer than 1 pc and brighter than $10^{-3}\,\mathrm{L_\odot}$ in Cygnus-X, one cannot reasonably conclude that Class II outflows must necessarily be short and faint in H_2.

Indeed, with the statistically larger Cygnus-X sample, not only was the expected striation between evolutionary stages from Orion A not found, the very shortest and faintest outflows are driven by Class I or potential Class 0 stars, not by Class II objects. This lack of correlation between evolutionary stage and the lengths and luminosities of the outflows suggests that the observed trends in Orion A may simply be the coincidental result of using a relatively small population (being 76 outflows, 8 of which were Class 0 sources). Since the outflows in Cygnus-X and Orion A are longer and brighter (in general) than those from Auriga and Cassiopeia, where the former are high-mass regions and the latter is low-mass, it is likely that the observed differences have less to do with the evolutionary stage of the driving source and that they depend more on other factors.

TABLE 6.4: Summary of the total lengths and luminosities of outflows from the Orion A molecular ridge (data from Stanke (2003)), and from UWISH2 for Auriga and Cassiopeia, and Cygnus-X. In Orion A, the classifications of Class II, Class I and Class 0 were used, whilst in Aur/Cas and Cygnus-X the Flat Spectrum class of sources were included. No average values can be calculated for Class II objects in Aur/Cas since only one object falls into this category.

	Orion A	Aur / Cas	Cygnus-X
Average total projected lengths [pc]			
Class II	0.3	–	0.5
Flat Spectrum	–	0.06	0.2
Class I	0.6	0.3	0.4
Class 0	0.8	0.01	0.1
Average total $L_{2.122}$ luminosities [$10^{-3}\,L_\odot$]			
Class II	2.5	–	14.0
Flat Spectrum	–	0.5	4.2
Class I	10	1.5	2.1
Class 0	25	0.3	5.6

6.3.2   Source luminosity

The RMS survey found high-mass, high-luminosity YSOs and UCHII regions. If there were a correlation between length or luminosity of the outflows, and a driving source associated with one of the RMS objects, this would imply a potential dependence on the driving source luminosity (and hence, mass). About 10 % of the driving sources in both the Auriga and Cassiopeia, and Cygnus-X regions are associated with RMS sources from the Lumsden et al. (2013) catalogue. These are therefore plotted in Fig. 6.10 (a), where the outflows from both regions are included (pale grey circles) and those objects with an associated RMS object are over-plotted in blue. It can be seen that longest, and particularly the most luminous, outflows are preferentially driven by sources detected in the RMS survey. Unfortunately, determining luminosities for the remaining driving sources to a similar accuracy as the RMS survey is far beyond the scope of this work. However, for outflows where the selected driving source has a luminosity from the YSO catalogue of Kryukova et al. (2014) or from Lumsden et al. (2013), we can use these as a proxy indicator as shown in Fig. 6.10. Only those objects with an associated detection in one of these two catalogues are plotted, and the colour of the points corresponds to the normalised source luminosity. On this scale, 1 corresponds to the luminosity of AFGL 2591. This plot excludes most of the outflows from Auriga and Cassiopeia, and those from the W 80 region, since these were not covered in the Kryukova et al. (2014) survey.

It can be seen from Fig. 6.10 (a) that the MSX-associated sources, and the rest, occupy largely the same space in terms of the outflow lengths. This suggests that the luminosity (and hence mass) of the driving sources may not have a strong influence on the overall length of the outflow. By contrast, the very bright objects are preferentially driven by MSX-associated sources. When taken a step further in Fig. 6.10 (b) where the colour of the points corresponds to the normalised driving

(a) MSX sources

(b) By source luminosity
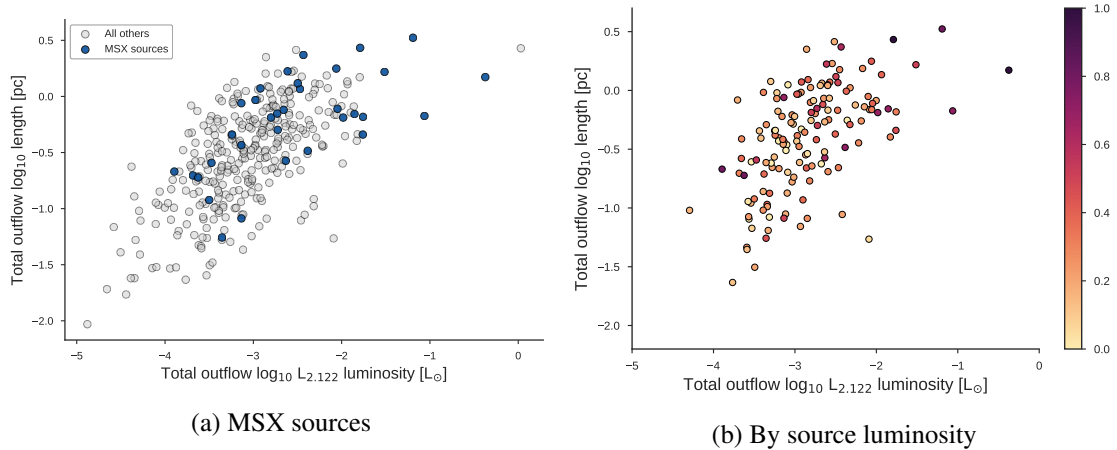
FIGURE 6.10: A scatter plot showing the $\log_{10}$ total outflow luminosities against the $\log_{10}$ projected total outflow lengths. In (a) the entire Cygnus-X population is split by whether or not the outflow is associated with an MSX object (either YSO or UCHII region). In (b) only those outflows with source luminosities from Kryukova et al. (2014) and Lumsden et al. (2013) are shown. The colours scale with the $\log_{10}$ luminosity of the driving source, corrected to the same distance as used for each corresponding outflow, and are normalised.

source luminosity (from Kryukova et al. (2014)), we see that the low-luminosity driving sources may occupy a different region of the graph than the higher-luminosity sources. However, given the small number of high-luminosity sources on this figure, any apparent correlation between the luminosity of the driving source and either the length or luminosity of the outflow, is more likely to be the coincidental result of small number statistics. That being the case, the fact that there seems to be a limit on the length of an outflow, and the fact that no low-luminosity sources drive extremely luminous outflows, suggests that despite the two parameters being correlated, they are governed by different mechanisms.

6.3.3 Environmental factors

As outlined in Chapter 2.9, the distribution of mass in Cygnus-X is not homogeneous, and the entire region has a different composition than Auriga and Cassiopeia, which is low-mass and sparsely populated. Therefore, it behoves us to also investigate whether there are any differences between the sub-regions of Cygnus-X, in addition to the differences between Auriga and Cassiopeia. In this way, it should be possible to confirm or rule out the differing environmental factors as drivers of the differences in the outflow parameters. In Fig. 6.11 the cumulative fractions of outflows are shown as a function of their environment. The four sub-regions of Cygnus-X used are; W 80, Cygnus-X north, Cygnus-X south, and the "remainder", i.e. those outflows in Cygnus-X not found in the previous three sub-regions. It should be noted that there is no statistically significant difference in the spread of α values in each sub-region so each region can be considered to contain driving sources at similar evolutionary stages.

Figure 6.11 (a), in which the projected total lengths are plotted, shows that the distributions of outflow lengths are significantly different between each of the different environments. Although it has already been shown that the outflows in Auriga and Cassiopeia are typically shorter than
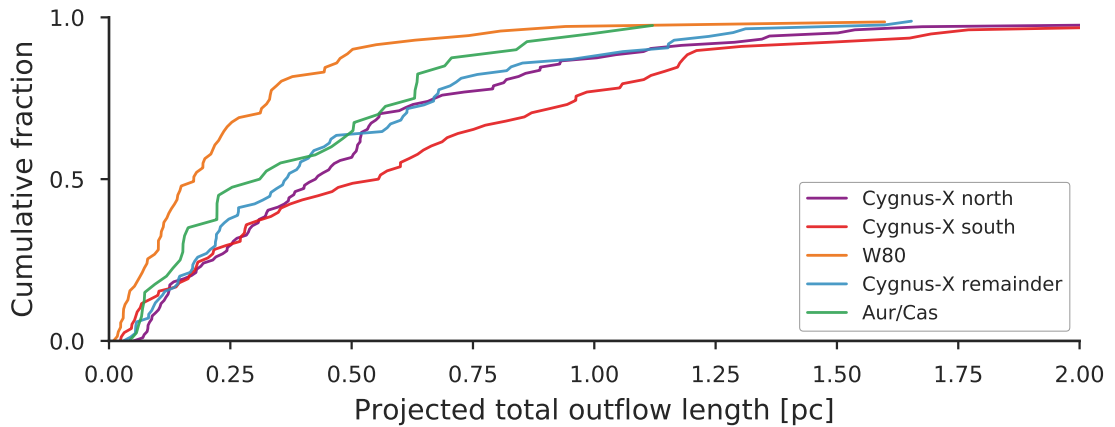
(a) Outflow total length
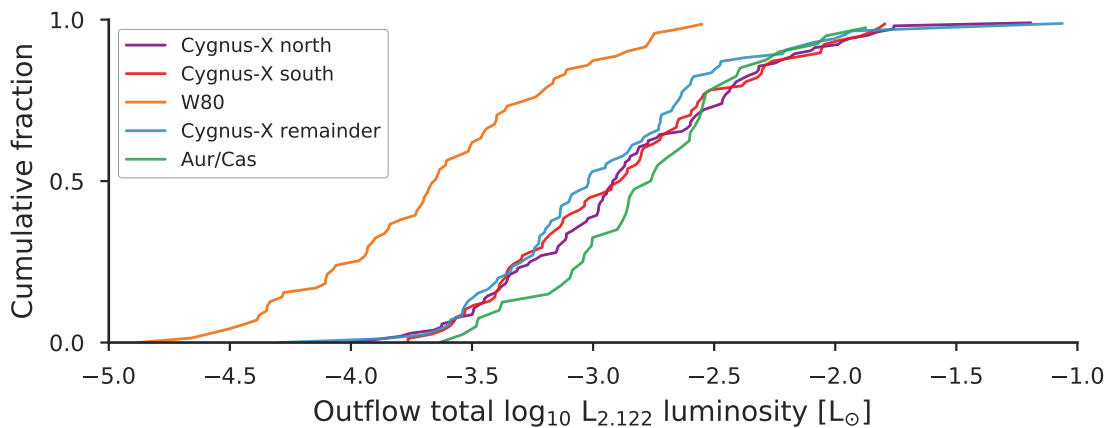
(b) Outflow total luminosity

FIGURE 6.11: Cumulative distribution functions showing the outflow total lengths (a), and luminosities (b), corrected for the individual distances, for each of the four sub-regions in Cygnus-X, and the sample from Auriga and Cassiopeia. The samples are distance-limited so that outlying objects at vastly different distances from the majority of outflows in each region are not included.

those in Cygnus-X, the outflows from W 80 are shorter still. This cannot be accounted for simply by considering the very nearby distance of W 80, since if the distributions were the same and only scaled with distance, then the Auriga and Cassiopeia outflows should be longer than those from all regions in Cygnus-X. For the same reason, it can be concluded that the outflows in Cygnus-X south are the longest in the sample, since the range of distances in Cygnus-X south is largely the same as those in the "remainder" sample. By contrast, in Fig. 6.11 (b) it can be seen that the distributions are not significantly different, suggesting that the environment may be less important in the overall luminosity of the outflows. Since the luminosity scales with distance squared, it is unsurprising that the distributions should be largely arranged in the order of distance of the outflows. However it should be noted that if the distance were the only governing factor then, again, the Auriga and Cassiopeia outflows near 2 kpc distance should be much brighter, as would those from Cygnus-X south and the "remainder". If we take the "remainder" sample to be representative of the general population in Cygnus-X, then it can be suggested that the outflows in Cygnus-X south are typically
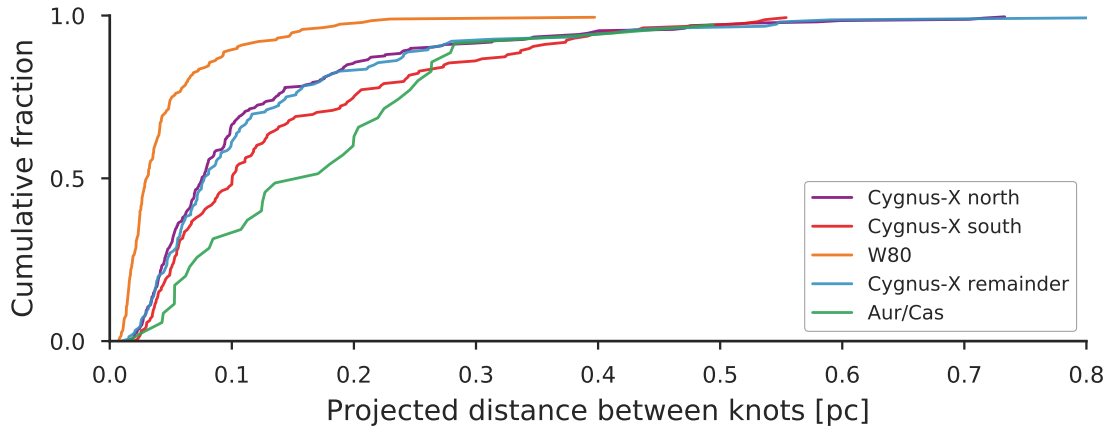
FIGURE 6.12: A cumulative distribution function of the lengths of gaps between subsequent outflow knots. The Cygnus-X population is split by sub-region, and only the gaps from outflows with an individual distance estimate are included. The x-axis is truncated at 0.5 pc, which excludes 18 knot gaps from the Cygnus-X region which are longer than this. All samples are distance-limited to exclude outflows at considerably different distances from the majority in each region.

brighter, and that the outflows from Cygnus-X north (projected ~ 200 pc closer to us) are therefore the brightest in Cygnus-X.

6.4 Outflow knots

6.4.1 Gaps between subsequent knots

Figure 6.12 shows the cumulative distributions of the distance-corrected gap lengths between subsequent outflow knots, and in Table 6.5 the typical knot gap properties from each of the sub-regions are also summarised. It can be immediately seen that the knot gaps are very short in W 80 (median gap length of 0.03 pc) when compared to the gaps from Auriga and Cassiopeia (median gap length 0.10 pc). Therefore, although the outflows themselves are similarly short in these two regions, and the lengths of the gaps have a similar range, the typical outflows in Auriga and Cassiopeia must have fewer detected knots per outflow length than their counterparts in W 80. Indeed, the lengths of the knot gaps in Auriga and Cassiopeia are most comparable to those from Cygnus-X south.

Cygnus-X south has the longest gap between subsequent knots, and the typical outflows in this region have slightly longer gaps than those from the other regions in Cygnus-X. Two objects in this region have been excluded since they are projected at much larger distances. The first is an outflow which has a gap length of 1.492 pc (OF 585) and the distance for this object is highly uncertain. The outflow appears to cross HH 166, which has a maser parallax distance of 3.3 kpc, but the Bayesian distance is only 1.6 kpc. Since OF 585 is very faint, it is not clear if it originates from the same cluster as HH 166 (and hence at 3.3 kpc), or if it is is at a much closer distance and projected onto HH 166 along the line of sight. The distance of 3.3 kpc has been assumed, which results in a gap length of 1.49 pc, but if it were at 1.6 kpc from us the gap would be only 0.3 pc in

TABLE 6.5: A table presenting the typical distance-corrected gaps between subsequent knots in the outflows. The Cygnus-X sample is spit by sub-region. Only knot gaps for outflows that have an individual distance estimate are included.

| | | Gap lengths [pc] | | |
Region	No. of gaps	Median	Mean	Range
Auriga and Cassiopeia	61	0.11	0.14	$0.015 - 0.494$
Cygnus-X overall	758	0.07	0.11	$0.007 - 1.492$
W 80	188	0.03	0.05	$0.007 - 0.397$
Cygnus-X north	258	0.08	0.12	$0.013 - 0.733$
Cygnus-X south	160	0.10	0.16	$0.020 - 1.492$
Cygnus-X remainder	152	0.08	0.12	$0.009 - 0.824$

length and thus it has been excluded from the figure. The longest gap in Cygnus-X south would then be comparable with the maximum values from Cygnus-X north. Between Cygnus-X north, and the remainder of the Cygnus-X outflows there is no statistically significant difference in the lengths of the subsequent knot gaps.

In the distance-corrected sample, there remains no statistically significant difference between knot gaps from outflows originating in clusters, and those that are isolated. The distance-corrected sample was also split according to the driving source evolutionary stages (in this case, Class II, flat spectrum and Class I objects) as shown in Fig. 6.13 to investigate if the evolutionary stage has an effect upon the gap lengths. It can be seen that there is no significant difference between the knot gap distributions in any of the sub-groups, with the exception of the Class I population from Auriga and Cassiopeia. In that subgroup, the median and mean gap lengths (0.13 pc and 0.16 pc respectively) are double the values of the flat spectrum sources in the same region (0.06 pc and 0.09 pc respectively, which are about the same as those from the Cygnus-X Class I and flat spectrum samples). The Class II objects in Cygnus-X typically have knots that are somewhat closer together (median 0.05 pc).

6.4.2 Knot luminosities

In F16 and M18, it was shown that the distributions of fluxes from the individual knots were better fit by exponentials than by power laws. This was primarily due to the fraction of very bright outliers in each region being higher than expected in a power law distribution. Furthermore, no significant difference was found between the fluxes of knots from protostars and YSOs, or between outflows originating from clusters or isolated environments. These distributions showed, however, that the completeness limit for detecting H_2 knots is around 10^{-18} W m^{-2} in both Auriga and Cassiopeia, and Cygnus-X. This is comparable to the estimated 5σ detection limit in UWISH2 (4.1×10^{-19} W m^{-2} (F15)), since most of the knots were larger in extent than a few square arcseconds.
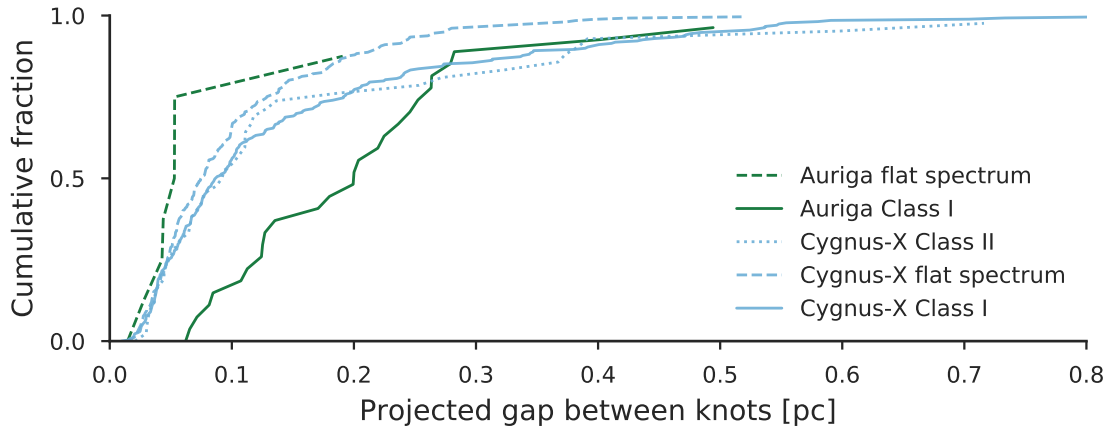
FIGURE 6.13: Cumulative distribution functions of the gaps between subsequent outflow knots, with the Cygnus-X population (light blue) being split for Class II, Class I and flat spectrum driving sources. Since there is only one Class II driving source in Auriga and Cassiopeia, the green lines represent the flat spectrum and Class I objects from that region. Note that the samples are distance limited to exclude outliers from vastly different distances from the majority.
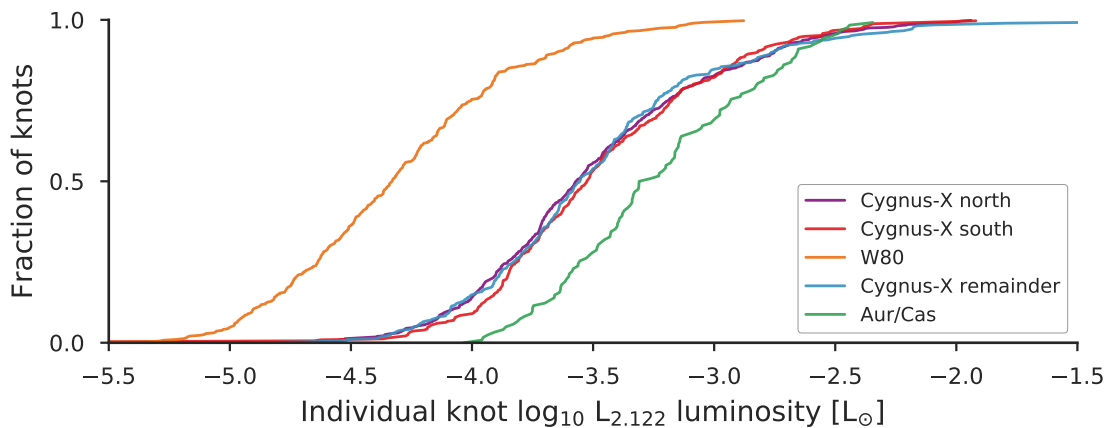
FIGURE 6.14: The cumulative distribution of knot luminosities from the four main regions of Cygnus-X, and Auriga and Cassiopeia. The samples are distance-limited.

Figure 6.14 shows the cumulative distribution of knot luminosities, for all knots that were part of an outflow with an individual estimated distance. The small subset of outflows located around 500 pc in Auriga and Cassiopeia have been excluded. The Auriga and Cassiopeia knots appear to be "brighter" than those from Cygnus-X, and the knots from the W 80 region are fainter, which suggests that the knot luminosity distributions are constant, and only scale with distance. The observed differences in the total outflow luminosity distributions suggests then that the knot density, i.e., the number of knots per outflow length, is what varies between each region. There is no statistically significant difference, within each of the five sub-regions, if the populations of knots are split between those from clustered outflows, and those from isolated outflows. There is also no difference between the luminosity of knots from bipolar outflows, single-sided outflows, and individual knots.

TABLE 6.6: A table presenting the typical distance-corrected knot luminosities. The Cygnus-X sample is split by sub-region. Only knots from outflows that have an individual distance estimate are included.

Region	No. of knots	Knot luminosities ($10^{-3}\,\mathrm{L_\odot}$)		
		Median	Mean	Range
Auriga and Cassiopeia	170	0.348	0.664	$0.008 - 4.519$
Cygnus-X overall	1671	0.205	0.654	$0.001 - 56.766$
W 80	390	0.047	0.096	$0.001 - 1.324$
Cygnus-X north	556	0.268	0.715	$0.022 - 11.490$
Cygnus-X south	338	0.298	0.692	$0.002 - 12.041$
Cygnus-X remainder	387	0.277	1.095	$0.004 - 56.766$

6.4.3 Typical outflow morphology

Since it is clear that there is a correlation between the length and luminosity of an outflow, it is worthwhile to investigate whether or not the morphology of the outflow may be responsible. This is not straightforward in the $1-0\,\mathrm{S}(1)$ line of H_2 since it only reveals the current shock strength, i.e. where the outflow is currently interacting with the local environment. Measuring parameters such as the opening angle is much more straightforward using molecules such as CO as tracers. However, if we assume that the bow shocks (those furthest from the driving source) represent the terminal working surface of the outflow, then it should be possible to determine if the typical outflow is cylindrical or conical in morphology. This is demonstrated in Fig. 6.15.

At time t_B, the bow shock is at point B, and has an apparent radius of r_B. The outflow lobe therefore has a length of h_B. At later time t_A, the outflow continues to propagate until it reaches length h_A, with the terminal shock now at point A. If the outflow lobe is conical in morphology, then as the outflow increases in length, the terminal/bow shock should similarly expand in radius. This would mean that the surface brightness of the bow shock decreases by a factor of $1/\sqrt{2}$ as a function of the lobe length. If the outflow is cylindrical, then $r_B = r_A$, and the surface brightness of the bow shock would remain constant as it propagates. The distribution of shock surface brightnesses is in fact flat, and below the line that represents the conical model, as can be seen from Fig. 6.16. This suggests that cylindrical morphologies are more typical. This is in agreement with the distribution of knot luminosities, which were found to only scale with distance. The objects with high surface brightness tend to be very close to the driving source. The bow shocks with the highest surface brightness are produced by AFGL 2591 and are not shown. Some of the outflows are in general agreement with the conical model (represented by the dashed red line) but only up to a lobe length of around $100''$. When splitting between clustered and non-clustered outflows, protostars and CTTS, precessing or non-precessing outflows, or those from W 80 vs. those from elsewhere in Cygnus-X, there is no statistically significant difference in the distributions.

(a) Conical   (b) Cylindrical
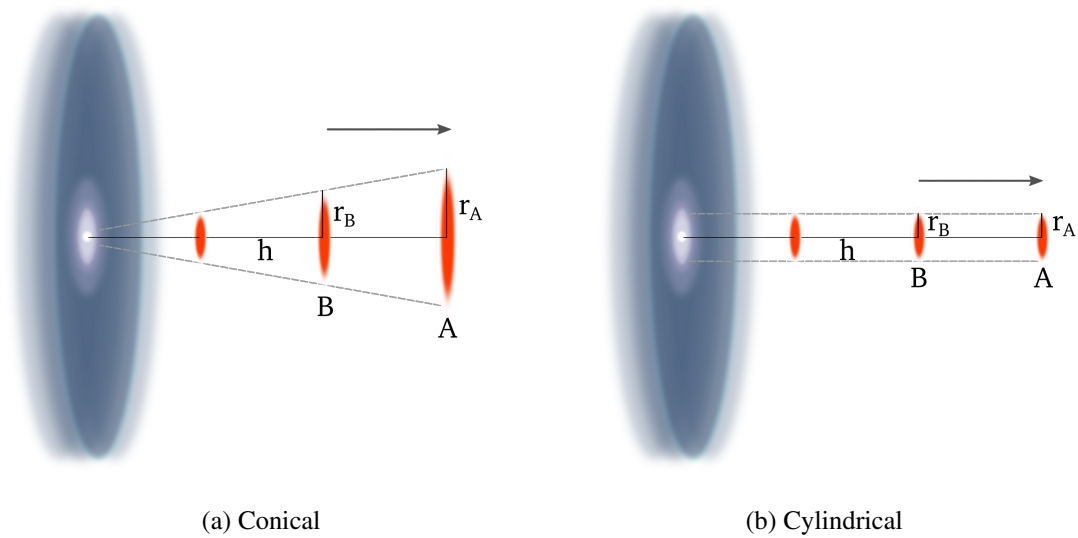
FIGURE 6.15: Schematic representation of the two most likely outflow morphologies. In the conical model, the shock front expands in extent as the outflow lobe propagates, so that the surface brightness increases as the outflow expands. In the cylindrical model the surface brightness of the shock front remains constant as the outflow propagates.

6.5 Statistically-corrected distributions

In order to account for the small sample size in Auriga and Cassiopeia, and the general distance uncertainties obtained towards the outflows in both regions, the final parameter distributions are statistically corrected (as was described in Chapter 3.3.5). The distributions determined in this section will be presented in terms of the outflow lobes, rather than the total lengths or luminosities, in order that the bipolar and single-sided outflows can be combined. Although this does preclude the possibility of comparing the distributions against historical populations from elsewhere in the Galaxy, it is beneficial in that the larger initial samples will produce more reliable results in the statistical correction process. In this Section, the data have all been corrected for the individual distances, and thus outflows with no individual distance are excluded.

6.5.1 Outflow lobe lengths

It was shown in both F16 and M18 that the outflow lobe length distributions (using common distances in each region) were better fit by exponentials than by power laws. The same result was also found when the lengths are corrected for the estimated distances. Figure 6.17 shows the projected lobe length distributions for Auriga and Cassiopeia (green diamonds) and Cygnus-X (light blue circles) with their respective fits (solid lines). In Fig. 6.17 (a), the lobe lengths have only been corrected for the distance toward the outflow. Figure 6.17 (b) shows the same data after statistical correction. The dashed lines in Fig. 6.17 (b) are the same as the solid lines in Fig. 6.17 (a), and have been included to demonstrate the change in the distributions wrought by the statistical correction. For this figure, the individual errors associated with the distance toward each outflow were used. However, after testing a range of errors from 0.001 % up to 200 %, it
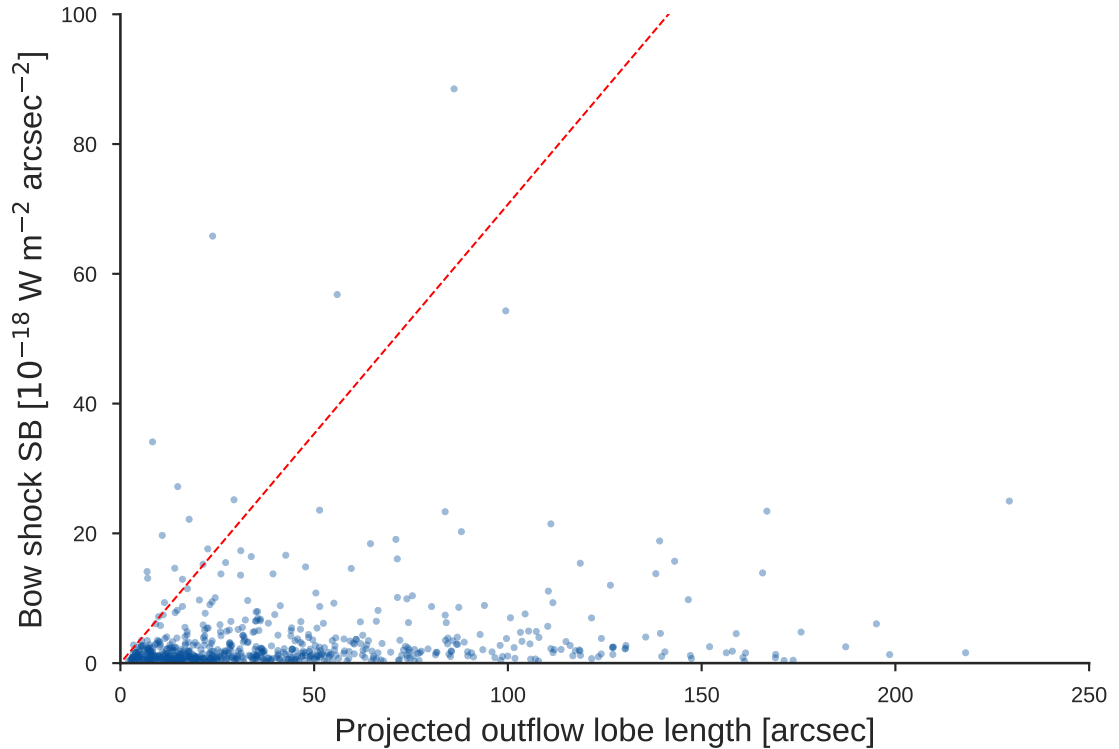
FIGURE 6.16: A plot of the shock front surface brightness as a function of position away from the driving source. The red dashed line indicates a conical outflow. Objects above this line are typically those where the bow shock is more plume-like and close to the driving source. The lobes of DR 21 and AFGL 2591 are excluded.

was found that the slope of the fits are largely insensitive to the generosity of the error bars up to an error of $\sim 50\,\%$. This is considerably more generous than the errors applied to each distance measurement, of which the median is $10\,\%$. Across the range of errors from $0.001\,\%$ to $200\,\%$ the mean statistically-corrected slopes are $\bar{\gamma}_{cyg} = -1.4 \pm 0.2$ and $\bar{\gamma}_{aur} = -2.5 \pm 1.1$ (using a bin width of 0.1 for both). With more generous errors, such as those used in IF12b (i.e. 1 kpc error for each distance), the slopes deviate more heavily from the uncorrected values. The width of the bins was found to have a far greater influence on the slopes of the fits than the errors in the distances. After testing a range of bin widths between 0.025 pc and 0.3 pc (in steps of 0.025 pc), it was found that a bin width of 0.1 pc provides the optimal R-value for each fit. Under these conditions, the mean statistically-corrected slopes are $\bar{\gamma}_{cyg} = -1.40 \pm 0.01$ and $\bar{\gamma}_{aur} = -2.14 \pm 0.06$. These statistically-corrected slopes are within the error margins of the original, uncorrected distributions (which are: $\gamma_{cyg} = -1.30 \pm 0.12$, and $\gamma_{aur} = -2.09 \pm 0.36$).

It has already been shown that there is no clear statistical difference between the lobe length distributions when the outflows are driven by protostars or CTTS in Cygnus-X. Therefore the differences between the two regions cannot simply be attributed to the predominance of protostellar driving sources in Auriga and Cassiopeia. The outflow total lengths are, however, affected by the environment in which they are found. To test the environmental factors, the lobe length distributions were split between each of the Cygnus-X sub-regions, as plotted in Fig. 6.18. In Cygnus-X south there is one object that has an uncertainty in the distance of 1.5 kpc, which is the single lobe

(a) Pre-statistical-correction

(b) Post-statistical-correction
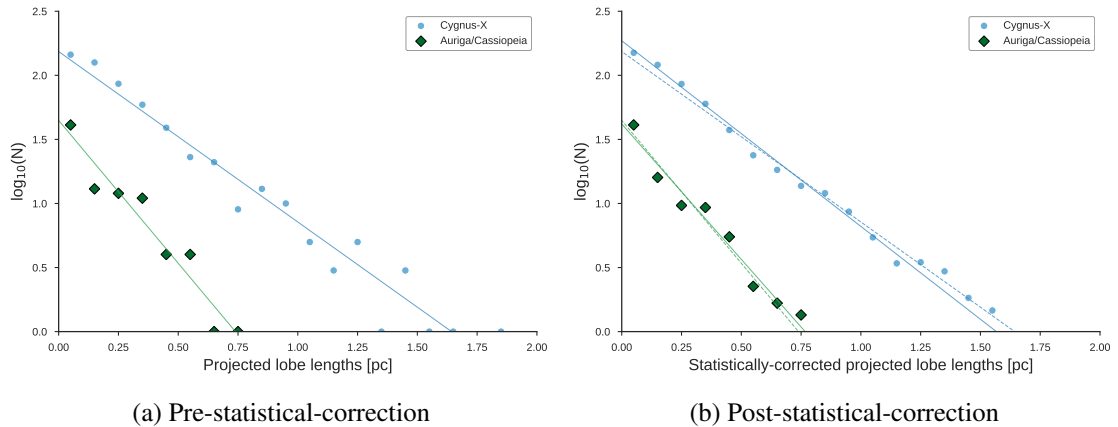
FIGURE 6.17: Plots of the distance-corrected lobe length distributions for Cygnus-X and Auriga and Cassiopeia; (a) is the distribution of the distance-corrected data, while (b) shows the same data after statistical correction. The solid lines represent the fits to the data plotted in each figure. In (b), the dashed lines correspond to the fits shown in (a) for reference.

(a) Including outliers

(b) Excluding outliers
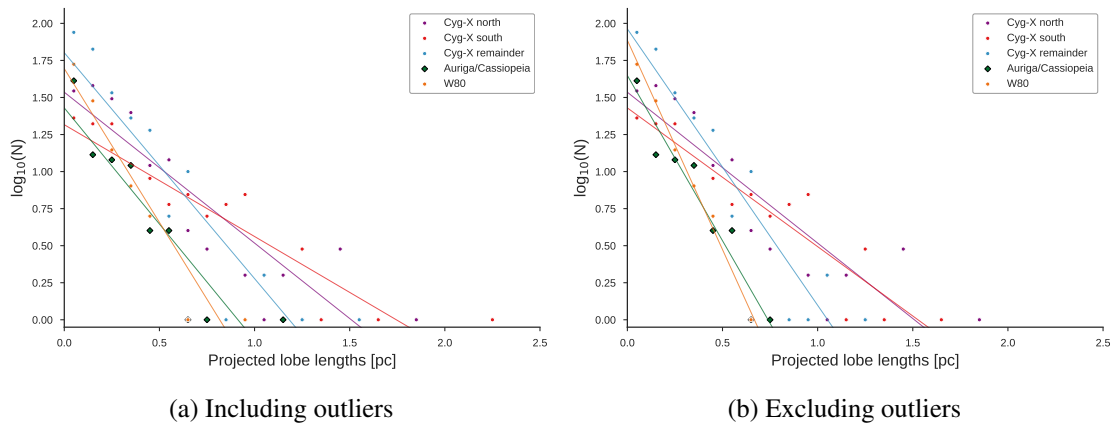
FIGURE 6.18: Plots of the distance-corrected lobe length distributions for Auriga and Cassiopeia, and the four sub-regions of Cygnus-X. In (a) outliers are included, but they are excluded in (b). Solid lines represent the fits to each set of data. The distributions from Cygnus-X north and Cygnus-X south, whilst similar to each other, are clearly different from the other regions and suggest a far higher fraction of long outflows.

over 2 pc in length. There is an outlier in Auriga and Cassiopeia that is over 1 pc, and one in W 80 that is over 0.9 pc. There is also an outlier in the "remainder" sample from Cygnus-X over 1.5 pc. Since this work is focused on bulk statistics rather than interesting exceptions, these outliers are excluded. Setting these values as the limits for the lobe lengths in each region excludes a single outlier from each of them, but increases the correlation coefficient in every case. The results of including these outliers are shown in Fig. 6.18 (a), and of excluding them in Fig. 6.18 (b).

Figure 6.19 shows the lobe length distributions in each of the sub-regions following statistical correction, with outliers excluded (also see Table 6.7 for a breakdown of the numerical values of the slopes as shown in the figure). It can be seen that the length distributions from Cygnus-X north and Cygnus-X south are the same, and closely match the overall distribution in Cygnus-X.

The population in the remainder of Cygnus-X is slightly steeper, suggesting a smaller fraction of very long outflows (lobes > 0.75 pc) than in either Cygnus-X north or south. The Auriga and
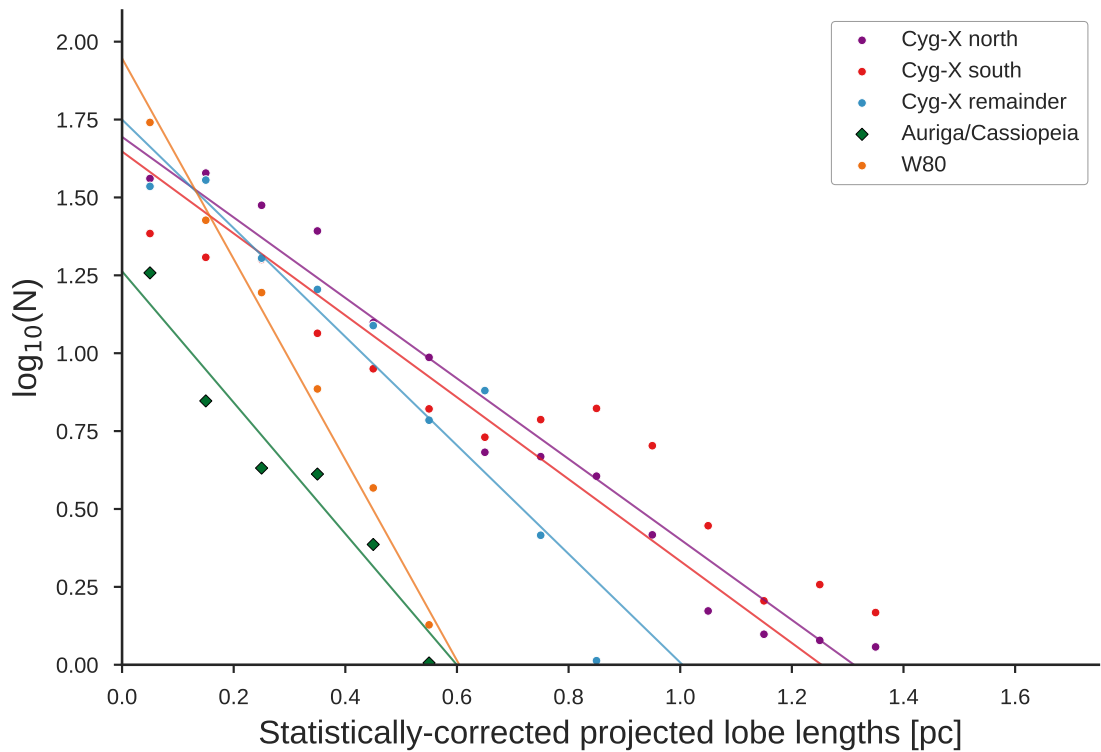
FIGURE 6.19: Distance-corrected lobe length distributions following statistical correction. Outliers have been excluded as outlined in the text. The solid lines represent the best fits to the data with a bin width of 0.1 pc.

Cassiopeia distribution is only slightly steeper than the Cygnus-X remainder distribution, suggesting that these two regions may be more representative of typical star-formation (i.e., low to intermediate mass). The W 80 region is highly unusual in that the length distribution in the region is considerably steeper than the others, and with a similar maximum lobe length to Auriga and Cassiopeia. The implications of these results shall be discussed in Chapter 7.

TABLE 6.7: A table of the mean lobe length distribution slopes for Auriga and Cassiopeia, and Cygnus-X, which has also been split for the four sub-regions. The individual errors associated with each distance are used, the median of which is 10 %. The mean slopes and the $1\,\sigma$ errors are calculated using a range of bin widths from 0.025 to 0.3 pc.

		Statistically-corrected
Region	Mean slope, $\bar{\gamma}$	Mean slope, $\bar{\gamma}$
Auriga and Cassiopeia	-2.09 $\pm$ 0.36	-2.14 $\pm$ 0.06
Cygnus-X (all)	-1.30 $\pm$ 0.12	-1.40 $\pm$ 0.01
Cygnus-X north	-1.05 $\pm$ 0.12	-1.28 $\pm$ 0.03
Cygnus-X south	-0.95 $\pm$ 0.17	-1.32 $\pm$ 0.03
Cygnus-X remainder	-1.83 $\pm$ 0.22	-1.75 $\pm$ 0.04
W80	-3.01 $\pm$ 0.51	-3.17 $\pm$ 0.10

6.5.2 Outflow lobe luminosities

There are two special cases in Cygnus-X which, between them, account for over 60 % of the total luminosity in the $1-0\,S(1)$ line of H_2 ($L_{2.122}$) as measured in the Cygnus-X sample. The AFGL 2591 outflow (at 3.33 kpc) accounts for 18 % of the luminosity, and DR 21 by itself comprises 46 % of the $L_{2.122}$ luminosity. The majority of outflows are far less luminous than this. Since these objects are such extreme outliers, they are both excluded from the plots in this section. In M18 and F16, it was shown that the outflow lobe fluxes were better fit by exponentials than by power laws, with the distributions deviating from power law fits above $35 \times 10^{-18}\,\mathrm{W\,m^{-2}}$ in Cygnus-X and above $30 \times 10^{-18}\,\mathrm{W\,m^{-2}}$ in Auriga and Cassiopeia due to the frequency of outliers in each sample. The lobe fluxes, when converted to luminosities using the corrected distances, should therefore also be better fit by exponentials. However, the total luminosities can be modelled by power laws, as was shown in Section 6.2.3.

When plotted on a log-log axis, the lobe luminosity distributions in both regions form a wide Gaussian curve and not the expected straight line. On a log-lin plot, the distribution forms not a single straight line, but at least two (see Fig. 6.20). This suggests there may be different distributions within each region, or that the luminosity distribution may be log-normal. If we consider that all of the objects whose lobes are more luminous than about $20 \times 10^{-3}\,\mathrm{L_\odot}$ are associated with objects in the MSX catalogue, it might suggest some segregation according to the driving source mass. When limited at about $4 \times 10^{-3}\,\mathrm{L_\odot}$, the luminosity distribution slopes in each region are the same, and in agreement with an exponential distribution. However, if the minimum luminosity is set at $1 \times 10^{-3}\,\mathrm{L_\odot}$ the slopes in both regions form straight lines on a log-log plot, suggesting they are best fit by power laws. When tested across the entire luminosity range, the log-normal distribution produced a worse fit than either the exponential or power law fits over the same range. The fits presented in this section are therefore performed in two distinct parts. Again, the distance errors used in statistical correction are those applicable to each individual object. The "exponential" fits are generated over a luminosity range from $0-4 \times 10^{-3}\,\mathrm{L_\odot}$ (inclusive) on log-lin plots. The "power law" fitting range is from $1-100 \times 10^{-3}\,\mathrm{L_\odot}$ (to exclude AFGL 2591 and DR 21), which on a log-log plot corresponds to an axis range of $0-2$. For the exponential fits, the bin widths ranged from 0.1 to 1 in steps of 0.1, whilst for the power law fits the bin widths are halved, i.e., between 0.05 to 0.5 in steps of 0.05.
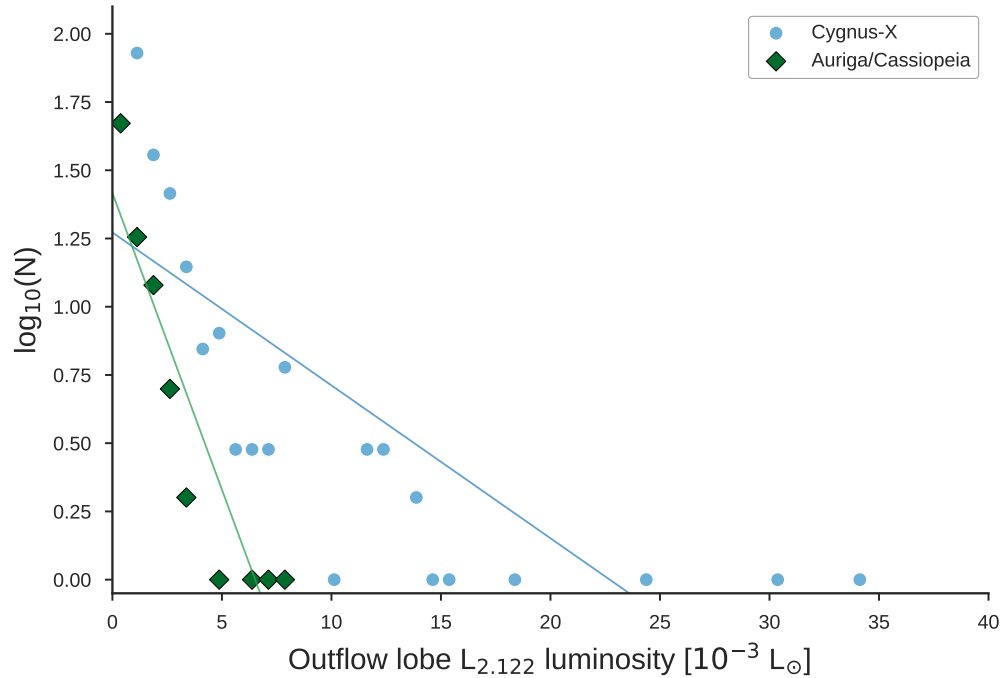
FIGURE 6.20: The distribution of outflow lobe $L_{2.122}$ luminosities for Auriga and Cassiopeia (dark green diamonds) and Cygnus-X (light blue circles). The axis is truncated at $40 \times 10^{-3} \, L_\odot$, to exclude DR 21 and AFGL 2591. Attempting to fit a single straight line to the Cygnus-X sample is clearly not possible.

(a) Exponential fit
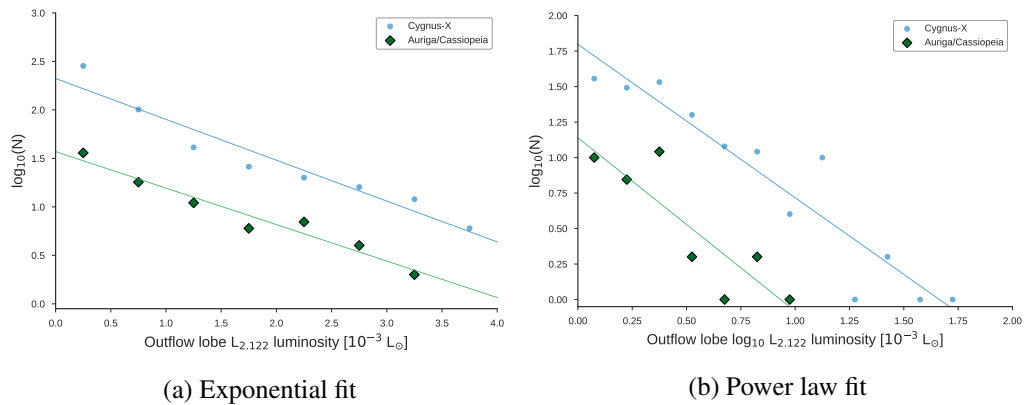
(b) Power law fit

FIGURE 6.21: The outflow lobe luminosity distributions (not statistically corrected) for Auriga and Cassiopeia and Cygnus-X. In (a), the exponential fit shown uses a bin width of 0.5. In (b), the power law fit uses a bin width of 0.15, and the DR 21 and AFGL 2591 objects are excluded.

TABLE 6.8: A table of the mean lobe luminosity distribution slopes for Auriga and Cassiopeia, and Cygnus-X, which has also been split for the four sub-regions. The individual errors associated with each distance are used, the median of which is 10 %. The exponential fits are calculated over a luminosity range of $0-4 \times 10^{-3}$ $L_\odot$ using bins from 0.1 to 1 in steps of 0.1. The power law fits use a range of $0-2$ (corresponding to $1-100 \times 10^{-3}$ $L_\odot$) with bins from 0.05 to 0.5 in steps of 0.05. The bin width ranges are used to calculate the mean slopes and 1σ errors.

		Statistically-corrected
Region	Mean slope, $\bar{\beta}$	Mean slope, $\bar{\beta}$
Exponential fits:		
Auriga and Cassiopeia	-0.381 $\pm$ 0.088	-0.420 $\pm$ 0.003
Cygnus-X (all)	-0.419 $\pm$ 0.019	-0.425 $\pm$ 0.008
Cygnus-X north	-0.300 $\pm$ 0.019	-0.322 $\pm$ 0.005
Cygnus-X south	-0.416 $\pm$ 0.058	-0.389 $\pm$ 0.007
Cygnus-X remainder	-0.574 $\pm$ 0.047	-0.527 $\pm$ 0.006
W 80	-0.947 $\pm$ 0.135	-1.063 $\pm$ 0.027
Power law fits:		
Auriga and Cassiopeia	-1.175 $\pm$ 0.335	-2.463 $\pm$ 0.602
Cygnus-X (all)	-1.083 $\pm$ 0.122	-1.228 $\pm$ 0.120
Cygnus-X north	-0.866 $\pm$ 0.196	-1.594 $\pm$ 0.284
Cygnus-X south	-0.641 $\pm$ 0.132	-1.638 $\pm$ 0.480
Cygnus-X remainder	-0.783 $\pm$ 0.167	-1.019 $\pm$ 0.147
W 80	-1.872 $\pm$ 1.050	-4.859 $\pm$ 1.111

Chapter 7

Discussion, conclusions and future work

7.1 Discussion

7.1.1 Clustering

In all three regions studied as part of the UWISH2 survey thus far, outflows are typically found in small groups containing a few members, and in regions of high column-density. In the case of Cygnus-X, and Auriga and Cassiopeia, however, the majority are not located in or associated with clusters. Indeed, despite the differences in the environments of those regions, the fraction of outflows originating from clusters seems to be constant (Cyg: 42 %, Aur: 41 %). The same result was found by Davis et al. (2009) in Orion A, which contains a mixture of high-mass and low-mass environments. Given that most stars form in clusters (Lada and Lada, 2003), this is unexpected.

It is possible that this represents a selection effect, and that the clusters are simply not detected in the NIR. This may happen if, for instance, the cluster is located far enough away that extinction can obsure it, and if the cluster is small and embedded. We might expect then that the outflow driving sources appear to us to be isolated in the NIR images. However, this does not explain why the same fraction is found in Orion A, which is located at a typical distance from us of around 450 pc. If this were simply a selection effect based on the distance making it more difficult to see the clusters, we should expect to see the fraction of isolated driving sources increase between Orion A and Cygnus, and increase again towards Auriga and Cassiopeia. If the fraction of isolated objects were significantly higher in Cygnus-X, we could reasonably conclude that extinction is the culprit. Additionally, if there were a significantly different fraction of isolated outflows between this study, and those from Orion A, this might have also suggested a selection effect based on the method of identifying clusters in the NIR.

The differences in the overall ISM distribution seem to be unimportant in the clustering or non-clustering of outflow driving sources, since the fraction is the same between low-mass and high-mass regions. Perhaps a more convincing explanation then is that this observed fraction represents more of an evolutionary trend. In other words, the stars identifiable in NIR clusters are more evolved than those in isolated environments, which may still be highly embedded. Since the majority of driving sources for which we have data in the MIR (Cyg: 80 %, Aur: 97 %) have a positive slope in their SEDs, this suggests that the outflows are more likely to be associated with

Class I driving sources. The outflow active state is relatively short and occurs early in protostellar development, so this does lend weight to this interpretation.

In Orion A, Davis et al. tested the clustering of the outflows using the density of YSOs around each outflow. Although this is something that could be done in Cygnus-X using the RGS 2011 and KMH 2014 catalogues, there is no single YSO survey that covers the entirety of the UWISH2 survey field and this would therefore not be considered an unbiased test. There are no large enough YSO catalogues to be able to perform this test in Auriga and Cassiopeia at all. As an alternative to using local YSOs to estimate the star formation density, the same test can be done with the outflows themselves, i.e. calculating the outflow density as a function of the distance to the Nth nearest neighbour. Although this calculation was done for the outflows, it has not been used as a metric in this thesis but could be useful in future work. However, it should be noted that even this metric is not free of selection effects. In Serpens and Aquila, the outflows were noted to be grouped into small collections of $3-5$ members, but in both Cygnus-X and Auriga and Cassiopeia this was a relatively rare occurrence, with median group populations of 1 to 2 outflows. The distance (and by extension, the increase in extinction at increasing distance) must therefore play a large selective role in whether a cluster will be detected or not, irrespective of the metric used. In other words, if one measures the nearest-neighbour distance toward the 5th nearest neighbour of the typical outflow in W 80, it is more likely that the distance will be small compared to the same object if it were located in Serpens and Aquila.

This is supported by the fact that in Serpens and Aquila, groups of outflows had a typical spatial extent of around 5 pc. By contrast, the largest group in Cygnus-X is the one encompassing the DR 22 cluster, with an extent of 5.3 pc (assuming a distance toward it of 1.35 kpc). However, although such groups can contain large numbers of outflows, groups of this size are not typical even in Cygnus-X. The median group radius is around $70''$, implying that at a distance of 1.5 kpc the typical group is only about a half a parsec in extent. In W 80, the largest group is half a parsec in extent. The most likely explanation is that at the typical distance range of $3-5$ kpc in Serpens and Aquila, only the largest star forming clusters, and the brightest outflows, can be detected. The implication is that the typical star forming groups, i.e. those containing less luminous outflows, are simply not observed since at that distance they fall below the detection limit.

It is important to consider the role that clustering plays on the development of co-evolving cluster members. The fraction of outflows found in X-shaped, multipolar systems is likely to be largely independent of the local environment (Cyg: 9 %, Aur: 12 %). Around 40 % of outflows in these systems show signs of precession compared to around 20 % of the general population. Precession can be a strong indication of gravitational interference caused by a close binary neighbour. Perhaps, then, the complex momentum feedback from outflows and winds can disrupt or inhibit the formation of outflows, either via gravitational disruption of the forming systems, or by clearing dust and gas from the cluster. The fact that the molecular outflows appear in small groups of a few, and are typically not seen in the more evolved young clusters where the interstellar dust has been cleared, would seem to be evidence in favour of this interpretation. However, these two interpretations are not mutually exclusive.

The distributions of the lengths and luminosities of outflows from clustered and non-clustered environments are very different, whether these parameters are corrected for the distances toward them or not. In both Auriga and Cassiopeia, and Cygnus-X, the median lengths of clustered outflows are typically twice those of isolated outflows, and the brighter outflows preferentially originate from clusters. This cannot be explained simply by the inclusion of the $\sim$ one fifth of objects that are at very nearby distances, since these objects are also fairly evenly mixed between clustered and non-clustered objects. Hence, we are not more likely to detect clusters simply because they are nearby. The most likely explanation that remains is that the isolated outflows represent less evolved systems where the column density of material in the parent clump is still too high for the cluster to be detected. It is worth investigating these cases at longer wavelengths, particularly as objects that originally appear to be a single object can often be found via radio observations to be clusters of co-evolving objects. One fine example of this would be the spectacular AFGL 2591, originally thought to be a "protostar-like object" (Kobayashi et al., 1980) but later found to be a young, high-mass cluster (Trinidad et al., 2003).

7.1.2 Outflow orientations

In both regions, the distribution of position angles in the bipolar outflows is in agreement with a homogeneous distribution. This supports the findings of Davis et al. (2009) and Stanke, McCaughrean, and Zinnecker (2002) in Orion A and of Davis et al. (2008) in Perseus west. It does, however, contradict the findings in Serpens and Aquila (IF12b), where a preference was found for outflows to be oriented perpendicular to the Galactic plane. On smaller scales, however, the situation is more complicated. In Cygnus-X, the single-sided outflows are not consistent with a homogeneous distribution, and most of the single-sided outflows with a preferential position angle are located in the DR 15 region of Cygnus-X. In this region, a long, dusty filament runs from east to west and many of the outflow axes appear to be parallel or perpendicular to this direction. When these objects are removed from the single-sided sample, the distribution is in agreement with a homogeneous distribution. In Davis et al. (2007), which studied outflows in the DR 21 ridge, the brightest outflows were more-or-less perpendicular to the main DR 21 filament. Outflows from low-mass stars, however, were oriented randomly.

Some apparently preferential orientation with respect to local dust lanes/filaments was noted amongst the more isolated outflows. It is unclear, however, whether such a preference exists, or if it is merely a projection effect i.e. that we cannot see outflows that propagate parallel to the filament due to the higher column density of obscuring material. This can be investigated using Herschel data, but it should be noted that Stephens et al. (2017) did this in the nearby Perseus region using CO measurements and found that the orientation of outflows with respect to local filaments was either random, or a mix of parallel and perpendicular configurations. They concluded that the protostellar angular momentum axis may be independent of the large-scale structure. Given the mixed results obtained in regions such as DR 15 and DR 21, it cannot be concluded that outflows must necessarily be randomly oriented on local scales of a few arcminutes. Follow-up observations in

CO or SiO are required in order to determine the real outflow orientations in three-dimensions, and then to compare these to the local filaments.

However, there is another possible explanation for the apparent local orientation preferences. It is more difficult to assign the correct driving source if only one lobe is visible, particularly in high-extinction regions where the source is embedded. This is especially the case in DR 15, where the vast majority of outflows along the filament have only one lobe visible and most of the driving sources are deeply embedded. Therefore, there is likely to be a systematic misidentification of driving sources for the single-sided outflows. There is a problem with this explanation, however, when one considers that the same issue applies in Auriga and Cassiopeia, and the single-sided outflows there were found to be homogeneously distributed. The method used to identify and measure outflows in the two regions was the same, so if the problem were simply that the sources are consistently misidentified then the distribution of single-sided outflows in Auriga and Cassiopeia should also be inhomogeneous.

Perhaps this issue of misidentification of driving sources in Cygnus-X is due to the fact that the bipolar outflow lobes in the region tend to be misaligned by up to 30°. In Auriga and Cassiopeia, most outflows were straight, with a median angle difference between the bipolar lobes ($\Delta\theta$) of $\sim 5°$ and only 8 outflows (14 % of the bipolar flows) with $\Delta\theta > 10°$. In Cygnus-X, although the median $\Delta\theta$ was 5.5°, there were 75 outflows (28 % of the bipolar flows) with $\Delta\theta > 10°$. The reason for this large fraction of "bent" outflows is unclear. It may be a bias resulting from the method we used to measure the position angle, i.e. measuring to the tip of the furthest knot, rather than through the centre of the outflow axis. However only 17 (23 %) of the outflows with $\Delta\theta > 10°$ show signs of precession, so this does not account for the remaining objects. The only object that appears to be genuinely "bent" is OF 477 (MHO 3405 / HH 555). This outflow is the only one with $\Delta\theta > 40°$, and it is being deflected by wind pressure from the most luminous stars carving the W 80 H II region (Bally et al., 2014). It may be that these "bent" outflows are in fact multipolar systems of two or more crossing outflows, with one lobe from each outflow being extincted. This would make sense, given that in Auriga and Cassiopeia, 12 % were found in multipolar systems, compared to only 9 % in Cygnus-X where the extinction is higher. In any case, the observed divergence from a homogeneous position angle distribution is likely best explained by a combination of these factors, and further study in this area could prove fruitful.

7.1.3   Variability

In Cygnus-X, when examining the sources that had three K-band magnitudes, it was found that the 2MASS K_s magnitudes were systematically brighter than the UGPS K_1 and K_2 magnitudes. Since most of Auriga and Cassiopeia only has UGPS imaging from one epoch, the data from that region were not reliable enough to positively identify variable stars. The problem is largely due to the improved resolution of UGPS over 2MASS. The fraction of stars identified as variable in Cygnus-X, where crowding by field stars is a problem, is also larger than in Auriga and Cassiopeia. In other words, this exacerbates the issue of the UGPS survey being able to resolve

stars that 2MASS cannot. In Cygnus-X, where objects detected in UGPS typically have magnitudes from two epochs, another problem exists in the identification of variable stars. When the highest-amplitude variables were cross-checked against the lists of Contreras Peña et al. (2017a,b) and Lucas et al. (2017), there were very few matches. This is largely due to the inclusion in our analysis of stars that were extended, and particularly those with reflection nebulae in the direction of the outflow axes, which makes the photometry unreliable in many cases.

Additionally, for stars which outburst periodically, but otherwise do not experience large fluctuations in their magnitudes, it is statistically unlikely that these will be detected given only two recorded magnitudes. It is therefore possible that many of the candidate driving sources are variable, or undergo periodic outbursting events that are responsible for the ejection of material that forms H_2 emission knots, but are not detected as variable stars because they are not currently outbursting. For these reasons, although the NIR magnitudes were measured, the variability of the driving sources was not used as a metric in this analysis. No correlations on the basis of driving source variability could be found, and hence no conclusions can be drawn with regard to the relationship between variability in the driving sources and the outflow properties.

7.1.4   Evolution of the driving sources

It was expected, based on the work of Stanke (2003), that the outflow properties would be greatly different depending on the evolutionary stage of the driving source. Stanke found that outflows driven by CTTS were short and faint, that Class I protostars drove outflows that were slightly longer and brighter, whilst Class 0 protostars produced outflows of any length or brightness in Orion A. From this, it was concluded that outflows grow rapidly in length and brightness to their maximum extent, and then become shorter and fainter as the driving source evolves. Although there were almost no CTTS driving sources identified in Auriga and Cassiopeia (97 % of the 80 % of sources with WISE detections had $\alpha > 0$ values), the driving sources identified as protostars can still be compared against the protostars from Cygnus-X to determine whether their outflows have the same properties. It is worth noting, however, that although 20 % of the driving sources (with WISE detections) in Cygnus-X have $\alpha < 0$, only 65 % of the Cygnus-X sources have detections in WISE. It is therefore not possible to conclude positively that the driving sources in Cygnus-X are more evolved than those from Auriga and Cassiopeia, simply because a higher fraction of them are identified as CTTS.

Conclusions drawn on the basis of evolutionary stage are done with caution due to (a) the inherent uncertainty in the assignment of driving sources, (b) the higher extinction and field crowding in Cygnus-X, (c) the fact that α was considered in the selection of the driving sources which may bias the selection against more evolved sources, and (d) the fact that none of the driving sources have had their nature confirmed spectroscopically as part of this study. The assumption in (c) was made on the basis of earlier findings; In Serpens and Aquila (IF12a), Orion A (Davis et al., 2009) and Perseus west (Davis et al., 2008), it was found that outflow driving sources tend to be less evolved than the general YSO population, with most driving sources having a slope (α) in their Spectral Energy Distributions between 0 and +3 suggesting they are Class I protostars (according

to the definitions of Class I and Class II sources from Adams, Lada, and Shu 1987; Lada and Wilking 1984 which used known CTTS stars in their studies). The results from Cygnus-X and Auriga and Cassiopeia are in agreement with this, and there is little difference in the distributions of the α values of the protostars between the two regions. Additionally, Davis et al. (2009) found no difference in the alpha distributions of outflow driving sources and protostars, thus concluding that they are the same objects.

Identifying the precise protostar or YSO responsible for a given outflow is not straightforward, and it should be stated clearly that it is likely that the incorrect source has been identified for some fraction of outflows. Nevertheless, in a co-evolving group the approximate evolutionary stage can be inferred using the methods in this thesis and should be correct even if the specific driving source is not. A potential Class 0 driving source that is highly embedded and detectable only in the sub-mm cannot reasonably be assumed to be a Class II YSO, and a NIR visible cluster will be evolved enough, and have cleared out enough material, that highly embedded Class 0 cluster members would be unlikely. Therefore, whilst individual outflows may have a large uncertainty in the source attributed to them, a large enough statistical sample should, on average, still reproduce the results of Stanke. However, the expected result was not found in either Cygnus-X or Auriga and Cassiopeia. Since all three Classes of objects produced outflows of any length and luminosity, it cannot be reasonably concluded that Class I protostars must drive shorter outflows than their Class 0 counterparts. Nor can it be said that Class II YSOs must drive short, faint outflows. Either there is something unique about the Orion A region that caused the observed striation in the outflow properties in that region, or they are the coincidental result of using a relatively small sample. If the problem was that the method used to classify evolutionary stages in Cygnus-X and Auriga and Cassiopeia was not rigorous enough, this can be rectified using follow-up observations.

There is another problem, however, that this result logically creates. It was previously suggested that clustered environments could be more evolved than their isolated counterparts, as the most reasonable explanation to explain the differences in the length and luminosity distributions from clustered vs. isolated sources. However, the differences in those same distributions from CTTS and protostars are not significant (in Cygnus-X), with KS and AD-tests proving indecisive for both lengths and luminosities. This is the case irrespective of whether or not the distances toward the outflows are corrected. If it were really the case that the isolated outflows are from less evolved sources, and the isolated outflows are shown to be typically shorter, then we should find that less evolved sources drive shorter outflows on average. Not only was this not found, but the Orion A results find the opposite result, i.e. that the CTTS drive the shortest outflows in Orion A.

The most likely explanation for this is that the evolutionary stages for the clustered driving sources are simply incorrect, or the driving sources themselves have been incorrectly assigned. In clusters, the longer wavelength bands do not have sufficient resolution to separate two nearby objects that may be resolved in the UGPS and UWISH2 images. Therefore, the magnitudes from the WISE bands may point to one or more stars proximate to the selected driving source. The longest wavelength bands would therefore contain contributions from multiple stars and the magnitudes would appear to be brighter, thus steepening the spectral index, α of the WISE point source. Alternatively, the driving source could be an embedded Class 0 object not yet visible in the mid-infrared.

Given this inherent uncertainty over the driving source assignment, it is most likely that the clustered driving sources are not necessarily the same population as the most evolved driving sources.

It may be possible to explain this conflict in the observed results if, instead of using the evolutionary stage of the driving sources, we consider instead the results in terms of the driving source luminosity (and by implication, the mass). In the 1 deg^2 area of Orion A used in the Stanke ([2003](#)) study, most of the outflows were driven by high or intermediate mass stars. Meanwhile, in the 78 deg^2 searched as part of this thesis, the outflows discovered are mainly from low and intermediate luminosity stars, with some high-mass complexes situated in the Cygnus-X region. However when the lengths and luminosities of the outflows were investigated as a function of the luminosity of the driving source (using association with objects from the MSX survey as a proxy for mass), it was shown that the "high luminosity" objects preferentially drive the longest, and especially the most luminous, outflows. Therefore, it may be more fruitful to investigate the luminosities (and by extension, the masses) of the driving sources as an indicator for the outflow properties.

7.1.5 Outflow lengths and luminosities

In both regions, correcting the distances towards the outflows had the effect of "skewing" the overall distributions of lengths and luminosities towards the shorter, fainter end of the distributions, as the fraction of very long objects reduced and the peak of very short objects increased. Some of the longest and brightest outflows in the original F16 and M18 samples have been identified as residents in much nearer clouds than originally thought. In F16 and M18, it was found that the median total outflow flux in each sample was $18 \times 10^{-18}\,\mathrm{W\,m^{-2}}$ (in Cygnus-X) and $5 \times 10^{-18}\,\mathrm{W\,m^{-2}}$ (in Auriga and Cassiopeia). These values correspond to about $1 \times 10^{-3}\,\mathrm{L_\odot}$ and $0.6 \times 10^{-3}\,\mathrm{L_\odot}$ respectively. Both of these values are at the faint end of the luminosity distribution in Serpens and Aquila as determined in IF12b, but the median flux values in each sample are comparable. This confirms that the Cygnus-X and Auriga and Cassiopeia samples include intrinsically fainter outflows that could not be detected in Serpens and Aquila.

After correcting for the individual distances toward the outflows, it was found that the median luminosity in Cygnus-X decreased slightly to $0.8 \times 10^{-3}\,\mathrm{L_\odot}$, and the median luminosity in Auriga and Cassiopeia increased to $1.3 \times 10^{-3}\,\mathrm{L_\odot}$. This implies that the distance toward the outflows has the greatest overall effect on the distribution of outflow luminosities. This is also supported by the fact that in Orion A, the range of luminosities is an order of magnitude smaller than in Serpens and Aquila, despite the similarity in the mean slopes of their luminosity distributions. In every region, the total outflow length distributions are best fit by exponentials, and the total luminosity distributions are best fit by power laws. This seems to be the case irrespective of whether the corrected distances are used or not.

The distance toward a given region, and the sensitivity of the survey employed, seems to be the greatest factor in determining the exponent or power law from one region to the next. Evidence in favour of the latter comes from Orion A. In the later, more sensitive survey performed by Davis et al. ([2009](#)), a larger proportion of short outflows were found than in the earlier survey by Stanke, McCaughrean, and Zinnecker ([2002](#)). These additional discoveries steepened the slope of the

length distribution in that region. However, the median lengths were not significantly different between the two surveys. In favour of the former, the shortest and faintest outflows are missing entirely from the distant Serpens and Aquila region (which is projected to be between 3 and 5 kpc from the Sun), and the median total length was 0.9 pc. The typical outflow in all of the other regions seems to be short (< 0.4 pc) irrespective of other factors. Up to just over 1 pc in length, the slopes of the total length distributions in every region (except Serpens and Aquila) are the same at -1.2, but the fact that each region has a fraction of very long outliers suggests that there may be some change in the physics after the outflow reaches a certain length. Since Cygnus-X and Orion A both contain outflows of comparable length to those in Serpens and Aquila, but also contain a majority of very short outflows, this adds weight to the claim that the short, faint outflows in Serpens and Aquila were simply undetected, and hence also explains the relatively large fraction of parsec-scale flows in that region.

In terms of the outflow lobes, the lobe length distributions were found to be best fit by exponentials, whilst the lobe luminosities were more complicated. The cut-off between the exponential fit to the faintest outflows ($< 4 \times 10^{-3}$ L$_\odot$), and the power law fit for the brighter flows is not well-defined, and the reasons for it are unclear. Firstly, it should be considered that there is a large degree of scatter due to the inherent uncertainty over the distances. Since luminosity scales with the square of the distance, and the typical distances have errors of between 10 and 30 %, the potential scatter in the luminosity measurements is considerable. Secondly, since the flux distributions are essentially the same in each region, our capacity to measure the faintest objects is also a large factor. Without the tall peak of very faint objects, it is likely that the distributions could be fit only by a power law. Thirdly, unlike with the outflow length asymmetry where the typical outflow has one lobe only about 30 % longer than the other and relatively few highly asymmetrical outflows, the distribution of flux ratios is almost homogeneous. A flux ratio of 0.5 means that one lobe is twice as bright as the other, and many outflows are even more asymmetrical than that. As a result, there is a steep peak of very faint outflows, and a corresponding tail of very bright ones.

To some extent, the previously-known sample of MHOs in Cygnus-X is the same as the clustered objects. If we consider that earlier surveys in this region were highly targeted on specific star-forming complexes, high mass clusters and UCHII regions, it is unsurprising that this should be the case. In Chapter 5 it was shown that the populations of the previously-known MHOs and those newly discovered as part of this work formed vastly different populations. The newly-discovered MHOs were predominantly short, whilst the distribution of already-known objects was almost flat, missing the peak of very short objects. This led to some speculation that there could be a strong bias in the already-known sample in favour of longer, brighter outflows. By correcting the distances, it was found that the missing peak of short objects (< 0.3 pc) was partially recovered in the already-known sample. However, the populations of previously-known and newly-discovered MHOs were still likely drawn from different parent samples, and the previously-known population is still preferentially longer and brighter than the typically isolated, short and faint outflows discovered as a result of this work. It is therefore shown that there is indeed a bias in the "known" sample, although not to the extreme that was suggested when using the common distance of 1.4 kpc.

When the outflows from Cygnus-X north and Cygnus-X south are compared, it was expected that

the outflows from Cygnus-X north should be brighter and longer than those from Cygnus-X south. This was based on the combination of two earlier findings. Firstly, Kryukova et al. (2014) found that the YSO luminosities were drawn from different distributions, with those from the Cygnus-X north complex being brighter than those from Cygnus-X south. Secondly, the Caratti o Garatti et al. (2006) finding that the source and outflow luminosities are correlated. In order to test if the original result in the KMH 2014 catalogue was simply a result of their using 1.4 kpc as a common distance to all YSOs, the driving source luminosities were "corrected" using the distances obtained for the outflows. When this was done, the same result was obtained as in Kryukova et al., i.e. the distributions are statistically different and the YSOs in Cygnus-X north are more luminous than those in Cygnus-X south. This suggests that the subset of YSOs that have been selected as candidate driving sources follow the same distributions as the YSO populations in general for the north and south regions.

The expected result was not found, and the lobe length and luminosity distributions from the two regions are statistically the same (irrespective of the distances used toward them). When we fit the statistically-corrected luminosity distributions in each region, the exponent for the faint objects is -0.3 and -0.4 in Cygnus-X north and south respectively, and the power for the bright objects is -1.6 for both (albeit with large errors). Therefore, we cannot conclude that the outflow and driving source luminosities are correlated in these regions based on the data presented. Perhaps the most convincing explanation for this is that the expected correlation found between outflow and driving source luminosity simply does not apply for the majority of our outflows, and only applies to Class 0 objects where the luminosity of the protostar is accretion-dominated. The outliers found by Caratti o Garatti et al. are all Class I objects, and all lie beneath or to the right of their empirical model. In Fig. 6.8 only three outflows agree with their model, and the remainder are far below the line. Since the KMH 2014 catalogue contains only Class I (or more evolved) objects, this seems to be a sensible interpretation. Follow-up observations may be worthwhile in order to confirm the correct driving sources of a significant enough proportion of the outflows, and to obtain bolometric luminosities of those driving sources, so that firmer conclusions can be drawn. The extent to which this would bring the highly-scattered objects into agreement with the empirical model is unclear.

This is also supported by the fact that there appears to be a maximum length of a few parsec for outflow lobes in the $1-0\,S(1)$ line of H_2. This result was also found by Navarete et al. (2015) using high-mass outflows. We know that outflows, as HH objects, can reach much greater distances (for example, HH 111 being 7.5 pc long (Reipurth, Bally, and Devine, 1997)). It is therefore likely that these measurements represent lower limits to the outflow lengths, particularly given that only the parts of the outflow interacting with the ambient medium are measured, and that no corrections were made for the inclination angle. The lengths of the MHOs seem to provide more of an indication of the extent and distribution of the molecular material in the parent cloud or local clump than any reflection of the driving source properties. Certainly, the brightest objects do not appear to be as long as might be expected from a visual inspection of Fig. 6.5. This apparent "turn-off" at the upper-right of the figure could be a simple visual effect from the relatively small fraction of very long, bright objects. It is likely that this represents a real physical effect, but better constrained distances are required towards the low- and intermediate-luminosity objects in order

to tighten the overall correlation and investigate its nature. Investigations using GAIA's second data release will be conducted as part of future work.

If the maximum length exists, but there is no corresponding maximum luminosity in the $1 - 0\,S(1)$ line, then it must necessarily be the case that the lengths and luminosities are governed by different mechanisms or parameters, at least for certain types of outflows. Certainly, the concept of a maximum length for molecular outflows makes sense, given that once an outflow enters the UV-rich ISM, the molecules that comprise the ejecta become dissociated or ionized, and can only be detected thenceforth using atomic tracers. It seems likely then that the outflow lengths are governed primarily by the environment into which they are propagating. In order to test this, the lengths in different sub-regions can be compared. The length distributions with the greatest differences are those of Cygnus-X south and W 80. Cygnus-X south forms a border around the southern and eastern edges of the Cyg OB 2 association, which is being ionized by the OB stars as they expand the HII region. This is a similar situation to W 80, where the edges of the Pelican and North America nebulae are being ionized by the stars behind L 935. However, the stars forming in W 80 typically produce very short outflows. If the environmental configuration were the dominant factor in the lengths of the outflows, then we might also expect that these two regions have similar length distributions, but they do not.

Delving further into each of these regions, the very longest outflows can be examined in order to confirm the type of environment in which they are found, i.e. whether they are located on the border of the HII region, or are typically more sheltered and far from the ionising stars. In W 80, the longest outflows are those over 0.5 pc in length (OF 451, OF 456, OF 462, OF 533, OF 543). These are all concentrated in the Gulf-of-Mexico region at $\sim$ RA: 314.4, DEC: 43.8. This small region is a dark clump adjacent to the L 935 dark cloud, and the extinction appears to be very high. In addition, the mid-infrared images from WISE show an apparent dark filament, along which the long outflows and multiple star forming cores are arrayed.

In Cygnus-X south, the longest outflows are those over 1.3 pc in length and they are clustered in two separate locations. OF 049, OF 225, and OF 227 are located at $\sim$ RA: 307.45, DEC: 39.4 in an isolated and extincted environment, far to the south of the OB 2 association, and also along a filament. The outflows OF 332, OF 345, and OF 351 are all located along the dark filament adjacent to DR 15. If we also consider the DR 21 ridge as being a collapsing filament, then it seems to be the case that isolated filamentary clouds are able to produce the longest outflows in each region. Meanwhile, the edges of HII regions seem not to produce long outflows in H_2, but can produce very long HH objects (as found by e.g. Bally et al. (2014)). It could be reasonably concluded that the distribution and configuration of the local environment is the key factor in the lengths of outflows (in the $1 - 0\,S(1)$ line of H_2), and that the maximal potential length of a given outflow is set by the radius of shielded material in the host core or local clump.

This does, however, bring us back to another key question; what determines the outflow luminosity? It has been seen that the MSX sources are preferentially associated with the very brightest outflows. This would seem to suggest that there is a correlation between the luminosity of an outflow and the driving source luminosity (and by extension, mass) even though it has already

been shown that this is not the case for our sample. This is a problem that can only be resolved through further study, however even if the initial mass of the protostar or YSO is what determines the luminosity of the outflow (in terms of the mass lost through accretion/ejection events), the initial mass of a given protostar is still governed by the mass of the clump in which it forms (i.e. the initial mass function). This would mean that even if the mass reservoir of a given protostar is responsible for determining the luminosity of its outflow, the luminosity distribution of outflows in a given cloud should theoretically follow the mass distribution of the cores in the cloud.

Alternatively, it could be that after reaching its maximum length, the jet breaks free from the molecular environment and into the UV-rich ISM (depending on the radius and density of the parent clump or filament), but continues to interact laterally with the molecular cloud as the cavity is carved out and expanded. We found that the outflows are likely to be mostly cylindrical in morphology as they propagate, which would imply that the knots would be constant in surface brightness along the outflow's length. In this case, the outflow length would be proportional to the luminosity. If the outflows were conical in morphology, the luminosity would increase as it propagates, implying a steeper slope in the length vs luminosity plot. To explain the observed plateau, perhaps a cylindrical propagation until $> 1.3 \, \mathrm{pc}$ as the jet drives into the denser material nearer to the driving source, followed after a particular distance by a lateral cylindrical expansion as the density of the parent cloud decreases, which could increase the luminosity without further increases in length. However, this does assume that the observed plateau is a real feature and is not simply a result of small number statistics at the very bright end of the luminosity distribution.

If the brightest objects in the Cygnus-X sample are considered as those brighter than $0.03 \, \mathrm{L_\odot}$, we find five outflows:

> **OF 213** (MHO 952, MHO 953) also known as HH 166 or AFGL 2591,
>
> **OF 238** (MHO 3493) newly discovered as part of this work
>
> **OF 471** (MHO 861, MHO 862, MHO 860) also known as IRAS 20126+4104
>
> **OF 510** (MHO 828, MHO 857, MHO 855, MHO 856, MHO 854) also known as W 75 N
>
> **OF 570** (MHO 898, MHO 899) also known as DR 21

These objects are mostly rather unique, well-studied and driven by high-luminosity sources, but are arguably not representative of typical outflows as found in the remainder of the population in terms of their morphology. It could therefore as well be the case that the correlation with MSX objects is coincidental to them being from high-mass complexes, and that these objects do not follow the same relation as "typical" outflows because they are not typical outflows. Certainly in the case of DR 21 and AFGL 2591, there remain questions about the precise nature of the objects and whether they may represent more "explosive" events such as Orion's OMC 1 rather than accretion-driven outflows.

7.1.6   Outflow knots

By measuring the gaps between subsequent pairs of knots in an outflow, it is possible to approximate the timescales between major mass accretion-ejection events, and reveal inhomogeneities in the density of the local environment. Determining which of these are responsible for a given individual knot gap is far from straightforward, but a large enough statistical sample should make it possible to draw general conclusions about the most likely primary cause of the H_2 emission knots that we detect. It is beyond the scope of this thesis, however, to attempt to decipher the accretion/ejection histories of outflows using the H_2 knots from this study alone. Such analysis would require time-domain studies of the outflows in H_2 in order to measure the proper motions.

On average, Cygnus-X outflows have around twice as many knots per outflow as Auriga and Cassiopeia, largely due to the W 80 region where the gap lengths are very short (typically 0.03 pc) and the knot density (the number of knots per outflow length) is larger than in any other region. The gap lengths in Cygnus-X overall are slightly shorter than those of Auriga and Cassiopeia, with median gaps of 0.07 pc and 0.11 pc respectively. That the knots of W 80 are also much fainter than in other regions suggests that we are able to detect intermediate, faint knots that otherwise appear as extended gaps in the other regions. There is a large difference in the distributions of the knot gaps between the two major regions. In Auriga and Cassiopeia, following distance-correction the gaps are almost homogeneously distributed between 0.025 and 0.275 pc. Originally, there was a long tail of very long gaps, but these belonged to the objects at the nearby distance. By contrast, the gaps in Cygnus-X are not homogeneously distributed, with a sharp peak between 0.025 and 0.075 pc with a continuous tail of long gaps up to around 0.8 pc.

There was no statistically significant difference between the gaps in outflows from clusters and those from isolated environments in either region. In Cygnus-X there was also not a significant difference in the gaps from protostars or CTTSs. However, when the knot gaps were split in each region according to Class I, Class II and flat spectrum sources, an interesting result emerges. For the most part, the distributions were the same, with the exception of the Class I objects from Auriga and Cassiopeia, which correspond to those that have the long gaps. There is no sensible explanation for why this should be the case, and thus would be an interesting subject of further investigation. A higher frequency of accretion bursts would be expected from younger sources, and hence mass ejection events (e.g. Vorobyov and Basu (2006)) if the ejection speeds are the same. In addition, one might expect a clumpier medium near to younger sources, and hence more material available to be shocked. These factors would lead one to assume that the gaps between knots would be much smaller around younger sources. It is possible to explain the fact that the Class I knot gaps in Cygnus-X have the same distribution as the flat spectrum and Class II objects if the eruptions are more frequent with slower ejection speeds in younger driving sources, and eruptions are less frequent with higher ejection speeds in older sources.

The observed result in the Class I sources from Auriga and Cassiopeia could be due to the non-detection of fainter, intermediate knots, or it could be that the low-mass environment is simply not dense enough to provide sufficient material for the lower-velocity outflows to shock against, i.e. that the outflows are able to travel relatively unimpeded for longer before colliding with denser

ambient material. Or, perhaps at earlier evolutionary stages where the ejection velocity is relatively low, the occurrence of active shocks is lower, or the extinction is higher. In those cases, however, the same result should also be found in the Class I objects in Cygnus-X. It could also be a result of the quick cooling time of the H_2 molecules (~ 1 year), so if the speeds decrease with distance from the source, the ejected material may have time to cool before it is overtaken by newer ejecta. Whether the real cause of the observed difference in Class I sources is as a result of one of these factors, or something else entirely, is not at all clear.

7.1.7   Dynamical timescales

In F16, the estimated typical time between accretion/ejection events in Auriga and Cassiopeia was reported as between 1 and 3 kyr. After correcting the distances toward these outflows, the gap lengths in Auriga and Cassiopeia occupy a relatively compact range that corresponds to a dynamical timescale of between 0.2 kyr and 6 kyr. The median gap length of 0.1 pc corresponds to 1.4 kyr between ejection events. This is still in agreement with the previously-reported findings in F16, but without the large fraction of originally-reported outliers. It also agrees with the dynamical timescale found in Serpens and Aquila of $1-2$ kyr between ejection events (IF12b, also using $80\,km\,s^{-1}$). For the Cygnus-X sample, the median gap between knots is 0.07 pc, and the mean is 0.1 pc. These correspond to typical dynamical timescales of 0.8 to 1.3 kyr between accretion/ejection events, which is slightly lower than the $0.9-1.4$ kyr reported in M18 (although not significantly so). The distances between subsequent knots ranges in Cygnus-X between 0.007 pc and 1.5 pc, corresponding to 0.09 kyr at the lower end, and 18 kyr at the higher end. If the single object with a 1.5 pc gap between two of the knots is excluded (due to the unreliable distance measurement), the maximum knot gap is around 0.8 pc, which corresponds to about 10 kyr between outflow knots. This range for Cygnus-X is wider than was reported in M18.

The very shortest knot gaps in the sample are around 0.007 pc which corresponds to a timescale of 86 years. This makes EX-Ors (Herbig, 1989, 2008) unlikely as potential driving sources since they outburst on a semi-regular basis every $1-10$ years. By contrast, the longest gaps in the sample are all over 0.5 pc in length, which equates to ~ 6 kyr between outburst events. This means that we cannot rule out FU-Ori style outbursts for these objects, since the ejection rate for FU-Ori stars is estimated to be $5-50$ kyr (Scholz, Froebrich, and Wood, 2013). It is worth considering that there is one known FU-Ori star, V 1057 Cyg, that is associated with H_2 emission knots from this sample, OF 125. It is located in the Pelican nebula in W 80, and hence a distance of around 600 pc can be assumed. One of its lobes is 0.06 pc in length and the other is 0.17 pc. These values correspond to 0.7 kyr and 2.1 kyr respectively.

If the eruption timescale for FU-Ori objects is lower than the canonical values predict, then FU-Ori type events could be responsible for significant fraction of the outflow knots, at least in Cygnus-X. It is possible then that the recently-classified sub-population of variable stars with outburst properties between those of FU-Oris and EX-Ors, dubbed MNors (Contreras Peña et al., 2017a), could be responsible for some of the shorter eruption timescales observed. As with many fields of study, however, small number statistics are a problem, and it is still not clear if these objects

are separate classes of pre-main-sequence stars, or if they are the same objects existing on a broad spectrum (Audard et al., 2014). Discovering stars that outburst on scales of thousands of years requires a large degree of luck in observations to find them before they begin one of these events, and the most recent large-scale ejection event for V 1057 Cyg lasted for decades. It is also not possible to completely rule out EX-Ors as possible driving sources. With all three object types, the populations are simply too small for the outburst timescales to be properly constrained.

However, even without incorporating deceleration or other velocity variations in the outflow speeds, and making the assumption that the H_2 knots are purely associated with accretion/ejection events, these orders-of-magnitude estimates are good enough to highlight potential FU-Ori or MN-Or driving sources. Therefore, although no firm conclusions are drawn regarding the accretion "fossil record" of the outflows and the specific types of variable stars that might drive them, these results may help to target future searches for such variable objects. Larger statistical samples will help to constrain the outburst timescales for each type of object, and their other general properties.

7.2   Conclusions

- In this project, a systematic and unbiased search has been completed for extended emission in the $1-0\,S(1)$ line of H_2 in Cygnus-X and the Auriga and Casssiopeia regions of the Galactic plane. The Cygnus-X survey covered 42 square degrees and revealed 572 outflows, of which 465 were totally new discoveries. In Auriga and Cassiopeia, the survey area of 35.5 square degrees yielded 98 outflows, all of which were previously unknown. In total, 800 outflows have been found as a result of the UWISH2 survey thus far, and they account for almost 40 % of the $\sim 2\,000$ currently known H_2 outflows in the MHO catalogue.

- The majority of the outflows are found in isolated ($\sim 60\,\%$), rather than clustered ($\sim 40\,\%$) environments, irrespective of whether the region is high-mass or low-mass, or the method of classifying "clusters". The outflows originating from clusters tend to be longer and more luminous than isolated outflows. This suggests a possible evolutionary trend, although this requires follow-up observations in order to verify since determining the exact driving source of an outflow from a cluster is almost impossible based on NIR data alone.

- Of the driving sources with point-source detections in the mid-infrared (WISE), the vast majority can be classified as Class I objects (protostars) rather than more evolved Class II or flat spectrum sources (YSOs). Although this is in agreement with previous studies, it should also be noted that this result is not free from bias and requires follow-up observations to confirm the correct driving sources.

- Almost fifty newly-discovered, near-infrared candidate clusters have been discovered as a result of being associated with the H_2 emission sources. Since an exhaustive search for clusters was not performed, there may be more yet to be found in the survey fields.

- The typical extent of the star clusters is much smaller than was found in Serpens and Aquila. Indeed, the typical group in Serpens and Aquila was around 5 pc in extent, whilst in both

Cygnus-X and Auriga and Cassiopeia the typical group size was closer to 0.5 pc. Since the largest groups in Cygnus-X are comparable in size to those of Serpens and Aquila, there is a clear distance bias which must be accounted for. In other words, that the typical "small" groups found in the more nearby Cygnus-X and Auriga and Cassiopeia regions were undetected in the region considered as representative of the Galactic plane. Similarly, the largest group in the very nearby W 80 region is of the order of the median group sizes from Cygnus-X. Therefore our ability to detect these NIR clusters depends heavily on their distance from us.

- The position angles of the outflows are in broad agreement with a homogeneous distribution in both regions. However, there are some visually interesting cases in Cygnus-X where the outflows appear to be preferentially oriented with respect to local filaments (e.g., in DR 15) or other features. A similar proportion of outflows in both regions ($\sim 10\%$) are organised into "multipolar" systems of outflows who axes are crossing. Although to some extent visual projection cannot be ruled out as a cause of these, given that the incidence of precessing outflows is higher in these systems than in the general population, it is more likely that they are caused by binarity or multiplicity in the driving sources.

- Most bipolar outflows in Auriga and Cassiopeia were straight, whereas 30 % of outflows in Cygnus-X had an angle difference between the lobes of over $10°$. This could be caused by the denser ambient medium in Cygnus-X deflecting the outflows, but could also be partly-extincted multipolar systems. This would also explain why Auriga and Cassiopeia has a slightly higher fraction of multipolar systems than Cygnus-X (12 % vs. 9 %).

- Of the 413 bipolar and single-sided outflows found in Cygnus-X, distances have been determined towards 341 (82 %) of them. Auriga and Cassiopeia had 74 bipolar and single-sided flows; of these, distances have been obtained for 49 of them (66 %). For consistency, the Bayesian distance calculator of Reid et al. (2016) was used in both regions.

- The typical outflow in the two samples is short (total length < 0.4 pc) with one lobe around 30 % longer than the other. This is most likely due in part to inclination effects that were not corrected for, as well as the fact that many of the outflows are misaligned. Hence the lengths can be considered as lower limits. Up to just over 1 pc, the length distributions are the same in every region studied, including Perseus west (Davis et al., 2008) and Orion A (Davis et al., 2009; Stanke, 2003).

- The typical outflow is also faint ($\sim 1 \times 10^{-3}$ L$_\odot$) and very few have luminosities over 0.1 L$_\odot$. Therefore, almost all of the detected outflows are driven by low or intermediate-luminosity objects. The lobe flux ratios are almost homogeneous distributed, meaning that although the total luminosities are governed by a power law, the lobe luminosity distribution has too many very faint objects for a power law to apply.

- There is some evidence for a maximum length for outflows in the $1-0\,$S(1) line of H$_2$. This agrees with the findings of Navarete et al. (2015). The limiting factor is most likely to be the extent of molecular material in the parent cloud of sufficient density to allow the excitation of H$_2$ with the outflows only observable using optical tracers thereafter. Outflow lengths

and morphologies in molecular lines therefore provide more of an indication of the extent and distribution of material close to the driving source rather than being a reflection of the properties of the driving source itself.

- There is a moderate correlation between the length and luminosity of an outflow, but these properties are unlikely to be governed by the same physical processes. Contrary to the findings of Stanke (2003), no correlation was found between the evolutionary stage of the driving sources and the lengths or luminosities. The most luminous outflows were preferentially associated with high-luminosity driving sources. Therefore, whilst the outflow luminosity might be partly determined by the mass (or mass-loss rate) of the driving source, the outflow lengths are most likely determined by the nature of the local environment. Therefore, it can be concluded that the key parameters of the outflows in the $1-0\,\mathrm{S}\,(1)$ line of H_2 are mainly governed by environmental factors and have little dependence on the evolution of the driving source.

7.3 Future work

- Searching the UWISH2 images for H_2 emission features, and then classifying them into outflows and measuring their properties was extremely time-intensive. For this work, a total area of about 78 square degrees was searched for outflows, and of the 209 square degrees of the original UWISH2 survey, only the 33 square degrees from Serpens and Aquila has been examined. This means that ~ 175 square degrees of UWISH2 images from the Galactic plane have yet to be viewed. From the areas that have been analysed so far, 801 MHOs have been found. There remain 176 square degrees of images in the Galactic plane that are yet to be analysed, suggesting at least 800 outflows that remain undetected. This analysis would be extremely time-intensive to carry out. Even with the automatic feature detection, the images must still be searched manually to detect the emission features, and the outflow properties must be measured. There are two possible ways that this could be most feasibly achieved: via machine learning, or with a citizen science project.

- The outflows discovered in Cygnus-X and Auriga and Cassiopeia have provided new insights into the properties of the most typical outflows. Although unique and interesting objects have also been detected, they are very different from the newly discovered population of mainly low- and intermediate luminosity objects that are arguably more representative of the ongoing star formation in the Galaxy. There is a wealth of star formation activity occurring outside of the highly-targeted high-mass complexes, and in order to increase the quality of the statistics coming from those regions, it would be advantageous to revisit them with unbiased coverage using the same resolution and depth as has been achieved with UWISH2.

- It is likely that some fraction of outflows from this survey have been assigned the incorrect driving source. This is particularly true for the single-sided outflows, where follow-up proper motion studies of the individual knots would assist in pinpointing the correct driving

sources. Combining this with further observations in CO or SiO would also allow the protostellar properties such as bolometric luminosity and mass to be determined, and for the momentum outputs and energetics of the jets to be measured.

- In addition, there seem to be mixed results from different studies regarding the orientation of outflows with respect to local filaments, cores or local magnetic fields. The orientation with respect to filaments can be determined using Herschel data. Using the large dataset of outflows determined from UWISH2, it would be possible to statistically investigate whether or not the outflows are indeed randomly oriented, whether they are preferentially oriented with respect to filaments, and it is the filaments themselves that are randomly oriented, and whether or not it is indeed only high-luminosity outflows that are preferentially oriented with respect to the local filaments.

- This study has also highlighted potential FU-Ori, EX-Or and MNor candidates, based on the dynamical timescales determined for the typical gaps between subsequent knots. Spectroscopic studies of these candidate objects would allow their nature to be determined, and could potentially increase the known populations of each type of object.

- Finally, although the second data release has come too late to be used in this work, GAIA DR2 provides highly accurate parallax measurements for billions of stars across the Galactic plane. Using this data to determine truly accurate distances towards the outflows would allow the inherent uncertainties to be reduced so that scatter present in the data that relies on the distance can be reduced, thus placing further constraints on the nature of the parameter distributions.

Bibliography

Adams, F. C., C. J. Lada, and F. H. Shu (1987). "Spectral evolution of young stellar objects". In: *ApJ* 312, pp. 788–806. DOI: 10.1086/164924.

Agra-Amboage, V. et al. (2009). "[O I] sub-arcsecond study of a microjet from an intermediate mass young star: RY Tauri". In: *A&A* 493, pp. 1029–1041. DOI: 10.1051/0004-6361:200810025.

Alves, J. F., C. J. Lada, and E. A. Lada (2001). "Internal structure of a cold dark molecular cloud inferred from the extinction of background starlight". In: *Nature* 409, pp. 159–161.

Ambartsumyan, V. A. (1971). "Fuors". In: *Astrophysics* 7, pp. 331–339. DOI: 10.1007/BF01003016.

Anderson, L. D. et al. (2009). "The Molecular Properties of Galactic H II Regions". In: *ApJS* 181, pp. 255–271. DOI: 10.1088/0067-0049/181/1/255. arXiv: 0810.3685.

André, P., S. Basu, and S. Inutsuka (2009). "The formation and evolution of prestellar cores". In: *Structure Formation in Astrophysics*. Ed. by G. Chabrier. Cambridge University Press, p. 254.

Andre, P., D. Ward-Thompson, and M. Barsony (1993). "Submillimeter continuum observations of Rho Ophiuchi A - The candidate protostar VLA 1623 and prestellar clumps". In: *ApJ* 406, pp. 122–141. DOI: 10.1086/172425.

André, P. et al. (2014). "From Filamentary Networks to Dense Cores in Molecular Clouds: Toward a New Paradigm for Star Formation". In: *Protostars and Planets VI*, pp. 27–51. DOI: 10.2458/azu_uapress_9780816531240-ch002. arXiv: 1312.6232.

Antoniucci, S. et al. (2008). "Accretion and ejection properties of embedded protostars: the case of HH26, HH34, and HH46 IRS". In: *A&A* 479, pp. 503–514. DOI: 10.1051/0004-6361:20077468. arXiv: 0710.5609.

Appenzeller, I. and R. Mundt (1989). "T Tauri stars". In: *A&A Rev.* 1, pp. 291–334. DOI: 10.1007/BF00873081.

Arce, H. G. and A. A. Goodman (2002). "Bow Shocks, Wiggling Jets, and Wide-Angle Winds: A High-Resolution Study of the Entrainment Mechanism of the PV Cephei Molecular (CO) Outflow". In: *ApJ* 575, pp. 928–949. DOI: 10.1086/341426. eprint: astro-ph/0204434.

Arce, H. G. et al. (2007). "Molecular Outflows in Low- and High-Mass Star-forming Regions". In: *Protostars and Planets V*, pp. 245–260. eprint: astro-ph/0603071.

Arce, H. G. et al. (2008). "Complex Molecules in the L1157 Molecular Outflow". In: *ApJ* 681, p. L21. DOI: 10.1086/590110. arXiv: 0805.2550.

Arce, H. G. et al. (2010). "The COMPLETE Survey of Outflows in Perseus". In: *ApJ* 715, pp. 1170–1190. DOI: 10.1088/0004-637X/715/2/1170. arXiv: 1005.1714 [astro-ph.SR].

Arce, H. G. et al. (2011). "A Bubbling Nearby Molecular Cloud: COMPLETE Shells in Perseus". In: *ApJ* 742, 105, p. 105. DOI: 10.1088/0004-637X/742/2/105. arXiv: 1109.3368 [astro-ph.SR].

Aspin, C. (1998). "Discovery of multiple non-axially symmetric near-IR bow shocks around the pre-main sequence binary {AFGL 961}". In: *A&A* 335, pp. 1040–1048.

Audard, M. et al. (2014). "Episodic Accretion in Young Stars". In: *Protostars and Planets VI*, pp. 387–410. DOI: `10.2458/azu_uapress_9780816531240-ch017`. arXiv: `1401.3368 [astro-ph.SR]`.

Bacciotti, F. et al. (2002). "Hubble Space Telescope/STIS Spectroscopy of the Optical Outflow from DG Tauri: Indications for Rotation in the Initial Jet Channel". In: *ApJ* 576, pp. 222–231. DOI: `10.1086/341725`. eprint: `astro-ph/0206175`.

Bachiller, R. (1996). "Bipolar Molecular Outflows from Young Stars and Protostars". In: *ARA&A* 34, pp. 111–154. DOI: `10.1146/annurev.astro.34.1.111`.

Bally, J. (2007). "Jets from young stars". In: *Ap&SS* 311, pp. 15–24. DOI: `10.1007/s10509-007-9531-7`.

– (2016). "Protostellar Outflows". In: *ARA&A* 54, pp. 491–528. DOI: `10.1146/annurev-astro-081915-023341`.

Bally, J. and D. Devine (1997). "Giant Herbig-Haro Flows". In: *Herbig-Haro Flows and the Birth of Stars*. Ed. by B. Reipurth and C. Bertout. Vol. 182. IAU Symposium, pp. 29–38.

Bally, J., B. Reipurth, and C. J. Davis (2007). "Observations of Jets and Outflows from Young Stars". In: *Protostars and Planets V*, pp. 215–230.

Bally, J. and N. Z. Scoville (1980). "Structure and evolution of molecular clouds near H II regions. I - CO observations of an expanding molecular shell surrounding the Pelican Nebula". In: *ApJ* 239, pp. 121–136. DOI: `10.1086/158094`.

Bally, J. et al. (2014). "Outflows, Dusty Cores, and a Burst of Star Formation in the North America and Pelican Nebulae". In: *AJ* 148, 120, p. 120. DOI: `10.1088/0004-6256/148/6/120`. arXiv: `1409.6762 [astro-ph.SR]`.

Banerjee, R. and R. E. Pudritz (2006). "Outflows and Jets from Collapsing Magnetized Cloud Cores". In: *ApJ* 641, pp. 949–960. DOI: `10.1086/500496`. eprint: `astro-ph/0508374`.

Banerjee, R., R. E. Pudritz, and D. W. Anderson (2006). "Supersonic turbulence, filamentary accretion and the rapid assembly of massive stars and discs". In: *MNRAS* 373, pp. 1091–1106. DOI: `10.1111/j.1365-2966.2006.11089.x`. eprint: `astro-ph/0609428`.

Bate, M. R. and I. A. Bonnell (2005). "The origin of the initial mass function and its dependence on the mean Jeans mass in molecular clouds". In: *MNRAS* 356, pp. 1201–1221. DOI: `10.1111/j.1365-2966.2004.08593.x`. eprint: `astro-ph/0411084`.

Bate, M. R., I. A. Bonnell, and V. Bromm (2002). "The formation of close binary systems by dynamical interactions and orbital decay". In: *MNRAS* 336, pp. 705–713. DOI: `10.1046/j.1365-8711.2002.05775.x`. eprint: `astro-ph/0212403`.

Bate, M. R. et al. (2000). "Observational implications of precessing protostellar discs and jets". In: *MNRAS* 317, pp. 773–781. DOI: `10.1046/j.1365-8711.2000.03648.x`.

Beck, T. L. et al. (2007). "The Structure of the Inner HH 34 Jet from Optical Integral Field Spectroscopy". In: *AJ* 133, pp. 1221–1235. DOI: `10.1086/511269`. eprint: `astro-ph/0611865`.

Bergin, E. A. and W. D. Langer (1997). "Chemical Evolution in Preprotostellar and Protostellar Cores". In: *ApJ* 486, pp. 316–328. DOI: `10.1086/304510`.

Berlanas, S. R. et al. (2018). "New massive members of Cygnus OB2". In: *A&A* 612, A50, A50. DOI: 10.1051/0004-6361/201731856. arXiv: 1711.06945 [astro-ph.SR].

Bernard, J. P. et al. (1999). "PRONAOS observations of MCLD 123.5 + 24.9: cold dust in the Polaris cirrus cloud". In: *A&A* 347, pp. 640–649.

Black, J. H. and A. Dalgarno (1976). "Interstellar H2 - The population of excited rotational states and the infrared response to ultraviolet radiation". In: *ApJ* 203, pp. 132–142. DOI: 10.1086/154055.

Blandford, R. D. and D. G. Payne (1982). "Hydromagnetic flows from accretion discs and the production of radio jets". In: *MNRAS* 199, pp. 883–903. DOI: 10.1093/mnras/199.4.883.

Bland-Hawthorn, J. and O. Gerhard (2016). "The Galaxy in Context: Structural, Kinematic, and Integrated Properties". In: *ARA&A* 54, pp. 529–596. DOI: 10.1146/annurev-astro-081915-023441. arXiv: 1602.07702.

Blitz, L. and F. H. Shu (1980). "The origin and lifetime of giant molecular cloud complexes". In: *ApJ* 238, pp. 148–157. DOI: 10.1086/157968.

Bodenheimer, P. (1995). "Angular Momentum Evolution of Young Stars and Disks". In: *ARA&A* 33, pp. 199–238. DOI: 10.1146/annurev.aa.33.090195.001215.

Bonnell, I. A., S. G. Vine, and M. R. Bate (2004). "Massive star formation: nurture, not nature". In: *MNRAS* 349, pp. 735–741. DOI: 10.1111/j.1365-2966.2004.07543.x. eprint: astro-ph/0401059.

Bonnell, I. A. et al. (2001). "Competitive accretion in embedded stellar clusters". In: *MNRAS* 323, pp. 785–794. DOI: 10.1046/j.1365-8711.2001.04270.x. eprint: astro-ph/0102074.

Boulanger, F. et al. (1988). "Small grains and IRAS colors". In: *ApJ* 332, pp. 328–334. DOI: 10.1086/166658.

Bouvier, J. et al. (1993). "Coyotes-I - the Photometric Variability and Rotational Evolution of T-Tauri Stars". In: *A&A* 272, p. 176.

Bouvier, J. et al. (2007). "Magnetospheric Accretion in Classical T Tauri Stars". In: *Protostars and Planets V*, pp. 479–494.

Brand, J. and L. Blitz (1993). "The Velocity Field of the Outer Galaxy". In: *A&A* 275, p. 67.

Cabrit, S. and A. Raga (2000). "Theoretical interpretation of the apparent deceleration in the HH 34 superjet". In: *A&A* 354, pp. 667–673.

Cabrit, S. et al. (2007). "PdBI sub-arcsecond study of the SiO microjet in HH212. Origin and collimation of class 0 jets". In: *A&A* 468, pp. L29–L32. DOI: 10.1051/0004-6361:20077387. arXiv: 0704.2685.

Cabrit, S. et al. (2012). "High SiO abundance in the HH212 protostellar jet". In: *A&A* 548, L2, p. L2. DOI: 10.1051/0004-6361/201219784. arXiv: 1211.1258.

Cambrésy, L. et al. (2002). "Extinction with 2MASS: Star Counts and Reddening toward the North America and Pelican Nebulae". In: *AJ* 123, pp. 2559–2573. DOI: 10.1086/339830. eprint: astro-ph/0201373.

Canto, J. and A. C. Raga (1991). "Mixing layers in stellar outflows". In: *ApJ* 372, pp. 646–658. DOI: 10.1086/170007.

Caratti o Garatti, A. et al. (2006). "H$_2$ active jets in the near IR as a probe of protostellar evolution". In: *A&A* 449, pp. 1077–1088. DOI: 10.1051/0004-6361:20054313.

Caratti o Garatti, A. et al. (2009). "First detection of acceleration and deceleration in protostellar jets? Time variability in the Chamaeleontis II outflows". In: *A&A* 502, pp. 579–597. DOI: 10.1051/0004-6361/200911664. arXiv: 0906.0561 [astro-ph.SR].

Caratti o Garatti, A. et al. (2012). "POISSON project. II. A multi-wavelength spectroscopic and photometric survey of young protostars in L 1641". In: *A&A* 538, A64, A64. DOI: 10.1051/0004-6361/201117781. arXiv: 1111.2455 [astro-ph.SR].

Caratti o Garatti, A. et al. (2015). "A near-infrared spectroscopic survey of massive jets towards extended green objects". In: *A&A* 573, A82, A82. DOI: 10.1051/0004-6361/201423992. arXiv: 1410.4041 [astro-ph.SR].

Carrasco-González, C. et al. (2010). "A Magnetized Jet from a Massive Protostar". In: *Science* 330, p. 1209. DOI: 10.1126/science.1195589. arXiv: 1011.6254 [astro-ph.GA].

Casali, M. et al. (2007). "The UKIRT wide-field camera". In: *A&A* 467, pp. 777–784. DOI: 10.1051/0004-6361:20066514.

Caselli, P. and P. C. Myers (1995). "The Line Width–Size Relation in Massive Cloud Cores". In: *ApJ* 446, p. 665. DOI: 10.1086/175825.

Caswell, J. L. et al. (1975). "Neutral hydrogen absorption measurements yielding kinematic distances for 42 continuum sources in the galactic plane". In: *A&A* 45, pp. 239–258.

Cesaroni, R. et al. (2017). "Chasing discs around O-type (proto)stars: Evidence from ALMA observations". In: *A&A* 602, A59, A59. DOI: 10.1051/0004-6361/201630184.

Cesaroni, R. et al. (2018). "Radio outburst from a massive (proto)star. When accretion turns into ejection". In: *ArXiv e-prints*. arXiv: 1802.04228 [astro-ph.SR].

Chen, C.-Y. and E. C. Ostriker (2014). "Formation of Magnetized Prestellar Cores with Ambipolar Diffusion and Turbulence". In: *ApJ* 785, 69, p. 69. DOI: 10.1088/0004-637X/785/1/69. arXiv: 1403.0582 [astro-ph.SR].

Ching, T.-C. et al. (2016). "Helical Magnetic Fields in the NGC 1333 IRAS 4A Protostellar Outflows". In: *ApJ* 819, 159, p. 159. DOI: 10.3847/0004-637X/819/2/159. arXiv: 1601.05229 [astro-ph.SR].

Choi, Y. K. et al. (2014). "Trigonometric Parallaxes of Star Forming Regions in the Perseus Spiral Arm". In: *ApJ* 790, 99, p. 99. DOI: 10.1088/0004-637X/790/2/99. arXiv: 1407.1609.

Chrysostomou, A. et al. (2008). "Investigating the transport of angular momentum from young stellar objects. Do H2 jets from class I YSOs rotate?" In: *A&A* 482, pp. 575–583. DOI: 10.1051/0004-6361:20078494. arXiv: 0802.1881.

Clark, B. G., V. Radhakrishnan, and R. W. Wilson (1962). "The Hydrogen Line in Absorption." In: *ApJ* 135, p. 151. DOI: 10.1086/147255.

Claussen, M. J. et al. (1998). "Distribution and Motion of the Water Masers near IRAS 05413-0104". In: *ApJ* 507, pp. L79–L82. DOI: 10.1086/311669.

Clemens, D. P. (1985). "Massachusetts-Stony Brook Galactic plane CO survey - The Galactic disk rotation curve". In: *ApJ* 295, pp. 422–428. DOI: 10.1086/163386.

Codella, C. et al. (2015). "Astrochemistry at work in the L1157-B1 shock: acetaldehyde formation". In: *MNRAS* 449, pp. L11–L15. DOI: 10.1093/mnrasl/slu204. arXiv: 1412.8318 [astro-ph.EP].

Coffey, D. et al. (2007). "Further Indications of Jet Rotation in New Ultraviolet and Optical Hubble Space Telescope STIS Spectra". In: *ApJ* 663, pp. 350–364. DOI: 10.1086/518100. eprint: astro-ph/0703271.

Cohen, M. and L. V. Kuhi (1979). "Observational studies of pre-main-sequence evolution". In: *ApJS* 41, pp. 743–843. DOI: 10.1086/190641.

Cohen, M., W. A. Wheaton, and S. T. Megeath (2003). "Spectral Irradiance Calibration in the Infrared. XIV. The Absolute Calibration of 2MASS". In: *AJ* 126, pp. 1090–1096. DOI: 10.1086/376474. eprint: astro-ph/0304350.

Comerón, F. and A. Pasquali (2005). "The ionizing star of the North America and Pelican nebulae". In: *A&A* 430, pp. 541–548. DOI: 10.1051/0004-6361:20041788.

Comerón, F. et al. (2002). "On the massive star contents of Cygnus OB2". In: *A&A* 389, pp. 874–888. DOI: 10.1051/0004-6361:20020648.

Connelley, Michael S. and Bo Reipurth (2018). "A Near-infrared Spectroscopic Survey of FU Orionis Objects". In: *ApJ* 861, 145, p. 145. DOI: 10.3847/1538-4357/aaba7b. arXiv: 1806.08880 [astro-ph.SR].

Contreras Peña, C. et al. (2014). "Extreme infrared variables from UKIDSS - I. A concentration in star-forming regions". In: *MNRAS* 439, pp. 1829–1854. DOI: 10.1093/mnras/stu063. arXiv: 1401.2336.

Contreras Peña, C. et al. (2017a). "A population of eruptive variable protostars in VVV". In: *MNRAS* 465, pp. 3011–3038. DOI: 10.1093/mnras/stw2801. arXiv: 1602.06267 [astro-ph.SR].

Contreras Peña, C. et al. (2017b). "Infrared spectroscopy of eruptive variable protostars from VVV". In: *MNRAS* 465, pp. 3039–3100. DOI: 10.1093/mnras/stw2802. arXiv: 1602.06269 [astro-ph.SR].

Crowther, Paul A. et al. (2010). "The R136 star cluster hosts several stars whose individual masses greatly exceed the accepted $150M_{solar}$ stellar mass limit". In: *MNRAS* 408, pp. 731–751. DOI: 10.1111/j.1365-2966.2010.17167.x. arXiv: 1007.3284 [astro-ph.SR].

Crutcher, R. M. (1999). "Magnetic Fields in Molecular Clouds: Observations Confront Theory". In: *ApJ* 520, pp. 706–713. DOI: 10.1086/307483.

Curtis, E. I. et al. (2010). "A submillimetre survey of the kinematics of the Perseus molecular cloud - II. Molecular outflows". In: *MNRAS* 408, pp. 1516–1539. DOI: 10.1111/j.1365-2966.2010.17214.x. arXiv: 1006.3218.

Cutri, R. M. and et al. (2013). "VizieR Online Data Catalog: AllWISE Data Release (Cutri+ 2013)". In: *VizieR Online Data Catalog* 2328.

Dame, T. M., D. Hartmann, and P. Thaddeus (2001). "The Milky Way in Molecular Clouds: A New Complete CO Survey". In: *ApJ* 547, pp. 792–813. DOI: 10.1086/318388. eprint: astro-ph/0009217.

Davis, C. J. et al. (2007). "WFCAM, Spitzer/IRAC and SCUBA observations of the massive star-forming region DR21/W75 - I. The collimated molecular jets". In: *MNRAS* 374, pp. 29–53. DOI: 10.1111/j.1365-2966.2006.11163.x. eprint: astro-ph/0610186.

Davis, C. J. et al. (2008). "A shallow though extensive H_2 2.122-μm imaging survey of Taurus-Auriga-Perseus - I. NGC 1333, L1455, L1448 and B1". In: *MNRAS* 387, pp. 954–968. DOI: 10.1111/j.1365-2966.2008.13247.x. arXiv: 0803.3075.

Davis, C. J. et al. (2009). "A census of molecular hydrogen outflows and their sources along the Orion A molecular ridge. Characteristics and overall distribution". In: *A&A* 496, pp. 153–176. DOI: 10.1051/0004-6361:200811096. arXiv: 0812.3733.

Davis, C. J. et al. (2010). "A general catalogue of molecular hydrogen emission-line objects (MHOs) in outflows from young stars". In: *A&A* 511, A24, A24. DOI: 10.1051/0004-6361/200913561. arXiv: 0910.5274 [astro-ph.SR].

Davis Jr., L. and J. L. Greenstein (1951). "The Polarization of Starlight by Aligned Dust Grains." In: *ApJ* 114, p. 206. DOI: 10.1086/145464.

Deb, S., R. Kothes, and E. Rosolowsky (2018). "A Case Study of Triggered Star Formation in Cygnus X". In: *MNRAS*. DOI: 10.1093/mnras/sty2389. arXiv: 1809.01619 [astro-ph.SR].

Devine, D. et al. (1997). "Kinematics and Evolution of the Giant HH34 Complex". In: *AJ* 114, p. 2095. DOI: 10.1086/118629.

Di Francesco, J. et al. (2001). "Infall, Outflow, Rotation, and Turbulent Motions of Dense Gas within NGC 1333 IRAS 4". In: *ApJ* 562, pp. 770–789. DOI: 10.1086/323854. eprint: astro-ph/0108022.

Dickel, H. R., H. Wendker, and J. H. Bieritz (1969). "The Cygnus X region. V. catalogue and distances of optically visible H II regions." In: *A&A* 1, pp. 270–280.

Dobbs, C. L. (2008). "GMC formation by agglomeration and self gravity". In: *MNRAS* 391, pp. 844–858. DOI: 10.1111/j.1365-2966.2008.13939.x. arXiv: 0809.1942.

Dobbs, C. L., I. A. Bonnell, and J. E. Pringle (2006). "The formation of molecular clouds in spiral galaxies". In: *MNRAS* 371, pp. 1663–1674. DOI: 10.1111/j.1365-2966.2006.10794.x. eprint: astro-ph/0602103.

Dougados, C. et al. (2010). "Deriving Physical Diagnostics from Observations". In: *Lecture Notes in Physics, Berlin Springer Verlag*. Ed. by P. J. V. Garcia and J. M. Ferreira. Vol. 793. Lecture Notes in Physics, Berlin Springer Verlag, p. 213. DOI: 10.1007/978-3-642-02289-0_7.

Draine, B. T., W. G. Roberge, and A. Dalgarno (1983). "Magnetohydrodynamic shock waves in molecular clouds". In: *ApJ* 264, pp. 485–507. DOI: 10.1086/160617.

Duarte-Cabral, A. et al. (2013). "CO outflows from high-mass Class 0 protostars in Cygnus-X". In: *A&A* 558, A125, A125. DOI: 10.1051/0004-6361/201321393. arXiv: 1308.6490.

Duley, W. W. and D. A. Williams (1993). "The formation of H2 on interstellar dust". In: *MNRAS* 260, pp. 37–42. DOI: 10.1093/mnras/260.1.37.

Dunham, M. M. et al. (2015). "Young Stellar Objects in the Gould Belt". In: *ApJS* 220, 11, p. 11. DOI: 10.1088/0067-0049/220/1/11. arXiv: 1508.03199.

Dwek, E. et al. (1997). "Detection and Characterization of Cold Interstellar Dust and Polycyclic Aromatic Hydrocarbon Emission, from COBE Observations". In: *ApJ* 475, pp. 565–579. DOI: 10.1086/303568. eprint: astro-ph/9610198.

Dyck, H. M. and C. A. Beichman (1974). "Observations of Infrared Polarization in the Orion Nebula". In: *ApJ* 194, pp. 57–64. DOI: 10.1086/153223.

Dye, S. et al. (2006). "The UKIRT Infrared Deep Sky Survey Early Data Release". In: *MNRAS* 372, pp. 1227–1252. DOI: 10.1111/j.1365-2966.2006.10928.x. eprint: astro-ph/0603608.

Eislöffel, J. (2000). "Parsec-scale molecular H_2 outflows from young stars". In: *A&A* 354, pp. 236–246.

Eisloffel, J. et al. (1994). "Near-infrared observations of the HH 46/47 system". In: *ApJ* 422, pp. L91–L93. DOI: 10.1086/187220.

Eisloffel, J. et al. (1996). "Molecular Hydrogen in the Outflow From CEP E". In: *AJ* 112, p. 2086. DOI: 10.1086/118165.

Eislöffel, J. et al. (2003). "Molecular Outflows in the Young Open Cluster IC 348". In: *ApJ* 595, pp. 259–265. DOI: 10.1086/377216. eprint: astro-ph/0306067.

Ellerbroek, L. E. et al. (2013). "The outflow history of two Herbig-Haro jets in RCW 36: HH 1042 and HH 1043". In: *A&A* 551, A5, A5. DOI: 10.1051/0004-6361/201220635. arXiv: 1212.4144 [astro-ph.SR].

Elmegreen, B. G. (1993). "Formation of interstellar clouds and structure". In: *Protostars and Planets III*. Ed. by E. H. Levy and J. I. Lunine, pp. 97–124.

– (2000). "Star Formation in a Crossing Time". In: *ApJ* 530, pp. 277–281. DOI: 10.1086/308361. eprint: astro-ph/9911172.

Elmegreen, B. G. and E. Falgarone (1996). "A Fractal Origin for the Mass Spectrum of Interstellar Clouds". In: *ApJ* 471, p. 816. DOI: 10.1086/178009.

Evans II, N. J. et al. (2009). "The Spitzer c2d Legacy Results: Star-Formation Rates and Efficiencies; Evolution and Lifetimes". In: *ApJS* 181, 321-350, pp. 321–350. DOI: 10.1088/0067-0049/181/2/321. arXiv: 0811.1059.

Ewen, H. I. and E. M. Purcell (1951). "Observation of a Line in the Galactic Radio Spectrum: Radiation from Galactic Hydrogen at 1,420 Mc./sec." In: *Nature* 168, p. 356. DOI: 10.1038/168356a0.

Federman, S. R., A. E. Glassgold, and J. Kwan (1979). "Atomic to molecular hydrogen transition in interstellar clouds". In: *ApJ* 227, pp. 466–473. DOI: 10.1086/156753.

Federrath, C. (2015). "Inefficient star formation through turbulence, magnetic fields and feedback". In: *MNRAS* 450, pp. 4035–4042. DOI: 10.1093/mnras/stv941. arXiv: 1504.03690 [astro-ph.SR].

Federrath, C. et al. (2014). "Modeling Jet and Outflow Feedback during Star Cluster Formation". In: *ApJ* 790, 128, p. 128. DOI: 10.1088/0004-637X/790/2/128. arXiv: 1406.3625 [astro-ph.SR].

Fedriani, R. et al. (2018). "Parsec-scale jets driven by high-mass young stellar objects. Connecting the au- and the parsec-scale jet in IRAS 13481-6124". In: *A&A* 616, A126, A126. DOI: 10.1051/0004-6361/201732180. arXiv: 1805.11512 [astro-ph.SR].

Feldt, C. and H. J. Wendker (1993). "The W 80 dark cloud: A case study of fragmentation. I - The observations". In: *A&AS* 100, pp. 287–303.

Feldt, M. et al. (1998). "The Chamaeleon infrared nebula revisited. Infrared imaging and spectroscopy of a young stellar object". In: *A&A* 332, pp. 849–856.

Fendt, C. (2011). "Jet Rotation Driven by Magnetohydrodynamic Shocks in Helical Magnetic Fields". In: *ApJ* 737, 43, p. 43. DOI: 10.1088/0004-637X/737/1/43. arXiv: 1105.6232.

Fernandez, M. et al. (1995). "Hα emission from pre-main sequence stars." In: *Astronomy and Astrophysics Supplement Series* 114, p. 439.

Ferrière, K. M. (2001). "The interstellar environment of our galaxy". In: *Reviews of Modern Physics* 73, pp. 1031–1066. DOI: 10.1103/RevModPhys.73.1031. eprint: astro-ph/0106359.

Field, G. B., W. B. Somerville, and K. Dressler (1966). "Hydrogen Molecules in Astronomy". In: *ARA&A* 4, p. 207. DOI: 10.1146/annurev.aa.04.090166.001231.

Field, G. B. et al. (1968). "Hydromagnetic Shock Waves and Their Infrared Emission in H i Regions". In: *ApJ* 151, p. 953. DOI: 10.1086/149496.

Figer, Donald F. (2005). "An upper limit to the masses of stars". In: *Nature* 434, pp. 192–194. DOI: 10.1038/nature03293. arXiv: astro-ph/0503193 [astro-ph].

Frank, A. et al. (2014). "Jets and Outflows from Star to Cloud: Observations Confront Theory". In: *Protostars and Planets VI*, pp. 451–474. DOI: 10.2458/azu_uapress_9780816531240-ch020. arXiv: 1402.3553 [astro-ph.SR].

Froebrich, D. and S. V. Makin (2016). "YSO jets in the Galactic plane from UWISH2 - III. Jets and outflows in Cassiopeia and Auriga". In: *MNRAS* 462, pp. 1444–1452. DOI: 10.1093/mnras/stw1766. arXiv: 1607.05049.

Froebrich, D. et al. (2003). "Far-infrared photometry of deeply embedded outflow sources". In: *MNRAS* 346, pp. 163–176. DOI: 10.1046/j.1365-2966.2003.07072.x. eprint: astro-ph/0311158.

Froebrich, D. et al. (2007). "A large-scale extinction map of the Galactic Anticentre from 2MASS". In: *MNRAS* 378, pp. 1447–1460. DOI: 10.1111/j.1365-2966.2007.11886.x. arXiv: 0704.2993.

Froebrich, D. et al. (2010). "Old star clusters in the FSR catalogue". In: *MNRAS* 409, pp. 1281–1288. DOI: 10.1111/j.1365-2966.2010.17390.x. arXiv: 1007.3410.

Froebrich, D. et al. (2011). "UWISH2 - the UKIRT Widefield Infrared Survey for H_2". In: *MNRAS* 413, pp. 480–492. DOI: 10.1111/j.1365-2966.2010.18149.x. arXiv: 1012.0782.

Froebrich, D. et al. (2015). "Extended H_2 emission line sources from UWISH2". In: *MNRAS* 454, pp. 2586–2605. DOI: 10.1093/mnras/stv1729. arXiv: 1507.08182.

Garden, R. P., A. P. G. Russell, and M. G. Burton (1990). "Images of shock-excited molecular hydrogen in young stellar outflows". In: *ApJ* 354, pp. 232–241. DOI: 10.1086/168683.

Gardiner, T. A. et al. (2003). "MHD Models and Laboratory Experiments of Jets". In: *Ap&SS* 287, pp. 69–74. DOI: 10.1023/B:ASTR.0000006202.93195.e3.

Gennaro, M. et al. (2011). "Mass segregation and elongation of the starburst cluster Westerlund 1". In: *MNRAS* 412, pp. 2469–2488. DOI: 10.1111/j.1365-2966.2010.18068.x. arXiv: 1011.5223.

Gledhill, T. M. and D. Froebrich (2017). "Planetary Nebulae in the UWISH2 Galactic Plane survey". In: *Planetary Nebulae: Multi-Wavelength Probes of Stellar and Galactic Evolution*. Ed. by X. Liu, L. Stanghellini, and A. Karakas. Vol. 323. IAU Symposium, pp. 32–35. DOI: 10.1017/S1743921317000813.

Gledhill, T. M. et al. (2018). "Planetary nebulae in the UWISH2 survey". In: *MNRAS* 479, pp. 3759–3777. DOI: 10.1093/mnras/sty1580. arXiv: 1807.01503.

Goldsmith, P. F. (1987). "Molecular clouds - an overview". In: *Interstellar Processes*. Ed. by D. J. Hollenbach and H. A. Thronson Jr. Vol. 134. Astrophysics and Space Science Library, pp. 51–70. DOI: 10.1007/978-94-009-3861-8_3.

Gong, M. and E. C. Ostriker (2015). "Prestellar Core Formation, Evolution, and Accretion from Gravitational Fragmentation in Turbulent Converging Flows". In: *ApJ* 806, 31, p. 31. DOI: 10.1088/0004-637X/806/1/31. arXiv: 1504.02140 [astro-ph.SR].

Goodwin, S. P. et al. (2007). "The Fragmentation of Cores and the Initial Binary Population". In: *Protostars and Planets V*, pp. 133–147. eprint: astro-ph/0603233.

Gordon, K. D. et al. (2003). "A Quantitative Comparison of the Small Magellanic Cloud, Large Magellanic Cloud, and Milky Way Ultraviolet to Near-Infrared Extinction Curves". In: *ApJ* 594, pp. 279–293. DOI: 10.1086/376774. eprint: astro-ph/0305257.

Gottschalk, M. et al. (2012). "The JCMT ^{12}CO(3-2) survey of the Cygnus X region. I. A pathfinder". In: *A&A* 541, A79, A79. DOI: 10.1051/0004-6361/201118600. arXiv: 1202.0832.

Grasha, K. et al. (2017). "Hierarchical Star Formation in Turbulent Media: Evidence from Young Star Clusters". In: *ApJ* 842, 25, p. 25. DOI: 10.3847/1538-4357/aa740b. arXiv: 1705.06281.

Green, D. A. (2009). "A revised Galactic supernova remnant catalogue". In: *Bulletin of the Astronomical Society of India* 37, pp. 45–61. arXiv: 0905.3699 [astro-ph.HE].

Greene, T. (2001). "Protostars". In: *American Scientist* 89, p. 316. DOI: 10.1511/2001.4.316.

Greene, T. P. et al. (1994). "Further mid-infrared study of the rho Ophiuchi cloud young stellar population: Luminosities and masses of pre-main-sequence stars". In: *ApJ* 434, pp. 614–626. DOI: 10.1086/174763.

Greenhill, L. J. et al. (1998). "Coexisting conical bipolar and equatorial outflows from a high-mass protostar". In: *Nature* 396, pp. 650–653. DOI: 10.1038/25299. eprint: astro-ph/9811318.

Greenhill, L. J. et al. (2013). "Dynamical Evidence for a Magnetocentrifugal Wind from a 20 M$_\odot$ Binary Young Stellar Object". In: *ApJ* 770, L32, p. L32. DOI: 10.1088/2041-8205/770/2/L32. arXiv: 1305.4150.

Gregersen, E. M. and N. J. Evans II (2000). "How to Identify Pre-Protostellar Cores". In: *ApJ* 538, pp. 260–267. DOI: 10.1086/309114. eprint: astro-ph/0003015.

Günther, H. M. (2013). "Accretion, winds and outflows in young stars". In: *Astronomische Nachrichten* 334, p. 67. DOI: 10.1002/asna.201211770. arXiv: 1210.4182 [astro-ph.SR].

Hagen, J. P., A. E. Lilley, and E. F. McClain (1955). "Absorption of 21-CM Radiation by Interstellar Hydrogen." In: *ApJ* 122, p. 361. DOI: 10.1086/146096.

Hambly, N. C. et al. (2008). "The WFCAM Science Archive". In: *MNRAS* 384, pp. 637–662. DOI: 10.1111/j.1365-2966.2007.12700.x. arXiv: 0711.3593.

Haro, G. (1952). "Herbig's Nebulous Objects Near NGC 1999." In: *ApJ* 115, p. 572. DOI: 10.1086/145576.

Hartigan, P. et al. (2005). "Proper Motions of the HH 47 Jet Observed with the Hubble Space Telescope". In: *AJ* 130, pp. 2197–2205. DOI: 10.1086/491673.

Hartmann, L. (2002). "Flows, Fragmentation, and Star Formation. I. Low-Mass Stars in Taurus". In: *ApJ* 578, pp. 914–924. DOI: 10.1086/342657. eprint: astro-ph/0207216.

Hartmann, L. and K. B. MacGregor (1982). "Protostellar mass and angular momentum loss". In: *ApJ* 259, pp. 180–192. DOI: 10.1086/160158.

Hartmann, L. and J. R. Stauffer (1989). "Additional measurements of pre-main-sequence stellar rotation". In: *AJ* 97, pp. 873–880. DOI: 10.1086/115033.

Hartmann, L. et al. (1998). "Accretion and the Evolution of T Tauri Disks". In: *ApJ* 495, pp. 385–400. DOI: 10.1086/305277.

Hayashi, C. (1966). "Evolution of Protostars". In: *ARA&A* 4, p. 171. DOI: 10.1146/annurev.aa.04.090166.001131.

Heiderman, A. and N. J. Evans II (2015). "The Gould Belt 'MISFITS' Survey: The Real Solar Neighborhood Protostars". In: *ApJ* 806, 231, p. 231. DOI: 10.1088/0004-637X/806/2/231. arXiv: 1503.06810.

Herbig, G. H. (1951). "The Spectra of Two Nebulous Objects Near NGC 1999." In: *ApJ* 113, pp. 697–699. DOI: 10.1086/145440.

– (1960). "The Spectra of Be- and Ae-Type Stars Associated with Nebulosity". In: *ApJS* 4, p. 337. DOI: 10.1086/190050.

– (1962). "The properties and problems of T Tauri stars and related objects." In: *Advances in Astronomy and Astrophysics* 1, pp. 47–103.

– (1989). "FU Orionis eruptions." In: *European Southern Observatory Conference and Workshop Proceedings*. Ed. by B. Reipurth. Vol. 33. European Southern Observatory Conference and Workshop Proceedings, pp. 233–246.

– (2008). "History and Spectroscopy of EXor Candidates". In: *AJ* 135, pp. 637–648. DOI: 10.1088/0004-6256/135/2/637.

Herbst, W. (1975). "R-associations III. Local optical spiral structure". In: *AJ* 80, p. 503. DOI: 10.1086/111771.

Hewett, P. C. et al. (2006). "The UKIRT Infrared Deep Sky Survey ZY JHK photometric system: passbands and synthetic colours". In: *MNRAS* 367, pp. 454–468. DOI: 10.1111/j.1365-2966.2005.09969.x. eprint: astro-ph/0601592.

Hirota, Tomoya et al. (2017). "Disk-driven rotating bipolar outflow in Orion Source I". In: *Nature Astronomy* 1, 0146, p. 0146. DOI: 10.1038/s41550-017-0146. arXiv: 1712.04606 [astro-ph.SR].

Hodapp, K.-W. and E. F. Ladd (1995). "Bipolar Jets from Extremely Young Stars Observed in Molecular Hydrogen Emission". In: *ApJ* 453, p. 715. DOI: 10.1086/176432.

Hollenbach, D. (1997). "The Physics of Molecular Shocks in YSO Outflows". In: *Herbig-Haro Flows and the Birth of Stars*. Ed. by B. Reipurth and C. Bertout. Vol. 182. IAU Symposium, pp. 181–198.

Hollenbach, D. and E. E. Salpeter (1971). "Surface Recombination of Hydrogen Molecules". In: *ApJ* 163, p. 155. DOI: 10.1086/150754.

Ikhsanov, R. N. (1961). "On the Nature of Cyg X". In: *Soviet Ast.* 4, p. 923.

Ilee, J. D. et al. (2016). "G11.92-0.61 MM1: a Keplerian disc around a massive young proto-O star". In: *MNRAS* 462, pp. 4386–4401. DOI: 10.1093/mnras/stw1912. arXiv: 1608.05561 [astro-ph.SR].

Ilovaisky, S. A. and J. Lequeux (1972). "A Study of Galactic Supernova Remnants. I. Distances, Radio Luminosity Function and Galactic Distribution". In: *A&A* 18, pp. 169–185.

Ioannidis, G. and D. Froebrich (2012a). "YSO jets in the Galactic plane from UWISH2 - I. MHO catalogue for Serpens and Aquila". In: *MNRAS* 421, pp. 3257–3265. DOI: 10.1111/j.1365-2966.2012.20550.x. arXiv: 1201.3237.

– (2012b). "YSO jets in the Galactic plane from UWISH2 - II. Outflow luminosity and length distributions in Serpens and Aquila". In: *MNRAS* 425, pp. 1380–1393. DOI: 10.1111/j.1365-2966.2012.21556.x. arXiv: 1206.5095.

Irwin, M. J. et al. (2004). "VISTA data flow system: pipeline processing for WFCAM and VISTA". In: *Optimizing Scientific Return for Astronomy through Information Technologies*. Ed. by P. J. Quinn and A. Bridger. Vol. 5493. Proc. SPIE, pp. 411–422. DOI: 10.1117/12.551449.

Ishihara, D. et al. (2010). "The AKARI/IRC mid-infrared all-sky survey". In: *A&A* 514, A1, A1. DOI: 10.1051/0004-6361/200913811. arXiv: 1003.0270 [astro-ph.IM].

Jappsen, A.-K. and R. S. Klessen (2004). "Protostellar angular momentum evolution during gravo-turbulent fragmentation". In: *A&A* 423, pp. 1–12. DOI: 10.1051/0004-6361:20040220. eprint: astro-ph/0402361.

Jeans, J. H. (1902). "The Stability of a Spherical Nebula". In: *Philosophical Transactions of the Royal Society of London Series A* 199, pp. 1–53. DOI: 10.1098/rsta.1902.0012.

Jenkins, E. B. and B. D. Savage (1974). "Ultraviolet photometry from the Orbiting Astronomical Observatory. XIV. An extension of the survey of Lyman-alpha absorption from interstellar hydrogen." In: *ApJ* 187, pp. 243–255. DOI: 10.1086/152620.

Jiang, Z.-b. et al. (2004). "Properties of the exciting source of the outflow in iras 20231+3440 region". In: *Chinese Astron. Astrophys.* 28, pp. 299–307. DOI: 10.1016/j.chinastron.2004.07.013.

Jiang, Z. et al. (2003). "A Near-Infrared Study of the Star-forming Region S269". In: *ApJ* 596, pp. 1064–1079. DOI: 10.1086/378150.

Joy, A. H. (1945). "T Tauri Variable Stars." In: *ApJ* 102, p. 168. DOI: 10.1086/144749.

Kahn, F. D. (1974). "Cocoons around early-type stars". In: *A&A* 37, pp. 149–162.

Katz, N. et al. (1999). "Molecular Hydrogen Formation on Astrophysically Relevant Surfaces". In: *ApJ* 522, pp. 305–312. DOI: 10.1086/307642. eprint: astro-ph/9906071.

Kenyon, S. J. and L. Hartmann (1995). "Pre-Main-Sequence Evolution in the Taurus-Auriga Molecular Cloud". In: *ApJS* 101, p. 117. DOI: 10.1086/192235.

Kerr, F. J. and G. Westerhout (1965). "Distribution of Interstellar Hydrogen". In: *Giornale di Astronomia*. Ed. by A. Blaauw and M. Schmidt. the University of Chicago Press, p. 167.

Khanzadyan, T. et al. (2004). "An unbiased search for the signatures of protostars in the ρ Ophiuchi A molecular cloud. I. Near-infrared observations". In: *A&A* 426, pp. 171–183. DOI: `10.1051/0004-6361:20041241`.

Khanzadyan, T. et al. (2011). "GM 2-4: a signpost for low- and intermediate-mass star formation". In: *MNRAS* 418, pp. 1994–2003. DOI: `10.1111/j.1365-2966.2011.19618.x`. arXiv: `1108.2193`.

Khanzadyan, T. et al. (2012). "A wide-field near-infrared H_2 2.122 μm line survey of the Braid Nebula star formation region in Cygnus OB7". In: *A&A* 542, A111, A111. DOI: `10.1051/0004-6361/201219124`. arXiv: `1205.1449`.

King, A. L. et al. (2015). "The Rate of Gas Accretion onto Black Holes Drives Jet Velocity". In: *ApJ* 799, L8, p. L8. DOI: `10.1088/2041-8205/799/1/L8`. arXiv: `1412.5695 [astro-ph.HE]`.

Kirk, J. M., D. Ward-Thompson, and P. André (2005). "The initial conditions of isolated star formation - VI. SCUBA mappingof pre-stellar cores". In: *MNRAS* 360, pp. 1506–1526. DOI: `10.1111/j.1365-2966.2005.09145.x`. eprint: `astro-ph/0505190`.

Klessen, R. S. et al. (2005). "Quiescent and Coherent Cores from Gravoturbulent Fragmentation". In: *ApJ* 620, pp. 786–794. DOI: `10.1086/427255`. eprint: `astro-ph/0306055`.

Knödlseder, J. (2000). "Cygnus OB2 - a young globular cluster in the Milky Way". In: *A&A* 360, pp. 539–548. eprint: `astro-ph/0007442`.

Kobayashi, Y. et al. (1980). "Narrow-Band Polarimetry of the Becklin/neugebauer Object and AFGL2591 Between 2-MICRONS and 4-MICRONS". In: *PASJ* 32, p. 295.

Kritsuk, A. G., C. T. Lee, and M. L. Norman (2013). "A supersonic turbulence origin of Larson's laws". In: *MNRAS* 436, pp. 3247–3261. DOI: `10.1093/mnras/stt1805`. arXiv: `1309.5926 [astro-ph.GA]`.

Krumholz, M. R., R. I. Klein, and C. F. McKee (2007). "Radiation-Hydrodynamic Simulations of Collapse and Fragmentation in Massive Protostellar Cores". In: *ApJ* 656, pp. 959–979. DOI: `10.1086/510664`. eprint: `astro-ph/0609798`.

Krumholz, M. R. et al. (2009). "The Formation of Massive Star Systems by Accretion". In: *Science* 323, p. 754. DOI: `10.1126/science.1165857`. arXiv: `0901.3157 [astro-ph.SR]`.

Krumholz, M. and A. Burkert (2010). "On the Dynamics and Evolution of Gravitational Instability-dominated Disks". In: *ApJ* 724, pp. 895–907. DOI: `10.1088/0004-637X/724/2/895`. arXiv: `1003.4513`.

Kryukova, E. et al. (2014). "The Dependence of Protostellar Luminosity on Environment in the Cygnus-X Star-forming Complex". In: *AJ* 148, 11, p. 11. DOI: `10.1088/0004-6256/148/1/11`.

Kuiper, R., N. J. Turner, and H. W. Yorke (2016). "Protostellar Outflows and Radiative Feedback from Massive Stars. II. Feedback, Star-formation Efficiency, and Outflow Broadening". In: *ApJ* 832, 40, p. 40. DOI: `10.3847/0004-637X/832/1/40`. arXiv: `1609.05208 [astro-ph.SR]`.

Kuiper, R., H. W. Yorke, and N. J. Turner (2015). "Protostellar Outflows and Radiative Feedback from Massive Stars". In: *ApJ* 800, 86, p. 86. DOI: 10.1088/0004-637X/800/2/86. arXiv: 1412.6528 [astro-ph.SR].

Kuiper, R. et al. (2010). "Circumventing the Radiation Pressure Barrier in the Formation of Massive Stars via Disk Accretion". In: *ApJ* 722, pp. 1556–1576. DOI: 10.1088/0004-637X/722/2/1556. arXiv: 1008.4516 [astro-ph.SR].

Kwan, J. and E. Tademaru (1988). "Jets from T Tauri stars - Spectroscopic evidence and collimation mechanism". In: *ApJ* 332, pp. L41–L44. DOI: 10.1086/185262.

Lada, C. J. (1985). "Cold outflows, energetic winds, and enigmatic jets around young stellar objects". In: *ARA&A* 23, pp. 267–317. DOI: 10.1146/annurev.aa.23.090185.001411.

Lada, C. J. and E. A. Lada (2003). "Embedded Clusters in Molecular Clouds". In: *ARA&A* 41, pp. 57–115. DOI: 10.1146/annurev.astro.41.011802.094844. eprint: astro-ph/0301540.

Lada, C. J., M. Lombardi, and J. F. Alves (2010). "On the Star Formation Rates in Molecular Clouds". In: *ApJ* 724, pp. 687–693. DOI: 10.1088/0004-637X/724/1/687. arXiv: 1009.2985.

Lada, C. J. and B. A. Wilking (1984). "The nature of the embedded population in the Rho Ophiuchi dark cloud - Mid-infrared observations". In: *ApJ* 287, pp. 610–621. DOI: 10.1086/162719.

Lada, C. J. et al. (2008). "The Nature of the Dense Core Population in the Pipe Nebula: Thermal Cores Under Pressure". In: *ApJ* 672, 410-422, pp. 410–422. DOI: 10.1086/523837. arXiv: 0709.1164.

Lagache, G. et al. (1998). "The interstellar cold dust observed by COBE". In: *A&A* 333, pp. 709–720. eprint: astro-ph/9812474.

Lagache, G. et al. (1999). "First detection of the warm ionised medium dust emission. Implication for the cosmic far-infrared background". In: *A&A* 344, pp. 322–332. eprint: astro-ph/9901059.

Larson, R. B. (1972). "The Collapse of a Rotating Cloud". In: *MNRAS* 156, p. 437. DOI: 10.1093/mnras/156.4.437.

– (1985). "Cloud fragmentation and stellar masses". In: *MNRAS* 214, pp. 379–398. DOI: 10.1093/mnras/214.3.379.

– (2003). "The physics of star formation". In: *Reports on Progress in Physics* 66, pp. 1651–1697. DOI: 10.1088/0034-4885/66/10/R03. eprint: astro-ph/0306595.

Laugalys, V. and V. Straižys (2002). "CCD Photometry and Classification of Stars in the North America and Pelican Nebulae Region. I. Molėtai Photometry". In: *Baltic Astronomy* 11, pp. 205–218. eprint: astro-ph/0209449.

Laugalys, V. et al. (2006). "CCD Photometry and Classification of Stars in the North America and Pelican Nebulae Region. III. The Dark Cloud L935". In: *Baltic Astronomy* 15, pp. 483–510.

Lee, C.-F. et al. (2000). "CO Outflows from Young Stars: Confronting the Jet and Wind Models". In: *ApJ* 542, pp. 925–945. DOI: 10.1086/317056.

Lee, C.-F. et al. (2001). "Hydrodynamic Simulations of Jet- and Wind-driven Protostellar Outflows". In: *ApJ* 557, pp. 429–442. DOI: 10.1086/321648. eprint: astro-ph/0104373.

Lee, C.-F. et al. (2015). "Jet Motion, Internal Working Surfaces, and Nested Shells in the Protostellar System HH 212". In: *ApJ* 805, 186, p. 186. DOI: 10.1088/0004-637X/805/2/186. arXiv: 1503.07362.

Lee, C.-F. et al. (2017). "A rotating protostellar jet launched from the innermost disk of HH 212". In: *Nature Astronomy* 1, 0152, p. 0152. DOI: 10.1038/s41550-017-0152. arXiv: 1706.06343.

Lee, E. J., M.-A. Miville-Deschênes, and N. W. Murray (2016). "Observational Evidence of Dynamic Star Formation Rate in Milky Way Giant Molecular Clouds". In: *ApJ* 833, 229, p. 229. DOI: 10.3847/1538-4357/833/2/229. arXiv: 1608.05415.

Lee, J.-J. et al. (2014). "UKIRT Widefield Infrared Survey for Fe$^+$". In: *MNRAS* 443, pp. 2650–2660. DOI: 10.1093/mnras/stu1146. arXiv: 1406.4271.

Lee, K. I. et al. (2016). "Misalignment of Outflow Axes in the Proto-multiple Systems in Perseus". In: *ApJ* 820, L2, p. L2. DOI: 10.3847/2041-8205/820/1/L2. arXiv: 1602.07397 [astro-ph.SR].

Lee, Y.-H., B.-C. Koo, and J.-J. Lee (2014). "Supernova Remnants in the UWISH2 and UWIFE Surveys". In: *Supernova Environmental Impacts*. Ed. by A. Ray and R. A. McCray. Vol. 296. IAU Symposium, pp. 370–371. DOI: 10.1017/S1743921313009873.

Lepp, S. and J. M. Shull (1983). "The kinetic theory of H2 dissociation". In: *ApJ* 270, pp. 578–582. DOI: 10.1086/161149.

Leurini, S. et al. (2013). "Evidence of a SiO collimated outflow from a massive YSO in IRAS 17233-3606". In: *A&A* 554, A35, A35. DOI: 10.1051/0004-6361/201118154. arXiv: 1304.4401.

Li, Z.-Y. et al. (2014). "The Earliest Stages of Star and Planet Formation: Core Collapse, and the Formation of Disks and Outflows". In: *Protostars and Planets VI*, pp. 173–194. DOI: 10.2458/azu_uapress_9780816531240-ch008. arXiv: 1401.2219 [astro-ph.SR].

Livio, M. (1999). "Astrophysical jets: a phenomenological examination of acceleration and collimation." In: *Phys. Rep.* 311, pp. 225–245. DOI: 10.1016/S0370-1573(98)00102-1.

– (2011). "Astrophysical Jets". In: *American Institute of Physics Conference Series*. Ed. by J. E. McEnery, J. L. Racusin, and N. Gehrels. Vol. 1358. American Institute of Physics Conference Series, pp. 329–333. DOI: 10.1063/1.3621799.

Lovelace, Richard V. E. et al. (2014). "On the origin of jets from disc-accreting magnetized stars". In: *Computational Astrophysics and Cosmology* 1, 3, p. 3. DOI: 10.1186/s40668-014-0003-5.

Lucas, P. W. et al. (2008). "The UKIDSS Galactic Plane Survey". In: *MNRAS* 391, pp. 136–163. DOI: 10.1111/j.1365-2966.2008.13924.x. arXiv: 0712.0100.

Lucas, P. W. et al. (2017). "Extreme infrared variables from UKIDSS – II. An end-of-survey catalogue of eruptive YSOs and unusual stars". In: *MNRAS* 472, pp. 2990–3020. DOI: 10.1093/mnras/stx2058. arXiv: 1708.02680 [astro-ph.SR].

Lumsden, S. L. et al. (2013). "The Red MSX Source Survey: The Massive Young Stellar Population of Our Galaxy". In: *ApJS* 208, 11, p. 11. DOI: 10.1088/0067-0049/208/1/11. arXiv: 1308.0134.

Lynds, B. T. (1962). "Catalogue of Dark Nebulae." In: *ApJS* 7, p. 1. DOI: 10.1086/190072.

Lynds, B. T. (1970). "The Distribution of Dark Nebulae in Late-Type Spirals". In: *The Spiral Structure of our Galaxy*. Ed. by W. Becker and G. I. Kontopoulos. Vol. 38. IAU Symposium, p. 26.

Mac Low, M.-M. and R. S. Klessen (2004). "Control of star formation by supersonic turbulence". In: *Reviews of Modern Physics* 76, pp. 125–194. DOI: 10.1103/RevModPhys.76.125. eprint: astro-ph/0301093.

Mac Low, M.-M. et al. (1998). "The Decay of Supersonic and Super-Alfvénic Turbulence in Star-Forming Clouds". In: *Ap&SS* 261, pp. 195–196. DOI: 10.1023/A:1002036113496.

Majaess, D. (2013). "Discovering protostars and their host clusters via WISE". In: *Ap&SS* 344, pp. 175–186. DOI: 10.1007/s10509-012-1308-y. arXiv: 1211.4032 [astro-ph.SR].

Makin, S. V. and D. Froebrich (2018). "YSO Jets in the Galactic Plane from UWISH2. IV. Jets and Outflows in Cygnus-X". In: *ApJS* 234, 8, p. 8. DOI: 10.3847/1538-4365/aa8862. arXiv: 1708.00394 [astro-ph.SR].

Marshall, H. L. et al. (2002). "A High-Resolution X-Ray Image of the Jet in M87". In: *ApJ* 564, pp. 683–687. DOI: 10.1086/324396. eprint: astro-ph/0109160.

Masson, J. et al. (2016). "Ambipolar diffusion in low-mass star formation. I. General comparison with the ideal magnetohydrodynamic case". In: *A&A* 587, A32, A32. DOI: 10.1051/0004-6361/201526371. arXiv: 1509.05630 [astro-ph.SR].

Mathis, J. S. (1990). "Interstellar dust and extinction". In: *ARA&A* 28, pp. 37–70. DOI: 10.1146/annurev.aa.28.090190.000345.

Matt, S. and R. E. Pudritz (2005). "Accretion-powered Stellar Winds as a Solution to the Stellar Angular Momentum Problem". In: *ApJ* 632, pp. L135–L138. DOI: 10.1086/498066. eprint: astro-ph/0510060.

McCaughrean, M. et al. (2002). "Standing on the shoulder of a giant: ISAAC, Antu, and star formation". In: *The Messenger* 109, pp. 28–36.

McGroarty, F., T. P. Ray, and D. Froebrich (2007). "Proper motion studies of outflows from Classical T Tauri stars". In: *A&A* 467, pp. 1197–1207. DOI: 10.1051/0004-6361:20066863. eprint: astro-ph/0703405.

McKee, C. F. and E. C. Ostriker (2007). "Theory of Star Formation". In: *ARA&A* 45, pp. 565–687. DOI: 10.1146/annurev.astro.45.051806.110602. arXiv: 0707.3514.

McKee, C. F. and J. C. Tan (2003). "The Formation of Massive Stars from Turbulent Cores". In: *ApJ* 585, pp. 850–871. DOI: 10.1086/346149. eprint: astro-ph/0206037.

McLeod, A. F. et al. (2018). "A parsec-scale optical jet from a massive young star in the Large Magellanic Cloud". In: *Nature* 554, pp. 334–336. DOI: 10.1038/nature25189. arXiv: 1801.08147 [astro-ph.SR].

Mestel, L. (1965). "Problems of Star Formation - I". In: *QJRAS* 6, p. 161.

Miszalski, B. et al. (2008). "MASH-II: more planetary nebulae from the AAO/UKST Hα survey". In: *MNRAS* 384, pp. 525–534. DOI: 10.1111/j.1365-2966.2007.12727.x. arXiv: 0711.2923.

Mocz, P. et al. (2017). "Moving-mesh Simulations of Star-forming Cores in Magneto-gravo-turbulence". In: *ApJ* 838, 40, p. 40. DOI: 10.3847/1538-4357/aa6475. arXiv: 1702.06133.

Mooney, T. J. and P. M. Solomon (1988). "Star formation rates and the far-infrared luminosity of Galactic molecular clouds". In: *ApJ* 334, pp. L51–L54. DOI: `10.1086/185310`.

Moscadelli, L. et al. (2002). "Kinematics of the 12 GHz Methanol Masers toward W3(OH)". In: *ApJ* 564, pp. 813–826. DOI: `10.1086/324304`.

Motte, F., S. Bontemps, and F. Louvet (2017). "High-Mass Star and Massive Cluster Formation in the Milky Way". In: *ArXiv e-prints*. arXiv: `1706.00118`.

Motte, F. et al. (2001). "A SCUBA survey of the NGC 2068/2071 protoclusters". In: *A&A* 372, pp. L41–L44. DOI: `10.1051/0004-6361:20010543`. eprint: `astro-ph/0105019`.

Motte, F. et al. (2005). "The earliest phases of massive star formation within entire molecular cloud complexes". In: *Massive Star Birth: A Crossroads of Astrophysics*. Ed. by R. Cesaroni et al. Vol. 227. IAU Symposium, pp. 151–156. DOI: `10.1017/S1743921305004473`.

Motte, F. et al. (2007). "The earliest phases of high-mass star formation: a 3 square degree millimeter continuum mapping of Cygnus X". In: *A&A* 476, pp. 1243–1260. DOI: `10.1051/0004-6361:20077843`. arXiv: `0708.2774`.

Mundt, R., T. P. Ray, and A. C. Raga (1991). "Collimation of Stellar Jets - Constraints from the Observed Spatial Structure - Part Two - Observational Results". In: *A&A* 252, p. 740.

Murphy, G. C. et al. (2008). "Interacting jets from binary protostars". In: *A&A* 478, pp. 453–460. DOI: `10.1051/0004-6361:20078609`. arXiv: `0711.3144`.

Murray, D. W. et al. (2017). "Collapse in self-gravitating turbulent fluids". In: *MNRAS* 465, pp. 1316–1335. DOI: `10.1093/mnras/stw2796`. arXiv: `1509.05910`.

Murray, D., S. Goyal, and P. Chang (2018). "The effects of protostellar jet feedback on turbulent collapse". In: *MNRAS* 475, pp. 1023–1035. DOI: `10.1093/mnras/stx3153`. arXiv: `1710.09415`.

Myers, A. T. et al. (2014). "Star cluster formation in turbulent, magnetized dense clumps with radiative and outflow feedback". In: *MNRAS* 439, pp. 3420–3438. DOI: `10.1093/mnras/stu190`. arXiv: `1401.6096`.

Myers, P. C. and G. A. Fuller (1992). "Density structure and star formation in dense cores with thermal and nonthermal motions". In: *ApJ* 396, pp. 631–642. DOI: `10.1086/171744`.

Myers, P. C. and E. F. Ladd (1993). "Bolometric temperatures of young stellar objects". In: *ApJ* 413, pp. L47–L50. DOI: `10.1086/186956`.

Nadeau, D., M. Riopel, and T. R. Geballe (1991). "The extinction to the H2 line emission in the DR 21 outflow source". In: *ApJ* 372, pp. L103–L106. DOI: `10.1086/186034`.

Nakamura, F. and Z.-Y. Li (2005). "Quiescent Cores and the Efficiency of Turbulence-accelerated, Magnetically Regulated Star Formation". In: *ApJ* 631, pp. 411–428. DOI: `10.1086/432606`. eprint: `astro-ph/0502130`.

Narita, S., C. Hayashi, and S. M. Miyama (1984). "Characteristics of Collapse of Rotating Isothermal Clouds". In: *Progress of Theoretical Physics* 72, pp. 1118–1136. DOI: `10.1143/PTP.72.1118`.

Navarete, F. et al. (2015). "A survey of extended H_2 emission from massive YSOs". In: *MNRAS* 450, pp. 4364–4398. DOI: `10.1093/mnras/stv914`. arXiv: `1504.06174 [astro-ph.SR]`.

Neugebauer, G. et al. (1984). "The Infrared Astronomical Satellite (IRAS) mission". In: *ApJ* 278, pp. L1–L6. DOI: `10.1086/184209`.

Nicholas, Jack (2016). "Photometry of the UWISH2 extended H2 source catalogue". PhD thesis. University of Kent. URL: http://kar.kent.ac.uk/54879/.

Nolan, C. A. et al. (2017). "Centrifugally driven winds from protostellar accretion discs - I. Formulation and initial results". In: *MNRAS* 471, pp. 1488–1505. DOI: 10.1093/mnras/stx1642. arXiv: 1707.01088 [astro-ph.SR].

Noriega-Crespo, A. et al. (2014). "Proper motions of young stellar outflows in the mid-infrared with Spitzer II HH 377/Cep E". In: *New Journal of Physics* 16.10, 105008, p. 105008. DOI: 10.1088/1367-2630/16/10/105008. arXiv: 1407.6009 [astro-ph.IM].

Offner, S. S. R. and H. G. Arce (2014). "Investigations of Protostellar Outflow Launching and Gas Entrainment: Hydrodynamic Simulations and Molecular Emission". In: *ApJ* 784, 61, p. 61. DOI: 10.1088/0004-637X/784/1/61. arXiv: 1312.0951 [astro-ph.SR].

– (2015). "Impact of Winds from Intermediate-mass Stars on Molecular Cloud Structure and Turbulence". In: *ApJ* 811, 146, p. 146. DOI: 10.1088/0004-637X/811/2/146. arXiv: 1508.07008.

Offner, S. S. R. and J. Chaban (2017). "Impact of Protostellar Outflows on Turbulence and Star Formation Efficiency in Magnetized Dense Cores". In: *ApJ* 847, 104, p. 104. DOI: 10.3847/1538-4357/aa8996. arXiv: 1709.01086.

Ouyed, R. and R. E. Pudritz (1997). "Numerical Simulations of Astrophysical Jets from Keplerian Disks. I. Stationary Models". In: *ApJ* 482, pp. 712–732. DOI: 10.1086/304170.

Padoan, P. and Å. Nordlund (2002). "The Stellar Initial Mass Function from Turbulent Fragmentation". In: *ApJ* 576, pp. 870–879. DOI: 10.1086/341790. eprint: astro-ph/0011465.

– (2011). "The Star Formation Rate of Supersonic Magnetohydrodynamic Turbulence". In: *ApJ* 730, 40, p. 40. DOI: 10.1088/0004-637X/730/1/40. arXiv: 0907.0248 [astro-ph.GA].

Padoan, P. et al. (2014). "The Star Formation Rate of Molecular Clouds". In: *Protostars and Planets VI*, pp. 77–100. DOI: 10.2458/azu_uapress_9780816531240-ch004. arXiv: 1312.5365.

Palau, A. et al. (2017). "Complex organic molecules tracing shocks along the outflow cavity in the high-mass protostar IRAS 20126+4104". In: *MNRAS* 467, pp. 2723–2752. DOI: 10.1093/mnras/stx004. arXiv: 1701.04802 [astro-ph.SR].

Panoglou, D. et al. (2012). "Molecule survival in magnetized protostellar disk winds. I. Chemical model and first results". In: *A&A* 538, A2, A2. DOI: 10.1051/0004-6361/200912861. arXiv: 1112.3248 [astro-ph.SR].

Parker, Q. A. et al. (2006). "The Macquarie/AAO/Strasbourg Hα Planetary Nebula Catalogue: MASH". In: *MNRAS* 373, pp. 79–94. DOI: 10.1111/j.1365-2966.2006.10950.x.

Pech, G. et al. (2012). "A Rotating Molecular Jet from a Perseus Protostar". In: *ApJ* 751, 78, p. 78. DOI: 10.1088/0004-637X/751/1/78. arXiv: 1204.3585.

Peretto, N., P. André, and A. Belloche (2006). "Probing the formation of intermediate- to high-mass stars in protoclusters. A detailed millimeter study of the NGC 2264 clumps". In: *A&A* 445, pp. 979–998. DOI: 10.1051/0004-6361:20053324. eprint: astro-ph/0508619.

Peters, T. et al. (2014). "Collective Outflow from a Small Multiple Stellar System". In: *ApJ* 788, 14, p. 14. DOI: 10.1088/0004-637X/788/1/14. arXiv: 1404.5463 [astro-ph.SR].

Piddington, J. H. and H. C. Minnett (1952). "Radio-Frequency Radiation from the Constellation of Cygnus". In: *Australian Journal of Scientific Research A Physical Sciences* 5, p. 17. DOI: 10.1071/PH520017.

Plunkett, A. L. et al. (2015). "Assessing Molecular Outflows and Turbulence in the Protostellar Cluster Serpens South". In: *ApJ* 803, 22, p. 22. DOI: 10.1088/0004-637X/803/1/22. arXiv: 1503.01111 [astro-ph.SR].

Pudritz, R. E., M. J. Hardcastle, and D. C. Gabuzda (2012). "Magnetic Fields in Astrophysical Jets: From Launch to Termination". In: *Space Sci. Rev.* 169, pp. 27–72. DOI: 10.1007/s11214-012-9895-z. arXiv: 1205.2073 [astro-ph.HE].

Pudritz, R. E. and C. A. Norman (1983). "Centrifugally driven winds from contracting molecular disks". In: *ApJ* 274, pp. 677–697. DOI: 10.1086/161481.

– (1986). "Bipolar hydromagnetic winds from disks around protostellar objects". In: *ApJ* 301, pp. 571–586. DOI: 10.1086/163924.

Raga, A. C., D. A. Williams, and A. J. Lim (2005). "The Formation of H[2] in Variable Herbig-Haro Jets". In: *Rev. Mexicana Astron. Astrofis.* 41, pp. 137–146.

Raga, A. and S. Cabrit (1993). "Molecular outflows entrained by jet bowshocks". In: *A&A* 278, pp. 267–278.

Ray, T. et al. (2007). "Toward Resolving the Outflow Engine: An Observational Perspective". In: *Protostars and Planets V*, pp. 231–244. eprint: astro-ph/0605597.

Rebull, L. M. et al. (2011). "The North American and Pelican Nebulae. II. MIPS Observations and Analysis". In: *ApJS* 193, 25, p. 25. DOI: 10.1088/0067-0049/193/2/25. arXiv: 1102.0573 [astro-ph.SR].

Reid, M. J. et al. (2009). "Trigonometric Parallaxes of Massive Star-Forming Regions. VI. Galactic Structure, Fundamental Parameters, and Noncircular Motions". In: *ApJ* 700, 137-148, pp. 137–148. DOI: 10.1088/0004-637X/700/1/137. arXiv: 0902.3913 [astro-ph.GA].

Reid, M. J. et al. (2014). "Trigonometric Parallaxes of High Mass Star Forming Regions: The Structure and Kinematics of the Milky Way". In: *ApJ* 783, 130, p. 130. DOI: 10.1088/0004-637X/783/2/130. arXiv: 1401.5377 [astro-ph.GA].

Reid, M. J. et al. (2016). "A Parallax-based Distance Estimator for Spiral Arm Sources". In: *ApJ* 823, 77, p. 77. DOI: 10.3847/0004-637X/823/2/77. arXiv: 1604.02433.

Reipurth, B. and J. Bally (2001). "Herbig-Haro Flows: Probes of Early Stellar Evolution". In: *ARA&A* 39, pp. 403–455. DOI: 10.1146/annurev.astro.39.1.403.

Reipurth, B., J. Bally, and D. Devine (1997). "Giant Herbig-Haro Flows". In: *AJ* 114, p. 2708. DOI: 10.1086/118681.

Reiter, M. et al. (2017). "Proper motions of collimated jets from intermediate-mass protostars in the Carina Nebula". In: *MNRAS* 470, pp. 4671–4697. DOI: 10.1093/mnras/stx1489. arXiv: 1706.04657 [astro-ph.SR].

Riaz, B. et al. (2017). "First Large-scale Herbig-Haro Jet Driven by a Proto-brown Dwarf". In: *ApJ* 844, 47, p. 47. DOI: 10.3847/1538-4357/aa70e8. arXiv: 1705.01170 [astro-ph.SR].

Riaz, R., S. Vanaverbeke, and D. R. G. Schleicher (2018). "Episodic accretion in binary protostars emerging from self-gravitating solar mass cores". In: *A&A* 614, A53, A53. DOI: 10.1051/0004-6361/201732076. arXiv: 1712.09646 [astro-ph.SR].

Rivera-Gálvez, S. et al. (2015). "The Young Stellar Population of the Cygnus-X DR15 Region". In: *AJ* 150, 191, p. 191. DOI: 10.1088/0004-6256/150/6/191. arXiv: 1510.02835 [astro-ph.SR].

Roman-Duval, J. et al. (2009). "Kinematic Distances to Molecular Clouds Identified in the Galactic Ring Survey". In: *ApJ* 699, pp. 1153–1170. DOI: 10.1088/0004-637X/699/2/1153. arXiv: 0905.0723 [astro-ph.GA].

Rosolowsky, E. et al. (2010). "The Bolocam Galactic Plane Survey. II. Catalog of the Image Data". In: *ApJS* 188, 123-138, pp. 123–138. DOI: 10.1088/0067-0049/188/1/123. arXiv: 0909.2871.

Rydgren, A. E., S. E. Strom, and K. M. Strom (1976). "The nature of the objects of Joy - A study of the T Tauri phenomenon". In: *ApJS* 30, pp. 307–336. DOI: 10.1086/190364.

Rygl, K. L. J. et al. (2012). "Parallaxes and proper motions of interstellar masers toward the Cygnus X star-forming complex. I. Membership of the Cygnus X region". In: *A&A* 539, A79, A79. DOI: 10.1051/0004-6361/201118211. arXiv: 1111.7023.

Sabin, L. et al. (2014). "First release of the IPHAS catalogue of new extended planetary nebulae". In: *MNRAS* 443, pp. 3388–3401. DOI: 10.1093/mnras/stu1404. arXiv: 1407.0109 [astro-ph.SR].

Samal, M. R. et al. (2018). "YSO jets in the Galactic plane from UWISH2 - V. Jets and outflows in M17". In: *MNRAS* 477, pp. 4577–4595. DOI: 10.1093/mnras/sty853. arXiv: 1803.11413.

Sandstrom, K. M. et al. (2007). "A Parallactic Distance of 389^{+24}_{-21} Parsecs to the Orion Nebula Cluster from Very Long Baseline Array Observations". In: *ApJ* 667, pp. 1161–1169. DOI: 10.1086/520922. arXiv: 0706.2361.

Schlegel, D. J., D. P. Finkbeiner, and M. Davis (1998). "Maps of Dust Infrared Emission for Use in Estimation of Reddening and Cosmic Microwave Background Radiation Foregrounds". In: *ApJ* 500, pp. 525–553. DOI: 10.1086/305772. eprint: astro-ph/9710327.

Schmeja, S. and R. S. Klessen (2004). "Protostellar mass accretion rates from gravoturbulent fragmentation". In: *A&A* 419, pp. 405–417. DOI: 10.1051/0004-6361:20034375. arXiv: astro-ph/0402433 [astro-ph].

Schmidt, M. (1965). "Rotation Parameters and Distribution of Mass in the Galaxy". In: *Giornale di Astronomia*. Ed. by A. Blaauw and M. Schmidt. the University of Chicago Press, p. 513.

Schneider, N. et al. (2006). "A new view of the Cygnus X region. KOSMA ^{13}CO 2 to 1, 3 to 2, and ^{12}CO 3 to 2 imaging". In: *A&A* 458, pp. 855–871. DOI: 10.1051/0004-6361:20065088.

Scholz, A., D. Froebrich, and K. Wood (2013). "A systematic survey for eruptive young stellar objects using mid-infrared photometry". In: *MNRAS* 430, pp. 2910–2922. DOI: 10.1093/mnras/stt091. arXiv: 1301.3152 [astro-ph.SR].

Scholz, A. and R. Jayawardhana (2006). "Variable Accretion and Outflow in Young Brown Dwarfs". In: *ApJ* 638, pp. 1056–1069. DOI: 10.1086/498973. eprint: astro-ph/0510629.

Scholz, F. W. and M. A. Stephens (1987). "K-Sample Anderson–Darling Tests". In: *Journal of the American Statistical Association* 82.399, pp. 918–924. DOI: 10.1080/01621459.1987.10478517. eprint: https://doi.org/10.1080/01621459.1987.10478517. URL: https://doi.org/10.1080/01621459.1987.10478517.

Seale, J. P. and L. W. Looney (2008). "Morphological Evolution of Bipolar Outflows from Young Stellar Objects". In: *ApJ* 675, pp. 427–442. DOI: `10.1086/526766`.

Shang, H., Z.-Y. Li, and N. Hirano (2007). "Jets and Bipolar Outflows from Young Stars: Theory and Observational Tests". In: *Protostars and Planets V*, pp. 261–276.

Shang, H. et al. (2004). "Free-free Radio Emission from Young Stellar Objects". In: *ApJ* 612, pp. L69–L72. DOI: `10.1086/424566`.

Sharpless, S. (1965). "Distribution of Associations, Emission Regions, Galactic Clusters and Supergiants". In: *Giornale di Astronomia*. Ed. by A. Blaauw and M. Schmidt. the University of Chicago Press, p. 131.

Shu, F. H. (1977). "Self-similar collapse of isothermal spheres and star formation". In: *ApJ* 214, pp. 488–497. DOI: `10.1086/155274`.

Shu, F. H., F. C. Adams, and S. Lizano (1987a). "Star formation in molecular clouds - Observation and theory". In: *ARA&A* 25, pp. 23–81. DOI: `10.1146/annurev.aa.25.090187.000323`.

– (1987b). "Star formation in molecular clouds - Observation and theory". In: *ARA&A* 25, pp. 23–81. DOI: `10.1146/annurev.aa.25.090187.000323`.

Shu, F. H. et al. (1991). "Star formation and the nature of bipolar outflows". In: *ApJ* 370, pp. L31–L34. DOI: `10.1086/185970`.

Shu, F. H. et al. (1997). "X-rays and fluctuating X-winds from protostars." In: *Science* 277, pp. 1475–1479. DOI: `10.1126/science.277.5331.1475`.

Shu, F. et al. (1994). "Magnetocentrifugally driven flows from young stars and disks. 1: A generalized model". In: *ApJ* 429, pp. 781–796. DOI: `10.1086/174363`.

Shull, J. M. and S. Beckwith (1982). "Interstellar molecular hydrogen". In: *ARA&A* 20, pp. 163–190. DOI: `10.1146/annurev.aa.20.090182.001115`.

Skrutskie, M. F. et al. (2006). "The Two Micron All Sky Survey (2MASS)". In: *AJ* 131, pp. 1163–1183. DOI: `10.1086/498708`.

Smith, M. D. (1995). "Predictions for JHK photometry of molecular shocks." In: *A&A* 296, p. 789.

Smith, M. D. and P. W. J. L. Brand (1990). "Cool C-shocks and high-velocity flows in molecular clouds". In: *MNRAS* 242, pp. 495–504. DOI: `10.1093/mnras/242.3.495`.

Smith, M. D., G. Suttner, and H. W. Yorke (1997). "Numerical hydrodynamic simulations of jet-driven bipolar outflows." In: *A&A* 323, pp. 223–230.

Snell, R. L., R. B. Loren, and R. L. Plambeck (1980). "Observations of CO in L1551 - Evidence for stellar wind driven shocks". In: *ApJ* 239, pp. L17–L22. DOI: `10.1086/183283`.

Snowden, S. L. et al. (1994). "Soft X-ray and H I surveys of the low N_H region in Ursa Major". In: *ApJ* 430, pp. 601–609. DOI: `10.1086/174434`.

Spitzer Jr., L. (1990). "Theories of the hot interstellar gas". In: *ARA&A* 28, pp. 71–101. DOI: `10.1146/annurev.aa.28.090190.000443`.

Stanke, T. (2000). "An unbiased infrared H2 search for embedded flows from young stars in Orion A". PhD thesis. PhD Thesis, Mathematisch-Naturwissenschaftlichen Fakultät der Universität Potsdam.

– (2003). "Observations of molecular jets in Orion A". In: *Ap&SS* 287, pp. 149–160. DOI: `10.1023/B:ASTR.0000006215.36397.fe`.

Stanke, T., M. J. McCaughrean, and H. Zinnecker (2002). "An unbiased H$_2$ survey for protostellar jets in Orion A. II\@. The infrared survey data". In: *A&A* 392, pp. 239–266. DOI: 10.1051/0004-6361:20020763.

Stephens, I. W. et al. (2017). "Alignment between Protostellar Outflows and Filamentary Structure". In: *ApJ* 846, 16, p. 16. DOI: 10.3847/1538-4357/aa8262. arXiv: 1707.08122.

Stone, J. M. and M. L. Norman (1993). "Numerical simulations of protostellar jets with nonequilibrium cooling. I - Method and two-dimensional results. II - Models of pulsed jets". In: *ApJ* 413, pp. 198–220. DOI: 10.1086/172988.

Stone, J. M., E. C. Ostriker, and C. F. Gammie (1998). "Dissipation in Compressible Magnetohydrodynamic Turbulence". In: *ApJ* 508, pp. L99–L102. DOI: 10.1086/311718. eprint: astro-ph/9809357.

Straižys, V. and V. Laugalys (2008). "O-Like Stars in the Direction of the North America and Pelican Nebulae". In: *Baltic Astronomy* 17, pp. 143–159. arXiv: 0809.3229.

Straizys, V. et al. (1989). "Interstellar extinction in the area of the North America and Pelican Nebulae complex". In: *A&A* 222, pp. 82–84.

Tan, J. C. et al. (2014). "Massive Star Formation". In: *Protostars and Planets VI*, pp. 149–172. DOI: 10.2458/azu_uapress_9780816531240-ch007. arXiv: 1402.0919.

Tan, J. C. et al. (2016). "An Ordered Bipolar Outflow from a Massive Early-stage Core". In: *ApJ* 821, L3, p. L3. DOI: 10.3847/2041-8205/821/1/L3. arXiv: 1601.07043.

Terquem, C. et al. (1999). "Precession of Collimated Outflows from Young Stellar Objects". In: *ApJ* 512, pp. L131–L134. DOI: 10.1086/311880. eprint: astro-ph/9812155.

Tilley, D. A. and R. E. Pudritz (2007). "The formation of star clusters - II. 3D simulations of magnetohydrodynamic turbulence in molecular clouds". In: *MNRAS* 382, pp. 73–94. DOI: 10.1111/j.1365-2966.2007.12371.x. eprint: astro-ph/0508562.

Trinidad, M. A. et al. (2003). "Observations of Water Masers and Radio Continuum Emission in AFGL 2591". In: *ApJ* 589, pp. 386–396. DOI: 10.1086/374618.

Urquhart, J. S. et al. (2012). "The RMS survey: resolving kinematic distance ambiguities towards a sample of compact H ii regions using H i absorption*". In: *MNRAS* 420, pp. 1656–1672. DOI: 10.1111/j.1365-2966.2011.20157.x. arXiv: 1111.1625.

Varricatt, W. P. et al. (2010). "A near-IR imaging survey of intermediate- and high-mass young stellar outflow candidates". In: *MNRAS* 404, pp. 661–720. DOI: 10.1111/j.1365-2966.2010.16356.x. arXiv: 1001.2708 [astro-ph.SR].

Vázquez-Semadeni, E., J. Kim, and J. Ballesteros-Paredes (2005). "Star Formation Efficiency in Driven, Supercritical, Turbulent Clouds". In: *ApJ* 630, pp. L49–L52. DOI: 10.1086/491650. eprint: astro-ph/0507637.

Véron, P. (1965). "Le complexe du Cygne". In: *Annales d'Astrophysique* 28, p. 391.

Vink, Jorick S. (2018). "Very massive stars: a metallicity-dependent upper-mass limit, slow winds, and the self-enrichment of globular clusters". In: *A&A* 615, A119, A119. DOI: 10.1051/0004-6361/201832773. arXiv: 1803.08042 [astro-ph.SR].

Vogel, S. N. and L. V. Kuhi (1981). "Rotational velocities of pre-main-sequence stars". In: *ApJ* 245, pp. 960–976. DOI: 10.1086/158872.

Vorobyov, E. I. and S. Basu (2006). "The Burst Mode of Protostellar Accretion". In: *ApJ* 650, pp. 956–969. DOI: 10.1086/507320. eprint: astro-ph/0607118.

Walter, F. M. (1986). "X-ray sources in regions of star formation. I - The naked T Tauri stars". In: *ApJ* 306, pp. 573–586. DOI: 10.1086/164367.

Wang, P. et al. (2010). "Outflow Feedback Regulated Massive Star Formation in Parsec-Scale Cluster-Forming Clumps". In: *ApJ* 709, pp. 27–41. DOI: 10.1088/0004-637X/709/1/27. arXiv: 0908.4129 [astro-ph.SR].

Ward-Thompson, D., P. André, and J. M. Kirk (2002). "The initial conditions of isolated star formation - V. ISOPHOT imaging and the temperature and energy balance of pre-stellar cores". In: *MNRAS* 329, pp. 257–276. DOI: 10.1046/j.1365-8711.2002.04969.x. eprint: astro-ph/0109173.

Weise, P. et al. (2010). "Rotational velocities of nearby young stars". In: *A&A* 517, A88, A88. DOI: 10.1051/0004-6361/201014453. arXiv: 1005.0984 [astro-ph.SR].

Wendker, H. J., D. Benz, and J. W. M. Baars (1983). "The Cygnus X region. XIV - The radio continuum of the North America-Pelican nebulae". In: *A&A* 124, pp. 116–122.

Whelan, E. T. et al. (2005). "A resolved outflow of matter from a brown dwarf". In: *Nature* 435, pp. 652–654. DOI: 10.1038/nature03598. eprint: astro-ph/0506485.

Whelan, E. T. et al. (2007). "Discovery of a Bipolar Outflow from 2MASSW J1207334-393254, a 24 M_{Jup} Brown Dwarf". In: *ApJ* 659, pp. L45–L48. DOI: 10.1086/516734. eprint: astro-ph/0703112.

Whitaker, J. S. et al. (2017). "MALT90 Kinematic Distances to Dense Molecular Clumps". In: *AJ* 154, 140, p. 140. DOI: 10.3847/1538-3881/aa86ad.

Whittet, D. C. B. et al. (1988). "Infrared spectroscopy of dust in the Taurus dark clouds - Ice and silicates". In: *MNRAS* 233, pp. 321–336. DOI: 10.1093/mnras/233.2.321.

Wienen, M. et al. (2015). "ATLASGAL - Kinematic distances and the dense gas mass distribution of the inner Galaxy". In: *A&A* 579, A91, A91. DOI: 10.1051/0004-6361/201424802. arXiv: 1503.00007 [astro-ph.SR].

Wilking, B. A. et al. (1990). "Shocked molecular hydrogen emission from Herbig-Haro objects and their exciting stars". In: *AJ* 99, pp. 344–352. DOI: 10.1086/115333.

Williams, D. R. W. and R. D. Davies (1954). "A Method for the Measurement of the Distance of Radio Stars". In: *Nature* 173, pp. 1182–1183. DOI: 10.1038/1731182a0.

Wolfire, M. G. and A. Konigl (1991). "Molecular line emission models of Herbig-Haro objects. I - H2 emission". In: *ApJ* 383, pp. 205–225. DOI: 10.1086/170777.

Wood, D. O. S. and E. Churchwell (1989). "The morphologies and physical properties of ultra-compact H II regions". In: *ApJS* 69, pp. 831–895. DOI: 10.1086/191329.

Yamamura, I. et al. (2010). "VizieR Online Data Catalog: AKARI/FIS All-Sky Survey Point Source Catalogues (ISAS/JAXA, 2010)". In: *VizieR Online Data Catalog* 2298.

Yorke, H. W. and C. Sonnhalter (2002). "On the Formation of Massive Stars". In: *ApJ* 569, pp. 846–862. DOI: 10.1086/339264. eprint: astro-ph/0201041.

Yu, K. C., J. Bally, and D. Devine (1997). "Shock-excited H_2 Flows in OMC-2 and OMC-3". In: *ApJ* 485, pp. L45–L48. DOI: 10.1086/310799. eprint: astro-ph/9706073.

Zapata, L. A. et al. (2010). "A rotating molecular jet in Orion". In: *A&A* 510, A2, A2. DOI: 10.1051/0004-6361/200810245. arXiv: 0903.5245.

Zapata, L. A. et al. (2013). "A 10,000 Year Old Explosion in DR21". In: *ApJ* 765, L29, p. L29. DOI: 10.1088/2041-8205/765/2/L29. arXiv: 1302.0208.

Zhang, M. et al. (2013a). "Proper motions of molecular hydrogen outflows in the ρ Ophiuchi molecular cloud". In: *A&A* 553, A41, A41. DOI: 10.1051/0004-6361/201220342. arXiv: 1304.0195 [astro-ph.SR].

Zhang, M. et al. (2015). "A Deep Near-infrared Survey toward the Aquila Molecular Cloud. I. Molecular Hydrogen Outflows". In: *ApJS* 219, 21, p. 21. DOI: 10.1088/0067-0049/219/2/21. arXiv: 1506.08372 [astro-ph.SR].

Zhang, Y. et al. (2013b). "A Massive Protostar Forming by Ordered Collapse of a Dense, Massive Core". In: *ApJ* 767, 58, p. 58. DOI: 10.1088/0004-637X/767/1/58. arXiv: 1302.3858.

Ziebarth, Kenneth (1970). "On the Upper Mass Limit for Main-Sequence Stars". In: *ApJ* 162, p. 947. DOI: 10.1086/150726.

Zinnecker, H., M. J. McCaughrean, and J. T. Rayner (1998). "A symmetrically pulsed jet of gas from an invisible protostar in Orion". In: *Nature* 394, pp. 862–865. DOI: 10.1038/29716.

Zinnecker, H. et al. (1999). "A search for young solar system analogues with the VLT". In: *A&A* 352, pp. L73–L78.